Transport of fine particles. Application to injectivity in geothermal reservoirs

Laurez Maya Fogouang

UNIVERSITÉ D'ORLÉANS

ÉCOLE DOCTORALE

Énergie - Matériaux - Sciences de la Terre et de l'Univers

Institut des Sciences de la Terre d'Orléans (ISTO)

THÈSE présentée par :

Laurez MAYA FOGOUANG

soutenue le : 14 Octobre 2024

pour obtenir le grade de : Docteur de l'Université d'Orléans

Discipline/ Spécialité : Sciences de l'univers

Transport of Fine Particles. Application to Injectivity in Geothermal Reservoirs

DIRECTEUR DE THESE :

Mr. SOULAINE Cyprien	Chargé de recherche, CNRS-ISTO

RAPPORTEURS :

Mr. BOURG Ian	Professeur, Princeton University
Mr. GOLFIER Fabrice	Professeur, Université de Lorraine

JURY :

Mme. RIBOT Magali	Professeure, Université d'Orléans, Présidente du jury
Mr. QUINTARD Michel	Directeur de recherche émérite, CNRS-IMFT, Examinateur
Mme. MARBACH Sophie	Chargée de recherche, CNRS-PHENIX, Examinatrice
Mr. MOLINS Sergi	Chercheur, Lawrence Berkeley National Lab, Examinateur
Mr. LEROY Philippe	Ing. de recherche, BRGM, Co-encadrement de thèse

MEMBRE INVITE :

Mr. ANDRÉ Laurent	Ing. de recherche, BRGM-ISTO, Co-encadrement de thèse

Acknowledgments

I would like to express my deepest gratitude to those who have supported and guided me throughout my doctoral journey.

First and foremost, I am profoundly thankful to my primary advisor, Cyprien Soulaine, for his unwavering guidance, insightful feedback, and encouragement. Your expertise and dedication have been instrumental in shaping this research and its completion. I am also deeply grateful to my BRGM advisors, Laurent André, and Philippe Leroy, for their invaluable contributions, constructive criticism, and continuous support throughout this process. Your diverse perspectives and profound knowledge have greatly enriched my research. I am also grateful to Laurent Oxarango, Olivier Liot, and Noura Eddaoui for their interesting discussions and suggestions regarding my papers submitted during this doctoral journey.

I extend my sincere appreciation to the Institute of Earth Sciences of Orléans (ISTO) for providing a stimulating research environment and fostering a collaborative atmosphere. The resources and facilities available at ISTO have been essential for the successful completion of this project. I would like to thank the Centre de Calcul Scientifique en région Centre-Val de Loire's (CaSciMoDOT) high-performance computational resources which provided computational tools to undergo parallel simulations during my Ph.D. thesis.

Special thanks go to the French Geological Survey (BRGM) and the Region Centre-Val de Loire for the funding of this doctoral thesis, which was accompanied by participation in conferences and summer schools, thus making it possible to create connections and discussions with scientific circles in the field of study. Particularly BRGM for its support and for creating an environment that encouraged academic and professional growth.

I would also like to acknowledge my colleagues and friends within the lab and the broader research community for their camaraderie, insightful discussions, and encouragement. Your support and friendship have made this journey not only productive but also enjoyable.

Lastly, I am deeply grateful to my family and loved ones for their unconditional support and patience. Your belief in me and your constant encouragement has been a source of strength and motivation throughout this endeavor.

Thank you all for being part of this academic journey.

Résumé étendu:

Transport de particules fines: application à l'injectivité dans les réservoirs géothermaux

Énergie géothermique et problème d'injectivité

Les énergies renouvelables telles que les centrales géothermiques conventionnelles exploitent des ressources hydrothermales naturelles, qui incluent des réservoirs d'eau chaude ou de vapeur situés relativement près de la surface de la Terre (Bertani, 2016). L'un des défis critiques dans l'exploitation efficace de ces systèmes, en interaction avec le sous-sol par des puits souterrains, est de maintenir une injectivité élevée (capacité du réservoir à accepter le fluide injecté et généralement exprimée en $m^3/s/MPa$) dans le réservoir. Un facteur significatif influençant l'injectivité est le colmatage des pores, un phénomène où la perméabilité de la roche du réservoir diminue en raison de l'accumulation de particules et d'autres substances dans les espaces poreux. L'impact du colmatage des pores sur l'injectivité est profond. À mesure que la perméabilité du réservoir diminue, la résistance à l'écoulement des fluides augmente, entraînant une baisse de l'injectivité. Cette réduction de l'injectivité peut entraîner des coûts opérationnels plus élevés, une efficacité réduite de l'extraction de chaleur et, finalement, le déclin prématuré du réservoir géothermique. Comprendre et atténuer le colmatage des pores est donc crucial pour la gestion durable des ressources géothermiques.

Injectivité et colmatage de pores par des particules solides

Différents mécanismes physico-chimiques de colmatage des pores contribuent à la perturbation et à la réduction de l'injectivité dans les réservoirs (voir figure A). Le sous-sol, constitué d'une matrice (par exemple, des minéraux) et de vide (par exemple, des pores, des cavités, des fractures), décrit un milieu poreux. Les fluides injectés contiennent des colloïdes (y compris des nanoparticules, des bactéries et des particules fines) en suspension provenant de la réactivité géochimique des fluides ou arrachés aux parois des pores. En effet, la précipitation in situ et le transport subséquent de particules solides réactives dans des conditions éloignées de l'équilibre ou le détachement et la mobilisation de fines – petites particules de sable ou d'argile faiblement attachées aux parois des pores – par des forces hydrodynamiques (Cerda, 1987) menacent l'injectivité des réservoirs géothermiques et pétroliers en réduisant la perméabilité près des puits.

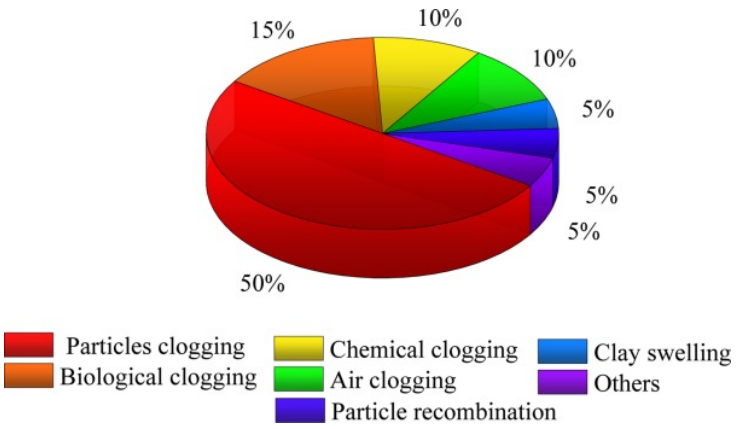

Figure A : Proportion de divers mécanismes de colmatage (Song et al., 2020).

Dans cette thèse, nous nous concentrons sur la réduction de la perméabilité due à la rétention de particules (Figure B). Trois mécanismes sont responsables du colmatage des pores par les particules : (i) le tamisage, (ii) le pontage, et (iii) l'agrégation des particules (Dressaire and Sauret, 2017). Le tamisage se réfère au blocage des particules basé sur l'exclusion par taille. Le pontage consiste en la formation de structures en forme de pont composées de quelques particules arrivant en même temps à l'entrée du pore où le flux converge. L'agrégation des particules résulte de dépôts successifs de particules colloïdales contrôlés par des forces électrochimiques à longue portée entre le fluide, les particules et la surface solide. Ainsi, une bonne compréhension de ces mécanismes de colmatage passe par une méthode précise de modélisation du transport des particules. Cependant, le transport des colloïdes conduisant au colmatage des pores est influencé par des paramètres physiques, chimiques et topologiques. La fluctuation locale des paramètres du fluide tels que le débit, la température, le pH, la force ionique et la composition ionique a un impact important sur les régimes de colmatage (Bradford et al., 2007; Li et al., 2008; Torkzaban et al., 2015; Xia et al., 2023; Rosenbrand et al., 2015; Yan et al., 2020; Muneer et al., 2020; Yuan et al., 2020; Pelley and Tufenkji, 2008; Sang et al., 2013; Gerber et al., 2019; Elimelech and O'Melia, 1990). De plus, la concentration, la taille et la forme des particules ont été signalées comme guidant le comportement de colmatage ainsi que la structure géométrique poreuse (Agbangla et al., 2012; Xie, 2014; Litton and Olson, 1996; Bennacer et al., 2017; Hafez et al., 2021; Auset and Keller, 2006).

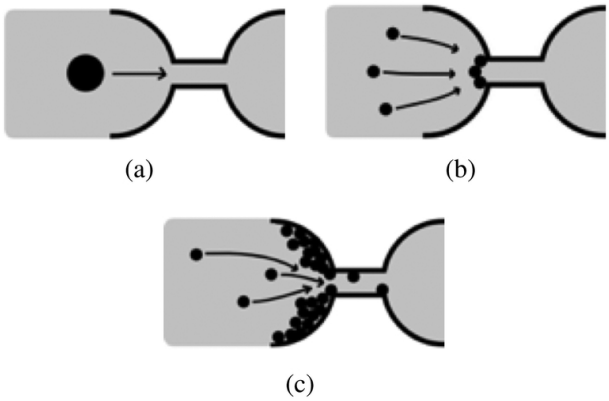

Figure B: Différents mécanismes responsables du colmatage des microcanaux à une constriction : (a) tamisage, (b) pontage, et (c) agrégation de particules Dressaire and Sauret (2017).

Stratégie scientifique pour modéliser le colmatage

Les milieux poreux peuvent être modélisés à l'aide de différents niveaux de description allant de l'échelle des pores à l'échelle continue du volume élémentaire représentatif. Ainsi, la description mathématique des processus impliqués dans l'écoulement dans les milieux poreux varie en fonction de la résolution de la modélisation et, par conséquent, de la taille du système étudié. Idéalement, ces deux descriptions devraient converger vers les mêmes résultats. Cependant, certaines différences fondamentales dans leur formalisme les en empêchent. Selon l'objectif, ces deux techniques sont fréquemment employées car elles sont complémentaires. La description à l'échelle des pores est nécessaire pour comprendre les phénomènes de surface comme l'adsorption de colloïdes, tandis que l'approche à l'échelle continue est souvent suffisante pour la conception de processus où l'écoulement des fluides, le transfert de chaleur et de masse sont de la plus haute importance. L'approche classique pour développer des modèles prédictifs à l'échelle continue consiste à envisager une stratégie de modélisation impliquant une cascade d'échelles imbriquées les unes dans les autres comme indiquée sur la figure C. Ensuite, des techniques d'homogénéisation et/ou une

analyse statistique sont utilisées pour combler l'écart entre les échelles.

Les récents progrès en imagerie, microfluidique et modélisation computationnelle offrent de nouvelles possibilités pour étudier le transport de particules et le colmatage des pores à l'échelle des pores. Les dispositifs microfluidiques sont de plus en plus utilisés dans le domaine des géosciences car ils permettent un contrôle précis ainsi qu'une visualisation directe et en temps réel des flux, des réactions et des mécanismes de transport à l'échelle des pores (Auset and Keller, 2006). Les modèles à l'échelle des pores pour le transport colloïdal sont encore rares. Les approches à la pointe de la technologie résolvent l'écoulement des fluides en utilisant les équations de Navier-Stokes, les méthodes de Lattice-Boltzmann, la dynamique des particules lissées (en anglais "smoothed particle hydrodynamics") ou encore les modèles de réseau de pores (Soulaine et al., 2021) et suivent le mouvement des particules de manière lagrangienne. D'autres méthodes modélisent le nuage de particules comme une phase continue (par exemple, modèle à deux fluides, modèle de transport de soluté), utilisant ainsi des lois constitutives pour modéliser les conditions interfaciales fluide-particules (Dennis, 2013). Le couplage entre l'écoulement des fluides et le transport des particules soulève d'importants défis ouverts. Premièrement, une description précise de la rétroaction entre le transport des particules et l'écoulement des fluides est essentielle pour capturer la rétention des particules et la réduction de la perméabilité. Deuxièmement, l'interaction entre les particules dépend non seulement des effets hydromécaniques (par exemple, flottabilité, traînée, contact) mais aussi des forces intermoléculaires. Enfin, il est nécessaire de confronter les prédictions des simulations avec des ensembles de données de référence.

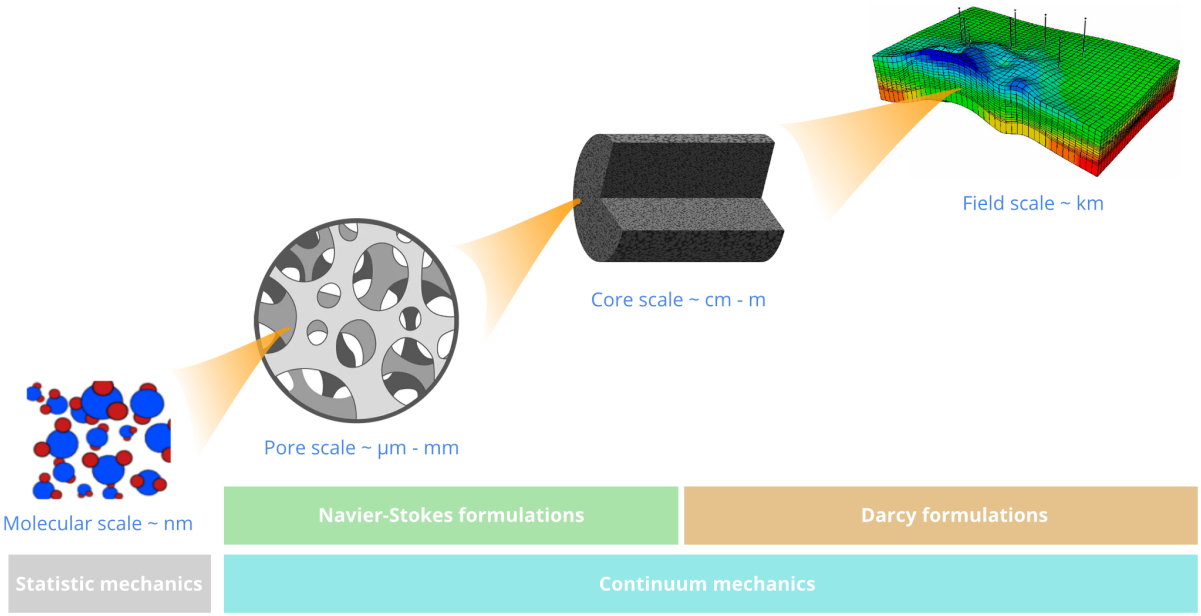

Figure C : Stratégie de modélisation utilisant une cascade d'échelles imbriquées les unes dans les autres pour le transport dans les milieux poreux.

Un nouveau simulateur pour le colmatage particulaire à l'échelle des pores.

Dans cette thèse, nous présentons une approche novatrice pour simuler le transport colloïdal à l'échelle des pores. Nous avons développé un nouveau simulateur basé sur l'approche "Computational Fluid Dynamics-Discrete Element Method" (CFD-DEM) (Tsuji et al., 1993). Cette approche appartient à la méthode Euler-Lagrange dans laquelle l'écoulement des fluides est résolu sur une grille eulérienne fixe

avec la méthode des volumes finis en utilisant une plateforme de dynamique des fluides computationnelle, et les particules sont suivies individuellement de manière lagrangienne en utilisant une méthode des éléments discrets. CFD-DEM est un couplage à quatre voies ("four-way" en anglais). Cela signifie que les particules sont transportées par le champ d'écoulement, qu'il y a une rétroaction des particules sur l'écoulement, et que les particules interagissent entre elles et avec les parois. Contrairement à d'autres méthodes CFD-DEM, notre approche est indépendante de la résolution et du type de grille (c'est-à-dire structurée ou non structurée) et n'est pas limitée aux particules plus petites que la taille de la cellule. Elle repose sur une formulation hybride résolue-non résolue pour le calcul de la force de traînée et une stratégie de recherche efficace – appelée recherche de pair à pair – pour identifier les cellules CFD couvertes par les particules DEM. Nous avons également mis en œuvre un filtre de lissage diffusif pour éliminer les oscillations non physiques lorsque les particules traversent l'interface de cellule à cellule.

L'écoulement continu du fluide porteur est calculé en résolvant les équations de Navier-Stokes moyennées par volume (VANS) (Whitaker, 1996) sur la grille eulérienne, qui tient compte de la présence des particules dans les cellules de la grille. Les équations VANS s'écrivent :

$$\frac{\partial(\epsilon\rho_f)}{\partial t} + \nabla.(\epsilon\rho_f \mathbf{v}^f) = 0,$$

$$\frac{\partial(\epsilon\rho_f \mathbf{v}^f)}{\partial t} + \nabla.(\epsilon\rho_f \mathbf{v}^f \mathbf{v}^f) = -\epsilon\nabla p + \epsilon\rho_f \mathbf{g} + \epsilon\nabla.(\mu_f(\nabla\mathbf{v}^f + (\nabla\mathbf{v}^f)^\intercal) - \epsilon^2\mu_f(\mathbf{v}^f - \overline{\mathbf{v}}^p)/K,$$

où ρ_f est la densité du fluide, et $\mathbf{v}^f$ est la vitesse moyenne du fluide dans la cellule. p est la pression, μ_f est la viscosité dynamique, $\mathbf{g}$ est l'accélération gravitationnelle, $\overline{\mathbf{v}}_p$ est la vitesse moyenne des particules sur la grille eulérienne, et K est la perméabilité locale de la cellule. Le dernier terme du côté droit est une force de traînée correspondant à la résistance à l'écoulement due à la présence de particules.

Le champ de porosité des cellules, ϵ, décrit la présence des particules dans une cellule de calcul (Figure D). Il est obtenu à partir de la projection de l'ombre des particules sur la grille. La force de traînée des particules est modélisée soit en utilisant des modèles sous-grille (par exemple, la force de traînée de Stokes) si les particules sont plus petites que la taille de la grille (approche non résolue), soit en calculant la contrainte de cisaillement à l'interface fluide-particule si les particules sont plus grandes que la taille de la grille (approche résolue).

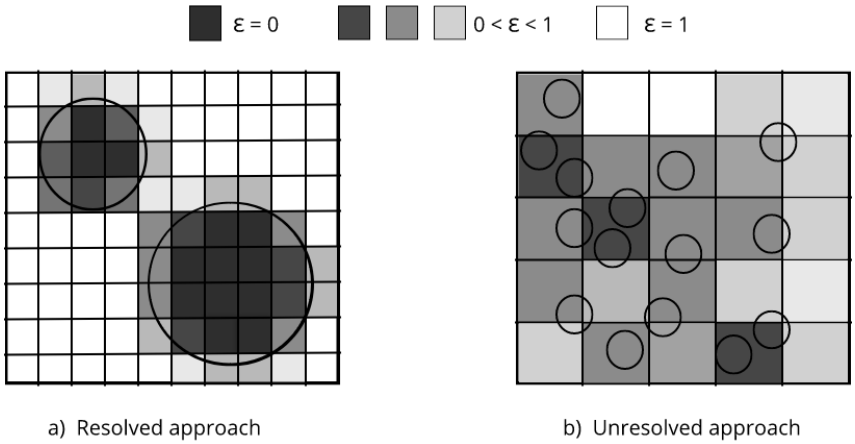

Figure D : Cartographie du champ de porosité, ϵ, sur la grille eulérienne pour (a) les particules résolues et (b) les particules non résolues.

Le mouvement du nuage de particules, en revanche, est calculé en résolvant la deuxième loi de Newton pour chaque particule. L'équilibre des forces sur une particule sphérique i de masse m_i et de moment

d'inertie I_i en contact avec n_i^c objets (particules et parois) s'écrit :

$$m_i \frac{d\mathbf{U}_i^p}{dt} = \sum_j^{n_i^c} \mathbf{F}_{ij}^c + \sum_j^{n_i^{nc}} \mathbf{F}_{ij}^{nc} + \mathbf{F}_i^f + \mathbf{F}_i^g,$$

et l'équilibre des moments suit :

$$I_i \frac{d\boldsymbol{\omega}_i}{dt} = \sum_j^{n_i^c} \mathbf{M}_{ij}^c + \sum_j^{n_i^{nc}} \mathbf{M}_{ij}^{adh} + \mathbf{M}_i^{hyd},$$

où $\mathbf{U}_i^p$ et $\boldsymbol{\Omega}_i$ sont les vitesses de translation et angulaire de la particule i, $\mathbf{F}_i^f$ et $\mathbf{F}_i^g$ sont les interactions hydrodynamiques particule-fluide et les forces gravitationnelles. $\mathbf{F}_{ij}^c$, $\mathbf{M}_{ij}^c$ et $\mathbf{M}_i^{hyd}$ sont les forces et les couples de contact décrits à l'aide du modèle de ressort-glissière-amortisseur de Hertz (Cundall and Strack, 1979). Les interactions à longue portée, y compris les forces électrochimiques, sont prises en compte par la force de non-contact, $\mathbf{F}_{ij}^{nc}$, et le couple adhésif $\mathbf{M}_{ij}^{adh}$.

Les interactions à longue portée sont modélisées en utilisant la théorie DLVO (Derjaguin, 1934; Verwey, 1948), qui consiste en la combinaison du potentiel attractif de van der Waals et du potentiel répulsif de la double couche électrique (couche de Stern + couche diffuse) comme indiqué sur la figure E. Leur effet dépend de la distance entre deux particules et entre une particule et une surface solide. Le potentiel DLVO présente un puits de minimum primaire infini si la distance entre les surfaces des particules atteint zéro. Pour éviter une interpénétration non physique importante des particules lors de l'adhésion, nous avons modifié le contact hertzien en ajoutant un comportement de solide élastique basé sur la théorie de Johnson-Kendall-Robert (JKR) (Johnson et al., 1971). La théorie JKR consiste à appliquer une force adhésive constante lorsque la distance entre les deux objets est inférieure à l'épaisseur de la couche de Stern (quelques nanomètres).

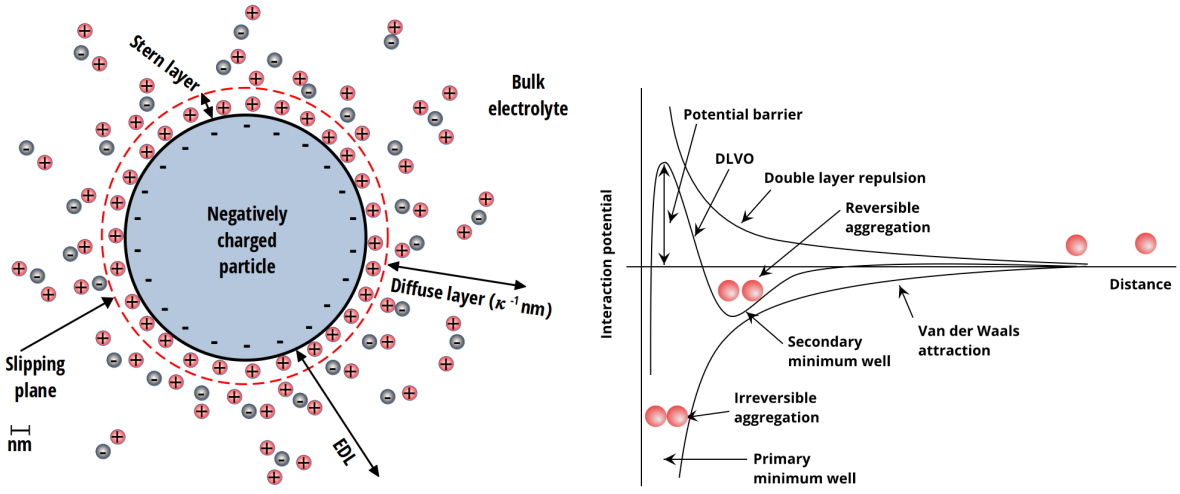

(a) (b)

Figure E :(a) Croquis de la double couche électrique (EDL) autour des particules chargées négativement immergées dans un électrolyte 1:1 comme le NaCl contenant des ions Na^+ et Cl^-. (b) Profil typique du potentiel DLVO.

Notre couplage à quatre voies non résolu-résolu CFD-DEM pour le transport colloïdal est implémenté dans la plateforme open-source de volumes finis *OpenFOAM version 9*. Notre implémentation est construi-

te sur la base du solveur *denseparticleFoam* existant, couplé avec le package DEM interne d'OpenFOAM pour simuler l'écoulement de particules denses ou diluées. Nous avons réalisé un ensemble complet de cas tests pour vérifier la robustesse et l'efficacité de notre implémentation :

- Nous analysons l'efficacité de la recherche pair-à-pair pour la cartographie des cellules couvertes : il s'avère que notre algorithme de recherche est aussi efficace que la recherche par courbe de Hilbert et plus facile à implémenter.
- Nous vérifions l'implémentation du terme d'échange de moment pour les particules résolues, nous observons un bon accord avec les solutions de référence pour différentes résolutions de maillage.
- Nous évaluons la précision de notre modèle pour différentes résolutions de maillage (résolu et non-résolu) dans le cas d'une bille en acier se déposant dans un tube d'eau pour lequel des données expérimentales existent.
- Nous vérifions l'implémentation des forces DLVO entre deux particules et entre une paroi et une particule en utilisant des cas tests pour lesquels nous avons dérivé des solutions semi-analytiques.
- Nous comparons avec succès la prédiction CFD-DEM de la formation d'agrégats de particules sous l'effets des forces DLVO avec un ensemble de données expérimentales.

Ces cas tests confèrent confiance dans la capacité prédictive de notre modèle numérique. Notre méthode non résolue-résolue a un grand potentiel pour explorer la rétroaction complexe due à l'injection, la rétention et la remobilisation des particules dans les milieux poreux à l'échelle des pores.

Étude numérique du colmatage dans un réseau de pores

Nous utilisons ensuite notre package CFD-DEM pour étudier la rétention des particules et la réduction de la perméabilité due au pontage et à l'agglomération des particules dans un milieu poreux représentant un dispositif microfluidique en PDMS (Polydiméthylsiloxane) (Roman et al., 2016). La géométrie consiste en un domaine de taille millimétrique contenant une structure poreuse hétérogène. La géométrie des pores et la procédure de maillage sont décrites dans Soulaine (2024). Nous appliquons une différence de pression constante $\Delta P = 0.2$ mbar entre l'entrée et la sortie.

Tout d'abord, nous simulons le colmatage des pores par le pontage des particules sous différentes concentrations de particules injectées $C_0 = 0.05,\ 0.1,\ 0.15\%$. La suspension est constituée de particules monodisperses de 6 microns de diamètre et est injectée jusqu'à un certain volume de pore $PV = 4$, puis nous arrêtons l'injection de particules et continuons l'injection de fluide jusqu'à ce que les particules restantes en suspension soient évacuées. Nous observons que certaines particules percolent tandis que d'autres restent piégées dans le milieu poreux, colmatant les pores. La rétention des particules modifie la porosité du système et dévie les lignes de flux locales, ce qui affecte la perméabilité du système. La fréquence de contact des particules et la probabilité d'arrivée simultanée des particules à une entrée de pore pour former un bouchon (formation d'arche) augmentent avec la concentration de particules. Pour $C_0 = 0.05\%$, nous n'observons aucune formation de bouchon. Pour $C_0 = 0.1\%$, nous observons plusieurs bouchons formés par le pontage de 2 particules à l'entrée de petits pores. Les bouchons sont très stables et persistent même après avoir arrêté l'injection de particules ($PV > 4$). Pour $C_0 = 0.15\%$, la fréquence de formation d'arche augmente car les particules sont plus susceptibles d'être proches les unes des autres lorsqu'elles atteignent une entrée de pore en raison des trajectoires convergentes. Nous observons toutefois que plusieurs bouchons non permanents se forment.

Deuxièmement, nous simulons le colmatage des pores par l'agrégation de particules sous différentes concentrations de NaCl dans le fluide [NaCl] = 1, 10, 100 mM. La suspension est constituée de particules monodispersées de 4 microns de diamètre. La suspension est injectée à une concentration constante $C_0 = 0.3\%$ depuis le côté gauche. Dans la Figure F, nous montrons des séquences d'images de la simulation du transport colloïdal sous différentes concentration en NaCl de l'électrolyte. Certaines particules réussissent à traverser le domaine, tandis que d'autres se déposent sur les grains solides et forment des bouchons. Dans d'autres cas, nous observons la formation d'agrégats pendant le transport qui sont plus grands que l'orifice du pore et sont finalement filtrés. Le profil de vitesse est mis à jour à chaque pas de temps. Nous voyons que le colmatage des pores dévie les lignes de courant du fluide au fil du temps. Ainsi, avec le dépôt rapide des particules aux entrées du milieu, un gâteau de filtration ("filter cake" en anglais) se forme, empêchant les particules en amont de traverser le milieu poreux. Étant donné que nous appliquons une pression constante ΔP, le débit diminue en raison du colmatage des pores. Macroscopiquement, cela correspond à une réduction de la perméabilité. L'évolution de la perméabilité en fonction du volume de pore injecté est mesurée, montrant une réduction de la perméabilité de 90% à la fin des simulations.

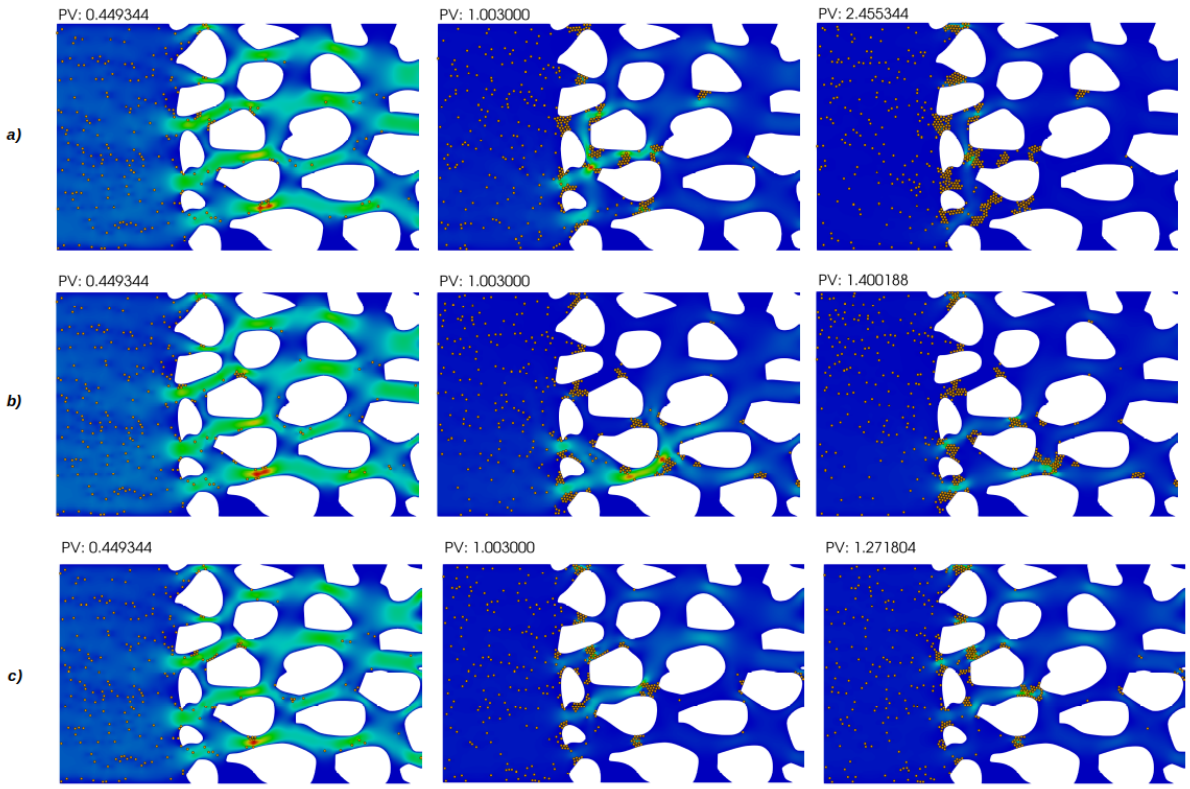

Figure F : Séquences d'images de la migration et du dépôt des particules pour différentes conditions de salinité : a) 1 mM, b) 10 mM, c) 100 mM NaCl. Les couleurs de fond correspondent à l'amplitude du champ de vitesse du fluide.

Étude théorique de la cinétique de déposition des colloïdes

Nous avons ensuite revisité la modélisation et la rétention de particules à l'échelle de Darcy en utilisant des modèles de filtration colloïdale basés sur la CFT (Colloidal Filtration Theory). Les bases et les limites de la CFT qui repose sur le le dépôt des particules par diffusion, interception et sédimentation ont été discutées. Bien que certaines extensions de la CFT prédisent le dépôt des particules dû à l'attraction, les

cas où la répulsion de la double couche électrique est dominante restent un défi pour la prédiction de la cinétique de déposition.

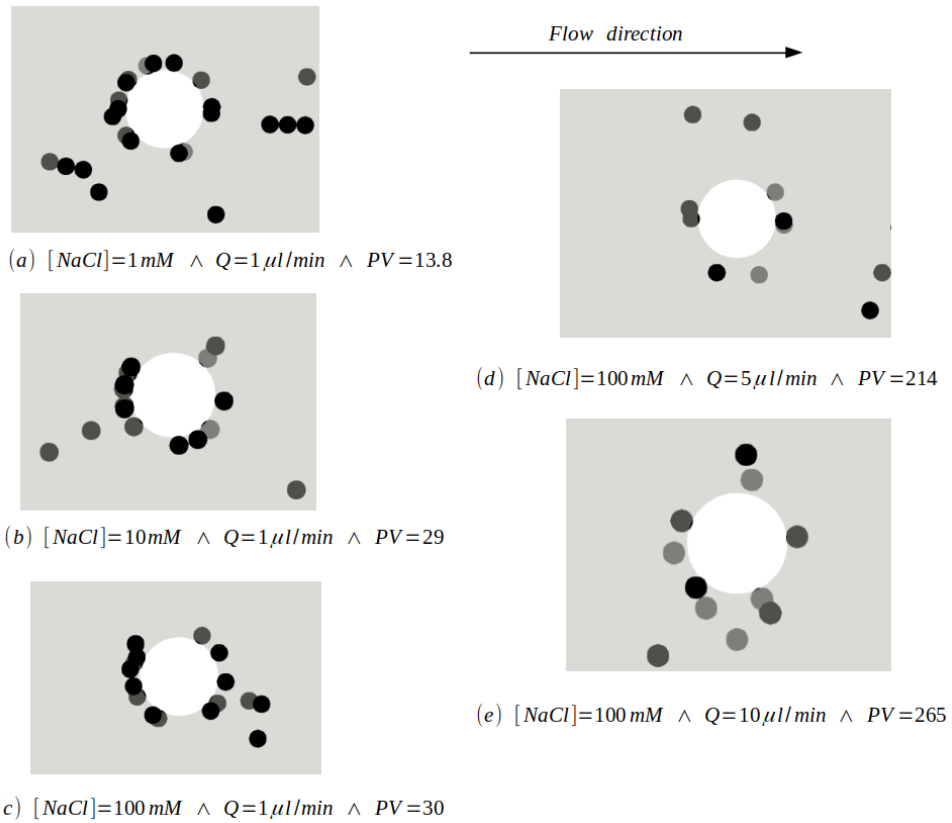

Figure G : Séquence d'images des morphologies de dépôt à différents débits et salinités de fluide [NaCl], pour des particules de latex de polystyrène carboxylé de 4.5 μm autour d'un collecteur cylindrique de 20 μm en PDMS, obtenus par simulations 3D CFD-DEM.

Ainsi, nous avons développé un modèle théorique dans lequel la capture au minimum secondaire (en cas de répulsion dominante) et la capture au minimum primaire (en cas d'attraction dominante) sont considérées ensemble. Pour ce faire, nous avons dérivé une nouvelle efficacité du collecteur impliquant un paramètre adimensionné Dl qui quantifie le rapport entre la force d'attraction de Van der Waals et la force de répulsion de la double couche électrique, et un autre δ qui quantifie le rapport de taille entre la double couche électrique et les particules. Les travaux futurs se concentreront sur la confrontation des prédictions de notre modèle théorique avec des données expérimentales. À cet égard, des expériences microfluidiques bien contrôlées pourraient être développées afin d'évaluer le dépôt sur une large gamme de conditions d'écoulement, de propriétés des particules et de salinité des fluides.

Une autre manière de valider l'approche est de réaliser des simulations CFD-DEM. Cependant, il est encore nécessaire de s'assurer qu'elles peuvent capturer correctement la morphologie du dépôt en les comparant avec des expériences de référence (Kusaka et al., 2010). Nous avons pour cela effectué des simulations préliminaires sur la morphologie des dépôts (Figure G). Nous obtenons un dépôt quasiment uniforme pour des faibles débits en accord avec la litérature. Cependant, nous n'avons pas observé de changements significatifs avec la variation de la salinité de la solution pour ce débit. Ces simulations ont mis en évidence la capacité du modèle CFD-DEM à étudier la cinétique de dépôt colloïdal. Les résultats sont encore préliminaires et les travaux futurs utiliseront des paramètres plus proches de ceux de Kusaka

et al. (2010) pour une meilleure comparaison.

Conclusions et perspectives

Comprendre le transport colloïdal dans les milieux poreux est complexe car il dépend de nombreux paramètres, notamment les géométries des pores, le débit, la taille et la concentration des particules, le pH et la salinité. Dans nos simulations, nous avons observé différents modèles de dépôt en fonction du débit d'injection et de la salinité de la solution, qui confirment les résultats des expériences en microfluidique, et nous avons suivi les diminutions de perméabilité dues au colmatage des pores. Notre modèle est implémenté dans la plateforme de simulation open-source OpenFOAM. Il comprend deux innovations : i) un couplage hybride résolu-non résolu pour surmonter une limitation bien connue liée à la taille des particules par rapport à la taille de la grille, et ii) le DEM considère les forces DLVO combinées avec la théorie JKR pour modéliser les flux colloïdaux dans l'approximation du potentiel de surface constant. Notre approche numérique peut capturer tous les mécanismes de colmatage des pores : tamisage, formation d'arcs et colmatage par agrégation de particules.

Plusieurs perspectives qui influencent l'étude du comportement des particules dans les milieux poreux sont mises en avant. Un défi majeur est le coût de calcul des simulations CFD-DEM. Bien que ces simulations offrent des informations très détaillées sur l'écoulement colloïdal et les interactions des particules à l'échelle des pores, elles nécessitent des ressources de calcul substantielles, les rendant peu pratiques pour des études à grande échelle ou à long terme. Cette limitation souligne la nécessité de développer des algorithmes plus efficaces ou des approches de modélisation alternatives qui puissent réduire la charge computationnelle sans compromettre la précision. Une solution pourrait être la mise en œuvre de l'algorithme de diffusion pour l'équilibrage dynamique de charge (Hu and Blake, 1999). Cette méthode est utilisée en calcul parallèle pour répartir uniformément la charge de travail computationnelle entre plusieurs processeurs ou nœuds de calcul. L'objectif est de minimiser le temps de calcul global en s'assurant qu'aucun processeur ne soit surchargé pendant que d'autres sont sous-utilisés.

Une autre perspective importante est la nécessité de déterminer le coefficient de dispersion colloïdale et de comprendre la relation entre la perméabilité et la porosité lors du colmatage des particules. Cette stratégie d'upscaling est essentielle pour traduire les résultats à l'échelle des pores en prédictions à l'échelle des réservoirs, mais elle reste une tâche complexe. L'estimation précise du coefficient de dispersion colloïdale est cruciale pour prédire comment les particules se distribueront et interagiront sous l'influence des forces à longue portée dans un réservoir plus vaste, affectant l'injectivité globale et les performances du réservoir à long terme.

Enfin, une approche lagrangienne moyenne innovante comme solution potentielle pour la mise à l'échelle du transport des particules est nécessaire. Cette approche vise à équilibrer le besoin de suivi détaillé des particules avec la faisabilité computationnelle requise pour des simulations à plus grande échelle. En moyennant le comportement des particules dans le temps et l'espace, cette méthode pourrait offrir un moyen plus précis afin de prédire le comportement de colmatage à différentes échelles. Cela représenterait un progrès significatif pour rendre les simulations de transport de particules plus accessibles à la gestion pratique des réservoirs géothermiques.

Les futurs travaux consisteront à comparer nos résultats numériques avec des expériences de microfluidique et de colonnes bien contrôlées, y compris des micro-puces de réseau de pores pour diverses conditions de débit, de salinité, de taille et de concentration de particules.

Contents

List of figures xiii

List of tables xxii

1 Geothermal Energy and Pore-clogging 1
- 1.1 The use of the subsurface in the energy transition . . . 1
  - 1.1.1 Geothermal energy . . . 1
  - 1.1.2 Challenges in the fluid reinjection in the subsurface . . . 3
  - 1.1.3 Other subsurface exploitation facing injectivity issues . . . 4
- 1.2 Principal clogging mechanisms . . . 5
  - 1.2.1 Physical clogging . . . 5
  - 1.2.2 Biological clogging . . . 10
  - 1.2.3 Chemical clogging . . . 10
  - 1.2.4 Air clogging . . . 11
  - 1.2.5 Clay swelling . . . 11
  - 1.2.6 Summary of extended damage mechanisms . . . 12
- 1.3 Review of the influencing factors in particle clogging . . . 13
  - 1.3.1 Influencing factors related to fluid properties and flow conditions . . . 13
  - 1.3.2 Influencing factors related to particle properties . . . 19
  - 1.3.3 Influencing factors related to porous matrix conditions . . . 22
- 1.4 Scientific challenges . . . 24
  - 1.4.1 Multi-scale couplings . . . 24
  - 1.4.2 Multi-physics couplings . . . 25
- 1.5 Scientific questions and outline of the thesis . . . 26

2 Review of Particle Transport Modeling in Porous Media 27
- 2.1 Particle dynamics . . . 27
  - 2.1.1 Particles description . . . 27
  - 2.1.2 Balance of forces . . . 28
- 2.2 Pore-scale description . . . 36
  - 2.2.1 Flow models at the pore-scale . . . 36
  - 2.2.2 Lagrangian approaches for particle transport . . . 40
  - 2.2.3 Eulerian models for particulate transport . . . 49
- 2.3 Darcy-scale description . . . 52
  - 2.3.1 Heterogeneous structure of porous media . . . 52

2.3.2 From pore-scale to Darcy-scale . . . 56
2.3.3 Darcy equations . . . 57
2.3.4 Deep bed filtration (DBF) . . . 57
2.4 Objectives and methodology of the thesis . . . 58
2.4.1 Objectives . . . 58
2.4.2 Methodology . . . 59

3 Unresolved-Resolved CFD-DEM for Colloidal Flow 61
3.1 Review of the CFD-DEM Model . . . 61
3.2 Computational Model . . . 63
3.2.1 Fluid motion in the CFD Eulerian grid . . . 64
3.2.2 Particle motion in the DEM Lagrangian frame . . . 65
3.2.3 CFD-DEM coupling strategy and numerical implementation . . . 73
3.3 Model Verifications . . . 78
3.3.1 Searching algorithm efficiency analysis . . . 78
3.3.2 Fluid flow around a stationary spherical particle . . . 79
3.3.3 Sedimentation of a steel ball in a water tube . . . 82
3.3.4 Verification of the implementation of DLVO forces . . . 82
3.3.5 Colloidal aggregation of a suspension . . . 86
3.4 Summary of the novelties . . . 89

4 Pore-scale Simulations of Particle Clogging in Porous Media 91
4.1 Clogging of a single pore: sieving and bridging . . . 91
4.1.1 Pore-clogging by sieving . . . 91
4.1.2 Pore-clogging by arch formation . . . 92
4.2 Sensitivity analysis of particle bridging in a single pore . . . 93
4.2.1 Case 1: effect of the particle concentration . . . 95
4.2.2 Case 2: effect of the particle diameter . . . 95
4.2.3 Case 3: effect of the flowrate . . . 95
4.2.4 Case 4: effect of the geometry aspect ratio . . . 96
4.3 Clogging inside heterogeneous pore network . . . 97
4.3.1 Pore-clogging due to hydrodynamic forces only . . . 97
4.3.2 Pore-clogging including colloidal interactions . . . 101
4.4 Summary and partial conclusions . . . 104

5 Colloidal Deposition Kinetics 105
5.1 Filtration models . . . 105
5.1.1 Colloid filtration theory (CFT) . . . 105
5.1.2 Extensions of the CFT . . . 107
5.2 Capture efficiency of single collector . . . 110
5.2.1 Interception capture . . . 111
5.2.2 Diffusion capture . . . 112
5.2.3 Sedimentation capture . . . 112
5.2.4 Discussion and limits of the current collector efficiency models . . . 112
5.3 A new collector efficiency including electrostatic effect . . . 112
5.3.1 Colloidal trajectory . . . 114

5.3.2 Asymptotic analysis of the particle trajectory near the collector 118
5.3.3 New collector efficiency 118
5.4 Analysis of deposits morphology 119
5.4.1 Experimental results from the literature 119
5.4.2 Numerical results with CFD-DEM for colloids 121
5.5 Summary of the novelties 122

6 General Conclusion and Perspectives **125**
6.1 General conclusion 125
6.2 Perspectives 127

Bibliography **129**

List of Figures

1.1 Schematic illustrating subsurface utilization to achieve decarbonization goals for net-zero carbon dioxide emissions. Decarbonization applications include nuclear waste storage (GDF-Geological Disposal Facility); Carbon Capture and Storage (CCS); geothermal heat and energy utilization (deep Enhanced/Engineered Geothermal Systems (EGS), hydrothermal systems, and shallow (<120 m) geothermal heat pumps); Underground Thermal Energy Storage (ATES, Aquifer Thermal Energy Storage; PTES, Pit Thermal Energy Storage; BTES, Borehole Thermal Energy Storage; MTES, Mine Thermal Energy Storage); Hydrogen storage in caverns and aquifers; and Compressed Air Energy Storage in Caverns (CAESC) and Aquifers (CAESA) (Kaminskaite et al., 2022). 2

1.2 Proportion of various clogging mechanisms (Song et al., 2020). 5

1.3 Different mechanisms responsible for the clogging of pores at a constriction: (a) sieving, (b) bridging, and (c) aggregation of particles Dressaire and Sauret (2017). 6

1.4 Series of images of a microgel particle being deformed as the applied pressure increases; from left to right: p = 100 Pa, 150 Pa, 200 Pa, 250 Pa, 300 Pa (Wyss et al., 2010). 6

1.5 (a) Flow and clogging by the bridging of a neurally buoyant suspension of PMMA (Polymethyl Methacrylate) particles in an axisymmetric tapered glass capillary (Dressaire and Sauret, 2017). (b) Particle arches formed at high flow velocity. Negatively charged 0.249 μm diameter polystyrene sulfate particles (white particles) flow through $1\mu m$ pores (black dots) (Ramachandran and Fogler, 1999). 7

1.6 Particle aggregation resulting in clog formation. (a–e) The density-matched suspension of polystyrene particles ($D_p = 3\ mm$) with sulfate charge groups flows through a constriction of width $W = 15.5\ mm$. The images are recorded at 3, 5, 10, and 36 minutes, with a flux of 2.8×10^4 particles per minute at the onset of the experiment (Dersoir et al., 2015). (f–h) Schematic representation of the aggregation process, from the deposition of the first particle to the clog formation (Dressaire and Sauret, 2017). 8

1.7 (a) Schematic of well impairment due to low-quality water injection (deep bed filtration and external filter cake formation, radial), (b–e) injection of suspension solids in core (1-D, experimental) (Tale et al., 2020). 9

1.8 On the left (a), images of biofilms after injection of Syto-9 (green fluorescent nucleic acid) in the ***a*** artificial-structure and ***b*** real-structure micromodels (scales are different in the images). On the right (b), ***a*** images of the micro-model after injection of Syto-9. Results of particle image velocimetry at the middle of the micro-model during injection of tracer particles indicating the field velocity map ***b*** without bacteria and ***c*** with bacteria. (Gaol et al., 2021) 10

1.9 Illustration of main groups of chemical clogging processes: 1 – dissolution (e.g., of calcite), 2 – precipitation (e.g., of iron hydroxide). After Anna Kottsova and Brehme (2022). . . . 11
1.10 Photograph of the foam transport in a heterogeneous micromodel at a foam quality of 80% (white color - trapped bubble; green color - flowing bubble) (Lv et al., 2020). 11
1.11 Clay particle expansion and pore space reduction by swelling (Civan, 2007). 12
1.12 Classification and order of the common formation damage mechanisms (Civan, 2007). . . 13
1.13 Effect of flow velocity on permeability (Xia et al., 2023). 14
1.14 Effluent concentration curves for 1.1 μm latex colloids in (a) 360 (b) 240 (c) 150 μm quartz sand when the ionic strength was 56 mM and the Darcy velocity was approximately 0.1, 0.2, and 0.45 $cm\ min^{-1}$ (Bradford et al., 2007). 14
1.15 (a) Videomicroscopic images of 0.93 μm polystyrene particles captured using 10X objective lens under temperature gradient maintained at 6846.9 K/m at 0 min, 20 min, 40 min, and 60 min, Particles are shown as black dots; (b) Number of deposited particles per unit area versus deposition time for four different temperature gradients at 78.9 K/m, 2136.5 K/m, 5516.1 K/m and 6846.9 K/m (Yan et al., 2020). 15
1.16 Breakthrough curves for polystyrene latex particles in silicon dioxide glass beads. Note: (a) shows the breakthrough curves of deionized water-washed groups in glass beads in attachment experiments; (b) shows the breakthrough curves of acid-washed groups in attachment experiments; (c) shows the breakthrough curves of deionized water-washed groups in elution experiments; and (d) shows the breakthrough curves of the acid-washed groups in the elution experiment (Yuan et al., 2020). 16
1.17 (a) Colloid deposition rate coefficients in saturated and unsaturated media (Sang et al., 2013). (b) Attachment efficiencies (α) for the 50 nm, 110 nm, and 1500 nm colloids suspended in KCl in the absence of natural organic matter over a wide range of solution ionic strengths (pH 5.7 $\pm$ 0.2) (Pelley and Tufenkji, 2008). 17
1.18 Confocal microscopy images of latex particles (red) deposited in the pore space between glass beads (black) in a $150 \times 150\ \mu m^2$ window at the entrance of the porous media, with the suspension flowing upwards. 4 conditions of ionic strength are presented at 4 times (Gerber et al., 2019). 18
1.19 (a)Particle breakthrough curves of the 0.753 μm latex particles with various concentrations of KCl. The residual particle concentration C/C_0 is plotted as a function of time. Experimental conditions were as follows: approach velocity 0.14 cm/s, bed depth 20 cm, collector size 0.2 mm. (b) Particle breakthrough curves of the 0.753 μm latex particles with various concentrations of $CaCl_2$ in the presence of 0.01 M KCl. The residual particle concentration C/C_0 is plotted as a function of time. Experimental conditions were as follows: approach velocity 0.14 cm/s, bed depth 20 cm, collector size 0.4 mm (Elimelech and O'Melia, 1990). 18
1.20 (a) $\phi = 10^{-3}v/v$; $q = 2ml\ h^{-1}$; no deposit of particles after 90 min of dead-end filtration. Latex suspensions are dispersed in ultra-pure water. (b) $\phi = 5.10^{-3}v/v$; $q = 2ml\ h^{-1}$; cluster formation after 90 min of dead-end filtration. Latex suspensions are dispersed in ultra-pure water (Agbangla et al., 2012). 19
1.21 The temporal evolution of the average thickness of particle deposit: $-*-$ $\phi = 10^{-3}v/v$; $q = 2ml\ h^{-1}$, and $-o-$ $\phi = 5.10^{-3}v/v$; $q = 2ml\ h^{-1}$ (dispersed in ultra-pure water) with snapshots of the cluster formation at t = 15, 55 and 85 min.(Agbangla et al., 2012). . . . 19
1.22 Relationship between permeability retention and cumulative injection volume for quartz sand particles (After Xia et al. (2023), modified from Xie (2014)). 20

1.23 The influence of particle size on the attachment efficiency α at $pH = 9.8$ as a function of ionic strength (a) for carboxylate latex (b) for sulfate latex and hematite (Litton and Olson, 1996). 21
1.24 Permeability recovery rate (R) as a function of ionic strength (IS). Influence of the particle size and flow velocity (Bennacer et al., 2017). 21
1.25 Dry granular flow: Clogging probability as a function of orifice-to-particle size ratio d_0/d for the spheres, 2D crosses, 3D crosses, and cubes (experimental results). The clogging probability is the ratio of the number of tests that clogged (within a maximum discharge of 4000 particles for spheres, 2D and 3D crosses, and 2000 particles for cubes) to the total number of tests (20 trials). Datapoints: 360 independent experimental realizations (Hafez et al., 2021). 22
1.26 Bridge topology (experimental results). CT scans of bridges formed by (a) spheres, (b) cubes, and (c) 3D crosses above the orifice during dry granular flow. Typical particle-particle interaction modes are shown below each scan (Hafez et al., 2021). 22
1.27 (a) Randomly mixed porous media analogues (PMA) with 17% "+" and 83% "−" charged beads. PMA labeled with "+" beads (red) and "−" beads (blue), as determined by the fluorescence labeling of "−" beads. (b) Breakthrough curves for the transport of 0.5 μm carboxylated colloidal particles in chemically heterogeneous porous media packed with amine-("+") and carboxyl-functionalized ("−") beads at different mixing ratios. Note that the percentage indicates the fraction of "+" beads in the mixing beads. The normalized concentration (C_{out}/C) at the outlet of the PMA is plotted as a function of injected pore volumes (PV). The dashed line indicates the time when deionized water flushing started (Guo et al., 2020). 23
1.28 (a) Collision efficiencies as a function of ionic strength for the 3 and 4 μm colloids in the smooth and rough micromodel. (b) Images of colloid deposition in a) micromodel A (smooth) and b) micromodel B (rough). Streamlines are drawn by hand to show the pathway of the colloids (Auset and Keller, 2006). 24
1.29 Modeling strategy using a cascade of scales nested within each other for transport in porous media. 24

2.1 Size ranges of particles transported in groundwater (De Zwart, 2007). 28
2.2 Some mineral dust particles (Agg I: agglomerate of Na-feldspar, illite, quartz, and magnesium-rich clay, Sil I: magnesium-rich silicate, Ca I: magnesium-bearing calcite, Dol I: dolomite). From the left to the right, scanning-electron microscope (SEM) images, the retrieved triangulated irregular network model of the surface, and the final volume representation from two different viewing angles (Lindqvist et al., 2014). 28
2.3 Representation of the different configurations of Van der Waals interactions between a dipole, an induced dipole, and an ion. After https://88guru.com/library/chemistry/van-der-waals-forces. 31
2.4 Examples of Hamaker constant values for different system configurations (grain, particle, liquid). Modified after Muneer et al. (2020). 32
2.5 Model of the electrochemical double layer at the solid-liquid planar interface (surface potential ψ_0, zeta potential ζ). Taken after https://wiki.anton-paar.com/fr-fr/potentiel-zeta/. 32
2.6 Zeta potential measurements for various environments with different base liquids. Modified after Muneer et al. (2020) 33

2.7 (a) DLVO potential profile over the distance h. (b) The overall potential profile between 2 particles over the distance h (DLVO potential + Born potential). $V_{min,1}$ and $V_{min,2}$ are the primary and secondary potential minimum, respectively. 34
2.8 Shematic description of the spring-slide-dashpot model (after Fernandes et al. (2018)). η_n and η_t are the normal and tangential damping coefficients. k_n and k_t are the normal and tangential stiffness coefficients. μ is the friction coefficient. 35
2.9 Pore-scale fluid flow simulation using NS equations in a trabecular bone based on micro-CT imaging (Daish et al., 2017). 37
2.10 Schematic of the (a) D2Q9 and the (b) D3Q19 configurations of the LBM space discretization (Chaaban et al., 2020). 38
2.11 3D view of the Nubian Sandstone pore-network. The solid phase is in gray, while the extracted pore elements are overlain. The pore bodies and pore throats are respectively rendered as red spheres and gray cylinders that are smaller than their actual sizes to improve visualization. (Hefny et al., 2020). 38
2.12 Schematic of the kernel function in the SPH method. (Yang et al., 2024). 39
2.13 In DEM, particles of arbitrary shapes can be modeled using a compound of packed particles with strong adhesive forces. (a) Spherical clump; (b) Disk clump; (c) Irregularly shaped particle (Shen et al., 2022). 41
2.14 The schematic diagram of particle surface representation of three typical shapes and one irregular shape (top: original shapes of particles; middle: surface meshes with triangles; bottom: distribution of contact nodes at particle surfaces). After Zhan et al. (2021). . . . 41
2.15 Specification of the 4-way CFD-DEM coupling. Each interaction is illustrated by an arrow (Puderbach et al., 2021). 42
2.16 Conventional CFD-DEM coupling approaches (a) resolved (b) unresolved (Kanitz and Grabe, 2019). 42
2.17 Particle build-up comparison between the CFD–DEM simulation on a wire-wrapped screen opening on the left, and particle shadowgraph velocimetry experiment from Kinsale and Nobes (2018) on a straight slot on the right (Razavi et al., 2021). 43
2.18 Snapshots of the particle suspensions flowing through a channel with a cavity for particle Reynolds number $Re_p = 56.88$ at different time points (for the top to the bottom) using LBM-DEM. (Liu and Wu, 2020). 44
2.19 Schematics of the pore network model: (a) Pore domains formed from close chains of bonded particles; and (b) The drag force on a particle, F_{fluid}, as a resultant from the pore pressures of surrounding pore domains (Huang et al., 2019). 45
2.20 (a) Fluidized bed simulation using PNM-DEM. The color indicates the particle ID. The meshing of the fluidized bed: (b) with the Delaunay tessellation; and (c) with the Voronoi tessellation (Wu et al., 2021). 45
2.21 Snapshots of gravity-driven fresh concrete flow with natural pebbles of arbitrary shapes at different times using SPH-DEM method (Peng et al., 2021). 46
2.22 Schematic representation of the MP-PIC method (Dymala et al., 2022). Parcels are constituted as groups of particles of the same physical properties and are transported as Lagrangian particles using the unresolved approach. 47
2.23 Different coupling configurations in Euler-Lagrange methods. (https://www.cfd-online.com/Forums/star-ccm/223996-cfd-dem-coupling.html) 47

2.24 Separated multiphase flow models describe the phase boundary in detail, while dispersed multiphase flow models only deal with volume fractions of one phase dispersed in a continuous phase (after https://www.comsol.com/blogs/modeling-and-simulation-of-multiphase-flow-in-co
2.25 Contour plots of normalized particle concentration on a realistic porous medium model, for superficial velocity u = 10^{-6} ms^{-1} (a), u = 10^{-5} ms^{-1} (b), u = 10^{-4} ms^{-1} (c). D_p is the particle diameter (Boccardo et al., 2014). 50
2.26 Two different representations of the physics of flow in porous media. The arrows represent the velocity vectors. (a) direct modeling or pore-scale approach where the solid is explicitly represented. (b) the continuum modeling or Darcy scale where the physics is governed by quantities averaged over control volumes. The color map represents the volume fraction of solid per control volume (Soulaine, 2022). 52
2.27 Different kinds of porous media (Xu et al., 2015). 53
2.28 Schematic of the pore structure and definitions of pore characteristics. The radius of the largest sphere that can pass freely through the porous material (leftmost black sphere) corresponds to the critical pore radius r_{cr} (Nishiyama and Yokoyama, 2017). 54
2.29 Order of magnitude of permeability of some porous media (Bear, 1988). 55
2.30 Two-dimensional slice of a rock representing a control volume V. The black region represents the void space (f-phase) while the white region represents the solid grains (s-phase). A_{sf} is the fluid-solid interface. 56
2.31 Thesis methodology for colloidal transport at core scale. 60

3.1 Mapping of the porosity field, ϵ, on the Eulerian grid (a) for resolved particles and (b) for unresolved particles. 64
3.2 Illustration of the forces acting on particle i from contacting particle j and the wall w. . . 66
3.3 The range of interaction of a particle (in green) is determined by a kernel (in purple) centered on the particle centroid and whose radius is equal to the particle diameter. The particles (in red) overlapping cells within this orbit are eligible for collision and long-range interactions. 67
3.4 (a) Sketch of the electrical double layer (EDL) around negatively charged particles immersed in a 1:1 electrolyte like NaCl containing Na^+ and Cl^- ions. (b) Typical profile of DLVO potential. 70
3.5 (a) Sketch of the JKR adhesion seen as an overlapping of two elastic spheres. (b) Profile of the potential function and forces including JKR adhesion for distance $0 \leq h_{ij} < \sigma_{St}$. . . 72
3.6 Detailled flowchart for the unresolved-resolved four-way coupling CFD–DEM numerical procedure including colloidal forces. 74
3.7 Principle of the peer-to-peer search algorithm. (a)–(d) Illustrations of the steps for searching nearby grid points in a two-dimensional 4×4 grid. Points correspond to cell centers. Lines correspond to the path to a newly identified cell. Their color changes gradually at each iteration. From an initially identified cell (black empty circle), the algorithm searches for cells adjacent to the newly identified cells, and iterates. (e) The peer-to-peer search is an efficient way to identify cells covered by particles. The red lines describe the path the algorithm took to research covered cells. (f) The peer-to-peer search also works in three-dimensional structured and unstructured grids – here, a $3 \times 3 \times 3$ regular domain. . 75
3.8 Temporal evolution for the fluid flow calculation compared to that of the particle dynamics calculation. 77

3.9 Efficiency of the peer-to-peer search compared with the traverse, octree, and Hilbert curve search results taken from Wang et al. (2019). (a) Efficiency for an increasing number of particles in a case with 10000 cells. (b) Efficiency for an increasing number of cells in a case with 10000 particles. 79
3.10 Schematic representation of the flow past a stationary single particle, (b)-(d) CFD-DEM approach with different mesh resolution, and (a) CFD approach. 80
3.11 (a) and (b), comparison of fluid velocity components U_x and U_y between results obtained from the model and a steady CFD solver of OpenFOAM (simpleFoam) calculated at the vertical line passing by the particle centroid. 80
3.12 Shematic representation of the domain, with (a)-(c) the local meshes refinement. 81
3.13 Comparison between the drag coefficient obtained with the unresolved-resolved CFD-DEM model and the empirical data of Schiller and Naumann (1935). 81
3.14 Comparison of the falling velocity obtained with unresolved CFD–DEM coupling on $D_p/\Delta x = 1$, with the resolved-unresolved CFD-DEM coupling on different mesh resolutions. 82
3.15 Representation of the two particles distant from h. 83
3.16 Particle-particle separation distance $h(t)$ and the relative velocity of particles $h^{'}(t)$: (a) for the attraction case with $h_0 = 2$ μm, (b) for the repulsion case with $h_0 = 0.04$ μm, and (c)-(d) for mixed attraction-repulsion with $h_0 = 2$ μm. 84
3.17 Representation of the particle and the wall distanced from h. 85
3.18 Particle-wall separation distance $h(t)$ and the velocity of the particle $h^{'}(t)$, (a) for the attraction case with $h_0 = 2$ μm, (b) for the repulsion case with $h_0 = 0.04$ μm, and (c)-(d) for mixed attraction-repulsion with $h_0 = 2$ μm. 86
3.19 Experimental images obtained by Earnshaw et al. (1996) of an aggregating 2D layer of 1 mm polystyrene spheres on the surface of an aqueous 0.73 M $CaCl_2$ solution. The images are 768×512 pixels^2, one pixel = 0.95 mm. The images correspond to t = 60 (a), 75 (b), 105 (c), and 135 min (d). 87
3.20 Image sequence of the simulation of 2D aggregation of the colloidal layer over time from initial setup to end time. The color represents the distinct objects (monomers+clusters) in the domain. Initially (t = 0 s), we have 1000 distinct monomers. 88
3.21 The number of separated objects (monomers and clusters) relative to their initial value at various times after the start of aggregation on a 0.73 M $CaCl_2$ brine aqueous solution, with a comparison of the experiment (obtained with $N_0 \simeq 6000$ objects) versus simulation. 88

4.1 Sieving of a large particle at different times. The background color corresponds to the fluid velocity magnitude (red-maximum, blue-minimum). 92
4.2 Unresolved CFD-DEM simulation of the sieving of a large particle ($D_p = 550$ μm).The background color corresponds to the fluid velocity magnitude (red-maximum, blue-minimum) 92
4.3 Bridging formation of 2 particles (214 μm and 287 μm) at different times. The background color corresponds to the fluid velocity magnitude (red-maximum, blue-minimum). 92
4.4 Evolution of the permeability damage calculated using Darcy's law in the case of sieving and bridging. 93
4.5 Geometry of the 2D simulation of a single pore 93
4.6 Numerical results of the time to clog a single pore by arch formation relative to the particle concentration, the Reynolds number, the geometry aspect ratio, and the particle diameter. 94

4.7 Particle arches formation and velocity magnitude field for different particle concentrations $C_0 = \{0.08\%, 0.1\%, 0.115\%, 0.13\%\}$ in a single pore. The orange spheres are particles and the color map represents the fluid velocity magnitude. t represents the time at which the clog forms. 95

4.8 Particle arches formation and velocity magnitude field for different particle-to-throat ratios $D_p/W = \{0.4, 0.45, 0.5, 0.6\}$ in a single pore. The orange spheres are particles and the color map represents the fluid velocity magnitude. t represents the time at which the clog forms. 96

4.9 Particle arches formation and velocity magnitude field for different Reynolds numbers $Re = \{0.005, 0.01, 0.05, 0.1\}$ in a single pore. The orange spheres are particles and the color map represents the fluid velocity magnitude. t represents the time at which the clog forms. 96

4.10 Particle arches formation and velocity magnitude field for different pore-to-throat ratios $D_{ch}/W = \{3, 4, 6, 8\}$ in a single pore. The orange spheres are particles and the color map represents the fluid velocity magnitude. t represents the time at which the clog forms. For all these geometries the throat width is $W = 50\ \mu m$. 97

4.11 (a) Geometry of the 2D simulation model of the porous media (length = 310 μm, width = 1050 μm). 98

4.12 Particle deposition and velocity magnitude field for $C_0 = 0.1\%$ during the injection of particles ($PV = 2.8$) and post-injection ($PV = 6.8$). The orange spheres are particles and the color map represents the fluid velocity magnitude. The clogs formed during the particle injection and remain stable when the particle injection is stopped. 99

4.13 Particle deposition and velocity magnitude field for $C_0 = 0.15\%$ during the injection of particles ($PV = 2.88$) and post-injection ($PV = 6.9$). Arches of particles are formed during the injection, but they are unstable, and most of them are remobilized. 99

4.14 (a) Particle cumulative BTC (Breakthrough Curves) normalized by the total number of injected particles. (b) Evolution of the current number of clogs (Current Nclog) in the system, and the number of clogs formed at different positions (Different Nclog) for different C_0. For $C_0 = 0.1\%$, each clog formed at a unique position. The pink zone represents the particle injection period. 100

4.15 (a) Permeability damage severity, K_r, and porosity damage severity, ϵ_r, for different particle concentration, C_0. (b) The probability density function of the fluid longitudinal velocity v_x^f for different C_0 at the end of the simulation compared with the case without particles. 100

4.16 Average of the permeability damage severity, K_r, over 5 replicates for different particle concentration, C_0. 101

4.17 DLVO potential (normalized by k_BT) for (a) particle-particle, and (b) particle-wall interactions for various NaCl salt concentrations. 102

4.18 Snapshots of the particle migration and deposition for various salinity conditions: a) 1 mM, b) 10 mM, c) 100 mM NaCl. The background colors correspond to the fluid velocity field magnitude. 103

4.19 (a) Evolution of permeability damage K_r and porosity damage ϵ_{rem} over the injected PV for various salt concentrations. (b) Probability density function (PDF) of the longitudinal flow velocity $|\mathbf{v}_x^f|$ over the domain-averaged flow velocity $\langle \mathbf{v}_x^f \rangle$ with no particles, and with particles for various salt concentrations at PV = 2.2 103

5.1 Schematic of a single-collector concept. Paths of a colloidal particle: trajectory a leads to a collision, trajectory b is the limiting trajectory, and trajectory c leads to no collision. Modified after Masliyah and Bhattacharjee (2005) . . . 106
5.2 (a) SEM picture of a sand grain sieved from crushed Boise sandstone within a size range of 90–105 μm; (b) Schematic of sand grain surface roughness and an impinging fluid velocity field near the surface. The orange points are attached nanoparticles that are accessible for recovery with the detachment path parallel to the flow direction, and the blue points represent the attached particles that are hard to detach with the escape direction opposite to the flow direction. The former may be modeled as "reversible" sites for attachment/detachment, while the latter may be modeled as "irreversible" sites for attachment (Zhang et al., 2016). . . . 109
5.3 The three major mechanisms controlling particle deposition onto a collector: gravity, interception (i.e., the combination of advection and steric effect), and Brownian motion (i.e., the combination of advection and Brownian diffusion (Boccardo et al., 2020). . . . 110
5.4 Capture due to interception by a spherical collector. Ψ_L is the limiting streamline at which the particles are intercepted by the collector. Modified after Masliyah and Bhattacharjee (2005). . . . 111
5.5 Collision efficiencies as a function of particle diameter using the relation from *i)* (Yao et al., 1971), *ii)* (Rajagopalan and Tien, 1976), *iii)* (Logan et al., 1995), *iv)* (Tufenkji and Elimelech, 2003), and *v)* (Messina et al., 2015). . . . 113
5.6 The flow geometry considered in this part. The system is two-dimensional with fluid flowing from the inlet to the outlet, with inert boundaries (wall). The central circle is a thin cylinder of diameter D_c (collector). (A) is the top view and (B) is the lateral view. . 114
5.7 Flow geometry of a particle at the vicinity of a larger spherical collector. (a) Overall geometry. The radial and angular velocity components of the fluid, v_r^f, and v_θ^f respectively, are shown for the polar coordinate system with the collector center as the origin. This velocity field can be represented as a linear superposition of two types of flow, namely, stagnation flow (b) and shear flow (c). Modified after Masliyah and Bhattacharjee (2005). 115
5.8 (a) Schematic drawing of the PDMS microfluidic channel, (b) Geometrical details for the cylindrical collector surface (zoom of the dashed rectangular part of the microchannel as drawn in panel a), and (c) Cross-section image (along the dashed line indicated in panel a) for the microchannel and cylindrical collector (obtained by optical microscopy). After Kusaka et al. (2010) . . . 120
5.9 Snapshots of deposit morphologies at various flow rates (indicated together with the corresponding Peclet numbers) for 1040PSL (panels a) and 3600PSL (panels b). Deposits were generated in 1.5 M KCl solution at $pH \simeq 6.9$. PSL denominates polystyrene sulfate latex. The scale bar indicates 0.1 mm (Kusaka et al., 2010). . . . 120
5.10 Illustrations of the geometry and the mesh of the numerical domain. . . . 121
5.11 Snapshots of deposit morphologies at various flow rates and fluid salinities [NaCl], for 4.5 μm of polystyrene carboxylated latex around a 20 μm cylindrical collector in PDMS obtained with CFD-DEM 3D simulations. . . . 122

List of Tables

1.1 Clogging in microfluidic systems: mechanisms, suspension properties, and channel geometry (Dressaire and Sauret, 2017). W is the width of the pore constriction and D_p is the particle diameter. 9

2.1 Summary of the hydrodynamic forces impacting the transport of solid particles in a fluid flow (modified after Kleinstreuer and Feng (2013)). 30
2.2 Contact force models (Zhu et al., 2007). 36
2.3 Summary of common fluid flow models coupled with Lagrangian DEM. 48
2.4 Capabilities and limitations of the two-fluid model and the scalar transport model. 51
2.5 Porosity magnitude order of environmental porous media (from https://www.saltworkconsultants.com/carbonate-porosity-sandstone-vs-carbonate/ and Neuzil (2019)). 53
2.6 Different formulations of porosity-permeability relationship. 55
2.7 Retention kinetics models (modified after Zhang et al. (2016)) 58

3.1 Features of the resolved, semi-resolved (Wang et al., 2019), unresolved and unresolved-resolved CFD–DEM. DNS: direct numerical simulation, FVM: finite volume method. . . . 63
3.2 Different formulations of the fluid-solid momentum exchange coefficient β are implemented, where C_d is the drag coefficient, Re_p is the particle Reynolds number, $D_{p,i}$ is the diameter of particle i. 68
3.3 Parameters for the DEM model. For the equivalent quantities, the case of particle-wall interaction is obtained assuming that the wall has infinite radius and mass. ν is the Poisson's ratio and α is given by the coefficient of elasticity. 69
3.4 Fluid, wall, and particle properties used in the model verification simulations (Yu et al., 2017). 83

4.1 Simulation configurations for bridging investigation. 94
4.2 Parameters of the CFD-DEM simulations used to investigate pore-clogging by aggregation of particles. 98

5.1 Single collector efficiency equations for a spherical collector. 113
5.2 Asymptotic behavior of the functions characterizing the hydrodynamic interactions (Spielman and Fitzpatrick, 1973). 116

Chapter 1

Geothermal Energy and Pore-clogging

This chapter discusses injectivity issues due to pore-clogging in porous media. First, we introduce the subsurface as a porous media solution for renewable energy (section 1.1). Second, in section 1.2, we present the main clogging mechanisms in subsurface processes. Third, in section 1.3, the problematics around the particle clogging in porous media are discussed. Then, in section 1.4, we show the scientific challenges of transport including pore-clogging in porous media. Finally, in section 1.5, we enumerate the scientific questions and describe the thesis outline.

1.1 The use of the subsurface in the energy transition

The subsurface is increasingly exploited for the various resources it contains. As well as harnessing minerals and water for a variety of uses (drinking water, industry, irrigation, spa, etc.), the subsurface also offers several advantages in terms of climate change and energy transition (see Fig. 1.1).

1.1.1 Geothermal energy

Geothermal energy is the technology used to harness the energy available beneath the Earth's surface. The temperature of the subsurface increases with depth. The geothermal gradient varies according to geological conditions, but it averages about $30°C/km$ on a global scale. This energy is primarily derived from the natural decay of radioactive isotopes in the Earth's crust and the residual heat from planetary formation. Then, according to the exploitation depth, different geothermal resources will be harnessed (Stober and Bucher, 2021).

Heat and electricity production

Up to about 200 m depth, subsurface temperatures (up to 25-30$°C$) allow the production of both heat and cold, which can be recovered at the surface using a heat pump. It corresponds to the so-called surface geothermal energy. It can be used on a scale ranging from single-family homes to eco-districts for heating and cooling, as well as for agricultural and industrial purposes.

At higher depths, temperatures rise to about $100°C$. Water is a sustainable way of producing heat that can be used directly to supply heating networks and industrial or agricultural processes. For example, a heat of around $80°C$ can be captured at a depth of 2,000 meters in the Paris Basin. Waters from the Dogger aquifer are exploited by about fifty geothermal doublets.

In some geological contexts (grabben, volcanic areas), it can also be used to generate electricity. Indeed, geothermal power plants can convert heat from subsurface reservoirs into electricity. These plants are classified into three types: dry steam, flash steam, and binary cycle plants. Each type is suited to different temperature and pressure conditions of geothermal resources (Dickson and Fanelli, 2003). These exploited resources are generally above $150°C$, but power has been generated at Chena Hot Springs Resort in Alaska using a $74°C$ geothermal resource (Lund, 2006).

Geothermal energy offers several advantages, such as a small land footprint, low greenhouse gas emissions, and the ability to provide baseload power, which is crucial for grid stability. Countries like Iceland, New Zealand, and the Philippines have successfully integrated geothermal energy into their energy mix, demonstrating its potential (Lund et al., 2011). However, the exploitation of geothermal energy also poses challenges, including pore-clogging and fouling, high upfront costs, site-specific resource availability, and potential environmental impacts such as induced seismicity and the management of geothermal fluids, which may contain harmful substances (Manzella et al., 2019).

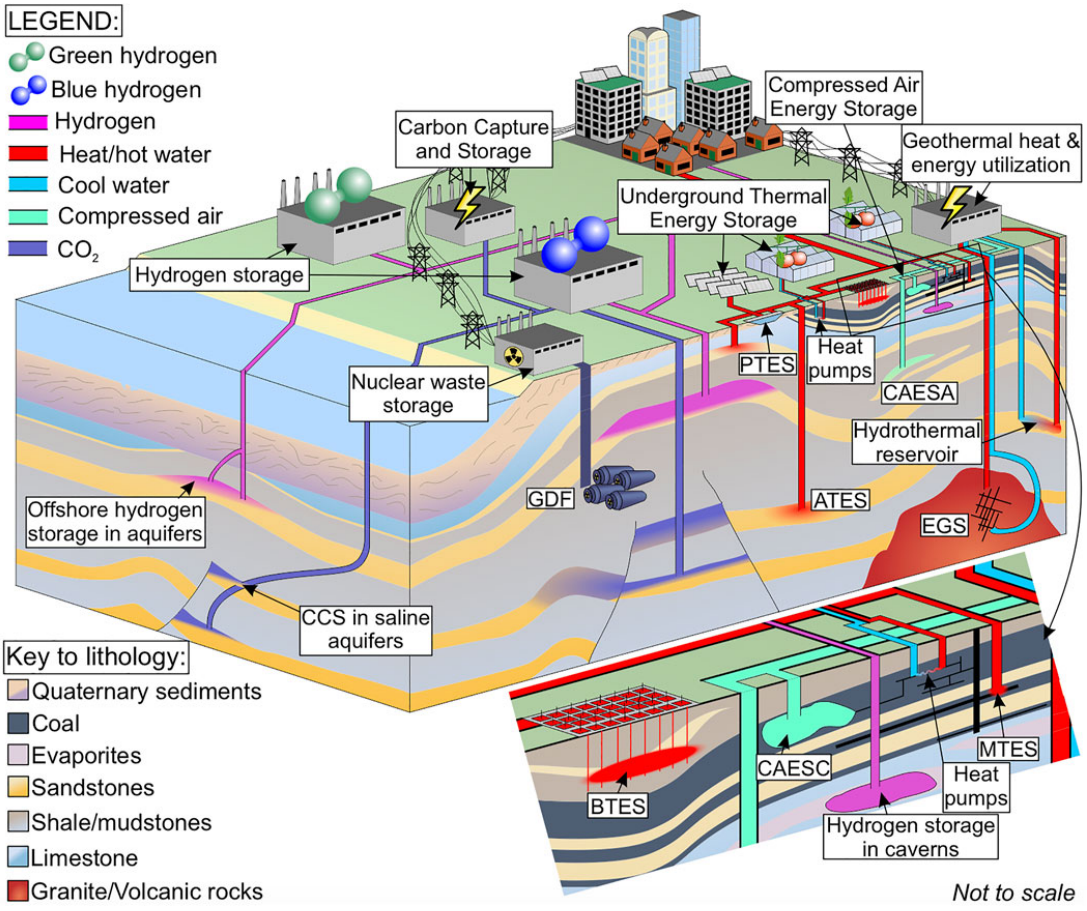

Figure 1.1: Schematic illustrating subsurface utilization to achieve decarbonization goals for net-zero carbon dioxide emissions. Decarbonization applications include nuclear waste storage (GDF-Geological Disposal Facility); Carbon Capture and Storage (CCS); geothermal heat and energy utilization (deep Enhanced/Engineered Geothermal Systems (EGS), hydrothermal systems, and shallow (<120 m) geothermal heat pumps); Underground Thermal Energy Storage (ATES, Aquifer Thermal Energy Storage; PTES, Pit Thermal Energy Storage; BTES, Borehole Thermal Energy Storage; MTES, Mine Thermal Energy Storage); Hydrogen storage in caverns and aquifers; and Compressed Air Energy Storage in Caverns (CAESC) and Aquifers (CAESA) (Kaminskaite et al., 2022).

Geothermal exploitation is increasingly recognized as a vital component of the global energy transition

towards sustainable and low-carbon energy systems. As the demand for clean energy grows, subsurface renewable energy offers significant potential due to its vast, consistent, and largely untapped energy reserves.

Thermal energy storage

Subsurface can be exploited to provide hot water, but it can also be used to store heat. Heat storage technologies in the subsurface meet two main objectives. *(i)* To regulate thermal energy production to better match supply with demand. For example, most solar energy is produced in summer, whereas demand is higher in winter when heating requirements are high. *(ii)* To promote the fatal heat, i.e. thermal energy indirectly produced as part of industrial processes, by waste incineration plants, data centers, water treatment plants, or nuclear power stations.

There are several technologies for underground thermal energy storage (UTES). The most common are:

- Aquifer Thermal Energy Storage (ATES): groundwater is pumped up and heated, then reinjected through a well or group of wells. The stored heat is recovered by reversing the direction of fluid flow.
- Borehole Thermal Energy Storage (BTES): this system uses a volume of soil or rock to store thermal energy via dozens of vertical geothermal probes spaced a few meters apart and a few dozen meters deep.
- Mine Thermal Energy Storage (MTES). This technology uses water from closed, flooded mines as a means of storage.

1.1.2 Challenges in the fluid reinjection in the subsurface

Conventional geothermal power plants exploit naturally occurring hydrothermal resources, which include hot water or steam reservoirs located relatively close to the Earth's surface (Bertani, 2016). This exploitation consists of pumping hot waters, extracting calories from the aqueous fluids, and reinjecting them into the reservoir. However, one of the critical challenges in the efficient operation of geothermal systems is maintaining high injectivity in the reservoir. Injectivity refers to the ability to inject fluids into a reservoir, which is essential for managing reservoir pressure and sustaining long-term production. A significant factor influencing injectivity is pore-clogging, a phenomenon in which the permeability of the reservoir rock decreases due to the accumulation of particles and other substances within the pore spaces.

The seasonal storage of heat in aquifers faces the same challenge (Fleuchaus et al., 2018). The chemical composition of the groundwater, high concentrations of dissolved gas in the water, fine-grained materials in a heterogeneous aquifer, and clay swelling are key factors that may initiate clogging of the injection wells. Regular cycles of production/injection can have an impact on the motion of particles in the reservoir that can alter the porosity and the permeability of the reservoir and by the end its injectivity/productivity.

The impact of pore-clogging on injectivity is profound. As the permeability of the reservoir decreases, the resistance to fluid flow increases, leading to a decline in injectivity. This reduction in injectivity can result in higher operational costs, reduced efficiency of heat extraction, and, ultimately, the premature decline of the geothermal reservoir. Understanding and mitigating pore-clogging is therefore crucial for the sustainable management of geothermal resources.

Several case studies have highlighted the challenges of pore-clogging in geothermal reservoirs. For instance, the Geysers geothermal field in California has experienced significant injectivity declines due to silica scaling (Stefansson, 1997). Researchers found that the injection of treated wastewater, which is rich in dissolved silica, led to the rapid formation of silica scales within the reservoir's pore spaces, severely impacting injectivity. The same loss of injectivity has been observed in different geothermal fields from Japan. Because of low reinjection temperatures, a loss of 30% of injectivity per year has been observed for some fields, mainly due to silica precipitation (Itoi et al., 1989).

To address pore-clogging, various mitigation strategies have been developed. Mechanical methods, such as backflushing and hydraulic fracturing, can help to remove clogs and restore permeability. Chemical treatments, including the use of scale inhibitors and acidizing, can prevent or dissolve mineral precipitates. Biological control measures, such as biocides, can inhibit the growth of microorganisms that contribute to biofouling. Additionally, optimizing the composition and temperature of injected fluids can minimize the risk of scaling and precipitation.

Pore-clogging is a significant challenge in the operation of geothermal reservoirs, impacting injectivity and the overall efficiency of geothermal energy extraction. Understanding the mechanisms of pore-clogging and implementing effective mitigation strategies is crucial for maintaining high injectivity and ensuring the sustainable management of geothermal resources. Continued research and innovation in this field will play a vital role in overcoming the challenges associated with pore-clogging and enhancing the prospects of geothermal energy and other applications.

1.1.3 Other subsurface exploitation facing injectivity issues

Carbon Capture Storage

With CO_2 levels rising in the atmosphere, research has been underway for over 30 years to store some of the CO_2 emitted by industry underground. Carbon Capture and Storage (CCS) is a critical technology for mitigating climate change by reducing CO_2 emissions from industrial sources and power plants. The process involves capturing CO_2 emissions, transporting them to a storage site, and injecting them into deep geological formations for long-term sequestration. CCS can be applied to various industries, including cement, steel, and chemicals, which are difficult to decarbonize through other means. The subsurface storage of CO_2 typically involves injecting the gas into depleted oil and gas fields, deep saline aquifers, or unmineable coal seams. These geological formations must have suitable porosity and permeability to accommodate the injected CO_2 and robust cap rocks to prevent their escape (Benson and Cole, 2008). Successful CCS projects, such as the Sleipner project in Norway and the Boundary Dam project in Canada, demonstrate the feasibility and effectiveness of this technology. The capacity of storage of the reservoirs is huge: deep saline aquifers represent a storage capacity with an estimation of 400 to 10,000 CO_2 Gton (Benson and Cole, 2008). However, CCS faces economic, technical, and regulatory hurdles, including high costs, the need for extensive monitoring to ensure CO_2 remains sequestered, and public acceptance (Fuss et al., 2018).

H_2 production and storage

More recently, hydrogen is considered a key element in the transition to a low-carbon energy system due to its versatility and potential for use in various sectors, including transportation, industry, and power generation. The production of hydrogen can be achieved through several methods, with steam methane reforming (SMR) and electrolysis being the most common. SMR, combined with CCS, can produce "blue hydrogen," while electrolysis, powered by renewable energy, produces "green hydrogen".

Subsurface storage of hydrogen is essential for balancing supply and demand, particularly given the intermittent nature of renewable energy sources like wind and solar. Large-scale hydrogen storage can be achieved in underground salt caverns, depleted gas fields, or aquifers. Salt caverns are particularly attractive due to their impermeability and ability to withstand repeated pressurization cycles (Crotogino et al., 2010). Successful examples of hydrogen storage in salt caverns include the Teesside facility in the UK and the Clemens Dome facility in the US (Lord et al., 2014). Despite its potential, hydrogen storage faces challenges such as high costs, the need for suitable geological formations, and technical issues related to hydrogen's low energy density and its interactions with storage materials (Smith et al., 2022).

1.2 Principal clogging mechanisms

The reinjection of fluids into geothermal wells for exploitation and extension of the life of the wells contributes to the perturbation and reduction of injectivity in the geothermal reservoir through different physicochemical mechanisms. Song et al. (2020) presented a repartition of the different clogging mechanisms encountered in sandstone aquifers during artificial recharge (see Fig. 1.2). It turns out that clogging occurs mostly due to particle retention, biological processes, chemical reactions, gas trapping, and clay swelling.

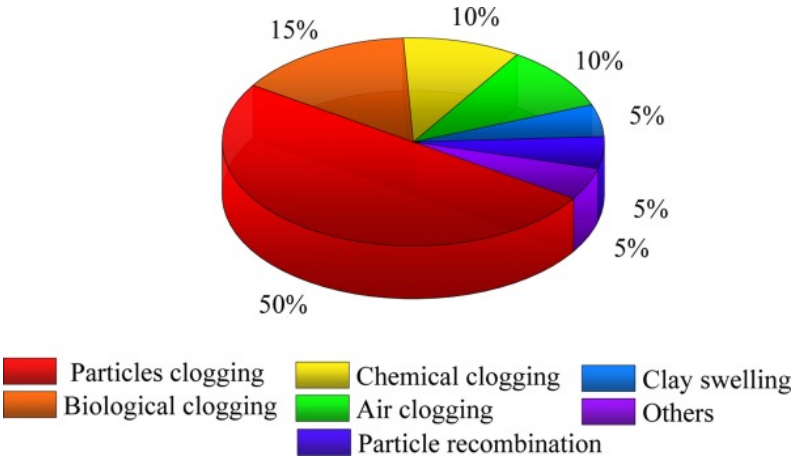

Figure 1.2: Proportion of various clogging mechanisms (Song et al., 2020).

1.2.1 Physical clogging

Physical clogging mostly relates to clogging by the transport and deposition of suspended particles (particle clogging). According to Bouwer (2002), particle clogging represents 50% of the encountered clogging into the subsurface during the artificial recharge of groundwater, and according to Rinck-Pfeiffer et al. (2000), more than 92% of all physical clogging. The sources of suspended particulate matter are multiple:

- Injected fluid carrying exogenous fine particles that were not filtered through the filtration process in the surface facilities or that were formed in the injection well before the injection (Song et al., 2021).
- Internal erosion of the matrix surfaces which results in detachments of a high fraction of fine particles (e.g. clay particles) by hydrodynamic forces (Russell, 2013; Feia et al., 2015).

- Colloidal particles formed by flocculation and precipitation resulting from the mix of the injected fluid with the formation water near the wellbore (Grolimund and Borkovec, 1999; Eppner et al., 2017).

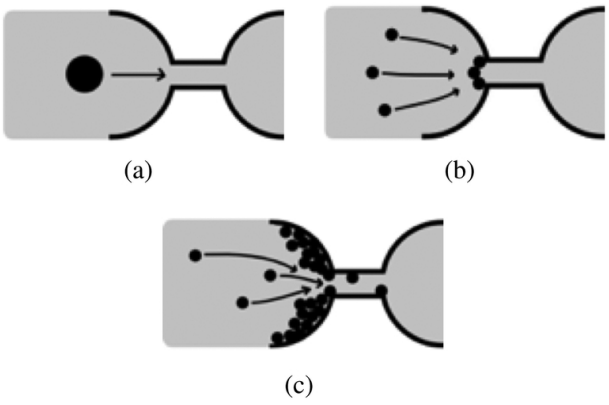

Figure 1.3: Different mechanisms responsible for the clogging of pores at a constriction: (a) sieving, (b) bridging, and (c) aggregation of particles Dressaire and Sauret (2017).

Different mechanisms involving different physics are responsible for the clogging of pores as presented in Fig. 1.3.

Sieving or straining

Sieving refers to the capture of a suspended particle of diameter D_p flowing through a pore with a constriction width W due to surface contact (see Fig. 1.3.a),

$$W \leq D_p. \tag{1.1}$$

It's the basic capture mechanism used in the filtration process or for size separation (Sanderson et al., 2001; Wei et al., 2011; Kim et al., 2014). It occurs for particles hydrodynamically transported (Mustin and Stoeber, 2010) or particles rolling on the matrix surfaces (Duru and Hallez, 2015).

For polydispersed suspensions, Dressaire and Sauret (2017) figure out by experimental measurements that the sieving of particles follows a Poisson distribution with a probability, $p(t_{clog}) = \frac{1}{\langle t_{clog} \rangle} \exp\left(-\frac{t_{clog}}{\langle t_{clog} \rangle}\right)$ where $\langle t_{clog} \rangle = 1/(C_l Q)$ is the average clogging time, with C_l the concentration of large particles ($D_p \geq W$) and Q the flow rate in the pore.

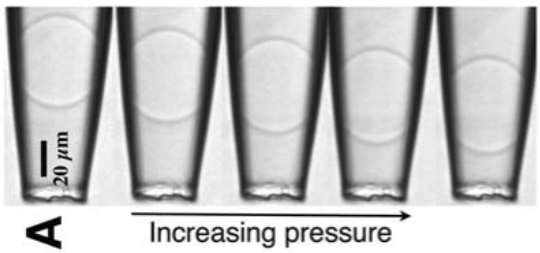

Figure 1.4: Series of images of a microgel particle being deformed as the applied pressure increases; from left to right: p = 100 Pa, 150 Pa, 200 Pa, 250 Pa, 300 Pa (Wyss et al., 2010).

Soft deformable particles (e.g. polymers, droplets, cells) can flow through a constriction smaller than their diameter depending on the applied pressure differences as shown in Fig. 1.4. Assuming the

particles are linearly elastic, the translocation pressure, Δp_{max}, needed to pass the pore constriction reads, $\Delta p_{max} \propto E \left(\frac{D_0}{W}\right)^{14/3}$, where E is the young modulus and D_0 is the diameter of the particle at rest.

Bridging

Bridging refers to the capture of particles by arch formation through surface contacts. It consists of particles arriving simultaneously at the entrance of the constrictions where they will form a more or less stable bridge (typically 2 to 10 particles) that spans over the entire cross-section of the pore. In this process, the particle diameter is smaller than the constriction size ($D_p < W$), and the bridging is most likely to occur if $0.33W < D_p < 0.46W$ according to Sharp and Adrian (2005). Bridging is carried by geometrical and hydromechanical effects and by particle concentration.

Unlike sieving, the bridging mechanism is often a non-permanent blockage. The arch formed can break under flow fluctuations, as the arch can withstand large forces in only one direction (Zuriguel, 2014). However, if particles are in an arching configuration, lateral forces induced by the shear flow on the arch can hold the particles in place and stabilize the arch (Sharp and Adrian, 2005).

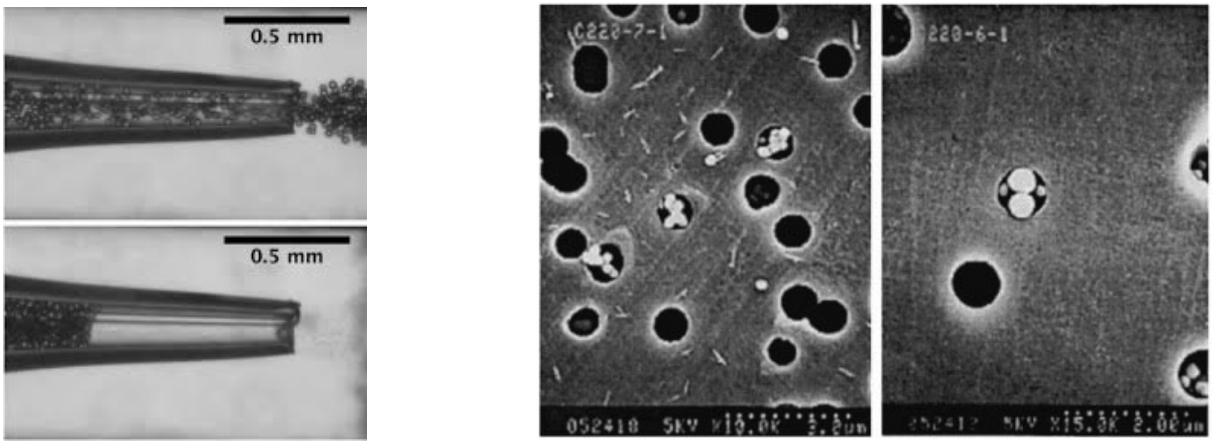

(a) (b)

Figure 1.5: (a) Flow and clogging by the bridging of a neurally buoyant suspension of PMMA (Polymethyl Methacrylate) particles in an axisymmetric tapered glass capillary (Dressaire and Sauret, 2017). (b) Particle arches formed at high flow velocity. Negatively charged 0.249 μm diameter polystyrene sulfate particles (white particles) flow through $1\mu m$ pores (black dots) (Ramachandran and Fogler, 1999).

Bridging casually occurs for different regimes of particle concentration:

- For dense suspensions (Fig. 1.5a): increasing the volume fraction of particles until a critical or jamming volume fraction, ϕ_m, implies a rheological non-Newtonian behavior of the fluid where particles are rearranged to form crystal structures (Genovese and Sprakel, 2011).
- For dilute suspensions (Fig. 1.5b): it has been shown that the creation of an arch can occur for particle concentrations lower than the jamming value (Ramachandran and Fogler, 1999). Goldsztein and Santamarina (2004) defined empirically the critical number of particles, n_{max}, arriving simultaneously at a circular constriction to observe bridging in dilute suspension as:

$$n_{max} \propto \frac{A_c D_p}{2V_p} \tag{1.2}$$

where A_c is the constriction area, and V_p is the particle volume.

Surface deposition or aggregation

In this process, particles can accumulate gradually through successive deposition of colloidal particles which reduce the cross-section of the seepage pore until clogging (see Fig. 1.6). Colloidal particles can also be self-assembled into clusters in the bulk suspension and transported until filtration. Whereas the two previous clogging mechanisms involve contact and hydrodynamic interactions, the aggregation implies long-range electrochemical forces such as attractive Van der Waals force and repulsive electrostatic force. These interactions apply only if the particles are close enough distance to one another. The geometrical features of the porous medium made of pores and throats act as flow convergent that transports the particles closer to each other. Thus the surface deposition mechanism is driven by the hydrodynamic and the interplay of the electrochemical effects.

For a single particle, two types of deposition behavior are reported:

- Favorable deposition: it occurs if the interactions between the particles and the wall are attractive for all separation distances.
- Unfavorable deposition: the energy profile is dominated by the repulsive interaction, and the deposition is driven by the roughness of the solid surfaces.

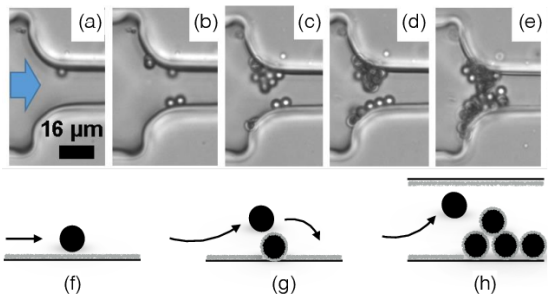

Figure 1.6: Particle aggregation resulting in clog formation. (a–e) The density-matched suspension of polystyrene particles ($D_p = 3\ mm$) with sulfate charge groups flows through a constriction of width $W = 15.5\ mm$. The images are recorded at 3, 5, 10, and 36 minutes, with a flux of 2.8×10^4 particles per minute at the onset of the experiment (Dersoir et al., 2015). (f–h) Schematic representation of the aggregation process, from the deposition of the first particle to the clog formation (Dressaire and Sauret, 2017).

The clog is formed when N^* particles have flown through the constriction, and N particles are deposited on the wall of the channel, forming a clog (Massenburg et al., 2016):

$$N^* \propto \frac{W^3 H}{6 D_p^4} \tag{1.3}$$

where H is the depth of the pore. Eq.(1.3) results are in good agreement with the experimental results (Dersoir, 2015).

Combination of particle clogging mechanisms

Table. 1.1 summarizes the main clogging mechanisms observed at small scales.

Table 1.1: Clogging in microfluidic systems: mechanisms, suspension properties, and channel geometry (Dressaire and Sauret, 2017). W is the width of the pore constriction and D_p is the particle diameter.

	Sieving	Bridging	Aggregation
Size comparison	$D_p \geq W$	$D_p \leq W$	$D_p \leq W$
Solid volume fraction ϕ in suspension	Low ϕ	Large ϕ	Low ϕ
Interaction needed	Rigid contact and hydrodynamic interactions	Rigid contact and hydrodynamic interactions	Attractive particle-wall and particle-particle interactions
Clog formation	Blockage by a single particle	Blockage by an arch of particles	Successive deposition of particles leading to blockage

Generally, particle clogging appears as a combination of deposition and bridging/sieving and follows ordered steps Tale et al. (2020):

- First, particles flowing in the vicinity of walls, are most likely to deposit, forming several layers of deposited particles.
- Second, the reduction of pore diameter due to layers of deposited particles will lead to pore-clogging by the arrival of upstream particles through bridging or sieving mechanisms.

Particle clogging mechanisms described earlier make a porous medium act as a filter when colloids are injected into it (Fig. 1.7). Suspended or colloidal particles getting retained inside a porous medium is known as internal filter cake or deep bed filtration. External filter cake is the term used to describe the suspended and colloidal particles retained at the entrance of a porous medium due to the size exclusion or bridging of particles.

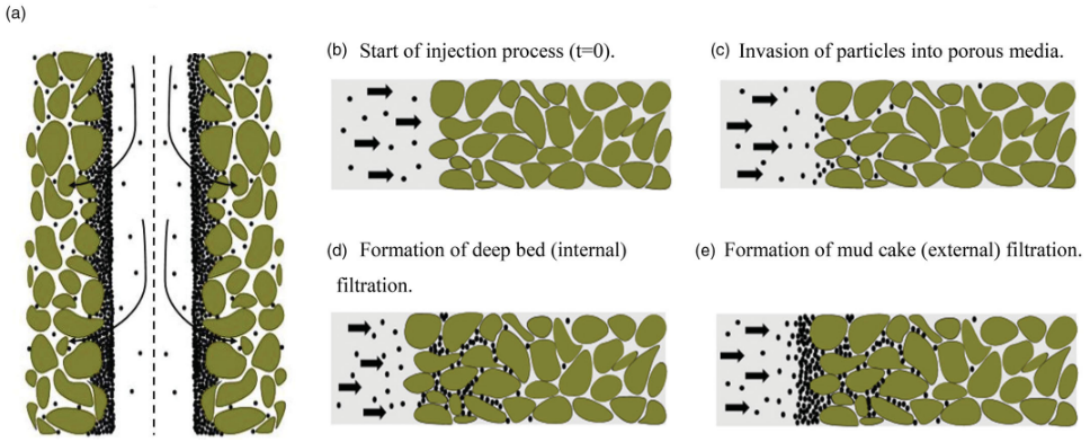

Figure 1.7: (a) Schematic of well impairment due to low-quality water injection (deep bed filtration and external filter cake formation, radial), (b–e) injection of suspension solids in core (1-D, experimental) (Tale et al., 2020).

1.2.2 Biological clogging

Referring to Bouwer (2002), biological clogging accounts for 15% of all clogging. The subsurface is an ecosystem where countless species of microorganisms (eg. algae and bacteria), live, breed, and multiply rapidly if the nutrient conditions are suitable (Fetter Jr and Holzmacher, 1974) as shown in Fig. 1.8. During the growing process, the microorganisms increase locally the viscosity of the fluid. We talk of biological clogging if, by biofilm growth, biological gas retention, and accumulation of organic matter, microorganisms contribute to the clogging of an effective pore channel (Zhao et al., 2009). The biological clogging process acts in 3: permeability drops sharply during the aerobic period; permeability remains almost stable or increases slightly during the transition period; and permeability decreases sharply then maintains a slow downward trend during the anaerobic period causing bio-clogging. Microorganisms multiply rapidly when the nutrient content in the injection fluid is high (Dillon et al., 2016).

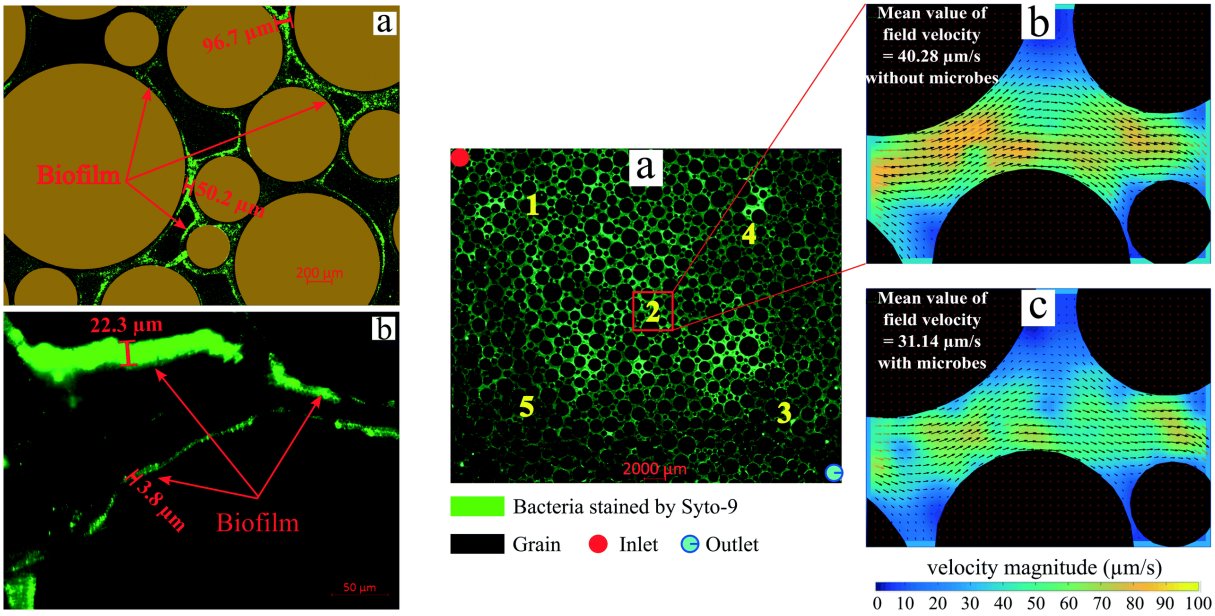

(a) (b)

Figure 1.8: On the left (a), images of biofilms after injection of Syto-9 (green fluorescent nucleic acid) in the ***a*** artificial-structure and ***b*** real-structure micromodels (scales are different in the images). On the right (b), ***a*** images of the micro-model after injection of Syto-9. Results of particle image velocimetry at the middle of the micro-model during injection of tracer particles indicating the field velocity map ***b*** without bacteria and ***c*** with bacteria. (Gaol et al., 2021)

1.2.3 Chemical clogging

The injection of cold fluid in the porous formation may lead to hydrogeochemical reactions where minerals will precipitate and accumulate, which obstruct the seepage channel and change the permeability leading to chemical clogging (see Fig. 1.9). Ungemach (2003) pointed out that the adverse thermochemical reaction caused by the injection of fluid is more relevant than the chemical incompatibility between the injection fluid and native fluid.

The clogging process is affected by the chemical properties of the injection fluid and native fluid, the operating conditions, and the environmental characteristics of the medium.

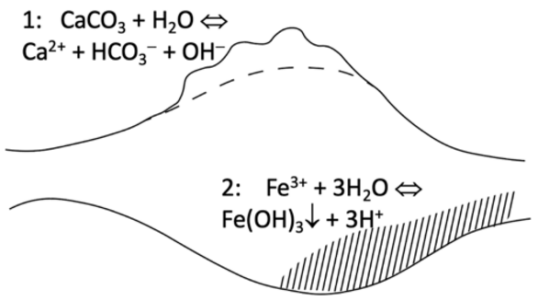

Figure 1.9: Illustration of main groups of chemical clogging processes: 1 – dissolution (e.g., of calcite), 2 – precipitation (e.g., of iron hydroxide). After Anna Kottsova and Brehme (2022).

1.2.4 Air clogging

Air clogging occurs when a gas is trapped inside a pore blocking the water delivery channel. Gas adheres to the hydrophobic base surface of the solids, reducing the permeability of the porous medium and leading to air clogging. It accounts for 10 % of all clogging (Yuhara and Maruyama, 1996). Gas can remain in bubbles form which obstructs the water path by capillary entrapment (Seki et al., 1998). Gas bubbles in recharge systems can be exogenous to the porous medium (entrapped air, see Fig. 1.10) or produced by microbial metabolisms (biogenic gases), such as CO_2, N_2, H_2, and NH_4 (Holocher et al., 2003; Beckwith and Baird, 2001). Gas bubbles tend to block the largest pore throats, leading to permeability decreases and elevated water levels.

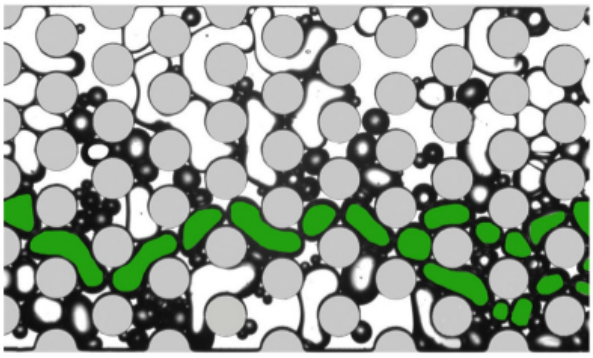

Figure 1.10: Photograph of the foam transport in a heterogeneous micromodel at a foam quality of 80% (white color - trapped bubble; green color - flowing bubble) (Lv et al., 2020).

1.2.5 Clay swelling

Clay is ubiquitous in geological reservoirs. Clay particles have a sheet structure which gives them specific properties depending on the chemical composition of the injected fluid. One of their known properties is the swelling process. According to Zhou (1995), *"clay swelling is a result of the increase in interlayer spacing between clay particles"*. Clay swelling occurs when the clay is exposed to aqueous solutions having brine concentration below the critical salt concentration (Khilar and Fogler, 1984). This corresponds to a solution with a low ionic strength configuration (typically below 0.1 M). In the presence of a high ionic strength solution, we are witnessing a shrinkage.

The swelling process reduces the opening of pores as shown in Fig. 1.11, and therefore, contributes to

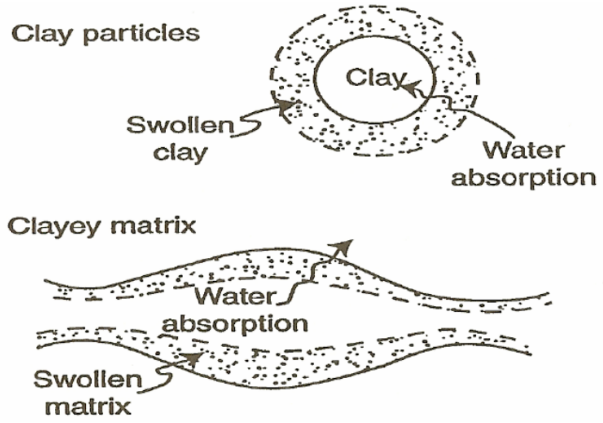

Figure 1.11: Clay particle expansion and pore space reduction by swelling (Civan, 2007).

the reduction of permeability and injectivity. That is why clay swelling is often considered as the main engineered component barrier in radioactive waste disposal as they are less permeable (Gens et al., 2004). Moreover, clay particles can be torn off and transported by fluid flow, and then, clog downstream pores which will reduce the permeability of the reservoirs.

1.2.6 Summary of extended damage mechanisms

Bennion (1999) classify the different formation damage mechanisms encountered in the subsurface into 3 principal parts (see Fig. 1.12): mechanical mechanisms, biological mechanisms, and chemical mechanisms. Then, Bishop (1997) summarizes into seven, formation damage mechanisms listed by Bennion (1999) through:

1. Fluid–fluid incompatibilities. For example, emulsions are generated between invading oil-based mud filtrate and formation water.

2. Rock-fluid incompatibilities. For example, contact of potentially swelling smectite clay or deflocculatable kaolinite clay by non-equilibrium water-based fluids with the potential to severely reduce near-wellbore permeability.

3. Solids invasion. For example, the invasion of weighting agents or drilled solids.

4. Phase trapping/blocking. For example, the invasion and entrapment of water-based fluids in the near wellbore region of a gas well.

5. Chemical adsorption/wettability alteration. For example, emulsifier adsorption changes the wettability and fluid flow characteristics of a formation.

6. Fines migration. For example, the internal movement of fine particulates within a rock's pore structure results in the bridging and plugging of pore throats.

7. Biological activity. For example, the introduction of bacterial agents into the formation during drilling and the subsequent generation of polysaccharide polymer slimes which reduce permeability.

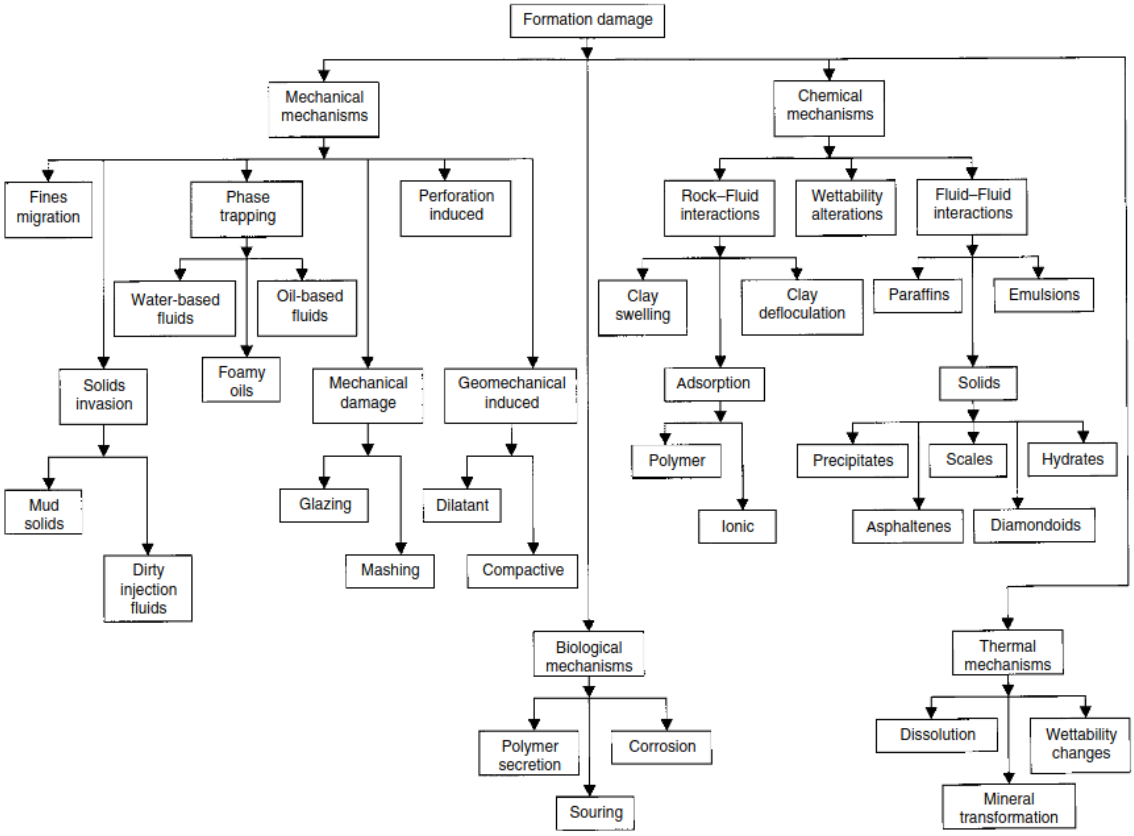

Figure 1.12: Classification and order of the common formation damage mechanisms (Civan, 2007).

1.3 Review of the influencing factors in particle clogging

With the transport of colloids leading to the clogging of pores through deposition, bridging, or sieving, a decline in permeability is consequently observed. Understanding the effect of particle clogging in porous media through qualitative analysis undergoes the study of the physical, chemical, and topological parameters influencing its behavior.

1.3.1 Influencing factors related to fluid properties and flow conditions

Particle transport in porous media is a non-stationary mechanism involving the local fluctuation of the fluid parameters such as the flow rate, temperature, pH, ionic strength, and ions in solutions.

Flow rate

Several studies investigate the effects of the flow rate on the retention and migration mechanisms (Bradford et al., 2007; Li et al., 2008; Zhang et al., 2015). In Fig. 1.13, Xia et al. (2023) show that low flow rates are prone to clogging, and high flow rates can prevent fine particles from forming bridges and clogging due to interruptions in pressure distribution and flow reversal.

Remobilization occurs if the pressure difference and frictional resistance generated by the fluid exceed the compressive strength of the formation. The critical flow velocity (around 0.007 cm/s for Berea sandstone (Gabriel and Inamdar, 1983)) is regarded as the minimum dynamic condition for the suspended particles to stop clogging. If the flow velocity is greater than the critical flow velocity, tiny particles

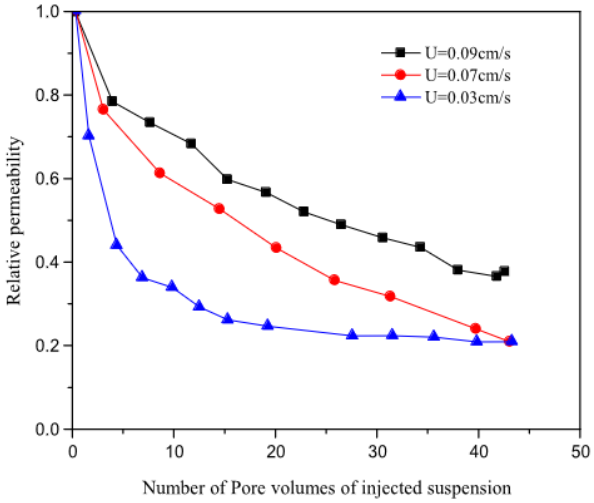

Figure 1.13: Effect of flow velocity on permeability (Xia et al., 2023).

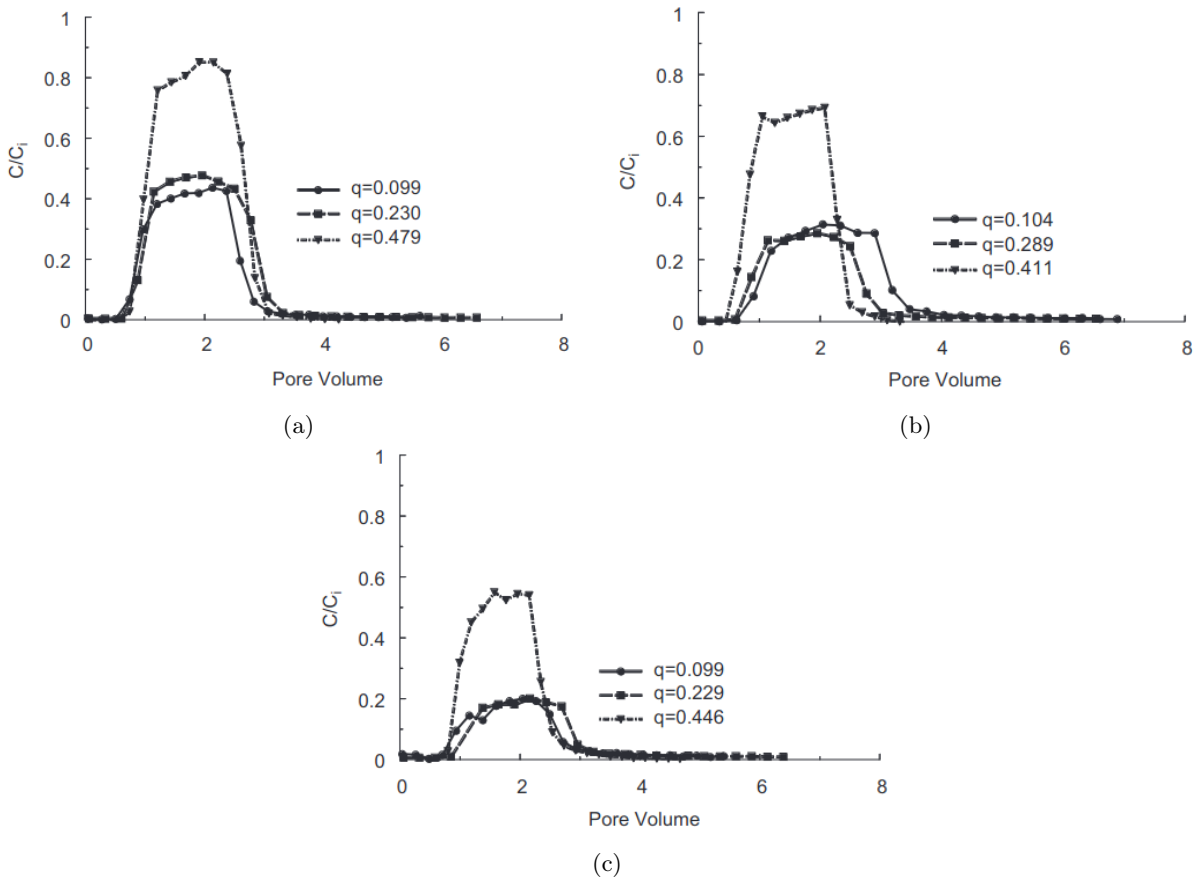

Figure 1.14: Effluent concentration curves for 1.1 μm latex colloids in (a) 360 (b) 240 (c) 150 μm quartz sand when the ionic strength was 56 mM and the Darcy velocity was approximately 0.1, 0.2, and 0.45 $cm\ min^{-1}$ (Bradford et al., 2007).

originally trapped on the pore surface of the medium will be carried by the fluid flow. However, exceeding the critical fluid velocity does not mean clogging will not occur (Ochi and Vernoux, 1998). Fig. 1.13 shows the effect of flow velocity on the permeability damage regarding the injected pore volume of the

suspension.

Moreover, Bradford et al. (2007) investigate the effect of fluid flow rate on the particle concentration retention under salinity (NaCl) in the injected fluid. Fig. 1.14 shows that a higher Darcy velocity produces an increase in the effluent concentration. Bradford et al. (2007) hypothesize that, in the case of the highest Darcy velocity ($q = 0.45cm\ min^{-1}$), the fluid drag forces were sufficient to inhibit colloid retention in regions of pore space that would otherwise retain colloids at lower Darcy velocities (0.1 and 0.2 $ml\ min^{-1}$).

Temperature

In the exploitation of geothermal energy, the temperature of the medium has an impact on the damage of the porous formation with the water reinjection process.

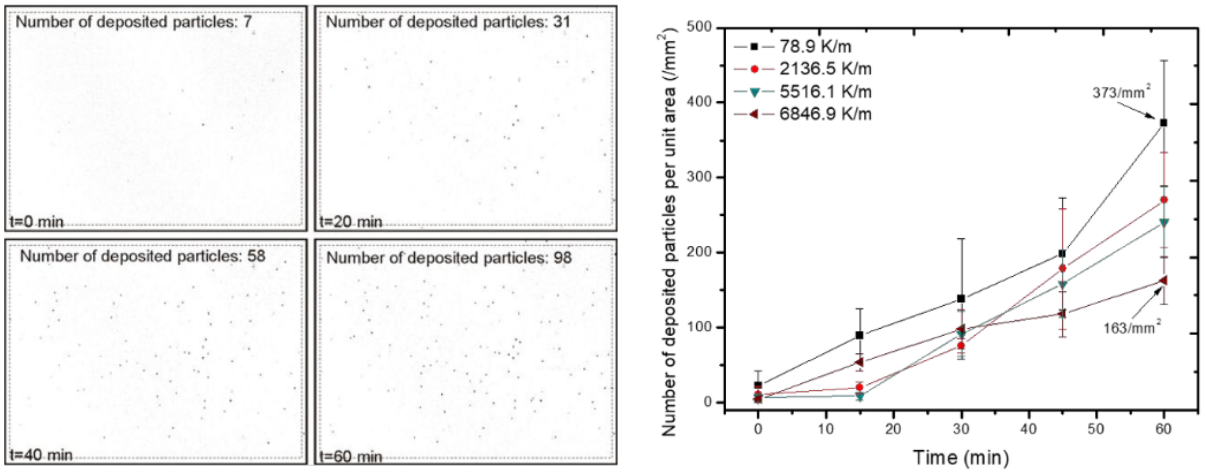

(a) (b)

Figure 1.15: (a) Videomicroscopic images of 0.93 μm polystyrene particles captured using 10X objective lens under temperature gradient maintained at 6846.9 K/m at 0 min, 20 min, 40 min, and 60 min, Particles are shown as black dots; (b) Number of deposited particles per unit area versus deposition time for four different temperature gradients at 78.9 K/m, 2136.5 K/m, 5516.1 K/m and 6846.9 K/m (Yan et al., 2020).

The increase in temperature has microscopic effects on both fluid properties, particle, and porous matrix characteristics (Rosenbrand et al., 2015):

- The increase in temperature reduces the dielectric constant of the solution and increases the repulsion force of particles and matrix surfaces which has a promotion effect on particle transport.
- The increase in temperature provokes an expansion of rocks (thermal expansion) that decreases the pore space and permeability. Experimental data has shown that heating sandstone rock samples from room temperature to 70–200°C decreases their permeability (Rosenbrand et al., 2014).
- The increase in temperature can increase the reaction rate of chemical interactions as dissolution/precipitation and then affect clogging.
- The increase in temperature decreases the viscosity of the fluid and changes the fluid density. This makes the separation torque of particles attached to the rock surface greater than the adhesion torque, leading to an increase in the separation of fine particles.

- The inner energy of motion of suspended particles increases with increasing temperature which accelerates the thermodynamics collision process between particles and changes the adsorption of the suspended particles on the porous medium.

Yan et al. (2020) study the particle deposition process in a microchannel along the direction of the applied temperature gradient. They show through Fig. 1.15a that, the number of deposited particles increases with the injection time when a temperature gradient is applied. In Fig. 1.15b, we observe a decrease in the number of deposited particles per unit area with the increase of the temperature gradient.

pH

The change in thermodynamic properties of geothermal water may produce unfavorable thermochemical reactions, and the pH value is the main factor affecting the reactions.

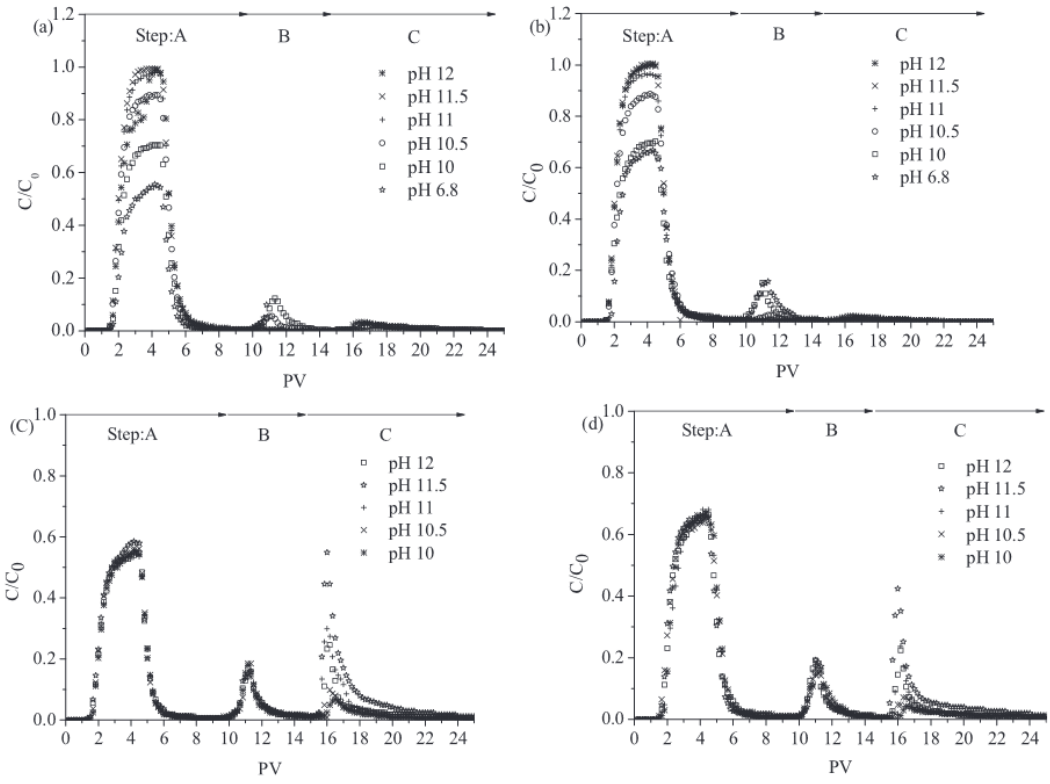

Figure 1.16: Breakthrough curves for polystyrene latex particles in silicon dioxide glass beads. Note: (a) shows the breakthrough curves of deionized water-washed groups in glass beads in attachment experiments; (b) shows the breakthrough curves of acid-washed groups in attachment experiments; (c) shows the breakthrough curves of deionized water-washed groups in elution experiments; and (d) shows the breakthrough curves of the acid-washed groups in the elution experiment (Yuan et al., 2020).

The pH value of the injected fluid significantly changes the surface charge of the colloids. In turn, this changes the repulsion and acid-base interaction forces, which affect the critical conditions for particle release (Muneer et al., 2020):

- Under acidic conditions, the positive charge on suspended particles (synthetic fines) increases and particles are easier to move to the solid matrix (silica glass beads).
- Under alkaline conditions, suspended particles with the same charge repel each other and are more likely to agglomerate and deposit.

- Neutral conditions are more favorable for the migration of suspended particles.

Vaidya and Fogler (1990) discussed the variation of the potential of colloidal particles (kaolinite clay) at different pH solutions and pointed out that with the increase in pH solution, the total potential of colloidal particles is positive, which corresponds to the domination of repulsive force. This causes the colloidal particles to migrate easily and block pores under hydrodynamic effects.

Recently, Yuan et al. (2020) have studied the coupled effects of high pH and chemical heterogeneity on colloid (polystyrene latex) retention and release in saturated porous media through column experiments (silicon dioxide glass beads). They presented through Fig. 1.16 that the increase in pH of the solution leads to a decrease in the retention behavior of the porous matrix surfaces concerning colloids.

Ionic strength

The ionic strength of the solution depends on the concentration of ions in the solution and on the ion valence. It is associated with clogging because it characterizes the repulsive force between the particles and porous matrix surfaces, and therefore, the deposition behavior of particles. The higher the ionic strength, the lower the repulsion force, and the higher the concentration of deposited particles. Several studies have been made on the impact of the solution ionic strength on the migration and retention of particles in porous media. Pelley and Tufenkji (2008); Sang et al. (2013); Gerber et al. (2019) use porous media made of quartz grains for experimental investigations.

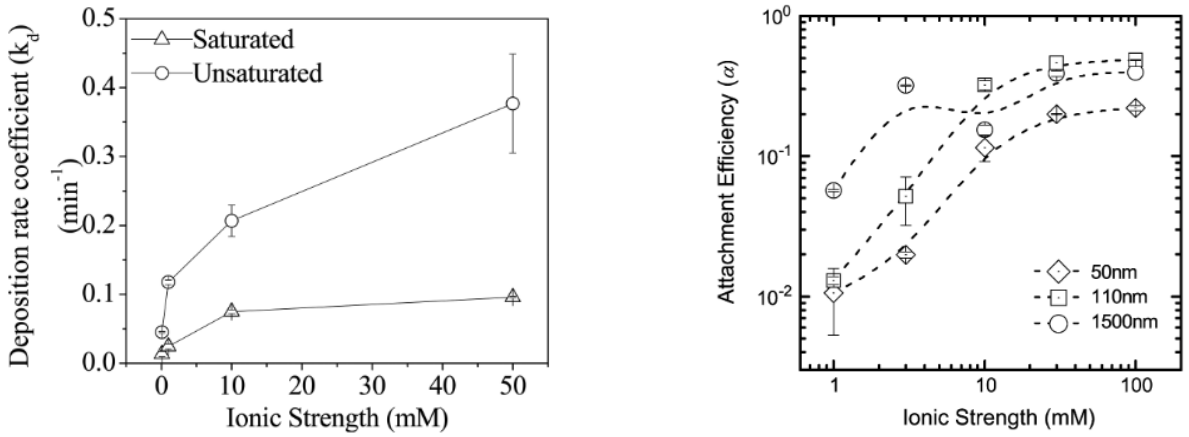

(a) (b)

Figure 1.17: (a) Colloid deposition rate coefficients in saturated and unsaturated media (Sang et al., 2013). (b) Attachment efficiencies (α) for the 50 nm, 110 nm, and 1500 nm colloids suspended in KCl in the absence of natural organic matter over a wide range of solution ionic strengths (pH 5.7 $\pm$ 0.2) (Pelley and Tufenkji, 2008).

Sang et al. (2013) shows the increase of the deposition rate coefficient (in minutes) of carboxylated red-dyed polystyrene particles with the increase in the ionic strength (NaCl) of the solution, both in saturated and unsaturated conditions (Fig. 1.17a). Pelley and Tufenkji (2008) shows the particle attachment efficiency (in %) increases with the increase of ionic strength (KCl) for different latex particle sizes (Fig. 1.17b). Gerber et al. (2019) confirms previous results by sequential images of the deposition of positively charged latex particles in borosilicate glass beads porous medium (Fig. 1.18) where the particle coverage increases with the ionic strength. These studies highlight that the deposition of particles grows until it reaches plateau values even with the increase of the ionic strength. This means that the total

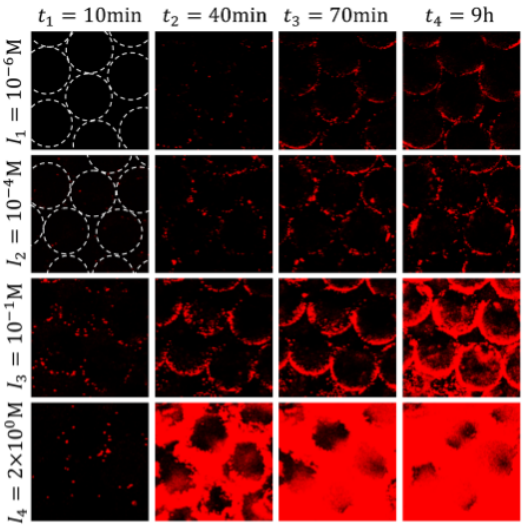

Figure 1.18: Confocal microscopy images of latex particles (red) deposited in the pore space between glass beads (black) in a 150×150 μm^2 window at the entrance of the porous media, with the suspension flowing upwards. 4 conditions of ionic strength are presented at 4 times (Gerber et al., 2019).

deposition of particles (attachment efficiency of 1) is never observed because the competition with the flow rate acting on the deposited layers stabilizes the deposition process until clogging (Gerber et al., 2019).

Ions in solution

The nature of the electrolyte influences the particle retention and migration mechanism.

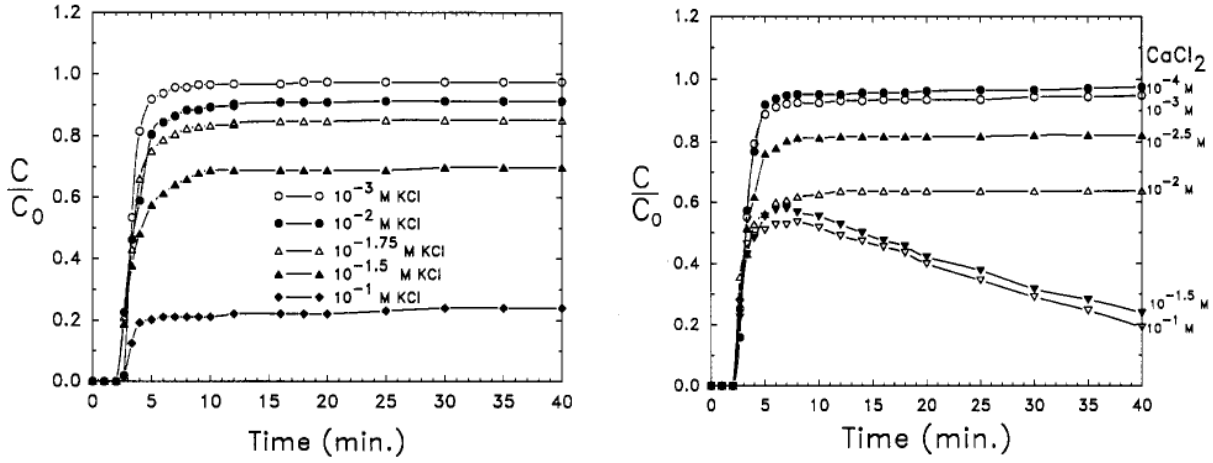

(a) (b)

Figure 1.19: (a)Particle breakthrough curves of the 0.753 μm latex particles with various concentrations of KCl. The residual particle concentration C/C_0 is plotted as a function of time. Experimental conditions were as follows: approach velocity 0.14 cm/s, bed depth 20 cm, collector size 0.2 mm. (b) Particle breakthrough curves of the 0.753 μm latex particles with various concentrations of $CaCl_2$ in the presence of 0.01 M KCl. The residual particle concentration C/C_0 is plotted as a function of time. Experimental conditions were as follows: approach velocity 0.14 cm/s, bed depth 20 cm, collector size 0.4 mm (Elimelech and O'Melia, 1990).

Elimelech and O'Melia (1990) have done column experiments (polystyrene latex particles in spherical glass beads) with two different electrolytes (KCl and $CaCl_2$), and latex particles of different diameters (0.046, 0.378, and 0.753 μm). They vary the electrolyte concentration to observe the effects of favorable and unfavorable conditions on deposition. Results in Fig. 1.19 show that in favorable conditions (high salinity), $CaCl_2$ is associated with lower effluent concentrations which means more deposits.

1.3.2 Influencing factors related to particle properties

Particle concentration

Particle concentration is one of the crucial characteristics of the suspension that guides the clogging behavior. Agbangla et al. (2012) investigated the effect of particle concentration on the formation of arches and deposits of latex microparticles (see Fig. 1.20).

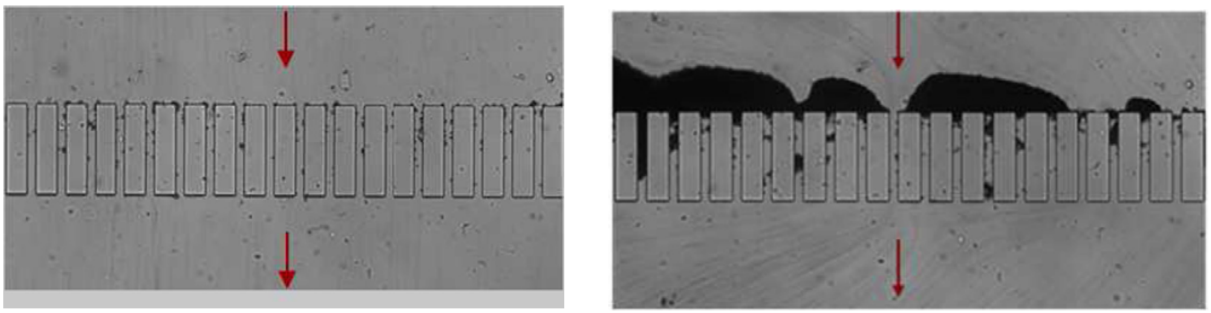

(a) (b)

Figure 1.20: (a) $\phi = 10^{-3}v/v$; $q = 2ml\ h^{-1}$; no deposit of particles after 90 min of dead-end filtration. Latex suspensions are dispersed in ultra-pure water. (b) $\phi = 5.10^{-3}v/v$; $q = 2ml\ h^{-1}$; cluster formation after 90 min of dead-end filtration. Latex suspensions are dispersed in ultra-pure water (Agbangla et al., 2012).

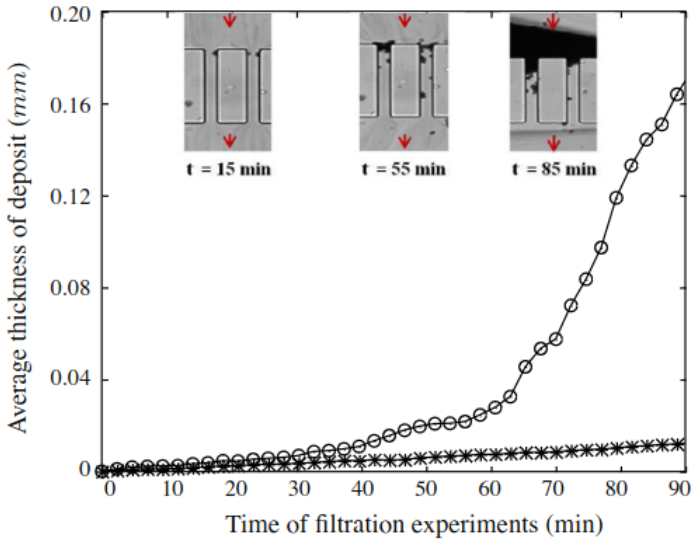

Figure 1.21: The temporal evolution of the average thickness of particle deposit: $-*-$ $\phi = 10^{-3}v/v$; $q = 2ml\ h^{-1}$, and $-o-$ $\phi = 5.10^{-3}v/v$; $q = 2ml\ h^{-1}$ (dispersed in ultra-pure water) with snapshots of the cluster formation at t = 15, 55 and 85 min.(Agbangla et al., 2012).

In their studies, the volume fraction of latex suspension injected at a constant flow rate ($q = 2ml\ h^{-1}$), has an important effect on the retention mechanism. After 90 min of filtration through a PDMS (Polydimethylsiloxane) microchip, no particle clogging is observed if the volume fraction is $\phi = 10^{-3}v/v$, whereas particle capture occurs if latex suspension concentration is increased to $\phi = 5.10^{-3}v/v$. If the volume fraction of particles increases, the flux of latex particles passing through the microchannel entrance is increased. Fig. 1.21 presents the evolution of the average thickness of deposit for the two volume fractions of particles used. For $\phi = 10^{-3}v/v$, no significant fouling is observed as the average thickness remains very low compared to the $\phi = 5.10^{-3}v/v$ case.

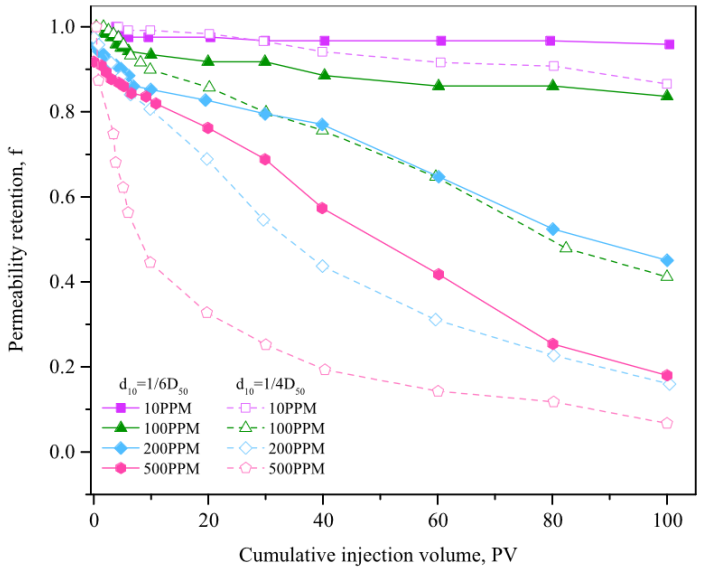

Figure 1.22: Relationship between permeability retention and cumulative injection volume for quartz sand particles (After Xia et al. (2023), modified from Xie (2014)).

Moreover, Xie (2014) show that, the larger the particle concentration, the lower the permeability retention for the same particle size case (see Fig. 1.22). The greater the particle concentration of the injected fluid, the more likely the particles accumulate on the surface of the medium to form a filter cake, resulting in sharp attenuation of the permeability of the medium.

Particle size ratio

Permeability damage is correlated with the particle size. Litton and Olson (1996) used different sizes of modified latex particles (addition of carboxyl or sulfate groups which influence the stability of the suspensions); their column injection study (bed of quartz grains) showed that for different values of ionic strength, the efficiency of attachment was systematically higher for particles whose diameters were the largest (see Fig. 1.23). In the case of hematite particles (Fig. 1.23b), higher attachment efficiency with smaller particle size is observed due to less negative surface charge compared to sulfate particles. These results also show the influence of the particle surface charge on the deposition.

Results were also confirmed by the work of Bennacer et al. (2017), where they observe a low permeability recovery rate for high particle size (see Fig. 1.24).

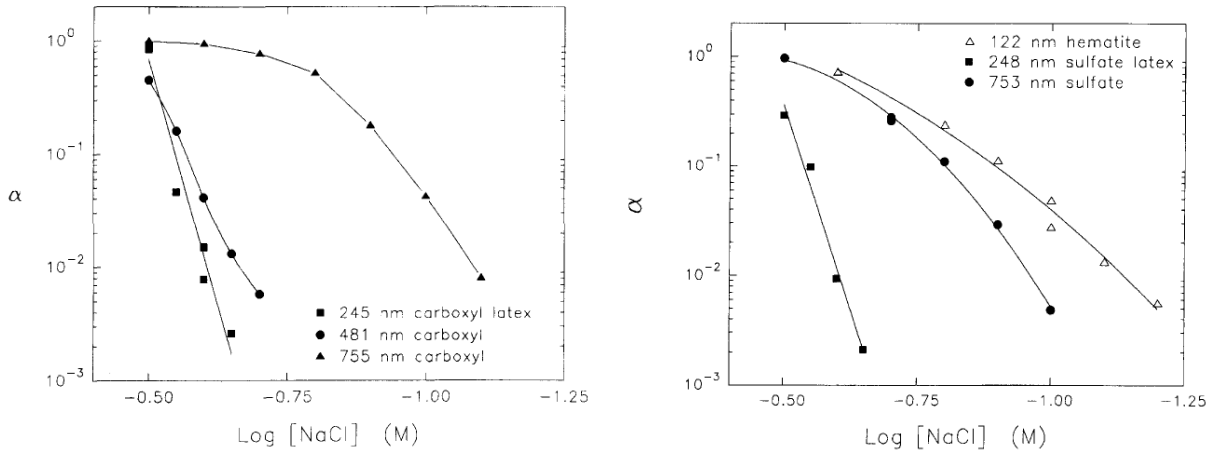

(a) (b)

Figure 1.23: The influence of particle size on the attachment efficiency α at $pH = 9.8$ as a function of ionic strength (a) for carboxylate latex (b) for sulfate latex and hematite (Litton and Olson, 1996).

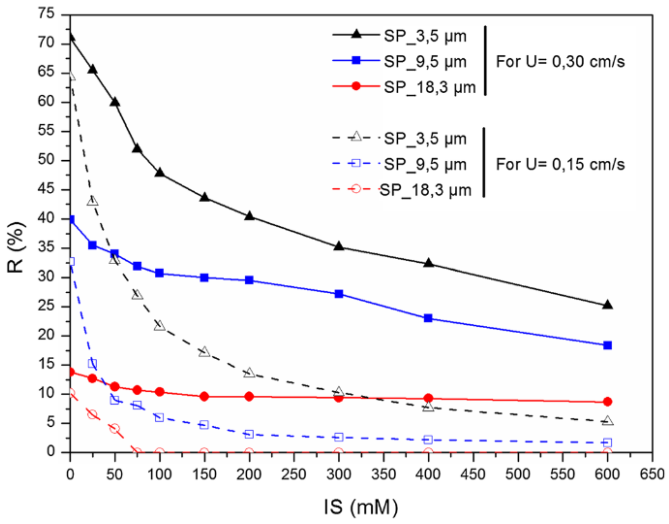

Figure 1.24: Permeability recovery rate (R) as a function of ionic strength (IS). Influence of the particle size and flow velocity (Bennacer et al., 2017).

Particle shape

In the subsurface, suspended particles have forms that differ from spherical particles used in idealized models and laboratory experiments. This aspect of form is, however, particularly important to consider to understand filtration rates.

Hafez et al. (2021) have studied the effect of particle shape (sphere, cube, 2D cross, 3D cross) on discharge and clogging. Fig. 1.25 illustrates the clogging probability as a function of the orifice-to-particle size ratio d_0/d for the different particle shapes. It shows that particle shape defines particle-to-particle interaction and relative mobility. Cubes and 3D crosses are the most prone to clogging. The superior clogging performance of the 3D crosses results from their ability to interlock (see Fig. 1.26). Face-to-face contact among cubes can resist torque and enhance the clogging probability.

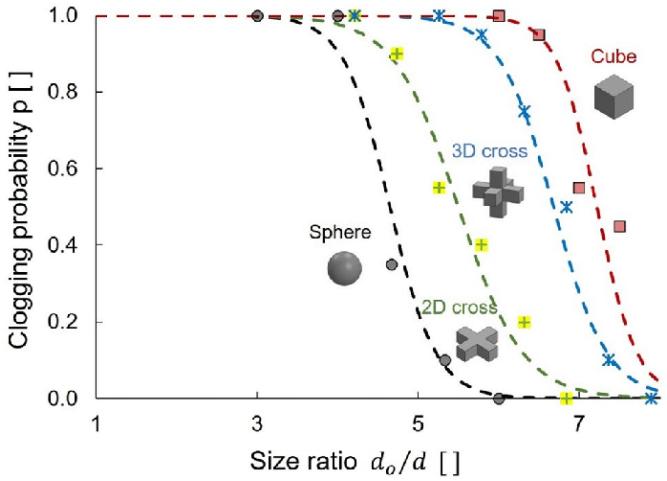

Figure 1.25: Dry granular flow: Clogging probability as a function of orifice-to-particle size ratio d_0/d for the spheres, 2D crosses, 3D crosses, and cubes (experimental results). The clogging probability is the ratio of the number of tests that clogged (within a maximum discharge of 4000 particles for spheres, 2D and 3D crosses, and 2000 particles for cubes) to the total number of tests (20 trials). Datapoints: 360 independent experimental realizations (Hafez et al., 2021).

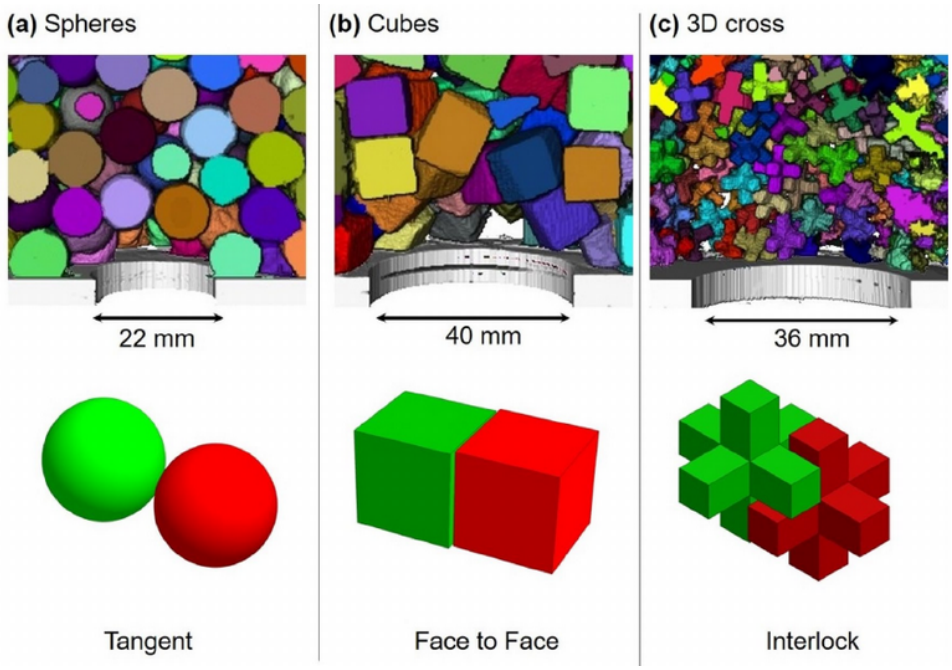

Figure 1.26: Bridge topology (experimental results). CT scans of bridges formed by (a) spheres, (b) cubes, and (c) 3D crosses above the orifice during dry granular flow. Typical particle-particle interaction modes are shown below each scan (Hafez et al., 2021).

1.3.3 Influencing factors related to porous matrix conditions

Surface chemical composition

Guo et al. (2020) investigate the transport of particles (carboxylated polystyrene) through different microfluidic porous media analogs constructed with oppositely charged polystyrene microspheres in various mixing ratios. In their experiments, six different ratios of "+" and "-" beads were set up (see Fig. 1.27).

For a homogeneous medium consisting only of "-" beads, a very low percentage of particles was deposited (C_{out}/C approximately equal to 1). The negligible deposition is due to electrostatic repulsion predominance. The addition of a small fraction of "+" charged beads is associated with a clear change in the breakthrough curves. The plateau value is shifted, and more than half of the incident particles in the suspension are retained by the porous medium. The slightly ascending nature of the breakthrough curves is due to the blocking phenomenon. Results suggest that the degree of geochemical variability and thus the availability of favorable surfaces for deposition plays a major role in the transport and deposition of colloids in the subsurface.

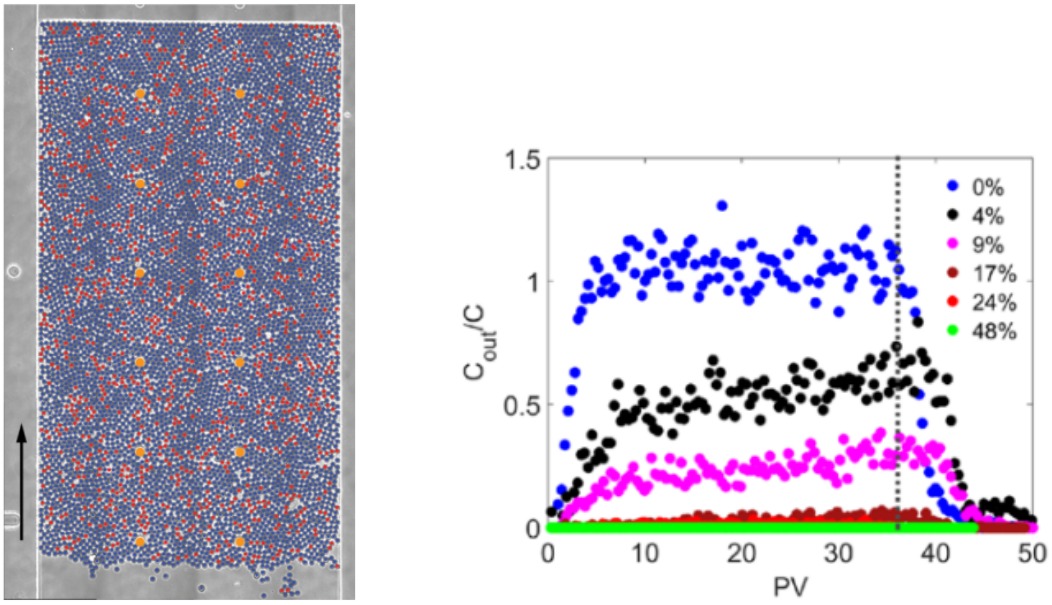

(a) (b)

Figure 1.27: (a) Randomly mixed porous media analogues (PMA) with 17% "+" and 83% "−" charged beads. PMA labeled with "+" beads (red) and "−" beads (blue), as determined by the fluorescence labeling of "−" beads. (b) Breakthrough curves for the transport of 0.5 μm carboxylated colloidal particles in chemically heterogeneous porous media packed with amine-("+") and carboxyl-functionalized ("−") beads at different mixing ratios. Note that the percentage indicates the fraction of "+" beads in the mixing beads. The normalized concentration (C_{out}/C) at the outlet of the PMA is plotted as a function of injected pore volumes (PV). The dashed line indicates the time when deionized water flushing started (Guo et al., 2020).

Porous structure

The porous structure through morphological parameters as the surface roughness affects the mobility and retention of particles in porous media. Auset and Keller (2006) through pore-scale visualization, investigate colloid straining and filtration in saturated porous media using micromodels. Roughness seems to affect hydrodynamics, altering the streamlines and thus inducing deposition of particles more important than for smoother collecting surfaces.

Furthermore, the collision efficiencies are statistically more significant in the rough porous medium than in that where the grains are smooth (see Fig. 1.28). Other results from column experiments show that surface roughness leads to significant retention of colloids both in saturated and unsaturated porous media (Morales et al., 2009; Bradford and Torkzaban, 2013).

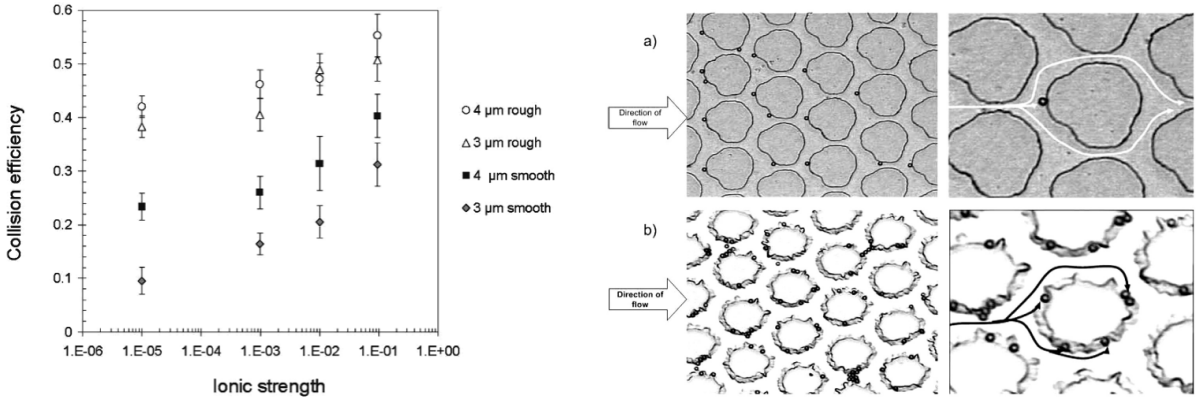

(a) (b)

Figure 1.28: (a) Collision efficiencies as a function of ionic strength for the 3 and 4 μm colloids in the smooth and rough micromodel. (b) Images of colloid deposition in a) micromodel A (smooth) and b) micromodel B (rough). Streamlines are drawn by hand to show the pathway of the colloids (Auset and Keller, 2006).

1.4 Scientific challenges

1.4.1 Multi-scale couplings

Porous media can be modeled using different levels of description, ranging from molecular scale to field scale. The mathematical description of flow and transport in porous media varies with the modeling resolution, and consequently with the size of the studied system. The classic approach to derive field scale predictive models rooted in the physical elementary principles is to consider a modeling strategy involving a cascade of scales nested within each other (see Fig. 1.29). Then, homogenization techniques and/or statistical analysis are used to bridge the gap between the scales.

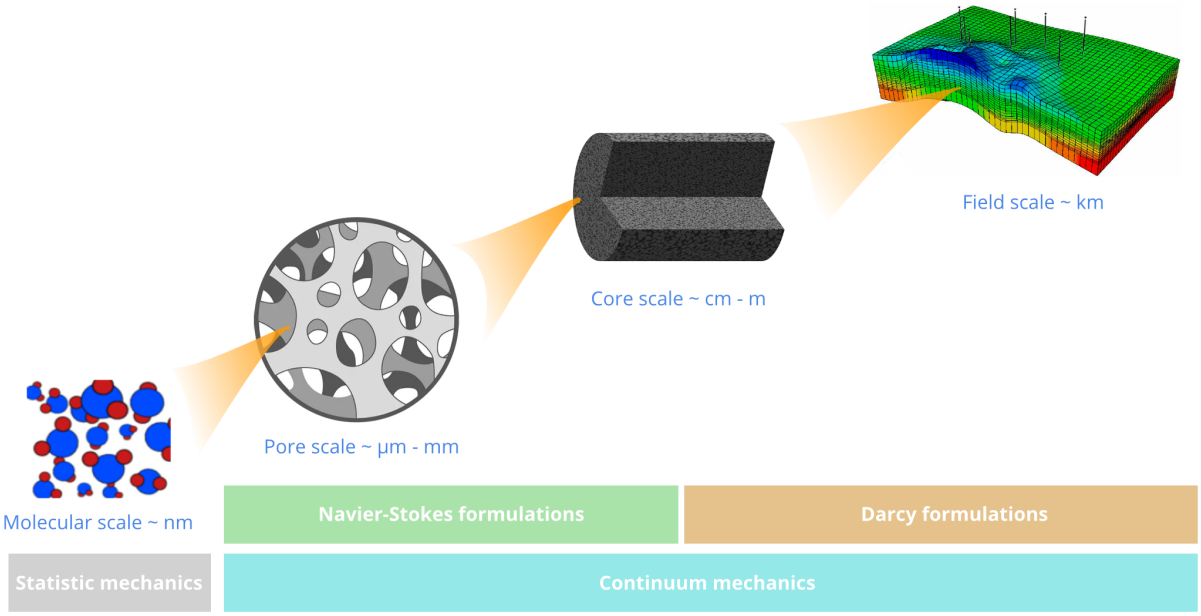

Figure 1.29: Modeling strategy using a cascade of scales nested within each other for transport in porous media.

Molecular scale

At this scale, the aim is to determine the intermolecular forces between the particles, the fluid, and the walls. All the interactions between fluid and solid atoms and molecules are described using molecular dynamics which relies on the knowledge of the bonds between atoms and the force fields applied to them.

Pore scale

At the pore scale, the porous medium structure is fully resolved and the particle-fluid separation is entirely described through sharp interfaces. Describing the processes occurring at these interfaces is key to understanding the challenges of colloidal transport and retention in porous media. At this scale, in the absence of poromechanics and chemical reactions with dissolution/precipitation, only the pore space is represented in the domain, and therefore continuum mechanics models (e.g. Navier-Stokes equations) are commonly used to model the fluid flow through it. At the pore scale, the aim is to understand the packing/clustering/flow and the force structures concerning different flow conditions.

Core scale

It is an intermediate scale between the pore and the field scale, where natural porous media (e.g. rock, soil) exhibit significant heterogeneity. Insights gained at this scale help in developing more reliable scale-up strategies, ensuring that models and methods can be effectively applied in the field. At the core scale, the geometrical details of pores are not known but are described by effective properties including porosity, specific surface area, and permeability. Fluid flow is governed by Darcy's law. It is derived by volume-averaging Navier-Stokes equations on a representative elementary volume (REV) of the porous medium. This volume is sufficiently large to out-pass enough pore-scale heterogeneities so that the porous medium is considered homogeneous in its averaged properties. The aim is to formulate governing equations with constitutive relations of interface and bulk processes and boundary conditions. Core-scale experiments provide empirical data that can be used to validate and refine theoretical models of particle transport.

Field scale

The porous microstructure is not described explicitly at the field scale. Each point of the domain corresponds to a fluid-solid aggregate and the fluid flow is described by Darcy's law or an equivalent law. The porous matrix topology and medium heterogeneity are lumped into effective parameters (see Section 2.3.1). At the field scale, the aim is to quantify flow and force fields, and process performance for optimization.

1.4.2 Multi-physics couplings

Particle transport in geological porous media involves processes that relate to different physics including hydromechanics, electrostatics, geochemistry, and poromechanics. The strong coupling between these physics in mechanisms like clogging limits the independent study of their actions. Understanding the interplay and feedback between these processes is crucial to unlocking dominant mechanisms and regime patterns in the real system. In this Ph.D. thesis, the main mechanisms identified in particle-clogging in porous media are the fluid flow, the particle transport in the pore space, and the electrostatic interactions (deposition/remobilization) at particles and matrix surfaces.

1.5 Scientific questions and outline of the thesis

This chapter discussed the injectivity issues encountered due to particle transport and clogging in geothermal reservoirs and porous media in general. A key question in colloidal transport and retention in porous media concerns the quantification of the fluid-mineral surface area that is not involved in the colloidal deposition. Indeed, the suspension is evenly distributed in the system due to local flow heterogeneity. We will focus our modeling at the pore-scale to bridge the gap between the molecular and core-scale.

The challenges surrounding these problems raise some scientific questions, namely:

- What are the deposition regimes observable on a single grain?
- How does colloidal deposition evolve in a heterogeneous medium?
- What dimensionless numbers characterize the interactions between retention and migration in a heterogeneous environment?
- How does the permeability of a porous medium vary during the injection of colloidal suspensions under the influence of the infiltration speed, the particle concentration, the particle size, and the salinity of the fluid?

To answer these questions, we develop an original modeling approach at the pore-scale that is presented in the present dissertation. The Ph.D. thesis continues following the outline:

In Chapter 2, we present a review of the particle transport numerical models used to simulate particulate flow in porous media from pore-scale to field-scale while describing the forces (electrochemical and hydromechanical) applied to the particles.

In Chapter 3, we present our numerical model for colloidal transport at the pore-scale based on CFD-DEM. We perform a comprehensive set of verification tests. These test cases give us confidence in the predictive capacity of our numerical model at pore-scale.

In Chapter 4, we use our simulator to investigate pore-clogging in a single pore and a heterogeneous porous medium. We study the effect of effect particle diameter, particle concentration, fluid flow rate, fluid salinity, and geometry aspect ratio on the permeability damage over the injected pore volume.

In Chapter 5, we present the modeling of particle transport through the advection-diffusion-reaction equation. We discuss the formalism of the deposition rate and we revisit the cylindrical collector efficiency in the presence of the attraction and double-layer repulsion. Comparison with numerical simulations and experimental data are performed to validate the proposed model.

In Chapter 6, we conclude with a summary of the overall work and present some perspectives on future investigations and developments.

Chapter 2

Review of Particle Transport Modeling in Porous Media

In this chapter, we review the models describing particle transport in porous media. First, we address the physics of particle transport, their forces, and interactions with fluids and objects (walls and particles) that guide this transport (section 2.1). Then, in sections 2.2 and 2.3, we present the state-of-the-art modeling of particle transport both at the pore-scale and field-scale. Finally, in section 2.4, we enumerate the objectives of the thesis and describe the methodology used in this thesis to simulate particle transport in porous media efficiently.

2.1 Particle dynamics

During the recharge process, the injected water contains suspended fine particles that infiltrate through the porous medium and damage the formation in the vicinity of the injection wells (Al-Abduwani, 2005). Before investigating the particle interactions leading to pore-clogging processes, it is important to define the kind of particles under investigation and to list the physicochemical forces involved.

2.1.1 Particles description

In the subsurface, the pores vary from nanometric size to micrometric size depending on the constitutive rocks. Thus, the suspended particles transported and deposited inside the porous matrix are in the same range of size. In this study, the term "particles" refers to **colloids** with the size of 0.1 to 10 μm, or **suspended materials** with the size of 1 μm to a few millimeters. Fig. 2.1 illustrates the different kinds of particles that exist in the subsurface sorted by their size. Particles sized below this range (nanoparticles) are not considered even if they can significantly cause noticeable clogging damage (Fopa et al., 2023). Bigger particles are filtered at the entrance of the porous medium with the formation of an external filter cake (De Zwart, 2007).

In this Ph.D. thesis, we study the dynamic of rigid spherical particles, even if natural mineral particles in the subsurface do not have regular shapes (see Fig. 2.2). In the literature, the major source of colloids in the injected water is due to the mobilization of existing colloids (Ryan and Elimelech, 1996). Therefore several conditions as water chemistry, pore size distributions, and hydrodynamic conditions are relevant besides the size of the particles. Large particles ($> 10\mu m$) are mainly subjected to hydrodynamic

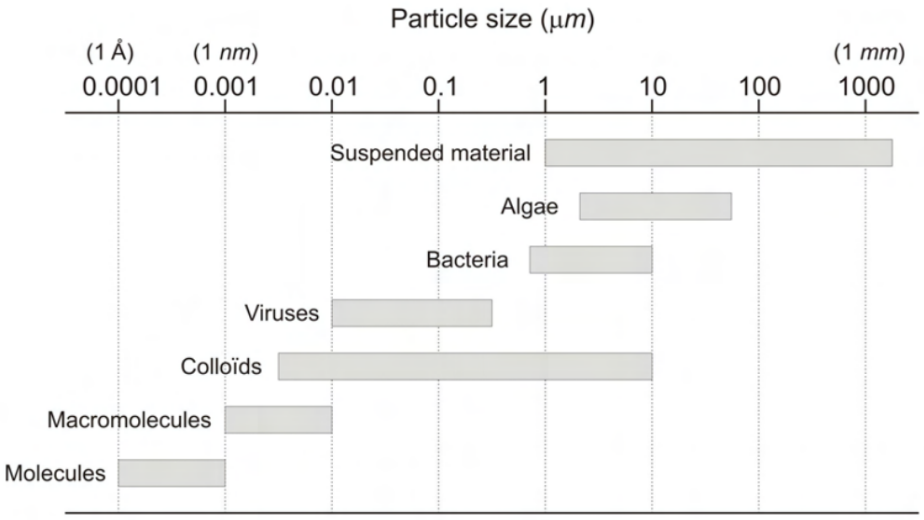

Figure 2.1: Size ranges of particles transported in groundwater (De Zwart, 2007).

conditions, smaller particles ($< 1\mu m$) are dominated by electrochemical forces, and particles intermediate are guided by the balance of their interactions.

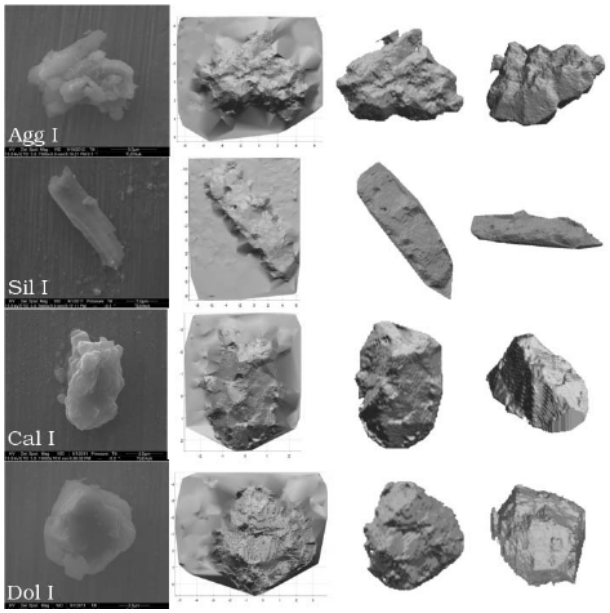

Figure 2.2: Some mineral dust particles (Agg I: agglomerate of Na-feldspar, illite, quartz, and magnesium-rich clay, Sil I: magnesium-rich silicate, Ca I: magnesium-bearing calcite, Dol I: dolomite). From the left to the right, scanning-electron microscope (SEM) images, the retrieved triangulated irregular network model of the surface, and the final volume representation from two different viewing angles (Lindqvist et al., 2014).

2.1.2 Balance of forces

In the subsurface, colloids and fine particles are transported by the fluid flow. Some of them deposit at the surface of the solid matrix and eventually lead to pore-clogging. The transport and deposition of solid particles is due to various forces. They include hydrodynamic, electrochemical, mechanical, and

Brownian motion forces. In the following, we describe briefly these forces.

Hydrodynamic forces

The dominant force affecting the particle transport is the hydrodynamic water velocity or the injection flow rate. Through the fluid velocity, hydrodynamic forces are induced and can either maintain the colloids in suspension or favor their deposition. Among these forces, we cite:

- **The buoyancy force**
  A particle in suspension in a fluid is subjected to a force dragging the particle in the direction of gravity. The sedimentation velocity vector, $\mathbf{v}_s$, for spherical particles in a viscous fluid under Stokes flow is (O'Sullivan, 2011):
  $$\mathbf{v}_s = \frac{D_p^2(\rho_p - \rho_f)\mathbf{g}}{18\mu_f}, \tag{2.1}$$
  where D_p is the particle diameter, ρ_p and ρ_f the particle and fluid densities respectively, $\mathbf{g}$ the gravitational acceleration vector and μ_f the fluid viscosity.

- **The drag force**
  The drag force is a force that opposes the movement of a body in a liquid or gas and acts as friction. A general expression reads,
  $$F_D = \frac{1}{2}\rho_f C_D v_r^2, \tag{2.2}$$
  where C_d is the drag coefficient, depending on the particle Reynolds number $Re_p = \rho_f v^f D_p/\mu_f$, v_r is the relative velocity between the fluid and the particle, and v^f is the fluid velocity. For a single particle in a Stokes flow ($Re_p < 1$), the drag coefficient and the drag forces are expressed by (Goldman et al., 1967):
  $$C_D = \frac{24}{Re_p} \text{ and } F_D = 3\pi\mu_f D_p v_r. \tag{2.3}$$
  This drag force is only valid in diluted suspensions. In the case of dense suspensions, which appear with converging flow at the pore entrance and in clogs, the hydrodynamic impact of the surrounding particles has to be considered. Constitutive drag forces have been proposed to account for the packing of the particles (Wen and Yu, 1966; Ergun, 1952).

- **Other hydrodynamic forces**
  Other hydrodynamic forces might play a role in the balance of forces and impact the transport. Among these forces, we have the pressure gradient force, the Basset force, the Saffman force, and the Magnus force (see Table 2.1).

Note that, only the drag and the buoyancy forces are considered because the other hydrodynamic forces are negligible compared to the drag force for the range of particle sizes considered in this thesis. The simplification also helps the theoretical study of particle clogging dynamics.

Electrochemical forces

Brine in the subsurface is an aqueous solution (i.e. an electrolyte) containing high concentrations of dissolved species. Particles with surface charges moving through an electrolyte are subjected to electrostatic interactions at long (typically tens of nanometers) and short (typically a few nanometers) separation distances. These forces highly influence particle mobility because they pilot particle aggregation and deposition toward other charged objects. The electrochemical forces become dominant over hydrodynamic

Table 2.1: Summary of the hydrodynamic forces impacting the transport of solid particles in a fluid flow (modified after Kleinstreuer and Feng (2013)).

Forces	Description	Negligibility conditions over the drag force
Drag force	Force due to the viscous friction of fluid on the particle	For purely advected particle ($v_r = 0$)
Buoyancy force	Force due to the difference in density between the fluid and particles	For particles that have the same density as the fluid ($\rho_f = \rho_p$).
Pressure gradient force Fernandes et al. (2018)	Force due to the pressure gradient around the particle	For small D_p and if the pressure gradient around particles is low.
Basset force (Zhu et al., 2007)	Force due to the acceleration of fluid around the particle	For $\rho_f << \rho_p$ and for submicrometer particles
Saffman force Saffman (1965)	Lift force due to inertia effects in the viscous flow around the particle	For small D_p
Magnus force (Xiong et al., 2005)	Induced lift force due to the rotation of the particle	For small D_p

forces if the surface-to-volume ratio is large, which is the case for colloid and fine particles. They are mainly made of Van der Waals attraction and electrical double-layer (EDL) repulsion that are described below.

- **Van der Waals force**
  Van der Waals force is due to the electrostatic interaction between dipoles, whether they are the permanent dipoles of molecules or the dipoles induced by the interaction (Israelachvili, 2011). Fig. 2.3 presents different configurations of Van der Waals interactions between dipole, induced dipole, and ion.

  We distinguish different Van der Waals interactions:
  - **Keesom force** if the electrostatic interaction is between two permanent multipoles,
  - **Debye force** if the interaction is between a permanent multipole and an induced multipole (induction effects),
  - **London force** if the electrostatic interaction is between two induced multipoles (dispersion effects).

  Van der Waals interactions are due to the "deformation" (fluctuating polarization in the case of the London force) of electron clouds creating an attractive electrostatic force between them at a certain distance. If the separation distance of the two approaching surfaces is in the order of tens of nm, the attractive interaction created by the Van der Waals force becomes dominant. A typical Van der Waals potential as a function of the separation distance is plotted in red in Fig. 2.7.

  The pair interaction energy for identical spherical particles of radius R_p separated from their center by h is based on the London-Van der Waals force and reads (Hamaker, 1937):

$$V^{VDW} = -\frac{A_H}{6}\left[\frac{2R_p^2}{h^2 - 4R_p^2} + \frac{2R_p^2}{h^2} + \ln\left(\frac{h^2 - 4R_p^2}{h^2}\right)\right], \tag{2.4}$$

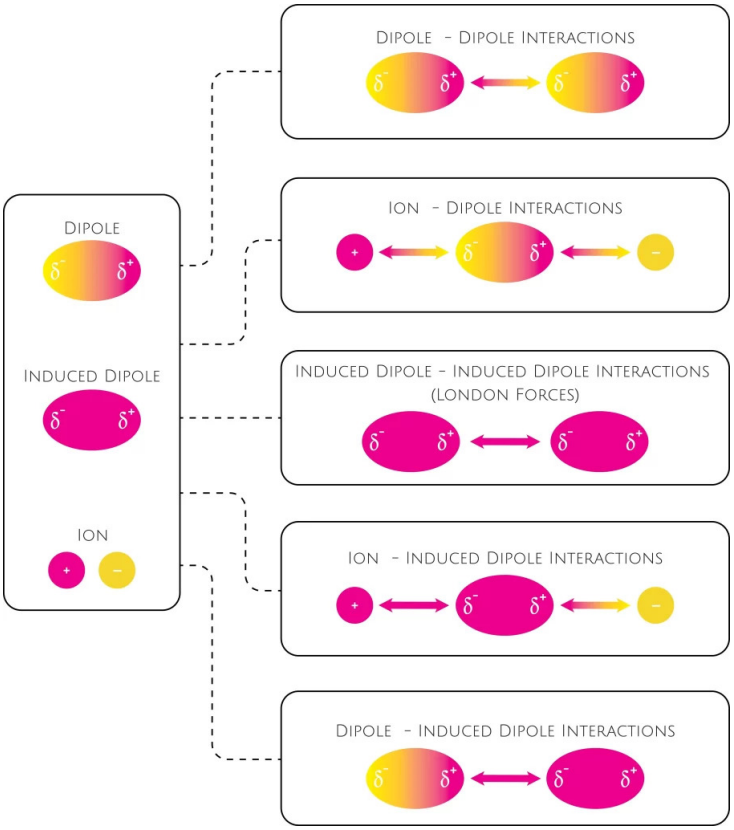

Figure 2.3: Representation of the different configurations of Van der Waals interactions between a dipole, an induced dipole, and an ion. After https://88guru.com/library/chemistry/van-der-waals-forces.

where A_H is the particle-fluid Hamaker constant (see Fig. 2.4). Its value is generally between 10^{-21} and 10^{-19} J. If subscript 1 designates the particle and 2 the fluid, the Hamaker constant is (Dersoir, 2015),

$$A_H = \frac{3}{4} k_B T \left(\frac{\epsilon_1 - \epsilon_2}{\epsilon_1 + \epsilon_2} \right)^2 + \frac{3\pi\hbar\nu_e}{8\sqrt{2}} \frac{(n_1^2 - n_2^2)^2}{(n_1^2 + n_2^2)^{3/2}} = A_{22} + A_{11} - 2A21 \simeq \left(\sqrt{A_{22}} - \sqrt{A_{11}} \right)^2, \quad (2.5)$$

with ϵ the dielectric constant, ν_e the orbiting frequency of the electron, k_B the Boltzmann constant, T the absolute temperature, $\hbar$ the Planck constant, and n the material refractive index.

- **Electrical Double Layer force**
  With the ions and counterions in the fluid and the presence of surface-charged particles, an electrical double-layer is created between the particle surface and the bulk solution. For particles with the same surface charge, the EDL acts as a Coulumbic repulsive barrier. It is typically composed of a diffuse layer and a Stern layer (see Fig. 2.5). The diffuse layer is made of mobile counter-ion in excess and of mobile co-ions in deficiency, which have a Boltzmann's exponential distribution that tends to the bulk ion concentration at a certain distance from the beginning of the diffuse layer (Grahame, 1947). In this region, the ions are not specifically absorbed but are influenced by the electric field created by the charged surface. The Stern layer – also called the stagnant layer – is made of the counter ions absorbed by the particles due to Coulomb attraction maintaining the

base liquid	pH	T (°C)	system	A_H (J)	experimental/theoretical
distilled water	12	149	kaolinite–quartz	1.61×10^{-20}	experimental
water	7	25	glass beads–water	6×10^{-21}	theoretical
0.03 M NaCl	7		metallic NPs	6.04×10^{-20}	experimental
water	7	25	glass beads–water	6×10^{-21}	theoretical
0.03 M NaCl	6.9	25	glass beads–brine	1×10^{-21}	theoretical
water	7	25	glass beads–water	6×10^{-21}	theoretical
0.03 M NaCl	6.5–7	25	sand–NaCl	1×10^{-20}	theoretical
0.2 wt % NaCl	8.1	65	oil/silica in water	8×10^{-21}	theoretical
water		25	kaolinite and quartz	2×10^{-20}	theoretical
0.035 M diluted sea water	7	25	limestone–brine	1×10^{-19}	theoretical
0.3 M NaCl	7	25	glass beads–brine	1×10^{-20}	theoretical
NaCl, $MgCl_2$ and $CaCl_2$	4–10	25	shale-oil	0.81×10^{-20}	theoretical
2 wt % KCl	7	25	coal–brine	4.62×10^{-20}	theoretical
0.01 M NaCl	7	25	carbonate–brine	1.3×10^{-20}	theoretical
0.6 M NaCl	7	25	kaolinite–sand	1.49×10^{-20}	experimental
0.1 M ALSW	7	25	calcite–brine	6.6×10^{-21}	theoretical
0.0005 M NaCl brine			clay–sand	2×10^{-21}	theoretical
0.001 M NaCl	7	25	silica–brine	3.91×10^{-21}	theoretical
0.007 M SDS and 0.0005 M NaCl		25	surfactant–water	5.2×10^{-20}	experimental

Figure 2.4: Examples of Hamaker constant values for different system configurations (grain, particle, liquid). Modified after Muneer et al. (2020).

electro-neutrality. The plane between the Stern layer and the diffuse layer marks the separation of fluid velocity and is called the slipping plane or shear plane. The difference between the slipping plane electrical potential and the bulk solution electrical potential is known as the zeta potential, ζ. This potential can be positive or negative depending on the surface charge of the particle or the wall, ions, and the counterions in the solvent. In practice, the electrical potential ψ_d at the beginning of the diffuse layer inferred from electrokinetic measurements is traditionally assumed to be equal to the zeta potential (Leroy et al., 2013).

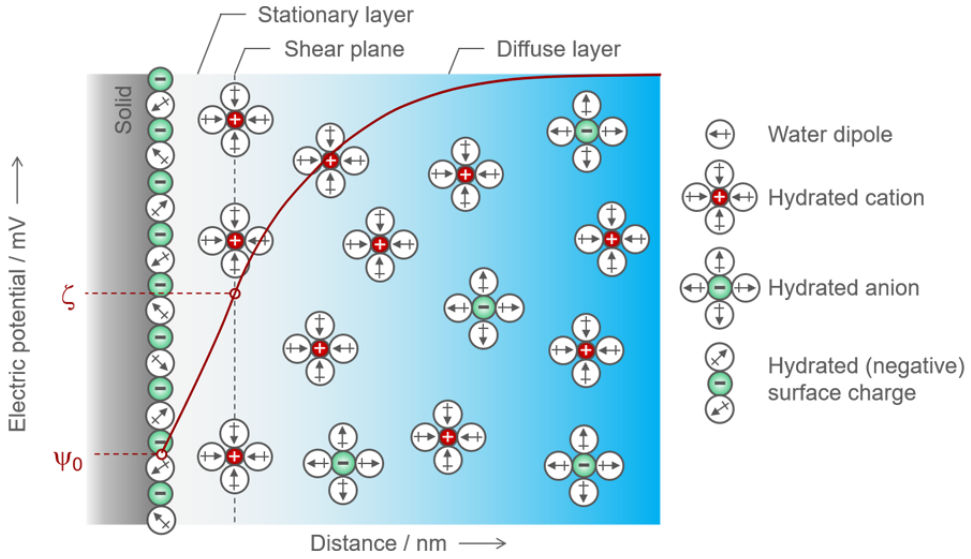

Figure 2.5: Model of the electrochemical double layer at the solid-liquid planar interface (surface potential ψ_0, zeta potential ζ). Taken after https://wiki.anton-paar.com/fr-fr/potentiel-zeta/.

The EDL potential of a spherical charged particle interacting with a planar surface is given by:

$$V^{EDL} = -\pi\epsilon_0\epsilon_r R_p \left[2\zeta_p\zeta_w \ln\left(\frac{1+e^{-\kappa h^*}}{1-e^{-\kappa h^*}}\right) + \left(\zeta_p^2+\zeta_w^2\right)\ln\left(1-e^{-2\kappa h^*}\right)\right], \tag{2.6}$$

where ϵ_0 and ϵ_r are the vacuum absolute permittivity and medium relative permittivity, respectively. κ is the inverse of the Debye length (the thickness of the diffuse layer) and varies depending on the ionic strength, I_s, and temperature, T, of the solvent. ζ_p and ζ_w are the zeta potential of the particle and the walls of the porous formation, respectively. $h^* = h - 2R_p$ is the surface-to-surface separation distance. This formula has been obtained by Hogg et al. (1966) who solved the Poisson-Boltzmann equation in the limit of weak potential using the Derjaguin (1934) approximation.

base liquid	salinity	pH	T (°C)	environment	ζ (mV)	apparatus/method
seawater	600 ppm	7–8	60	carbonate	−13	Zetasizer
NaCl brine	0.2 wt %	7.7	25	Berea SS	−35	phase-analysis light-scattering PALS
NaCl brine	0.5 M	–	25	sand	−20	–
formation water	14000 ppm	8	25	limestone	−15	phase-analysis light-scattering PALS
0.2 wt % NaCl	0.2 wt %	8.1	65	sandstone	−23.7	Zetasizer
NaCl brine	0.2 wt %	–	25	sandstone	−33	–
distilled water	0	9.2	25	quartz	−23	Zetasizer
diluted seawater	0.035 M	7	25	limestone	−11	Zetasizer
KCl	2 wt %	7	25	coal–brine	−12.61	micro-electrophoresis
NaCl brine	0.01 M	7	25	carbonate	−50	–
NaCl brine	0.6 M	7	25	sand	−20	Zetasizer
NaCl brine	0.7 M	7.2	50	crude oil	−23	ζ analyzer
smart water	5761 ppm	7.4	–	carbonate	−8	Smoluchowski equation
0.1 M KCl	0.1 M	7	30	clay–brine	4.9	Zetasizer
ALSW	0.1 M	7	25	calcite–brine	−3.72	Zetasizer
NaCl brine	0.000513 M	–	–	clay–sand	−50	Zetasizer
NaCl brine	0.001 M	7	25	silica–brine	−39	–
7 mM SDS and 0.5 m NaCl brine	–	–	25	surfactant–water	−80	–

Figure 2.6: Zeta potential measurements for various environments with different base liquids. Modified after Muneer et al. (2020)

- **Born or Pauli force**

  At very short distances (a few nanometers), a strong repulsion force is used to avoid interpenetration of the electronic clouds of the atoms constituting the particles. The potential energy for two spherical particles of radius, R_p, reads (Feke et al., 1984),

$$V^B = -\frac{A_H}{37800}\left(\frac{\sigma_c}{R_p}\right)^6 \frac{1}{r}\left[\frac{r^2-14r+54}{(r-2)^7} + \frac{60-2r^2}{r^7} + \frac{r^2+14r+54}{(r-2)^7}\right], \tag{2.7}$$

  with $r = h/2R_p$ the dimensionless center-to-center particle separation distance, and σ_c the collision diameter (few Angströms).

- **Hydration force**

  The hydration force is a strong repulsive short-range force that acts between polar surfaces separated by a thin layer (<3 nm) of water. It is primarily due to structured water molecules around the

hydrophilic surfaces. The formula for the hydration force between two spherical particles can be complex due to the nature of the interactions involved. However, a simplified and commonly used form is based on the exponential decay of the force with distance. The general form of the hydration force F_h between two spherical particles can be expressed as (Donaldson and Alam, 2008):

$$F_h = F_0 \exp(-\frac{h}{\lambda_h}), \tag{2.8}$$

where F_0 is the hydration force constant (the force at zero separation distance), λ_h is the decay length of the hydration force, often related to the thickness of the hydration layer.

The DLVO theory developed by Verwey (1948); Derjaguin and Landau (1941) describes the electrochemical interactions acting on colloids as a combination of the Van der Waals attraction and the electrical double-layer repulsion forces. The equivalent potential is the sum of the Van der Waals and the EDL potentials:

$$V^{DLVO} = V^{VDW} + V^{EDL}. \tag{2.9}$$

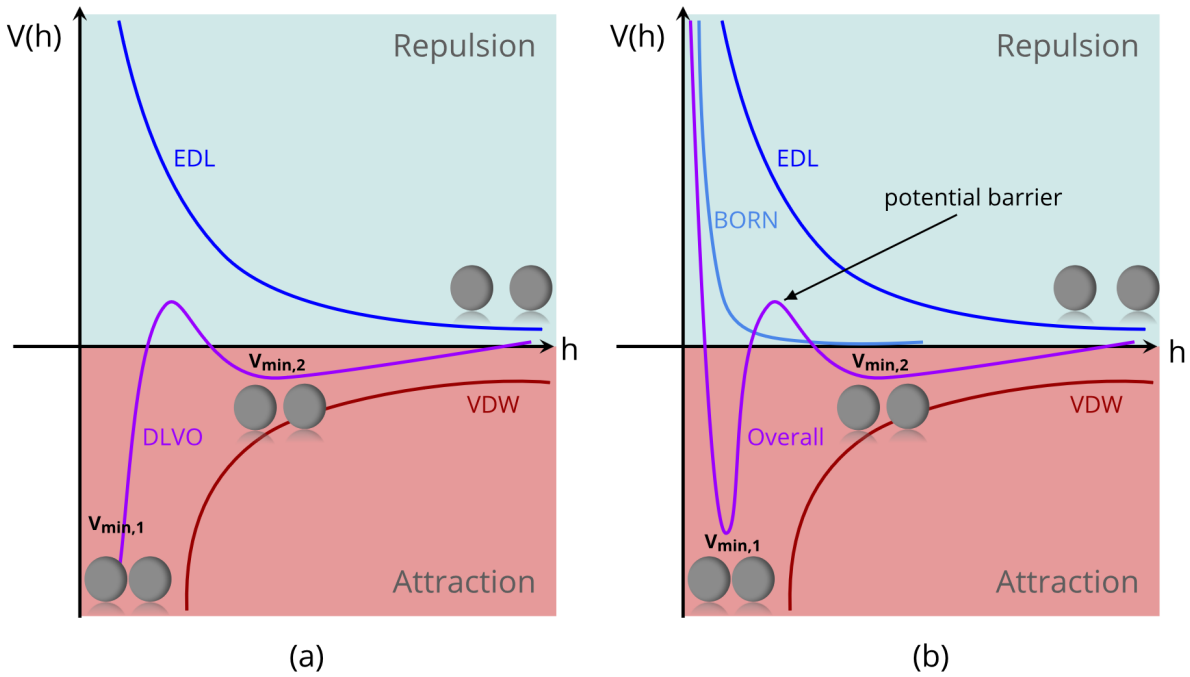

Figure 2.7: (a) DLVO potential profile over the distance h. (b) The overall potential profile between 2 particles over the distance h (DLVO potential + Born potential). $V_{min,1}$ and $V_{min,2}$ are the primary and secondary potential minimum, respectively.

As shown in Fig. 2.7, for two distant particles (hundreds of nanometers) the DLVO potential is very weak and does not affect the dispersion or diffusion of the particles. If particles are closer to each other, they start attracting under DLVO potential until they reach the secondary minimum $V_{min,2}$. The secondary minimum corresponds to reversible attachment and weak aggregate. If they have enough energy to pass the potential barrier, they end up in the primary minimum $V_{min,1}$. The primary minimum corresponds to an irreversible attachment and strong aggregate.

Near the contact, the DLVO potential results in an infinite well, that is not physical (see Fig. 2.7a). We will see in Chapter 3 that this infinite well raises important challenges to simulate the aggregation and attachment. An extension of the DLVO theory uses short-range repulsive forces including Born repulsion and hydration forces to get rid of this infinite well. As we can see in Fig. 2.7b, the addition of Born repulsion removes the infinite attractive well and the resulting potential becomes highly repulsive near contact.

Brownian motion

The phenomenon where submicron particles make random fluctuations of their positions inside a fluid is commonly known as Brownian motion (Feynman, 1964). This is principally due to the thermal agitation of the solvent molecules. Brownian motion results in a diffusive mechanism which is characterized by a diffusion coefficient relative to the particle size and obtained using the Stokes-Einstein relation by (Einstein, 1905):

$$D = \frac{k_B T}{3\pi\mu_f D_p}. \tag{2.10}$$

Mechanical forces

The principal mechanical-based forces are the inter-particle contact force (between the particles) and the particle-walls contact force. Contact interactions are often neglected in a dilute suspension (volume fraction of particles $<< 1$). This allows the particles to behave as if they were dispersed independently from each other within the suspending medium. In dense suspension, however, the probability of collision between objects (particles and walls) increases with the concentration of particles. Thus, contact interactions can significantly impact the deposition kinetics depending on the particle concentration. The contact force can be decomposed as the sum of normal and tangential components. The latter will create additional torque on the rotational movement of the particles when they are in contact.

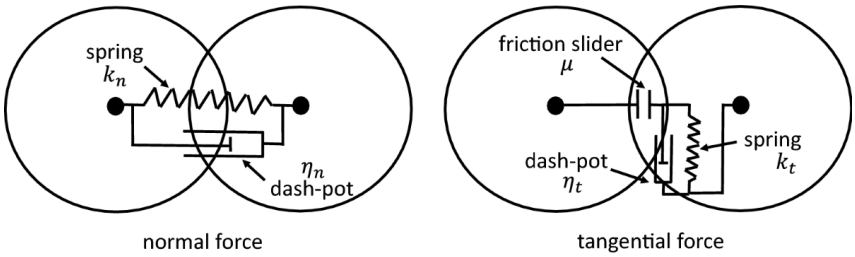

Figure 2.8: Shematic description of the spring-slide-dashpot model (after Fernandes et al. (2018)). η_n and η_t are the normal and tangential damping coefficients. k_n and k_t are the normal and tangential stiffness coefficients. μ is the friction coefficient.

Contact interactions are classically described using the linear spring-slider-dashpot contact model (Tsuji et al., 1993; Cundall and Strack, 1979) as presented in Fig. 2.8. In this system, the spring plays the role of the reaction force on contact, the dashpot is the shock absorber, and the slider controls the frictional force resisting the motion of the two particles during tangential contact. Other models exist and a non-exhaustive list of contact models is presented in Table 2.2. A more in-depth mathematical description of the spring-slider-dashpot model is found in Chapter 3.

Contact model	References
Linear spring-slider-dashpot model	Cundall and Strack (1979)
Non-linear simplified Hertz-Midlin and Deresiewicz model	Zhou et al. (1999); Zhu and Yu (2002)
Walton and Braun's model	Walton and Braun (1986); Walton (1993)

Table 2.2: Contact force models (Zhu et al., 2007).

2.2 Pore-scale description

At the pore-scale, the solid skeleton is fully resolved. It means that the fluid flow in each pore is described explicitly using the standard equations of fluid dynamics. In this representation, boundary conditions apply at the fluid-solid interface. In this section, we review the approaches for solving fluid flow at the pore-scale. Then, we review the state-of-the-art methods including Euler-Lagrange and Euler-Euler to transport a cloud of particles.

2.2.1 Flow models at the pore-scale

At the pore-scale several methods are used to model the fluid flow, they include computational fluid dynamics, lattice-Boltzmann method, smoothed particle hydrodynamic, and pore network model. In the following, we describe the principles of these approaches.

Computational Fluid Dynamics (CFD)

Volume-averaged Navier-Stokes (VANS) equations are used to simulate the flow of a suspension. They are obtained by cell-averaging of the Navier-Stokes equations (NS). The continuity and momentum conservation read (Whitaker, 1996):

$$\frac{\partial(\epsilon\rho_f)}{\partial t} + \nabla\cdot\left(\epsilon\rho_f\mathbf{v}^f\right) = 0, \tag{2.11}$$

$$\frac{\partial(\epsilon\rho_f\mathbf{v}^f)}{\partial t} + \nabla\cdot\left(\epsilon\rho_f\mathbf{v}^f\mathbf{v}^f\right) = -\epsilon\nabla p^f + \nabla\cdot\epsilon\boldsymbol{\tau}^f - \xi(\mathbf{v}^f - \mathbf{v}^p) + \epsilon\rho_f\mathbf{g}, \tag{2.12}$$

where $\boldsymbol{\tau}^f$ is the Newtonian fluid viscous stress tensor, p^f is the fluid pressure, $\mathbf{v}^f$ is the fluid velocity vector, ρ_f is the fluid density, ϵ is the volume fraction of fluid in each cell (local porosity), and ξ is the interphase drag force coefficient, $\mathbf{v}^f$ is the fluid velocity and $\mathbf{v}^p$ is the particle velocity. In Eq. (2.12), the left-hand side represents the inertia effects, the first term of the right-hand side relates to the load losses, the second refers to the viscous effects, and the last term is the gravitational effects. If $\epsilon = 1$, the VANS equations boil down to the Navier-Stokes equations used to simulate the fluid flow at pore-scale (see Fig. 2.9).

In CFD, the VANS equations are solved by discretizing the spatial differential operators on an Eulerian grid using techniques such as the finite element method (FEM), the finite volume method (FVM), or the finite difference method (FDM) (Ferziger et al., 2020). FVM is usually preferred as it is locally conservative and deals with unstructured grids by construction.

Solution algorithms of the VANS equations usually rely on predictor-corrector strategies to solve for the pressure-velocity coupling. Pressure Implicit with Splitting Operators (PISO) is the most used algorithm for solving transient flow (Issa, 1986).

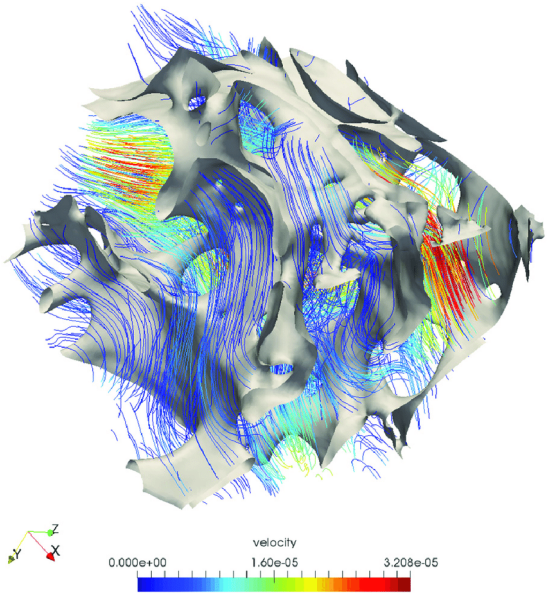

Figure 2.9: Pore-scale fluid flow simulation using NS equations in a trabecular bone based on micro-CT imaging (Daish et al., 2017).

Lattice-Boltzmann Method (LBM)

'LBM is an approach that represents the fluid as discrete fictitious parcels moving in a fixed lattice along a finite number of directions (He and Luo, 1997). It uses simple collision rules, has a robust implementation of complex geometries for porous media, and can accommodate multiphase flow (Chen et al., 2003). It is based on the Boltzmann equation that describes the probability of finding a given particle at a given position with a given velocity. Unlike CFD, LBM does not solve continuous partial differential equations (PDEs) as Navier-Stokes equations, which simplify its numerical implementation.

In LBM, the degree of freedom is determined by the nature of the lattice classified with the nomenclature DnQm where n corresponds to the dimension of the lattice and m stands for the number of directions (see Fig. 2.10). Then, the D2Q9 model refers to a lattice-Boltzmann method of a two-dimensional simulation with 9 directions for the velocity. The associated lattice-Boltzmann equation reads (Guo et al., 2002),

$$f_\alpha\left(\mathbf{x}+\mathbf{e}_\alpha\delta_t,\ t+\delta_t\right)-f_\alpha\left(\mathbf{x},t\right)=\frac{1}{\tau}\left[f_\alpha\left(\mathbf{x},t\right)-f_\alpha^{(eq)}\left(\mathbf{x},t\right)\right]+F_\alpha\left(\mathbf{x},t\right)\delta_t, \tag{2.13}$$

where $\mathbf{x}$ is the grid node position, α refers to the direction, $\mathbf{e}_\alpha$ is the discrete velocity vector defined by Eq.(2.15), δ_t is the time-step, τ is the relaxation time, $f_\alpha(\mathbf{x},t)$ is the distribution function and $f_\alpha^{(eq)}(\mathbf{x},t)$ is the equilibrium distribution function given by ,

$$f_\alpha^{(eq)}=\omega_\alpha\rho\left[1+\frac{\mathbf{e}_\alpha\cdot\mathbf{v}^f}{c_s^2}+\frac{(\mathbf{e}_\alpha\cdot\mathbf{v}^f)^2}{2c_s^4}-\frac{\mathbf{v}^{f2}}{2c_s^2}\right], \tag{2.14}$$

$$\mathbf{e}_\alpha=\begin{cases}(0,0), & \alpha=0\\ \left(\cos\left[(\alpha-1)\pi/2\right],\sin\left[(\alpha-1)\pi/2\right),\right. & \alpha=1,2,3,4\\ \sqrt{2}\left(\cos\left[(\alpha-5)\pi/2+\pi/4\right],\sin\left[(\alpha-5)\pi/2+\pi/4\right),\right. & \alpha=5,6,7,8\end{cases} \tag{2.15}$$

with c_s the lattice sound speed, ω_α the weigh coefficient. $F_\alpha\left(\mathbf{x},t\right)$ is an external force that can account

for the momentum exchange between fluid and particles. If the interaction force from particle to fluid flow, $\mathbf{F}_{pf}(\mathbf{x}, t)$ is known, the external force term, $F_\alpha(\mathbf{x}, t)$, is obtained by (Zhu et al., 2011),

$$F_\alpha(\mathbf{x}, t) = \left(1 - \frac{1}{2\tau}\right) \omega_\alpha \left(\frac{\mathbf{e}_\alpha - \mathbf{v}^f}{c_s^2} + \frac{\mathbf{e}_\alpha \cdot \mathbf{v}^f}{c_s^4} \mathbf{e}_\alpha\right) \mathbf{F}_{pf}(\mathbf{x}, t)\,. \tag{2.16}$$

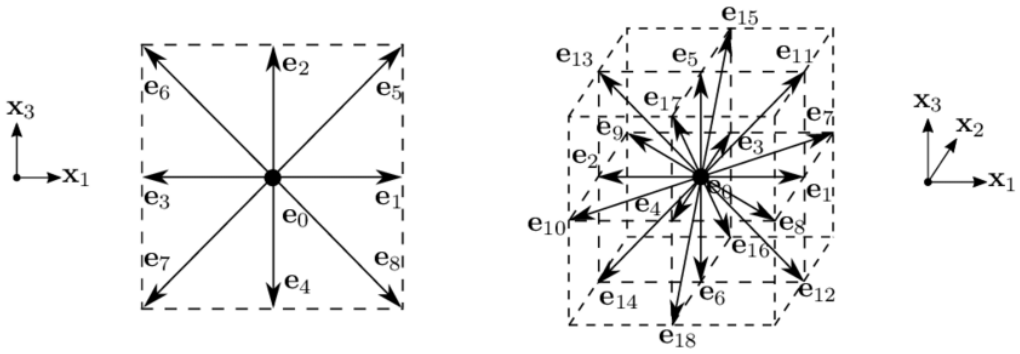

Figure 2.10: Schematic of the (a) D2Q9 and the (b) D3Q19 configurations of the LBM space discretization (Chaaban et al., 2020).

Pore Network Model (PNM)

PNM is the historical method introduced by Fatt (1956) to simulate flow in porous media at the pore-scale. It consists of representing the pore space geometry as a discrete network of pores interconnected by throats (see Fig. 2.11). The throats are idealized as pipes of simple forms (e.g. cylinders and prisms).

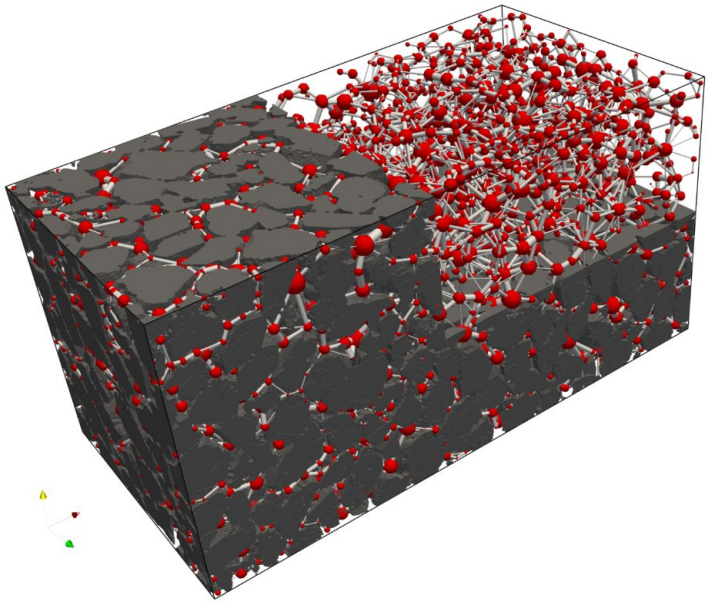

Figure 2.11: 3D view of the Nubian Sandstone pore-network. The solid phase is in gray, while the extracted pore elements are overlain. The pore bodies and pore throats are respectively rendered as red spheres and gray cylinders that are smaller than their actual sizes to improve visualization. (Hefny et al., 2020).

For a given node the mass balance equation for the fluid flow reads (Wu et al., 2019),

$$\sum_{j}^{n} Q_{i,j} = \sum_{j}^{n} \int_{S_{i,j}} \left(\mathbf{v}^f - \mathbf{v}^p\right) \cdot \mathbf{n} \, dS = -\frac{\partial V_i}{\partial t}, \tag{2.17}$$

where $\mathbf{n}$ is the local normal vector of the cross-sectional area $S_{i,j}$, and $Q_{i,j}$ is the local flow rate of the throat linking pore i and pore j. V_i is the volume of the pore i. $\mathbf{v}^p$ is the velocity of the particle. The momentum balance is based on the Hagen-Poiseuille law that relates the pressure difference, ΔP_{ij}, with the mean flow rate in a pore throat. We have,

$$\Delta P_{ij} = \frac{32 \mu_f L_{i,j}}{D_{i,j}^{*2}} \frac{Q_{i,j}}{S_{i,j}} \tag{2.18}$$

where $D_{i,j}^{*}$ is the mean diameter and $L_{i,j}$ is the length of the (i,j) throat connecting pore i to pore j.

Smooth Particle Hydrodynamics (SPH)

SPH is a method used to simulate continuum mechanics including solid mechanics and fluid flows (Gingold and Monaghan, 1977). SPH is the most mature mesh-free method. It is convenient for modeling complex flows with multiple phases (Liu et al., 1995). Indeed, in SPH the differential operators are discretized by moving particles. The particles have a spatial distance over which their properties are smoothed by a kernel function centered on the particles (see Fig. 2.12). This distance defines the sphere of influence for each particle and is used to reconstruct continuous variables such as fluid density.

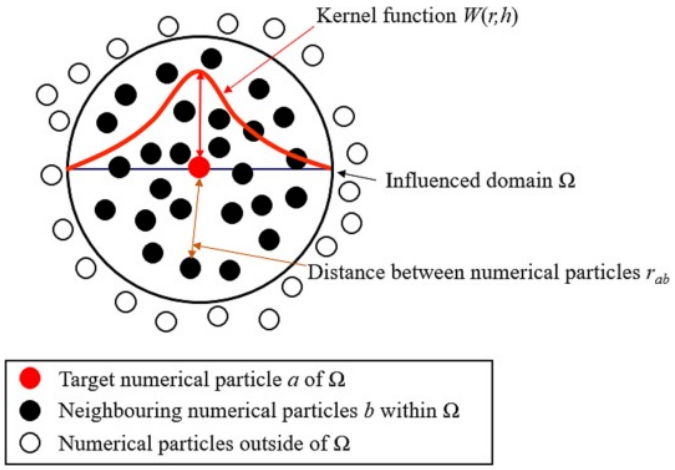

Figure 2.12: Schematic of the kernel function in the SPH method. (Yang et al., 2024).

In SPH, the continuity equation which reads,

$$\frac{D\rho_{f,i}}{Dt} = \sum_j m_j \left(\mathbf{v}_i^f - \mathbf{v}_j^f\right) \cdot \nabla_i W_{ij} + \delta h c_0 \sum_j \frac{2m_j}{\rho_{f,j}} \left(\rho_{f,i} - \rho_{f,j}\right) \frac{\mathbf{r}_{ij}}{||\mathbf{r}_{ij}||^2 + 0.01h^2} \cdot \nabla_i W_{ij}, \tag{2.19}$$

and a momentum conservation is,

$$\frac{D\mathbf{v}_i^f}{Dt} = \sum_j m_j \left(\frac{\boldsymbol{\sigma}_j}{\rho_{f,j}^2} + \frac{\boldsymbol{\sigma}_i}{\rho_{f,i}^2} - \boldsymbol{\Pi}_{\boldsymbol{ij}}\right) \nabla_i W_{ij} + \mathbf{g} + \mathbf{F}_i^{ext}. \tag{2.20}$$

where W_{ij} is the smooth kernel function. h is the smoothing length. $\delta \simeq 0.1$ is a constant used to control the intensity of the density diffusion. A too-small δ is not enough to give smooth pressure results, whereas

a too-large δ induces excessive damping. c_0 is the speed of sound. $\mathbf{r}_{ij}$ is the displacement vector from fluid particle i to j. m is the fluid particle mass. $\boldsymbol{\sigma}$ is the Cauchy stress tensor. $\boldsymbol{\Pi_{ij}}$ is a stabilization tension term including the corrections by artificial viscosity and artificial pressure. The artificial viscosity is used to prevent numerical instability and unphysical particle penetration, whereas artificial pressure is employed to alleviate the tensile instability (Monaghan, 1994). $\mathbf{F}^{ext}$ is a momentum source term.

In a recent literature review, Wang et al. (2016) reports that SPH can deal with moving interfaces and particulate transport more easily than conventional grid-based methods including Particle in Cell PIC (Matyash et al., 2007), Volume of Fluid VOF (Hirt and Nichols, 1981), and Level Set Method LSM (Peng et al., 1999) because by construction, the solid elements are also described by moving particles. Nevertheless, SPH is still in its infancy, and leading-edge SPH methods' computational cost per number of particles is significantly larger than the cost of grid-based simulations per number of cells when the metric of interest is not directly related to density (Price, 2011).

2.2.2 Lagrangian approaches for particle transport

We have introduced in the previous section the different engines for solving the fluid flow at the pore-scale in the presence of solid particles. In this section, we review approaches where these engines are coupled with Lagrangian particle tracking to describe the particle's motion including their mutual interactions.

Principle of the Discrete Element Method (DEM)

One of the most widely used Lagrangian approaches to describe particle dynamics is the Discrete Element Method, originally developed by Cundall and Strack (1979). DEM is well-suited for modeling hydromechanical processes because it considers all the forces applied to the particles including contact laws.

The translational and rotational velocities, $\mathbf{U}^p$, $\boldsymbol{\omega}^p$, of an individual particle are governed by Newton's second law of motion. We have,

$$m\frac{d\mathbf{U}^p}{dt} = \sum_j \mathbf{F}_{p,j}, \tag{2.21}$$

$$I\frac{d\boldsymbol{\omega}^p}{dt} = \sum_j \mathbf{M}_{p,j}, \tag{2.22}$$

where $\mathbf{F}_{p,j}$ and $\mathbf{M}_{p,j}$ are the forces and torques applied to the particle, respectively. These forces and torques are described in section 3.2.2 and include contacts, hydrodynamics, and electrochemical interactions. Subscript j designates all the objects (e.g. particles and walls) in interactions with the particle. m and I are the particle mass and moment of inertia.

DEM uses the assumptions of rigid and spherical particles (Tsuji et al., 1993). Particles of arbitrary shapes (e.g. spherical, disk, irregular), can be modeled with DEM using the multi-sphere method (MSM) as shown in Fig. 2.13 or the surface mesh representation (SMR) as shown in Fig. 2.14. When the multi-sphere model is used, forces from sub-particles are assembled and applied on the clump. The clump is treated as a rigid body, and then the sub-particle motion is updated according to this rigid-body motion (Shen et al., 2022). In SMR, particle surfaces are discretized using contact nodes, which can be conveniently determined in preprocessing as the vertices of the surface mesh (Zhan et al., 2021).

The accuracy of DEM for mechanical contacts has been demonstrated by many authors (Coetzee,

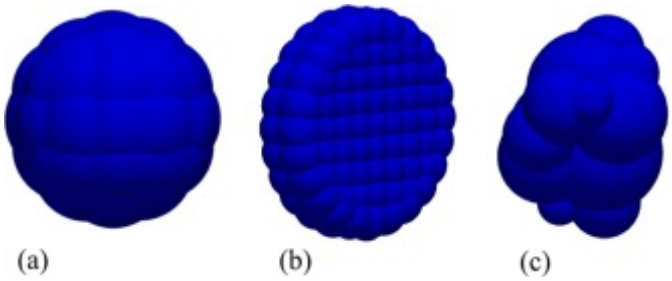

Figure 2.13: In DEM, particles of arbitrary shapes can be modeled using a compound of packed particles with strong adhesive forces. (a) Spherical clump; (b) Disk clump; (c) Irregularly shaped particle (Shen et al., 2022).

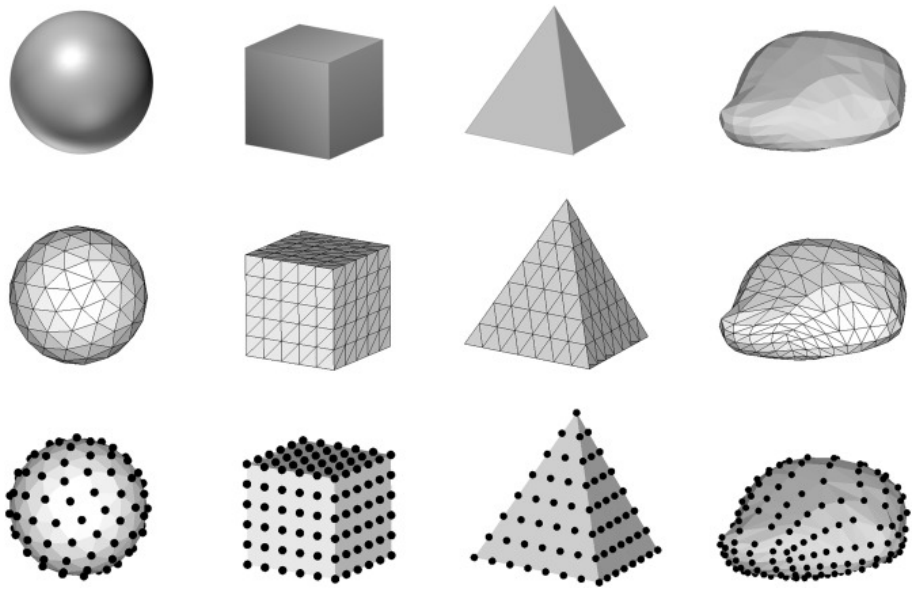

Figure 2.14: The schematic diagram of particle surface representation of three typical shapes and one irregular shape (top: original shapes of particles; middle: surface meshes with triangles; bottom: distribution of contact nodes at particle surfaces). After Zhan et al. (2021).

2017; Guo and Ye, 2023). For example, Kruggel-Emden et al. (2008) conclude that multi-sphere DEM accurately captures collisions using a multi-contact model (van der Haven et al., 2023). Hanley and O'Sullivan (2016) have demonstrated that the choice of the time-step Δt_{DEM} is crucial to minimizes the numerical error (truncation + round-off errors). The numerical errors in idealized DEM simulations were investigated analytically by comparing energy balances applied at the beginning and end of one time-step. The number of contacts affects the accuracy, and one can deduce that because 2D simulations contain fewer inter-particle contacts than the equivalent 3D simulations, they have lower accrued simulation errors.

Since its early development, DEM has been coupled with various approaches to simulate particulate flow for a wide range of applications. The coupled approaches between flow models described in section 2.2.1 and DEM are described below. A summary of their capabilities and limitations is provided in Table 2.3.

CFD-DEM

The CFD-DEM model is one of the most widely methods used for modeling particulate flows (Tsuji et al., 1993). CFD-DEM is a **four-way coupling** because the particles are driven by the fluid flow, the particle's presence has feedback on the flow streamlines, and inter-particle and particle-wall interactions are considered. The four-way coupling is presented in Fig. 2.15.

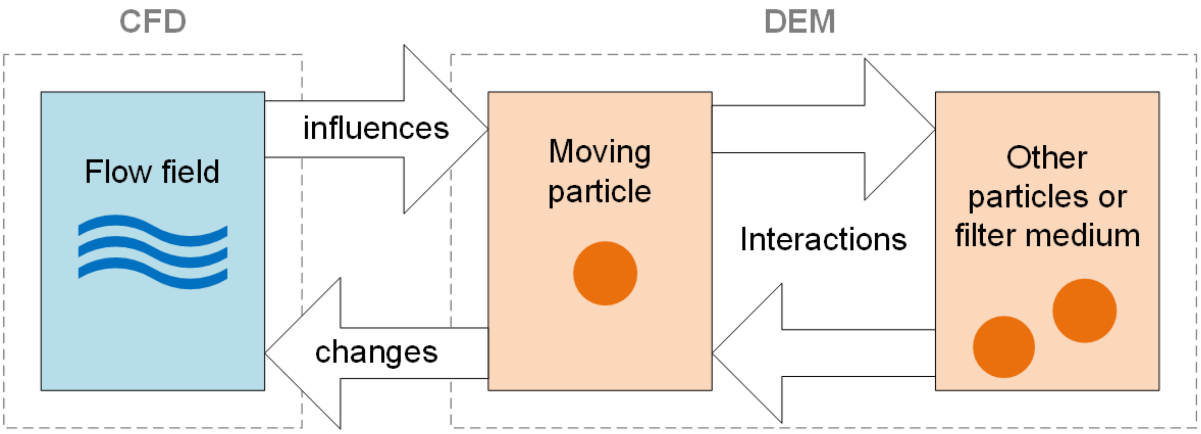

Figure 2.15: Specification of the 4-way CFD-DEM coupling. Each interaction is illustrated by an arrow (Puderbach et al., 2021).

Based on how we can model the fluid-particle interactions, 2 coupling approaches exist (see Fig. 2.16) namely, the unresolved (or Averaged Volume Method AVM) and the resolved (or Immersed Method IM) approaches (van der Hoef et al., 2008). In the unresolved approach, the fluid-particle forces are based on constitutive relationships that depend on local relative velocities and solid volume fractions. This approach used a large grid size, which is computationally efficient compared to the resolved approach. Alternatively, in the resolved approach, the DEM particle interfaces serve as boundaries for the fluid phases, and the interaction forces are calculated along the particle surfaces (Zhong et al., 2016). The resolved approach is more accurate than the unresolved approach since particles are treated like moving boundaries.

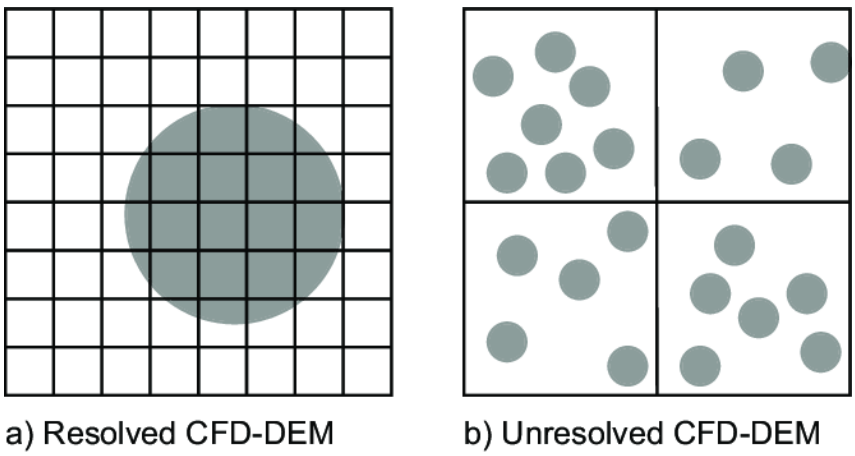

Figure 2.16: Conventional CFD-DEM coupling approaches (a) resolved (b) unresolved (Kanitz and Grabe, 2019).

Kloss et al. (2012) present an overview of the unresolved and resolved approaches, their mathematical

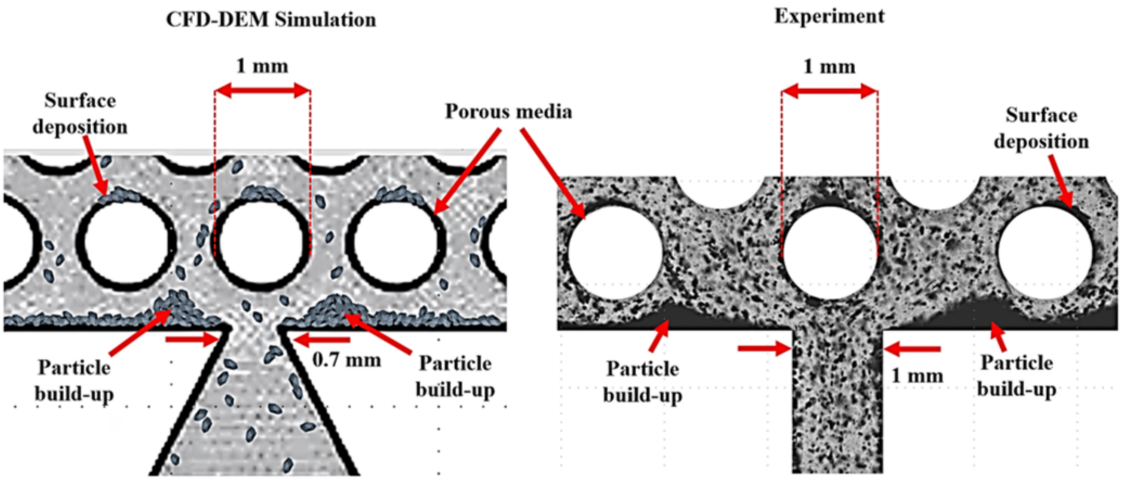

Figure 2.17: Particle build-up comparison between the CFD–DEM simulation on a wire-wrapped screen opening on the left, and particle shadowgraph velocimetry experiment from Kinsale and Nobes (2018) on a straight slot on the right (Razavi et al., 2021).

formulations, numerical implementations, and validations of the CFD-DEM. Chen et al. (2012) use an unresolved CFD-DEM applied to gas-solid two-phase flow in pulmonary airways to investigate particle transport and deposition. Zhao and Shan (2013) used an unresolved coupled CFD-DEM to investigate geomechanics systems. Shen et al. (2022) used a coupling CFD-DEM for modeling two-phase fluid with transport of irregularly shaped particles. Razavi et al. (2021) applied unresolved CFD-DEM to predict the retention mechanisms that occur at the opening of sand filters under laminar steady flow conditions of the well-bore. The filter slots under investigation have different geometries: straight, wire-wrapped screen and the particles are considered with different shapes and different aspect ratios and size distributions (see Fig. 2.17).

LBM-DEM

Most of the LBM-DEM coupling in the literature is based on the resolved coupling. Indeed Rettinger and Rüde (2017) report numerical issues for unresolved particles.

For example, Li and Prigiobbe (2018) and Zhou et al. (2018) use the LBM-DEM coupled with the Immersed Boundary Method (IBM) for simulating the migration of fine particles in porous media. However, they do not consider long-range interactions and cannot capture the aggregation. Samari Kermani et al. (2020) use LBM-DEM with Smoothed Profile Method (SPM) which assumed resolved particles to investigate the impact fluid flow velocity, colloid size, and pore structure on retention and transport of particles at pore-scale with aggregation of particles. Liu and Wu (2020) use LBM-DEM to perform the inertial migration of dense particle suspensions, the agglomeration of adhesive particle flows in channel flow, and the sedimentation of particles in cavity flow (see Fig. 2.18). Lu et al. (2024) investigate the effect mechanism of the grain material of artificial porous media coating quartz sand, titanium dioxide, zinc oxide, and polystyrene on the motion and deposition of suspended particles using the LBM-DEM with IBM.

If LBM is often considered an efficient and easy approach to simulate fluid flow, Wang et al. (2022) reports that LBM-DEM is less computationally efficient compared with CFD-DEM in 3D cases.

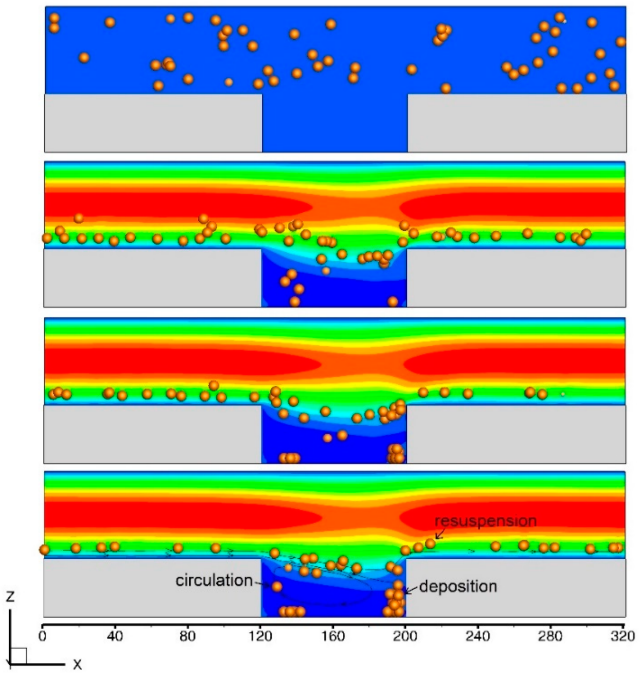

Figure 2.18: Snapshots of the particle suspensions flowing through a channel with a cavity for particle Reynolds number $Re_p = 56.88$ at different time points (for the top to the bottom) using LBM-DEM. (Liu and Wu, 2020).

PNM-DEM

PNM is widely used to determine flow properties and is suitable for coupling with the DEM as it effectively describes the essential skeleton of the porous medium. Pore bodies and their pore throat are defined locally through a regular Delaunay triangulation of the particle assemblies (see Fig. 2.19), and thus we can obtain fluid pressure applied on particles. When particles change their position due to particle-fluid forces, the associated pore structure changes and results in a new fluid flow.

On the particle's side, the particle-fluid force is composed of a drag force $\mathbf{F}_{d,ij}$ and a pressure gradient force $\mathbf{F}_{p,ij}$ Chareyre et al. (2011).

$$\mathbf{F}_{d,ij} = A_{s,ij}\Delta P_{ij}\mathbf{n}_{ij} \tag{2.23}$$

$$\mathbf{F}_{p,ij} = A_{f,ij}\Delta P_{ij}\mathbf{n}_{ij} \tag{2.24}$$

where $A_{p,ij}$ and $A_{f,ij}$ are the solid and fluid part of the interface respectively, $\mathbf{n}_{ij}$ is a unit vector pointing from the center of pore i to that of pore j.

Chareyre et al. (2011) use this method to simulate the viscous flow in dense sphere packings, Wu et al. (2021) use the PNM-DEM for particle-fluid flow in a dynamic cell, gas-fluidized bed, and a packed bed and they found good agreement with LBM-DEM or experiments results (see Fig. 2.20). Zhu et al. (2023) investigate the fluid injection in dense granular media with the PNM-DEM modeling. PNM is also used to capture poromechanical effects (Catalano et al., 2013).

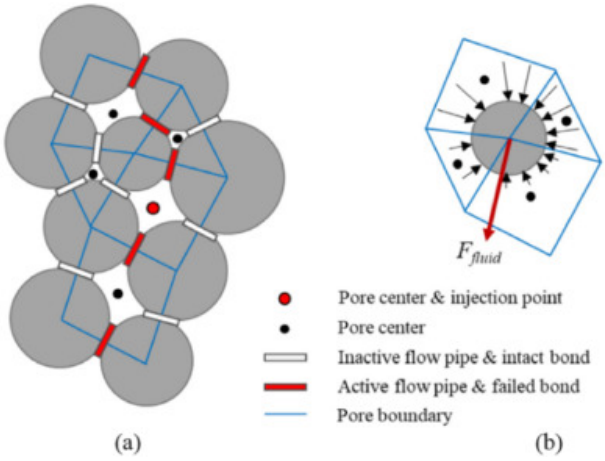

Figure 2.19: Schematics of the pore network model: (a) Pore domains formed from close chains of bonded particles; and (b) The drag force on a particle, F_{fluid}, as a resultant from the pore pressures of surrounding pore domains (Huang et al., 2019).

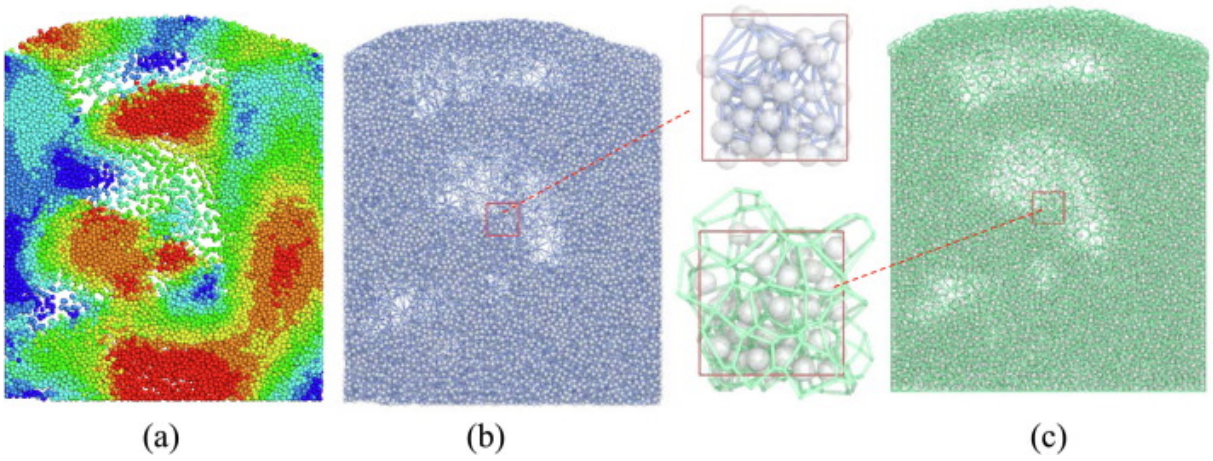

Figure 2.20: (a) Fluidized bed simulation using PNM-DEM. The color indicates the particle ID. The meshing of the fluidized bed: (b) with the Delaunay tessellation; and (c) with the Voronoi tessellation (Wu et al., 2021).

SPH-DEM

Tang et al. (2018) use the SPH-DEM for studying fluid-solid interactions with free surface flows. Their DEM particles are deformable using the Mohr-Coulomb criterion. They are capable of simulating failure and deformation under complex flow conditions with accuracy. Robinson et al. (2014) study 3D particle sedimentation and Rayleigh-Taylor instability with a two-way coupled SPH-DEM at the pore-scale. Peng et al. (2021) use the SPH-DEM to study fluid-solid interactions for heterogeneous suspension in non-newtonian fluids with arbitrary shapes of particles (see Fig. 2.21).

Parametrization of SPH simulations might be challenging. For example, Shadloo et al. (2016) explain that settling boundary conditions at the inlet, outlet, and walls is more difficult than with grid-based methods.

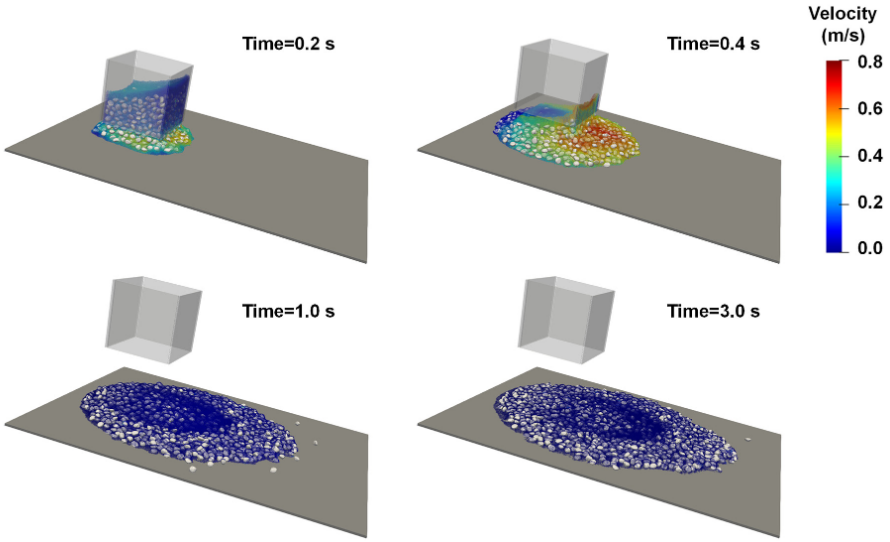

Figure 2.21: Snapshots of gravity-driven fresh concrete flow with natural pebbles of arbitrary shapes at different times using SPH-DEM method (Peng et al., 2021).

Other Lagrangian modeling approaches

- **Multi-phase Particle-In-Cell (MP-PIC) method**: The MP-PIC used an Eulerian grid for modeling the fluid flow while a Liouville equation gives access to the particle distribution function of the Lagrangian computational particles (Andrews and O'Rourke, 1996). In this approach, computational parcels are used to represent a defined number of particles with identical properties such as size, velocity, and location Dymala et al. (2022). This situation is illustrated in Fig. 2.22. The Liouville equation treats parcels as a continuous fluid and calculates their motion by computing the derivative on the Eulerian grid. Then, the motion of each parcel is mapped onto the Lagrangian frame. This results in a multiphase model that can handle particle transport with a distribution of particle sizes and properties in dilute or dense suspension. However, this method has the limitation that the particles need to be small compared to the Eulerian grid for accurate interpolation. Also, it uses a particle stress model instead of resolving collisions for particle-particle interactions. Snider (2001) use incompressible MP-PIC to simulate dense particle flows. Tian et al. (2020) used compressible MP-PIC coupled with coarse-grained DEM on gaz-particle systems.

- **Random Walk Particle Tracking (RWPT)**: It uses Lagrangian description to simulate the transport of solute seen as a huge amount of particles for the analysis of dispersion in porous media Kinzelbach (1988). This method models the trajectories of individual particles as they undergo random displacements at each time step. The displacement of each particle is typically determined by a combination of deterministic components (e.g. advection due to the flow) and stochastic components (e.g. diffusion or dispersion). RWPT allows the accommodation of non-linear processes and interactions between particles and the medium. RWPT is scalable as it can be applied from microscopic to macroscopic levels. However, with RWPT the results can exhibit statistical noise, especially when the number of particles is low. Ensuring accurate results may require simulating a large number of particles LaBolle et al. (1996). The accuracy of the method relies on the correct specification of parameters such as diffusion coefficients. Importantly, this approach is a one-way coupling (see Fig. 2.23) and therefore, does not consider the feedback of the particles on the flow or the particle-particle interactions.

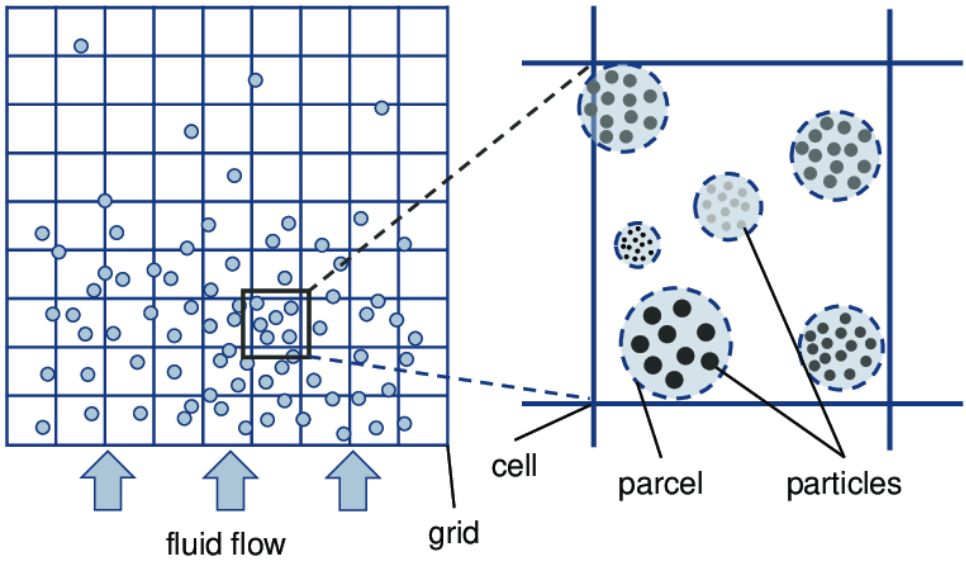

Figure 2.22: Schematic representation of the MP-PIC method (Dymala et al., 2022). Parcels are constituted as groups of particles of the same physical properties and are transported as Lagrangian particles using the unresolved approach.

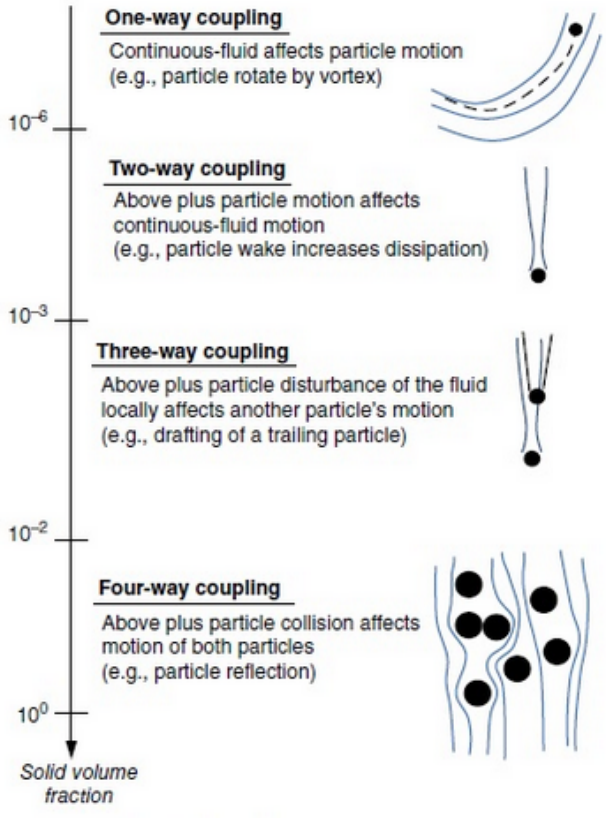

Figure 2.23: Different coupling configurations in Euler-Lagrange methods. (https://www.cfd-online.com/Forums/star-ccm/223996-cfd-dem-coupling.html)

Table 2.3: Summary of common fluid flow models coupled with Lagrangian DEM.

Method	Basic theory	Capabilities	Limitations
CFD-DEM	Averaged Navier-Stokes equations (continuum + discrete)	1. Coupling flow, transport, and evolution of porous media properties. 2. Accurately capture the complex interactions between the fluid and particulate phases. 3. Simulate a wide range of flow regimes, from dilute to dense particulate flows.	1. CFD-DEM simulations are computationally intensive. 2. the accuracy of CFD-DEM depends on the coupling approaches for fluid-particle interactions.
LBM-DEM	Mesoscopic dynamics (continuum + discrete)	1. Coupling flow, transport, and evolution of porous media properties. 3. Operates at a mesoscopic scale, offering high-resolution insights into fluid dynamics. 4. Simple calculation procedure	1. Schemes with higher dimensions with more velocity directions are computationally expensive. 2. The method is sensitive to particle-fluid interaction coefficients. 3. Less accurate for very small-scale phenomena involving microscale interactions due to resolution limits.
PNM-DEM	Hagen-Poiseuille equation (pseudo-discrete + discrete)	1. Provides an affordable computational tool and a reduced impact on the numerical simulations as the pore volume is increased, unlike other methods. 2. Ease of implementing material heterogeneity. 3. Able to simulate multiphase flow in porous media	1. Constructed with simplifying assumptions of the pore geometry. 2. The governing assumption can make the prediction less accurate. 3. The challenge of identifying the critical features relevant to the process of interest.
SPH-DEM	Kernel interpolation theory (discrete + discrete)	1. Coupling flow, transport, and evolution of porous media properties. 2. Triviality of simulating multiphase flows with complex boundary problems. 3. The lack of mesh simplifies the model implementation and its parallelization. Both SPH and DEM can adaptively refine the particle resolution in regions of interest.	1. High computation cost compared to grid-based methods. 2. The method often relies on constitutive closure models for interphase momentum, heat, and mass transfer. 3. Difficulty in using high-order discretization schemes unlike mesh-based methods, leads to the difficulty of ensuring numerical stability and convergence.

2.2.3 Eulerian models for particulate transport

The Eulerian method describes the flow of particles collectively as a continuous phase through the particle concentration distribution or a probability density function to access the evolution in space and time of the particle phase in a control volume. The Eulerian method enables simulations in larger domains. However, it relies on constitutive laws for describing hydrodynamical, mechanical, and electrochemical interactions. We introduce two models. In the Two-Fluid Model, the solid particle phase motion is described as a continuous fluid with its momentum balance equations. In the scalar transport model, the motion of the particle concentration field is computed using the fluid velocity. Table. 2.4 summarizes the capabilities and limitations of these two models.

Two-Fluid Model (TFM)

Two-fluid model is an Euler-Euler model in which both the particulate and fluid phases are considered as two separate interpenetrating continua, described with their own momentum and mass balance equations that are coupled by mutual interaction terms Herman and Prigogine (1979). Constitutive laws represent the inter-field interaction. TFM has been widely used to model two-phase flow with dispersed bubble (see Fig. 2.24) and gas-solid systems including fluidized beds (Schneiderbauer et al., 2012; Wang et al., 2014; Zhao et al., 2021; Esgandari et al., 2023). It has also been used for particulate transport in porous media (Biesheuvel, 2011).

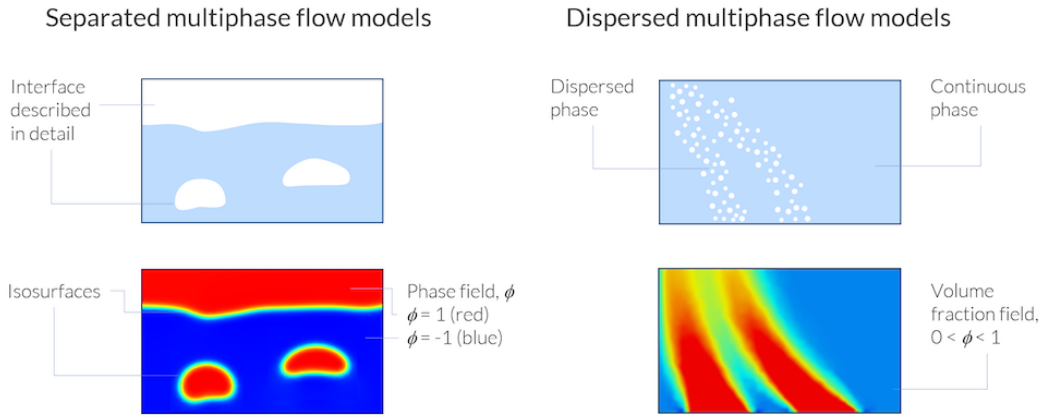

Figure 2.24: Separated multiphase flow models describe the phase boundary in detail, while dispersed multiphase flow models only deal with volume fractions of one phase dispersed in a continuous phase (after https://www.comsol.com/blogs/modeling-and-simulation-of-multiphase-flow-in-comsol-part-1).

The continuity and momentum equations of the fluid phase are based on VANS equations (Eq. 2.11-2.12). The particulate phase equations are (van der Hoef et al., 2008):

$$\frac{\partial[\epsilon_p \rho_p]}{\partial t} + \nabla \cdot [\epsilon_p \rho_p \mathbf{v}^p] = 0, \tag{2.25}$$

$$\frac{\partial[\epsilon_p \rho_p \mathbf{v}^p]}{\partial t} + \nabla \cdot [\epsilon_p \rho_p \mathbf{v}^p \mathbf{v}^p] = -\epsilon_p \nabla p^f - \nabla p^p - \nabla \cdot \epsilon_p \boldsymbol{\tau}^p - \xi(\mathbf{v}^f - \mathbf{v}^p) - \epsilon_p \rho_p \mathbf{g}. \tag{2.26}$$

In the two-fluid model, the interactions between particles are included through a "solid pressure" term, p^p. ϵ_p is the particle volume fraction in each cell.

The deposition of particles at the solid surface is modeled through kinetic boundary conditions (i.e. Robin conditions) (Carrillo and Bourg, 2019). The determination of the kinetic coefficient is complex because it depends on the flow conditions, particle size, concentration, pH, and salinity. A standard multi-scale approach to obtain the constitutive TFM laws is to volume-average the Euler-Lagrange solution (Quintard and Whitaker, 1995).

Scalar Transport Model

The scalar transport model is used to describe physical phenomena where particles, energy, or other physical quantities are transferred through a domain due to two processes: diffusion (transfer by concentration gradient) and advection (transfer by fluid flow). The advection-diffusion equation used in the scalar transport model applied to transfer a cloud of particles defined by its volume fraction ϵ_p reads,

$$\frac{\partial \epsilon_p}{\partial t} = \nabla \cdot \left(D \nabla \epsilon_p - \mathbf{v}^f \epsilon_p - \frac{D\ \mathbf{F}}{k_B T} \epsilon_p \right) + S_T, \tag{2.27}$$

where $\mathbf{v}^f$ is given by Navier-Stokes equations, and $\mathbf{F}$ is the vector of forces experienced by the phase (colloidal forces described previously). S_T is a source/sink term and D is the diffusion or dispersion coefficient.

Boccardo et al. (2014) investigate particle deposition in porous media with microscale simulations using the scalar transport model with the colloidal filtration theory (CFT) developed by Yao et al. (1971), where only Brownian motions and steric interception are accounted for as deposition mechanisms (see Fig. 2.25). Li et al. (2008) investigate the transport and deposition of Nanoparticles in Quartz sand under varying flow conditions. They use a scalar transport model with CFT to investigate effluent concentration breakthrough curves and deposition profiles through attachment kinetics and maximum retention capacity.

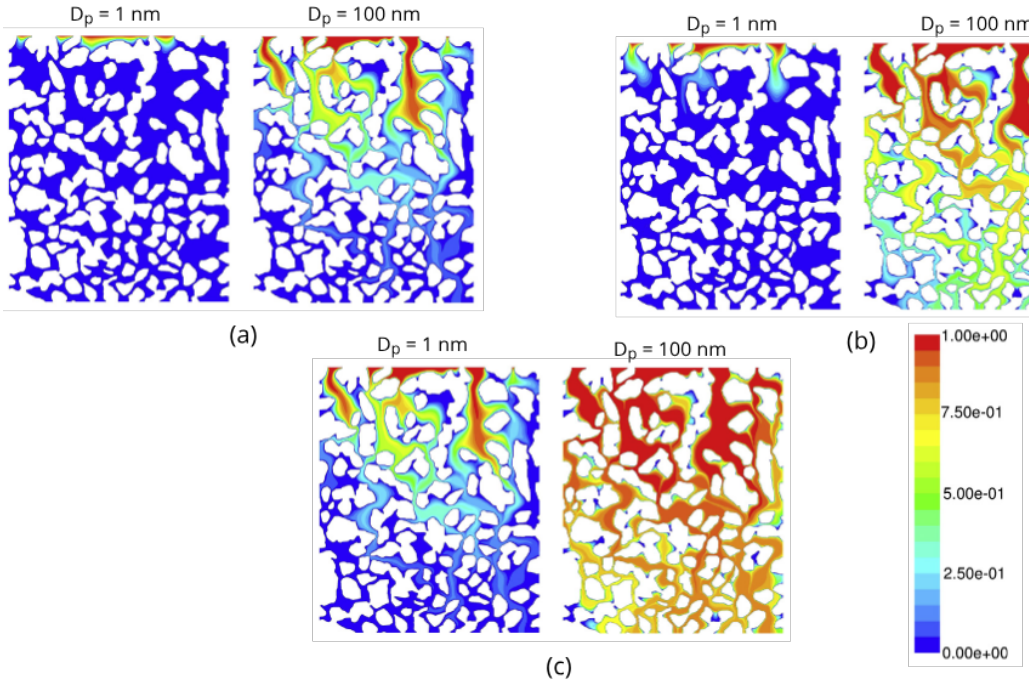

Figure 2.25: Contour plots of normalized particle concentration on a realistic porous medium model, for superficial velocity u = 10^{-6} ms^{-1} (a), u = 10^{-5} ms^{-1} (b), u = 10^{-4} ms^{-1} (c). D_p is the particle diameter (Boccardo et al., 2014).

Table 2.4: Capabilities and limitations of the two-fluid model and the scalar transport model.

Model	Capabilities	Limitations
Two-Fluid Model	- High predictive accuracy on the void fraction distribution. - Combined with kinetic theory, it can describe two-phase flow at relatively large scales, yet retain the physics of particle-particle interactions (Dennis, 2013). - It can be applied to a wide range of particulate flow problems, including gas-solid, liquid-solid, and liquid-liquid flows. - Computationally more efficient than the Euler-Lagrange model for large domains.	- Trouble modeling flows with a distribution of particle densities and sizes because separate continuity and momentum equations must be solved for each size and density (Gidaspow, 1994). - The interphase term is accessible over several correlations and the model is more complex to implement. - Closure relations are needed for contact parameters that are no longer measurable properties, and then do not allow for the rheological characteristics of the solid phase. (Dennis, 2013). -Defining appropriate boundary conditions for both phases can be challenging, especially at phase interfaces, and can be computationally demanding for 3D simulations. - Rely on constitutive relationship for the modelization of particle retention (i.e. deposition kinetics, permeability-porosity relation)
Scalar Transport Model	- It uses a simple equation, allowing analytical solutions for linear and homogeneous conditions (Ogata and Banks, 1961). - It can be scaled for both macroscopic scale and microscopic resolution problems. - By accurately modeling the underlying processes, the model can predict the spatial and temporal distribution of particulate matter. - The model can incorporate certain physical processes such as chemical or biological processes (Rubin, 1983). - Computationally more efficient than TFM for large domains.	- The assumption of constant diffusion coefficient, linear reaction, or homogeneous properties of the medium. - Accurate predictions require well-defined boundaries and initial conditions, and accurate determination of model parameters (advection velocities, diffusion coefficients) (LeVeque, 2002). - The model equation may trigger in its basic form when accounting for non-linear effects such as high concentration gradient, high-velocity flows, or non-linear reactions (Sachdev, 1990). - Rely on constitutive relationship for the modelization of particle retention (i.e. deposition kinetics, permeability-porosity relation). - Solving the model equation, especially in three dimensions or with complex boundary conditions, can be computationally intensive.

2.3 Darcy-scale description

For large domains including core-scale and field-scale, the description of flow, particles, and species transport within each pore is not feasible, as the pore space is no longer explicitly described (see Fig. 2.26). Instead, volume-averaged equations are used to describe flow and particle transport. Similar to Euler-Euler equations, volume-averaged equations consider the sub-scale effects through constitutive relationships. One of the standard approaches for modeling particulate transport at Darcy's scale is a combination of Darcy's law, a permeability-porosity relationship, and a mass balance equation for the particle volume fraction. Electrochemical processes are described through deposition and detachment rates that must be informed by pore-scale physics.

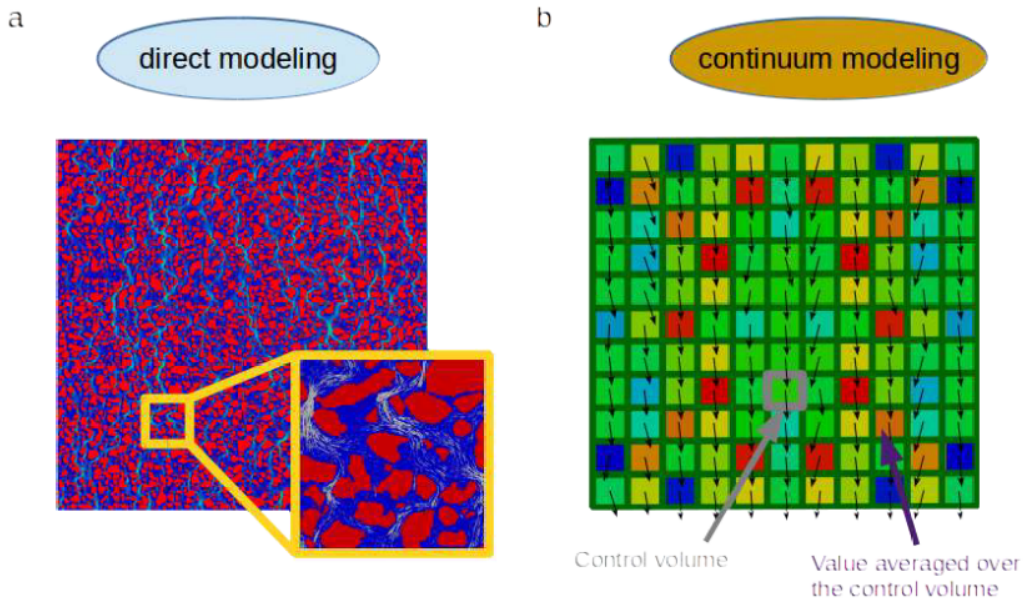

Figure 2.26: Two different representations of the physics of flow in porous media. The arrows represent the velocity vectors. (a) direct modeling or pore-scale approach where the solid is explicitly represented. (b) the continuum modeling or Darcy scale where the physics is governed by quantities averaged over control volumes. The color map represents the volume fraction of solid per control volume (Soulaine, 2022).

2.3.1 Heterogeneous structure of porous media

Porous media can be declined in various aspects with homogeneous and heterogeneous pore space as shown by Fig. 2.27. There are typical topological and physical parameters to characterize their structure complexity.

Porosity

A porous medium is characterized by its porosity. The porosity or void fraction ϕ measures the void spaces in a volume of porous medium. It is expressed as the fraction of the volume of pore spaces, over the total volume of the medium (porous matrix and pores) and varies between 0 and 1.

$$\phi = \frac{\sum V_{pore}}{V_{total}} \tag{2.28}$$

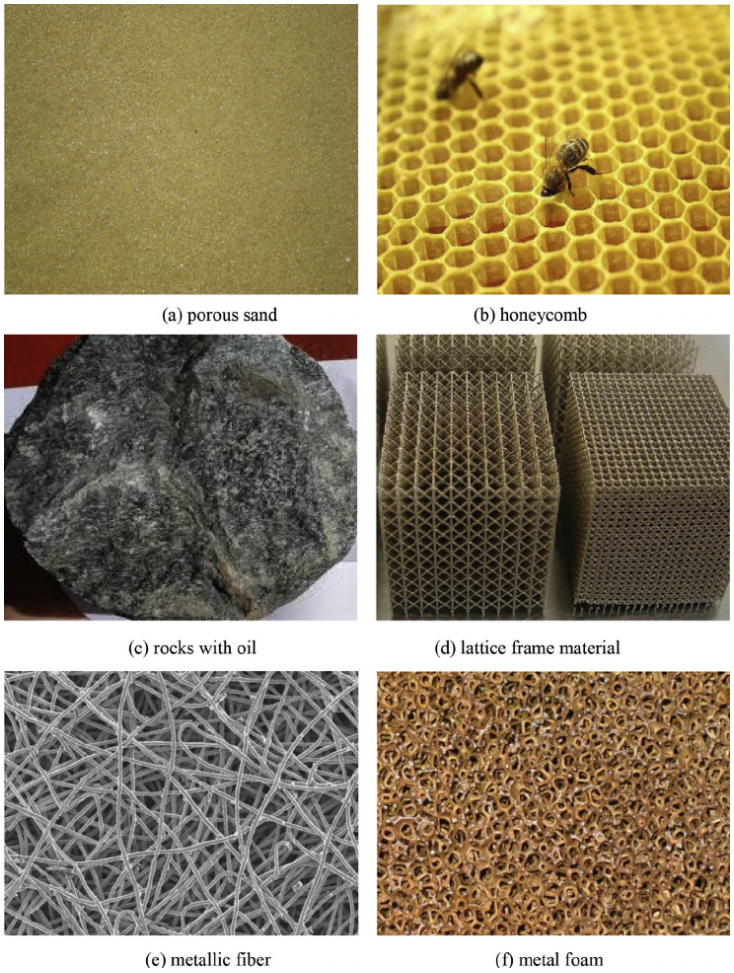

Figure 2.27: Different kinds of porous media (Xu et al., 2015).

Depending on the type of porous medium, the porosity ranges to very different values as shown in Table 2.5. Clay reservoirs have high porosity values, but the effective porosity (the fraction of pore space that can contribute to fluid flow) is much lower (1 - 2%) because a significant portion of the pore space is not interconnected or is too small to allow fluid flow. In comparison, sandstone has an effective porosity of around 10 - 25% (Olivier and Mulongo, 1997), which are range of values typically associated with geothermal reservoirs (Kristensen et al., 2016; Wadas and von Hartmann, 2022).

Table 2.5: Porosity magnitude order of environmental porous media (from https://www.saltworkconsultants.com/carbonate-porosity-sandstone-vs-carbonate/ and Neuzil (2019)).

Medium	Porosity (%)
Limestone reservoirs	5 - 30
Sandstone reservoirs	25 - 40
Clay reservoirs	30 - 50
Carbonate reservoirs	40 - 70

The closed porosity is created by isolated pores, and with the existence of dead-end pores, the concept

of effective porosity due to transport pores only is introduced as shown in Fig. 2.28.

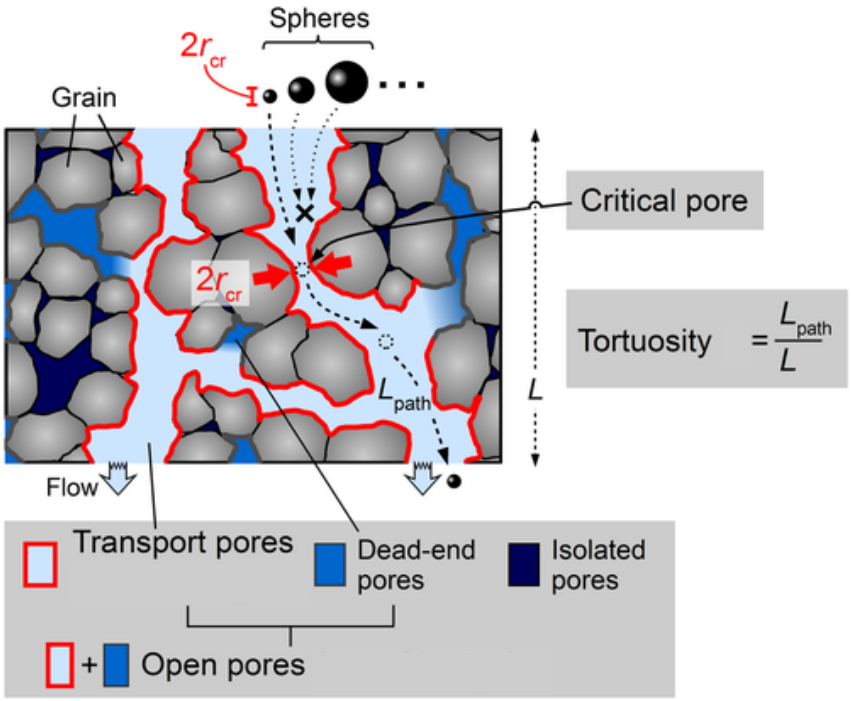

Figure 2.28: Schematic of the pore structure and definitions of pore characteristics. The radius of the largest sphere that can pass freely through the porous material (leftmost black sphere) corresponds to the critical pore radius r_{cr} (Nishiyama and Yokoyama, 2017).

Tortuosity

Tortuosity is a widely used criterion to characterize the morphological property of porous microstructures. The tortuosity τ is the fraction of the length of the path L_{path} over the distance between its ends L. It reads,

$$\tau = \frac{L_{path}}{L}. \tag{2.29}$$

Specific surface area

The specific surface area, A_e, defines the ratio of the total surface area A_{int} (area covered by the solid-pore interface) over the total solid volume.

$$A_e = \frac{A_{int}}{V_{total}}, \tag{2.30}$$

This parameter becomes interesting with surface phenomena such as adsorption-desorption. The finer the grains which constitute the porous medium, the higher the specific surface area. In geochemistry, the specific surface area is the surface area of the pore walls divided by the solid mass (in m^2/g).

Permeability

Permeability noted K, is the measure of the capacity of porous materials to let fluid flow through them. Permeability is strongly linked to the effective porosity and specific surface area. Similar to porosity

values, the permeability can be widely different from one material to another (see Fig. 2.29).

Permeability	**Pervious**				**Semi-pervious**				**Impervious**				
Unconsolidated sand and gravel	Well sorted gravel		Well sorted sand or sand and gravel		Very fine sand, silt, loess, loam								
Unconsolidated clay and organic					Peat		Layered clay		Unweathered clay				
Consolidated rocks	Highly fractured rocks				Oil reservoir rocks			Fresh sandstone		Fresh limestone, dolomite		Fresh granite	
***k* (cm²)**	0.001	0.0001	10^{-5}	10^{-6}	10^{-7}	10^{-8}	10^{-9}	10^{-10}	10^{-11}	10^{-12}	10^{-13}	10^{-14}	10^{-15}
***k* (m²)**	10^{-7}	10^{-8}	10^{-9}	10^{-10}	10^{-11}	10^{-12}	10^{-13}	10^{-14}	10^{-15}	10^{-16}	10^{-17}	10^{-18}	10^{-19}
***k* (millidarcy)**	10^{+8}	10^{+7}	10^{+6}	10^{+5}	10,000	1,000	100	10	1	0.1	0.01	0.001	0.0001

Figure 2.29: Order of magnitude of permeability of some porous media (Bear, 1988).

If the pore morphology changes because of particle deposition and pore-clogging, the porosity and permeability are modified. In the literature, permeability-porosity $K(\phi)$ relationships attempt to assess the permeability reduction due to a change in porosity. The most common relationships are presented in Table 2.6. We know, however, that the structure of the deposition depends strongly on other parameters including flow conditions, suspension concentration, and solution chemistry.

Table 2.6: Different formulations of porosity-permeability relationship.

Description	Porosity-permeability relation
Kozeny-Carman's equation for predicting permeability based on porosity and grain size (Kozeny, 1927; Carman, 1937)	$K = \frac{c\ \epsilon^3}{(1-\phi)^2\ A_e^2}$, with c the Kozeny-Carman constant
Lucia's model specifically for carbonate reservoirs, relating porosity to permeability based on rock fabric (Lucia, 1983)	$K = a \cdot \phi^n$, with a and n are empirical constants that vary with rock fabric
Pittman's relation is an empirical relationship for sandstones, taking into account grain size and sorting (Pittman, 1992)	$K = \phi^m \cdot D^n$, with D the mean grain size, m and n are empirical constant
Hilfer's relation is used to relate porosity to permeability in clean, consolidated sandstones using Archi's law (Archie, 1942; Hilfer, 1993)	$K = b\left(\frac{F}{a}\right)^{-\frac{n}{m}}$, with F the formation factor related to the electrical conductivity, a is a constant coefficient, b, n are empirical parameters and m is the cementation exponent
The power law is a generalized relationship often used in various forms (Nelson, 1994)	$K = \phi^n$, n is an empirical constant.

2.3.2 From pore-scale to Darcy-scale

Control volumes are defined all over the medium, and the physical quantities are averaged over these control volumes. The definition of this control volume is crucial for the accuracy of the results (Bear, 1988). It needs to be a Representative Elementary Volume (REV) which is the smallest volume over which a measurement can be made that will yield a value representative of the whole.

The operator $(-)$ and $(-^{\beta})$ over the quantities denote, the superficial average and the intrinsic β-phase average over the control volume respectively. Let the function Γ_f associated with the fluid f-phase in the control volume V (see Fig. 2.30), its superficial average reads Whitaker (1986),

$$\overline{\Gamma}_f = \frac{1}{V}\int_{V_f} \Gamma_f dV \tag{2.31}$$

and its intrinsic phase average which means the average in the void space only reads,

$$\overline{\Gamma}_f^f = \frac{1}{V_f}\int_{V_f} \Gamma_f dV. \tag{2.32}$$

with V_f the pore volume. The two previous formulations are linked through,

$$\overline{\Gamma}_f = \phi \overline{\Gamma}_f^f. \tag{2.33}$$

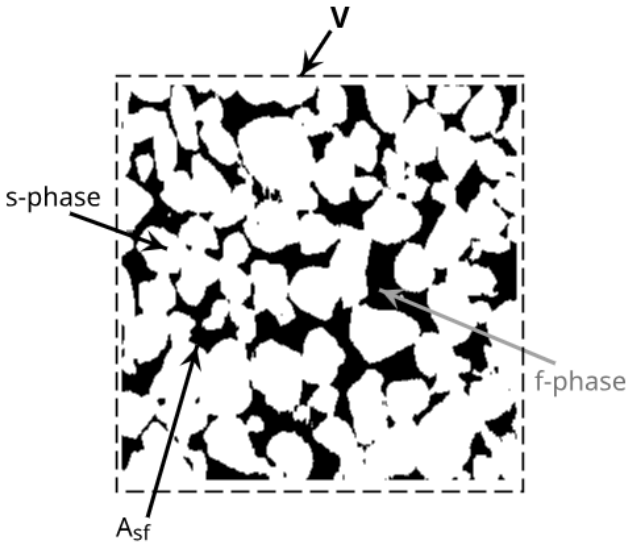

Figure 2.30: Two-dimensional slice of a rock representing a control volume V. The black region represents the void space (f-phase) while the white region represents the solid grains (s-phase). A_{sf} is the fluid-solid interface.

In the case of a non-deformable medium, ϕ is constant over time. For example, the unknown quantities describing the flow of a f-phase in a porous medium are the averaged phase velocity vector $\overline{\mathbf{v}}_f$ and averaged phase pressure $\overline{p}_f^f$.

The average of the derivative $\overline{\nabla\Gamma_f}$ involves the derivative of the average $\nabla\overline{\Gamma}_f$ and the boundary information at the solid through,

$$\overline{\nabla\Gamma_f} = \nabla\overline{\Gamma}_f + \frac{1}{V}\int_{A_{sf}} \mathbf{n}_{sf}\Gamma_f dA. \tag{2.34}$$

with $\mathbf{n}_{sf}$, the normal vector at the solid walls, and A_{sf} the fluid-solid interface.

2.3.3 Darcy equations

As the pore network of the medium is not accessible at this scale, Darcy's law is used to access unknown averaged quantities Darcy (1856),

$$\begin{cases} \nabla \cdot \overline{\mathbf{v}}_f = 0, \\ \overline{\mathbf{v}}_f = -\frac{1}{\mu_f} K \cdot \left(\nabla \overline{p}_f^f - \rho_f \mathbf{g} \right) \end{cases} \tag{2.35}$$

where K is the permeability tensor of the porous medium. K contains information relating to the topology of the pore matrix.

2.3.4 Deep bed filtration (DBF)

The reduction in porosity is deduced from the evolution of the suspended particle concentration, $C = \overline{\epsilon}_p^f$, where $\overline{\epsilon}_p^f$ is the intrinsic particle volume fraction averaged in the void space. The transport equation of the particle concentration is an advection-dispersion-reaction partial differential equation. We have,

$$\frac{\partial \phi C}{\partial t} + \nabla \cdot (\overline{\mathbf{v}}_f C) = \nabla \cdot (\phi \mathsf{D} \cdot \nabla C) - \rho_b \frac{\partial S}{\partial t}, \tag{2.36}$$

where D is the dispersion tensor and ρ_b is the porous medium bulk density. The last term represents the rate of particle retention and S is the attachment concentration on the matrix surface. $\overline{\mathbf{v}}_f$ is the fluid velocity obtained with Darcy's equations (Eq. 2.35).

Dispersion tensor

The dispersion D results from a combination of molecular diffusion $\mathbf{D}_m$ and hydrodynamic dispersion $\mathbf{D}_h$ (Soulaine et al., 2021).

$$\mathsf{D} = \mathsf{D}_m \tau^{-1} \left(\mathsf{I} + \mathsf{D}_h \right), \tag{2.37}$$

where τ is the tortuosity of the medium. Bear (1988) proposed a formula for the hydrodynamic dispersion coefficient in one-dimension $D_h = a_L (\overline{v}_f^f)^n$, with a_L the longitudinal dispersivity and n is an empirical exponent. For a high Peclet number $Pe = L\overline{v}_f / D_m >> 1$, the molecular diffusion is negligible, with L the length of the domain.

Retention kinetics

The retention term can be described using several adsorption isotherm expressions (Madhan Nur Agista, 2017):

$$\frac{\rho_b}{\phi} \frac{\partial S}{\partial t} = kC \qquad \textbf{(Linear)}, \tag{2.38}$$

$$\frac{\rho_b}{\phi} \frac{\partial S}{\partial t} = \frac{k_1 C_m}{1 + k_2 C_m} \qquad \textbf{(Langmuir)}, \tag{2.39}$$

$$\frac{\rho_b}{\phi} \frac{\partial S}{\partial t} = k C^{1/n}, \ n > 1 \qquad \textbf{(Freundlich)}, \tag{2.40}$$

$$\frac{\rho_b}{\phi}\frac{\partial S}{\partial t} = k_1 C - k_2 C^2 \qquad \textbf{(Quadratic)}, \tag{2.41}$$

$$\frac{\rho_b}{\phi}\frac{\partial S}{\partial t} = k_1 \exp^{-k_2/C} \qquad \textbf{(Exponential)}, \tag{2.42}$$

where ρ_b is the porous medium bulk density, k, k_1, k_2, are attachment rates, C_m, and n is a fitting exponent. Several models have been developed based on different theories (e.g. colloidal filtration, colloidal filtration with site blocking, colloidal filtration with detachment, kinetic Langmuir model, dual-site model, and linear adsorption model) and are presented in Table 2.7. These models will be described and discussed in Chapter 5.

Table 2.7: Retention kinetics models (modified after Zhang et al. (2016))

Model	References	Deposition term
Colloid Filtration Theory (CFT)	Yao et al. (1971)	$\frac{\rho_b}{\phi}\frac{\partial S}{\partial t} = k_{dep} C$
Filtration Model + Maximum site	Li et al. (2008); Liu et al. (2009); Cullen et al. (2010)	$\frac{\rho_b}{\phi}\frac{\partial S}{\partial t} = k_{dep}\left(1 - \frac{S}{S_{max}}\right) C$
Filtration Model + Detachment	Bradford et al. (2002)	$\frac{\rho_b}{\phi}\frac{\partial S}{\partial t} = k_{dep} C - \frac{\rho_b}{\phi} k_{det} S$
Kinetic Langmuir Model	Wang et al. (2008)	$\frac{\rho_b}{\phi}\frac{\partial S}{\partial t} = k_{dep}\left(1 - \frac{S}{S_{max}}\right) C - \frac{\rho_b}{\phi} k_{det} S$
Two Site Model	Zhang et al. (2016)	$\frac{\rho_b}{\phi}\frac{\partial S}{\partial t} = k_{irr}\left(1 - \frac{S_1}{S_{1max}}\right) C + k_{ra}\left(1 - \frac{S_2}{S_{2max}}\right) C - \frac{\rho_b}{\phi} k_{rd} S_2$
Modified Linear Adsorption Model	Madhan Nur Agista (2017)	$\frac{\partial S}{\partial t} = k_c \eta_0 \frac{\partial C}{\partial t}$

In Table 2.7, k_{dep} is the deposition rate, k_{det} is the detachment rate, k_{irr} is the irreversible attachment rate, k_{ra} is the reversible attachment rate, k_{rd} is the reversible detachment rate, S_{max}, S_{1max}, S_{2max} are the particle retention capacities, S_1 and S_2 are the concentration of irreversible and reversible attachments, respectively. η_0 is the single collector capture efficiency, k_c is the concentration distribution.

2.4 Objectives and methodology of the thesis

2.4.1 Objectives

Through our literature review, we have seen that the modeling of particulate transport in porous media at a large scale relies on constitutive relationships that depend on a wide range of parameters including flow rates and suspension properties.

A standard strategy to derive large-scale models rooted in elementary physical principles is to start at the pore-scale where the physics is better understood and to upscale the results to larger scales. At the pore-scale, however, the state-of-the-art modeling approach is not able to reproduce the main clogging mechanisms (e.g. sieving, bridging, aggregation).

In this Ph.D. thesis, we aim to develop a robust and efficient simulator to describe the transport of particles within the porous matrix at the pore-scale. The model should be able to capture the three main clogging mechanisms. It will be used to propose and validate new kinetic deposition rates and permeability-porosity relationships.

2.4.2 Methodology

To achieve our objectives, we develop a new CFD-DEM coupling model. The model is implemented within the open-source CFD platform OpenFOAM. OpenFOAM is a general-purpose simulator that solves partial differential equations using the Finite-Volume Method.

OpenFOAM already has a CFD-DEM solver. It comes, however, with strong limitations: the electro-chemical interactions are not considered and the particles must be smaller than the grid size (unresolved approach).

In Chapter 3, we present our new unresolved-resolved CFD-DEM simulator for colloidal particles. We perform a comprehensive set of verification tests. These test cases give us confidence in the predictive capacity of our numerical model.

In Chapter 4, we use our CFD-DEM numerical model to investigate pore-clogging at the pore-scale in a single pore and a representation of a heterogeneous porous medium. We investigate the effect of fluid properties, particle properties, and flow conditions on the permeability reduction over the injected pore volume.

In Chapter 5, based on the colloidal filtration theory which describes particles as a continuum phase transported by advection, diffusion, and reaction, we revisit the deposition kinetic law to investigate deposition patterns on a cylindrical collector with comparison to experimental results.

A graphical flowchart of the thesis methodology is presented in Fig. 2.31.

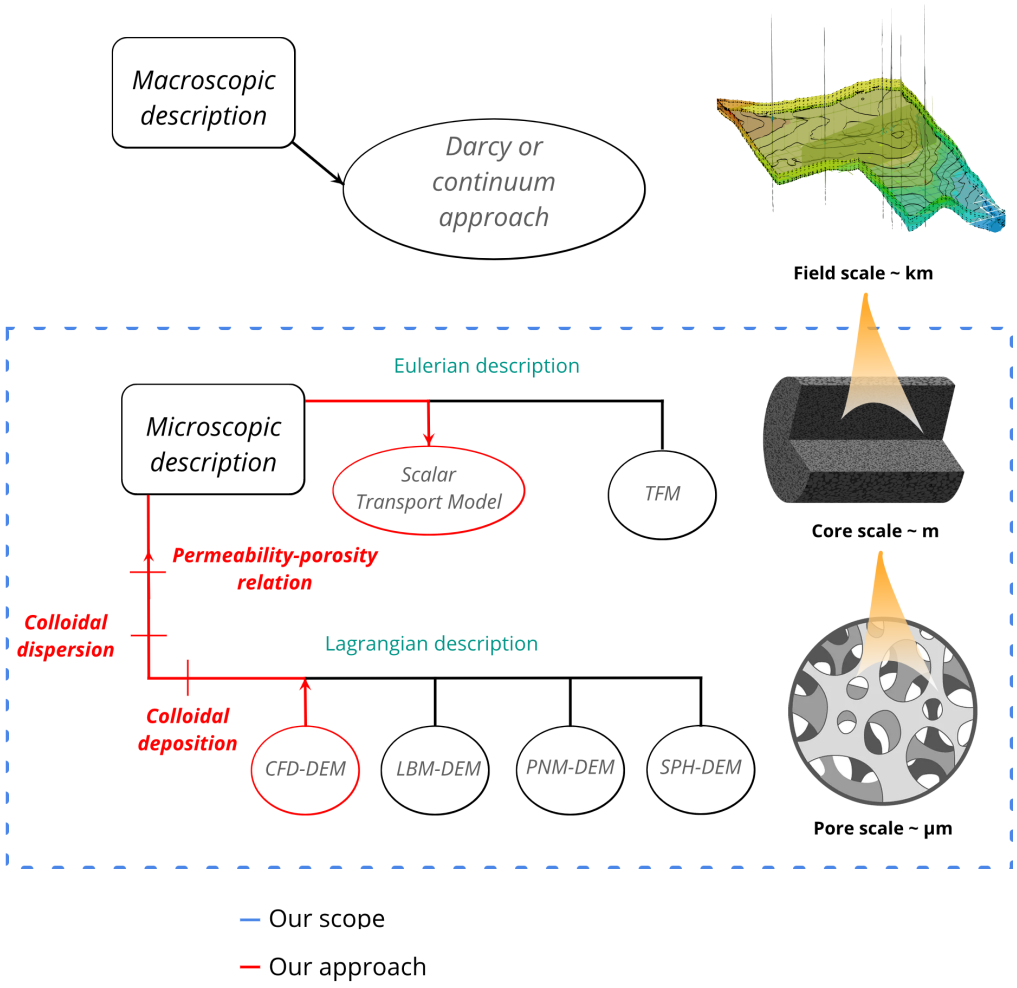

Figure 2.31: Thesis methodology for colloidal transport at core scale.

Chapter 3

Unresolved-Resolved CFD-DEM for Colloidal Flow

In this chapter, we introduce a novel hybrid unresolved-resolved CFD-DEM four-way coupling approach combined with DLVO forces and the adhesive JKR contact force to simulate spherical, rigid particulate flows in porous media at the pore-scale with migration, deposition, and retention mechanisms. Our hybrid model includes: (i) *a drag force that accounts for both resolved and unresolved particles,* (ii) *the associated hydrodynamic torque,* (iii) *an efficient algorithm for identifying particle-fluid cells, and* (iv) *a diffusive layer to smooth the particle-fluid interface. The chapter is organized as follows. In section 3.1, we introduce the CFD-DEM model and its limitations. In section 3.2, we describe the governing equations of the fluid and particles and the coupling algorithms. Then, in section 3.3, we show the accuracy, consistency, and efficiency of our approach using cases for which reference solutions exist. Finally, we close with a summary and concluding remarks.*

3.1 Review of the CFD-DEM Model

CFD-DEM is an Euler-Lagrange method commonly used to simulate particle transport (Tsuji et al., 1993). It consists of solving Navier-Stokes equations on a fixed Eulerian grid using computational fluid dynamics (CFD) to compute the continuous carrier phases' flow and resolve the particle dynamics using a Lagrangian discrete element method (DEM). State-of-the-art CFD-DEM relies on the so-called four-way coupling which states that the fluid transports the particles, the presence of particles impacts the fluid flow, and particle-particle and particle-wall interactions are considered, which avoids the assumption of diluted suspension (O'Sullivan, 2011). Two main fluid-particle coupling approaches exist whether particle diameter, D_p, is bigger or not than the grid cell size, Δx. On the one hand, the unresolved coupling approach is used if the particle size is smaller than the grid resolution. The drag force between fluid and particle is calculated using a sub-grid model. On the other hand, in resolved coupling, the particle size is bigger than the grid resolution, and the fluid-particle shear stress forces acting on the particle are an output of the simulation.

Limitations exist in both resolved and unresolved approaches. Pirker et al. (2011); Marshall and Sala (2013) reported that unresolved coupling leads to significant errors and instabilities if $\Delta x < 3D_p$. Despite its faster calculation time, this approach presents discontinuities in the calculation of the particle velocity because the particle oscillates when it crosses two adjacent cells that have different fluid velocities (Peng

et al., 2014). Importantly, sieving cannot be simulated using unresolved coupling because the grid size is necessarily smaller than the pore-throat and then the particle size. This lack of capture of the dynamics of flows around the particles which guides the aggregation or remobilization process of colloids is a big limitation. In resolved coupling, the size ratio has to be at least $D_p/\Delta x > 10$, to ensure an accurate resolution of the particle surface on the Eulerian grid (Hager, 2014; Uhlmann, 2005). This results in large computational times that increase with the particle number which limits this method for simulating large quantities of particles. Moreover, the complexity of the porous geometry with pores of different sizes often requires computational grids made of cells with different sizes, and the same particle might be resolved in some parts of the domain and unresolved in others. Some approaches intend to overcome the aforementioned limitations by developing hybrid unresolved-resolved approaches. For example, the semi-resolved CFD-DEM described in Wang et al. (2019) corrects the fluid velocity around the particle and the volume fraction in the drag force model using kernel-based approximations. Their model half-theoretical half-empirical leads to inaccurate calculations of the fluid-particle forces for dense suspensions of large particles. Kuruneru et al. (2018) proposed a mixed resolved-unresolved CFD-DEM approach that uses an Immersed Boundary Method (IBM), a specific contact handling algorithm to compute particle contact forces, and a Brinkman penalization technique for the momentum sink term of the fluid phase. However, their model works only for regular grids which is limiting for heterogeneous porous media with confined pores. The unresolved-resolved CFD-DEM approach introduced in this chapter overcomes these limitations relative to particle sizes over the Eulerian grid refinement (see Table 3.1). However, modeling colloidal transport leading to clogging by aggregation in porous media requires additional forces and appropriate treatment of the colloid adhesion (Poon and Haw, 1997).

Colloidal forces for the aggregation mechanism arise if particles are submicrometer in size and electrochemical interactions become dominant (Liang et al., 2007). These forces are due to long-range interactions whose influence applies from typically tens of nanometers down to nearly surface-to-surface contact. They are classically described using the Derjaguin-Landau-Verwey-Overbeek (DLVO) theory (Verwey, 1948; Derjaguin and Landau, 1941) that combines London-Van der Waals attraction and electrical double-layer (EDL) repulsion. DLVO forces are very sensitive to salinity and pH due to electrostatic forces depending on the surface electrical potential commonly assumed to be similar to the zeta potential (Sameut Bouhaik et al., 2013). Crystal structure and related electrochemical reactions at the surface of the particle in contact with water are responsible for the dependency of surface electrical potential on water chemistry (Leroy et al., 2022). DLVO forces can be implemented in CFD-DEM by modifying the Lagrangian force balance (Agbangla et al., 2014; Samari-Kermani et al., 2021). Because the DLVO theory is based on the direct collision hypothesis, however, the force and torque caused by collisions are missing. Therefore, if the separation distance between the particles approaches zero, there are numerical singularity problems due to the infinitely attractive DLVO potential. This is a major concern for modeling pore-clogging by aggregation of particles because adhesive contact is not handled properly and can lead to unphysical particle-particle and particle-wall interpenetrations. To circumvent this issue, Abbasfard et al. (2016) introduces a cut-off distance between the surfaces below which DLVO forces vanish. The selection of an adequate cut-off length is challenging because it is system-dependent, and to avoid numerical errors, the particle displacement between time steps should be less than the cut-off distance (Mihajlovic et al., 2020). Another approach uses the Born repulsion – a highly repulsive short-range force – introduced by Ruckenstein and Prieve (1976) to avoid the interpenetration of particle-particle and particle-wall (Muneer et al., 2020; Schumacher and van de Ven, 1987; Liu et al., 2023). Parametrization of the Born repulsion force requires precise knowledge of the system's atomic collision diameter (the finite intermolecular separation distance at which the Lennard-Jones potential associated with Van der Waals interactions is equal

to zero). Moreover, the Born repulsion force becomes dominant if the separation distance is less than 1 nm (Mahmood et al., 2001) which requires small enough time steps to capture particle displacement and to avoid highly non-physical repulsion of the particles in contact. Another possibility is to consider repulsive Stern layers and/or repulsive hydration/steric forces (van Oss, 2006, 2008). Alternatively, the Johnson-Kendall-Roberts (JKR) theory is a physically-rooted adhesion contact model known to predict the contact area accurately (Johnson et al., 1971). JKR theory considers the interaction between surface energy on particles and material surface and does not rely on fitting parameters. It has already been used in some Euler-Lagrange approaches with DLVO theory for simulating fine migration (Trofa et al., 2019; Zhou et al., 2021; Cheng et al., 2023), but not on an unresolved-resolved CFD-DEM four-way coupling. To our knowledge, DLVO and JKR theory had never been coupled to a four-way CFD-DEM approach handling both resolved and unresolved coupling approaches.

Table 3.1: Features of the resolved, semi-resolved (Wang et al., 2019), unresolved and unresolved-resolved CFD–DEM. DNS: direct numerical simulation, FVM: finite volume method.

	Resolved CFD-DEM	Semi-resolved CFD-DEM	Unresolved CFD-DEM	Unresolved-resolved CFD-DEM
Particle surface	Resolved	Not resolved	Not resolved	Resolved for $D_p/\Delta x > 1$ and unresolved for $D_p/\Delta x \leq 1$
Particle-fluid force	Particle-resolved DNS	Drag force model	Drag force model	Combined particle-resolved DNS and drag force model
Background velocity	Fluid velocities resolved in FVM cells	Fluid velocities resolved in neighboring FVM cells	Fluid velocities in the local FVM cell only	Fluid velocities calculated in FVM cells around resolved particles and in local FVM cells for unresolved particles
Particle to cell ratio $D_p/\Delta x$	> 10	$\simeq 1$	$< 1/3$	No restriction

3.2 Computational Model

In this part, we present the new unresolved-resolved four-way coupling CFD-DEM. First, we introduce the CFD approach to model fluid flow in an Eulerian grid (Section 3.2.1). Then, we introduce the DEM approach including long-range interaction forces to simulate the particle displacement in a Lagrangian frame (Section 3.2.2). Finally, we show the strategy to couple CFD and DEM together (Section 3.2.3).

3.2.1 Fluid motion in the CFD Eulerian grid

The Eulerian computational grid is used to solve fluid flow accounting for the presence of the particles. The latter is described by a local porosity field ϵ, defined as,

$$\epsilon = \begin{cases} 1, & \text{if the cell is occupied by fluids only,} \\ ]0,1[, & \text{if the cell contains a fluid-solid aggregate or a fluid-solid interface,} \\ 0, & \text{if the cell is occupied by solids only.} \end{cases} \tag{3.1}$$

The two situations illustrated in Fig 3.1 can exist concomitantly whether the particle diameter is larger or smaller than the cell size. On the one hand, in unresolved cases, particles are smaller than the cell size. A cluster of particles can occupy a computational cell and $\epsilon \in]0,1[$. On the other hand, in resolved cases, the particle is larger than the cell size, and its shadow covers an ensemble of cells. The particle shadow is obtained by a projection on the Eulerian-covered cells identified through a searching algorithm described in Section 3.2.3. In this situation, intermediate values of the phase indicator $\epsilon \in]0,1[$, correspond to the fluid-particle interface. When a cell is fully covered by a particle, we impose a minimum porosity value, $\epsilon_{min} = 0.001$, instead of $\epsilon = 0$ to have flow equations valid everywhere in the computational domain regardless of the cell content (Soulaine et al., 2017).

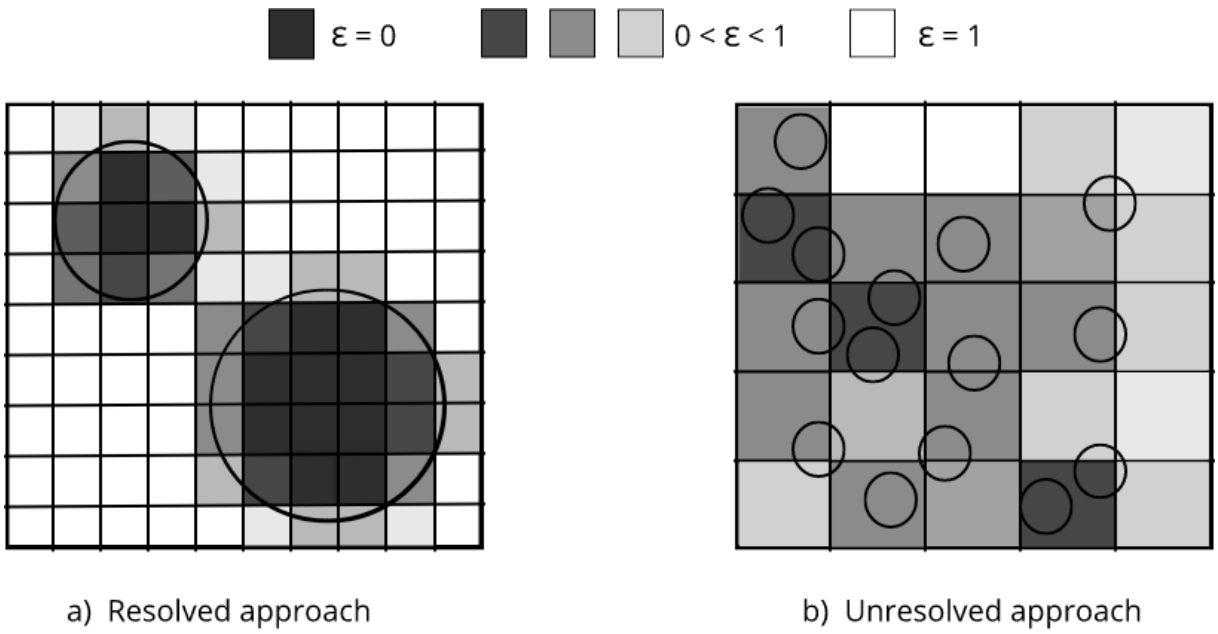

Figure 3.1: Mapping of the porosity field, ϵ, on the Eulerian grid (a) for resolved particles and (b) for unresolved particles.

The fluid motion is modeled by solving incompressible Volume-Averaged Navier-Stokes (VANS) equations (Whitaker, 1996; Zhou et al., 2010). The mass balance equation for the fluid phase reads

$$\frac{\partial(\epsilon\rho_f)}{\partial t} + \nabla.(\epsilon\rho_f \mathbf{v}^f) = 0, \tag{3.2}$$

where ρ_f is the fluid density, and $\mathbf{v}^f$ is the cell-averaged fluid velocity.

The fluid momentum balance equation is:

$$\frac{\partial(\epsilon\rho_f \mathbf{v}^f)}{\partial t} + \nabla.(\epsilon\rho_f \mathbf{v}^f \mathbf{v}^f) = -\epsilon\nabla p + \epsilon\rho_f \mathbf{g} + \epsilon\nabla.(\mu_f(\nabla\mathbf{v}^f + (\nabla\mathbf{v}^f)^\intercal) - \epsilon^2\mu_f(\mathbf{v}^f - \overline{\mathbf{v}}^p)/K, \tag{3.3}$$

where p is pressure, μ_f is the dynamic viscosity, $\mathbf{g}$ is the gravitational acceleration, $\overline{\mathbf{v}}^p$ is the averaged particle velocity on the Eulerian grid, and K is the local cell-permeability. The last term of the right-hand side is a drag force corresponding to the flow resistance due to the presence of particles. $\epsilon^2\mu_f/K$ is the is the interphase drag force coefficient, ξ, defined in Eq (2.12). VANS momentum tends asymptotically towards the Navier-Stokes equation in regions that contain fluid only ($\epsilon = 1$ and the drag force vanishes) and toward Darcy's law in cells containing fluid-solid aggregates ($0 < \epsilon < 1$) because inertia and viscous dissipation are negligible in front of the drag force (Auriault, 2009).

The transition between these two asymptotic behaviors is obtained using a cell-permeability that varies with the cell porosity in a way that $K^{-1} \to 0$ if $\varepsilon = 1$ and to a finite value if $\epsilon < 1$. In the latter case, K is determined differently whether the cell is occupied by resolved or unresolved particles. In resolved cases, particles are seen as low-porosity ($\epsilon = \epsilon_{min}$) low-permeability media and the drag force acts as a penalization term to drop the velocity within the occupied cells near zero value and to approach no-slip condition on the particle-fluid interfaces (Soulaine and Tchelepi, 2016; Angot et al., 1999). In this case, K is calculated using a modified Kozeny-Carman formula (Minto et al., 2019),

$$K = K_0 \frac{\epsilon^3}{(1-\epsilon)^2}, \tag{3.4}$$

where K_0 is a sufficiently low given permeability. In unresolved cases, K is the permeability of the ensemble of particles seen as a porous medium and obtained using the drag forces applied on particles (see section 3.2.2).

3.2.2 Particle motion in the DEM Lagrangian frame

The motion of a cloud of particles is solved in a Lagrangian frame using a four-way coupling Discrete Element Method (DEM). In this approach, the particle flow is driven by interactions with the carrier fluid, and particle-particle and particle-wall interactions. The total velocity, $\mathbf{v}_i^p$, of particle i reads,

$$\mathbf{v}_i^p = \mathbf{U}_i^p + \boldsymbol{\omega}_i \times \mathbf{r}_i, \tag{3.5}$$

where $\mathbf{U}_i^p$ and $\boldsymbol{\omega}_i$ are the translational and the angular velocity of particle i, respectively, and $\mathbf{r}_i$ is the position vector. The description of the translational and rotational motion in DEM is based on Newton's second law applied to a spherical particle of mass m_i and moment of inertia I_i in contact with n_i^c objects (particles and walls). Long-range interaction forces are applied to n_i^{nc} objects (particles and walls) that are not necessarily in contact with particle i but in its close neighborhood. The balance of forces is illustrated in Fig 3.2. We have (Cundall and Strack, 1979):

$$m_i \frac{d\mathbf{U}_i^p}{dt} = \sum_j^{n_i^c} \mathbf{F}_{ij}^c + \sum_j^{n_i^{nc}} \mathbf{F}_{ij}^{nc} + \mathbf{F}_i^f + \mathbf{F}_i^g, \tag{3.6}$$

$$I_i \frac{d\boldsymbol{\omega}_i}{dt} = \sum_j^{n_i^c} \mathbf{M}_{ij}^c + \sum_j^{n_i^{nc}} \mathbf{M}_{ij}^{adh} + \mathbf{M}_i^{hyd}, \tag{3.7}$$

where $\mathbf{F}_i^f$ and $\mathbf{F}_i^g$ are the particle-fluid interactions and gravitational forces acting on particle i at time

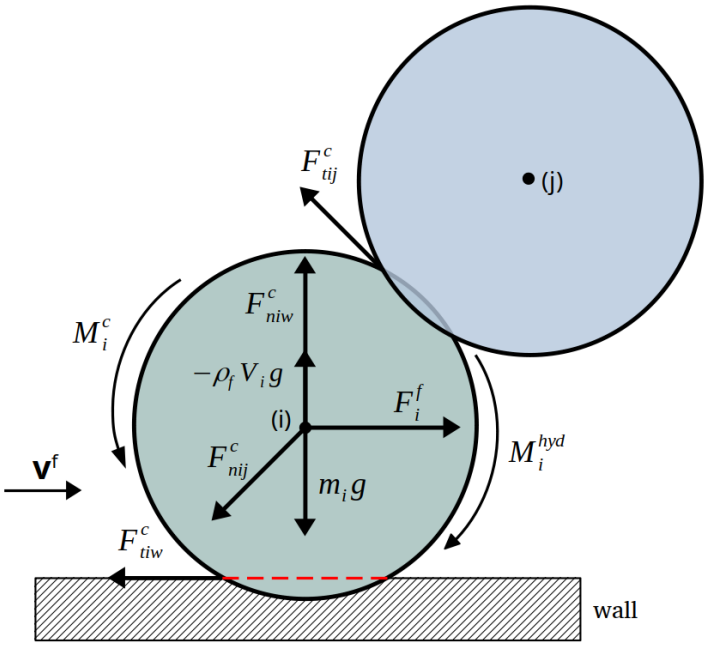

Figure 3.2: Illustration of the forces acting on particle i from contacting particle j and the wall w.

t, respectively. $\mathbf{F}^c_{ij}$, $\mathbf{M}^c_{ij}$ and $\mathbf{M}^{hyd}_i$ are the contact forces, the contact torques, and the hydrodynamic torque acting on particle i, respectively. Long-range interaction forces are considered through $\mathbf{F}^{nc}_{ij}$, the non-contact forces and $\mathbf{M}^{adh}_{ij}$, the adhesive torque acting on particle i in interaction with $j = 1, 2, ..., n^{nc}_i$ objects (particles and walls) at time t, respectively. To reduce the computational costs, we consider that only the objects j (particles and walls) within a kernel centered on the centroid of particle i and with a radius equal to the particle diameter are candidates for particle-particle and particle-wall interactions. If an object j covers a cell that is overlapping with that radius (see Fig. 3.3), the object j is added to the interaction list of particle i, and long-range interaction forces are applied until they collide with each other or move away.

For particulate flow in a charged solution, adsorption of high concentrations of ions and water molecules at its surface creates a viscous thin layer known as the Stern layer (see Fig. 3.4a), where the ion concentration gradient is constant (Leroy et al., 2022). Therefore, the long-range interactions behave differently whether they occur inside or outside the Stern layer. The non-contact forces are, therefore, defined as,

$$\mathbf{F}^{nc}_{ij} = \begin{cases} \mathbf{F}^{DLVO}_{ij}, & \text{if the interactions take place outside the Stern layer,} \\ \mathbf{F}^{JKR}_{ij}, & \text{if the interactions take place within the Stern layer,} \end{cases} \tag{3.8}$$

where $\mathbf{F}^{DLVO}_{ij}$ and $\mathbf{F}^{JKR}_{ij}$ are the DLVO forces and the adhesive JKR force, respectively. All these forces and torques are described in the following.

Hydrodynamic forces

In the four-way approach, the surrounding fluid in contact with a particle creates particle-fluid interactions on the particle i among which the drag, the pressure gradient, the virtual mass, and the lift

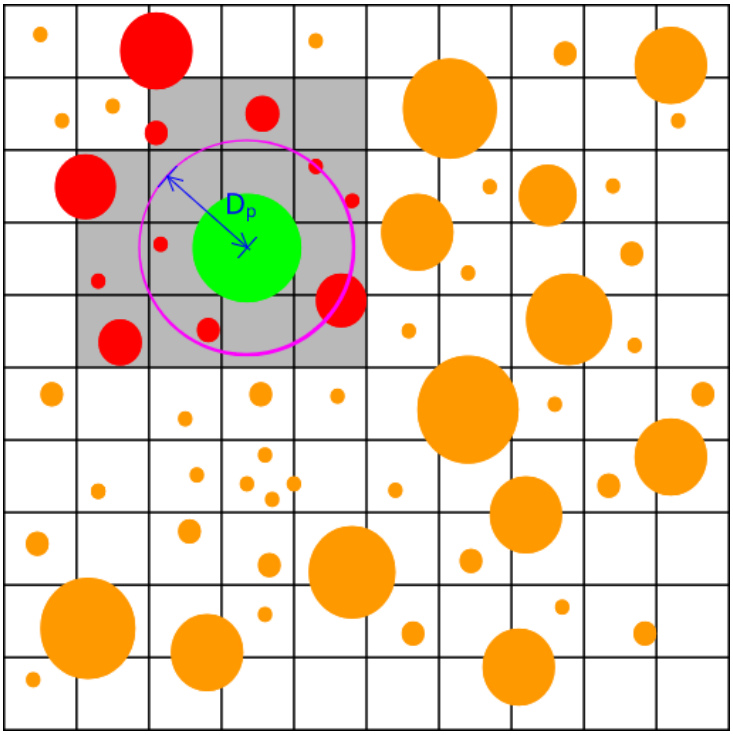

Figure 3.3: The range of interaction of a particle (in green) is determined by a kernel (in purple) centered on the particle centroid and whose radius is equal to the particle diameter. The particles (in red) overlapping cells within this orbit are eligible for collision and long-range interactions.

forces. We only considered the drag force. The drag force applied on particles is calculated through the appropriate porosity-permeability relationship if particles are unresolved and with the summation of the stress divergence terms over the cells containing the particle for resolved coupling. We have,

$$\mathbf{F}_i^f = \begin{cases} V_{p,i}\beta\left(\mathbf{v}^f - \mathbf{v}_i^p\right)\frac{1}{(1-\epsilon)}\ , & \text{if unresolved coupling.} \\ \sum_k^{n^k} V_{c,k}\left(1-\epsilon_k\right)\left(-\rho_f \nabla p_k + \nabla.\boldsymbol{\tau}_k\right), & \text{if resolved coupling.} \end{cases} \tag{3.9}$$

where n^k is the total number of cells covered by the particle, $V_{c,k}$ the volume of cell k, $\boldsymbol{\tau}_k = \mu_f(\nabla \mathbf{v}^f + (\nabla \mathbf{v}^f)^\intercal)$ the fluid shear-rate tensor of cell k, p_k and ϵ_k the fluid pressure and the porosity in cell k, and $V_{p,i}$ the volume of the particle i. The fluid-particle momentum exchange coefficient, β, is defined in Table 3.2.

The gravitational force for a spherical particle considering buoyancy effects reads,

$$\mathbf{F}_i^g = \frac{4}{3}\pi\rho_i R_i^3 \mathbf{g} - \frac{4}{3}\pi\rho_f R_i^3 \mathbf{g} = m_i \mathbf{g}\left(1 - \frac{\rho_f}{\rho_i}\right), \tag{3.10}$$

where ρ_i, is the particle's density and R_i is the particle's radius.

Contact forces

A particle can be in contact with other particles (particle-particle interactions) or with walls (particle-wall interactions). We consider rigid spherical particles, and the contact between two elements is not at a single point but a finite area corresponding to the overlapping of the two objects (O'Sullivan, 2011). The overlapping distance obeys the Hertzian spring-slider-dashpot model (Tsuji et al., 1993; Hertz, 1882)

	β formulation	Description
Stokes law	$\beta = 6\pi\mu_f R_i \frac{(1-\epsilon)}{V_{p,i}}$, and $Re_p = \rho_f \lvert\mathbf{v}^f - \mathbf{v}_i^p\rvert \frac{D_{p,i}}{\mu_f}$	For a single particle with $Re_p < 1$
Kozeny-Carman law	$\beta = 180 \frac{(1-\epsilon)^3}{\epsilon^2} \frac{\mu_f}{D_{p,i}^2}$	For $Re_p < 1$ and dense suspensions
Ergun law (Ergun, 1952)	$\beta = 150 \frac{(1-\epsilon)^2}{\epsilon} \frac{\mu_f}{D_{p,i}^2} + 1.75\,(1-\epsilon)\,\frac{\rho_f}{D_{p,i}} \lvert\mathbf{v}^f - \mathbf{v}_i^p\rvert$	For dense suspensions ($\epsilon < 0.8$) and $Re_p > 1$
Wen and Yu law (Wen and Yu, 1966)	$\beta = \frac{3}{4} C_d \frac{\epsilon(1-\epsilon)}{D_{p,i}} \rho_f \lvert\mathbf{v}^f - \mathbf{v}_i^p\rvert \epsilon^{-2.65}$, with $C_d = \begin{cases} \frac{24}{Re_p}(1 + 0.15 Re_p^{0.687}) & \text{if } Re_p \le 1000, \\ 0.44 & \text{if } Re_p > 1000. \end{cases}$	For dilute suspensions ($\epsilon \ge 0.8$)

Table 3.2: Different formulations of the fluid-solid momentum exchange coefficient β are implemented, where C_d is the drag coefficient, Re_p is the particle Reynolds number, $D_{p,i}$ is the diameter of particle i.

in which the spring realizes the elastic deformation, the dashpot realizes the viscous dissipation, and the slider realizes the frictional dissipation. These effects act on particles through the stiffness k, the damping coefficient η, and the friction coefficient μ. These parameters are based on particle properties including radius, mass, Poisson coefficient, and Young modulus (see Table 3.3). The contact force $\mathbf{F}_i^c$ has two components – a normal and a tangential – described as follows:

(a) Normal component

The normal component of the inter-particle and particle-wall contact ($\mathbf{F}_{nij}^c$) acting on particle i in contact with object j (particle or wall) is given by the sum of the forces related to the spring and dashpot

$$\mathbf{F}_{nij}^c = (-k_{nij} |\boldsymbol{\delta}_{nij}|^{3/2} - \eta_{nij} \mathbf{v}_{ij}^p \cdot \mathbf{n}_{ij}) \mathbf{n}_{ij}, \tag{3.11}$$

where k_{nij} and η_{nij} are respectively the equivalent normal stiffness and damping coefficients of particles i with object j. $|\boldsymbol{\delta}_{nij}|$ is the normal overlapping distance given by,

$$|\boldsymbol{\delta}_{nij}| = \begin{cases} R_i + R_j - |\mathbf{p}_j - \mathbf{p}_i|, & \text{for particle-particle contact,} \\ R_i - |\mathbf{p}_i - \mathbf{p}_w|, & \text{for particle-wall contact,} \end{cases} \tag{3.12}$$

where $\mathbf{p}_i$ is the position vector of particle i. The vector $\mathbf{p}_w$ corresponds to the nearest point to $\mathbf{p}_i$ located on the wall. The relative velocity, $\mathbf{v}_{ij}^p$, is given by $\mathbf{v}_{ij}^p = \mathbf{v}_i^p - \mathbf{v}_j^p$, where for a wall, $\mathbf{v}_j^p$ is the slip velocity of any sphere-wall contact point. The unit vector $\mathbf{n}_{ij}$ points either from the center of particle i to that of particle j in particle-particle contact, or points from the wall to the computational domain and is normal to the wall for particle-wall contact.

(b) Tangential component

The tangential component of the particle-particle and particle-wall forces ($\mathbf{F}_{tij}^c$) acting on particle i depends on the tangential overlap, $\boldsymbol{\delta}_{tij}$, and on the tangential slip velocities, $\mathbf{v}_{tij}^p$, according to

$$\mathbf{F}_{tij}^c = -k_{tij} \boldsymbol{\delta}_{tij} - \eta_{tij} \mathbf{v}_{tij}^p, \tag{3.13}$$

where k_{tij} and η_{tij} are the tangential equivalent stiffness and damping coefficients of particle i with

object j. The formula for the tangential overlap $\boldsymbol{\delta}_{tij}$ for particle-particle and particle-wall contacts is found in Deen et al. (2007). The tangential slip velocities are given by $\mathbf{v}_{tij}^{p} = \mathbf{v}_{ij}^{p} - (\mathbf{v}_{ij}^{p} \cdot \mathbf{n}_{ij})\mathbf{n}_{ij} + (R_i\boldsymbol{\omega}_i + R_j\boldsymbol{\omega}_j) \times \mathbf{n}_{ij}$. Notes that for particle-wall contact with immobile walls, $\boldsymbol{\omega}_j = 0$.

If the relation, $|\mathbf{F}_{tij}^{c}| \geq \mu|\mathbf{F}_{nij}^{c}|$, is satisfied, then particle i is sliding over object j and the tangential force is modeled by Coulomb-type sliding friction,

$$\mathbf{F}_{tij}^{c} = -\mu|\mathbf{F}_{nij}^{c}|\frac{\boldsymbol{\delta}_{tij}}{|\boldsymbol{\delta}_{tij}|}. \tag{3.14}$$

Parameter	Equation
Equivalent normal stiffness	$k_{nij} = \frac{4}{3}\sqrt{r_{ij}}E_{ij}$
Equivalent normal damping coefficient	$\eta_{nij} = \alpha\ \delta_{nij}^{0.25}\sqrt{m_{ij}k_{nij}}$
Equivalent tangential stiffness	$k_{tij} = 8G_{ij}\sqrt{r_{ij}\delta_{nij}}$
Equivalent tangential damping coefficient	$\eta_{tij} = \eta_{nij}$
Equivalent Young modulus	$E_{ij} = \left(\frac{1-\nu_i^2}{E_i} + \frac{1-\nu_j^2}{E_j}\right)^{-1}$
Equivalent shear modulus	$G_{ij} = \left(\frac{2(1+\nu_i)(2-\nu_i)}{E_i} + \frac{2(1+\nu_j)(2-\nu_j)}{E_j}\right)^{-1}$
Equivalent mass	$m_{ij} = \left(\frac{1}{m_i} + \frac{1}{m_j}\right)^{-1}$
Equivalent radius	$r_{ij} = \left(\frac{1}{R_i} + \frac{1}{R_j}\right)^{-1}$

Table 3.3: Parameters for the DEM model. For the equivalent quantities, the case of particle-wall interaction is obtained assuming that the wall has infinite radius and mass. ν is the Poisson's ratio and α is given by the coefficient of elasticity.

DLVO forces

Long-range interactions outside the Stern layer are modeled using the well-established DLVO theory that consists of a combination of an attractive and a repulsive force (see Fig. 3.4b). The first, known as the London-Van der Waals attraction force, is caused by correlations in the fluctuating polarizations of the electron clouds around nearby atoms and molecules. This force is usually described as a combination of the London dispersion force between instantaneously induced dipoles, the Debye force between permanent dipoles and induced dipoles, and the Keesom force between permanent molecular dipoles whose rotational orientations are dynamically averaged over time (Oss et al., 1986). The second, referred to as the electrostatic repulsion force, is related to the interactions between charged surfaces with the generation of a repulsive EDL (when the surface charges of the two interaction surfaces have the same sign) composed typically of a diffuse layer and a Stern layer (see Fig. 3.4a). The diffusive layer – also called the Gouy-Chapman layer – is the region where the ions are distributed under the action of electrical forces and thermal motions. The electrostatic repulsion force occurs between charged objects across liquids and its strength increases with the magnitude of the electrical surface potential commonly considered to be equal to the zeta potential (the electrical potential located at the shear or slipping plane Leroy et al. (2013)).

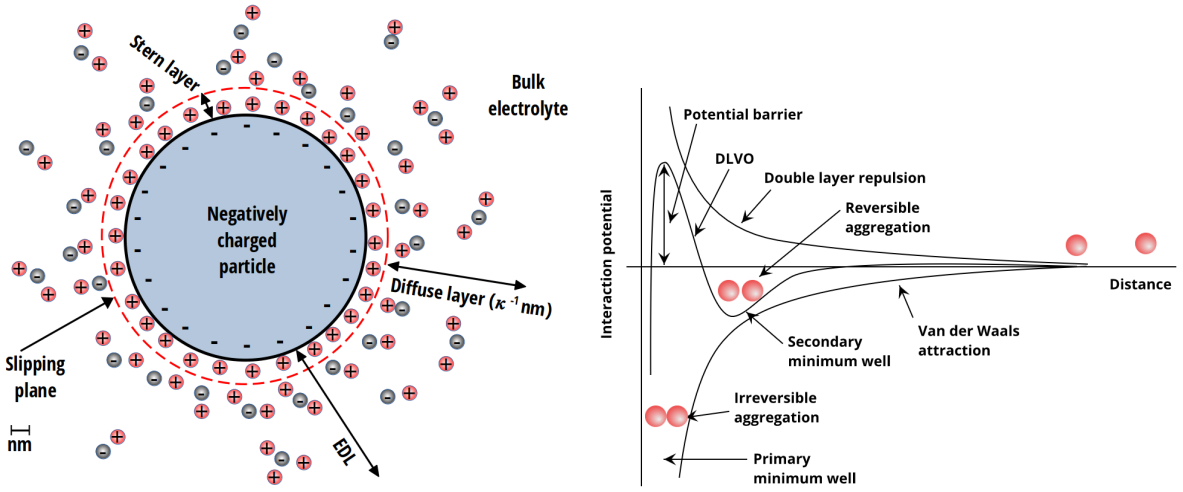

(a) (b)

Figure 3.4: (a) Sketch of the electrical double layer (EDL) around negatively charged particles immersed in a 1:1 electrolyte like NaCl containing Na^+ and Cl^- ions. (b) Typical profile of DLVO potential.

DLVO forces applied on particle i derive from the Van der Waals and electrostatic potentials,

$$\mathbf{F}_{ij}^{DLVO} = -\frac{d}{dh_{ij}}\left(V_{ij}^{VDW} + V_{ij}^{EDL}\right)\mathbf{n}_{ij}, \tag{3.15}$$

where h_{ij} is the smallest surface-to-surface separation distance, $\mathbf{n}_{ij}$ is the unit vector normal to object j surface and pointing to particle i centroid. Particle-particle and particle-wall potentials have different formulations denoted with the superscript "pp" and "pw" in the following.

The Van der Waals attraction potential between two spherical particles with smooth surfaces was approximated in 1937 by Hamaker (1937), (using London's famous equation for the dispersion interaction energy between atoms/molecules as the starting point (London, 1937). It reads,

$$V_{ij}^{VDW_{pp}} = -\frac{A_{iLj}}{6}\left(\frac{2R_iR_j}{d_{ij}^2-(R_i+R_j)^2} + \frac{2R_iR_j}{d_{ij}^2-(R_i-R_j)^2} + \ln\left(\frac{d_{ij}^2-(R_i+R_j)^2}{d_{ij}^2-(R_i-R_j)^2}\right)\right), \tag{3.16}$$

where A_{iLj} is the Hamaker constant of the particle i, the particle j, and the liquid medium L, expressed as $A_{iLj} = A_{ij} + A_{LL} - A_{iL} - A_{jL}$. $d_{ij} = h_{ij} + R_i + R_j$ is the center-to-center separation distance between particles, R_i and R_j are the radius of particle i and particle j, respectively. If the spheres are very close to each other, $h_{ij} \ll R_i, R_j$, and using the equivalent radius, $r_{ij} = R_iR_j/(R_i+R_j)$, the attraction potential becomes,

$$V_{ij}^{VDW_{pp}} = -\frac{A_{iLj}\ r_{ij}}{6h_{ij}}. \tag{3.17}$$

The electrostatic repulsion potential between two spherical charged particles dispersed in a solvent is calculated by (Verwey, 1948),

$$V_{ij}^{EDL_{pp}} = 64\pi\epsilon_0\epsilon_r r_{ij}\left(\frac{k_BT}{Ze}\right)^2 \tanh\left(\frac{Ze\psi_i}{4k_BT}\right)\tanh\left(\frac{Ze\psi_j}{4k_BT}\right)e^{-\kappa h_{ij}}, \tag{3.18}$$

where $\epsilon_0\epsilon_r$ is the dielectric constant of the solvent, ψ_i is the surface potential of the particle i, $\kappa^{-1} = \sqrt{\frac{\epsilon_0\epsilon_r k_BT}{2\times10^3 N_A e^2 I_S}}$ is the Debye screening length corresponding to the EDL thickness for a given electrolyte,

k_B is the Boltzmann's constant, T is the absolute temperature, Z is the valence of the electrolyte, e is the charge of the electron, N_A is the Avogadro's number, and I_S is the electrolyte ionic strength. Eq.(3.18) is based on the constant surface potential approximation (no ion adsorption or condensation on the surface), with the surface potential taken as the potential at the slipping plane. In this paper, we consider particles of identical material which leads to $\psi_i = \psi_j = \psi$. Therefore, the electrostatic potential becomes,

$$V_{ij}^{EDL_{pp}} = 64\pi\epsilon_0\epsilon_r r_{ij}\left(\frac{k_BT}{Ze}\right)^2 \tanh\left(\frac{Ze\psi}{4k_BT}\right)^2 e^{-\kappa h_{ij}}. \tag{3.19}$$

Finally, the particle-particle DLVO force reads,

$$\mathbf{F}_{ij}^{DLVO_{pp}} = \left(-\frac{A_{iLj}\ r_{ij}}{6h_{ij}^2} + 64\pi\epsilon_0\epsilon_r r_{ij}\kappa\left(\frac{k_BT}{Ze}\right)^2 \tanh\left(\frac{Ze\psi}{4k_BT}\right)^2 e^{-\kappa h_{ij}}\right)\mathbf{n}_{ij}. \tag{3.20}$$

To model the long-range interactions between a sphere ($R_i,\ \psi_i$) and a wall ($R_j \to \infty,\ \psi_j$), we use the retarded London-Van der Waals attraction potential (Schenkel and Kitchener, 1960) and the electrostatic repulsion potential proposed by Hogg et al. (1966). The attraction potential reads,

$$V_{ij}^{VDW_{pw}} = -\frac{A_{iLj}R_i}{6h_{ij}\left(1+14\frac{h_{ij}}{\lambda}\right)}, \tag{3.21}$$

where λ is the characteristic wavelength of the interaction (retardation length assumed to be around 100 nm). The retarded London-Van der Waals potential is an adequate approximation for separation distance, h_{ij}, up to $R_i/5$ (Gregory, 1981).

The particle-wall electrostatic repulsion potential based on constant surface potential approximation is,

$$V_{ij}^{EDL_{pw}} = \pi\epsilon_0\epsilon_r R_i\left(\psi_i^2+\psi_j^2\right)\left(\frac{2\psi_i\psi_j}{\psi_i^2+\psi_j^2}\ln\left(\frac{1+e^{-\kappa h_{ij}}}{1-e^{-\kappa h_{ij}}}\right)+\ln\left(1-e^{-2\kappa h_{ij}}\right)\right). \tag{3.22}$$

Finally, the DLVO force for particle-wall interactions is,

$$\mathbf{F}_{ij}^{DLVO_{pw}} = \left(-\frac{A_{iLj}\ R_i\left(1+28\frac{h_{ij}}{\lambda}\right)}{6h_{ij}^2\left(1+14\frac{h_{ij}}{\lambda}\right)^2} + 2\pi\epsilon_0\epsilon_r R_i\kappa\left(\frac{2\psi_i\psi_j e^{-\kappa h_{ij}} - \left(\psi_i^2+\psi_j^2\right)e^{-2\kappa h_{ij}}}{1-e^{-2\kappa h_{ij}}}\right)\right)\mathbf{n}_{ij}. \tag{3.23}$$

Adhesive contact force

DLVO potential has an infinite primary well due to the Van der Waals contribution if the distance between two particle surfaces approaches zero (see Fig. 3.4b). In CFD-DEM, this results in a large inter-penetration of the particles that is unphysical and unrealistic. To avoid the latter and describe accurately adhesive particle contacts, we modified the Hertzian contact (Tsuji et al., 1993; Hertz, 1882) by adding an elastic solid-body behavior based on the Johnson-Kendall-Roberts (JKR) theory (Johnson et al., 1971). This was achieved by modifying the normal overlapping distance $|\boldsymbol{\delta}_n|$ of the spring-slider-dashpot model described above.

In the JKR theory, a sphere in contact with an object (particle or wall) under the action of an external force deforms irreversibly (soft sphere model). It means that a finite contact area remains even if the external force vanishes. The JKR method consists of applying a constant attractive force (see Fig. 3.5b) based on the Derjaguin approximation (Derjaguin and Landau, 1941) when the surface separation distance is smaller than the Stern layer thickness, σ_{St} (a few nanometers maximum). Within

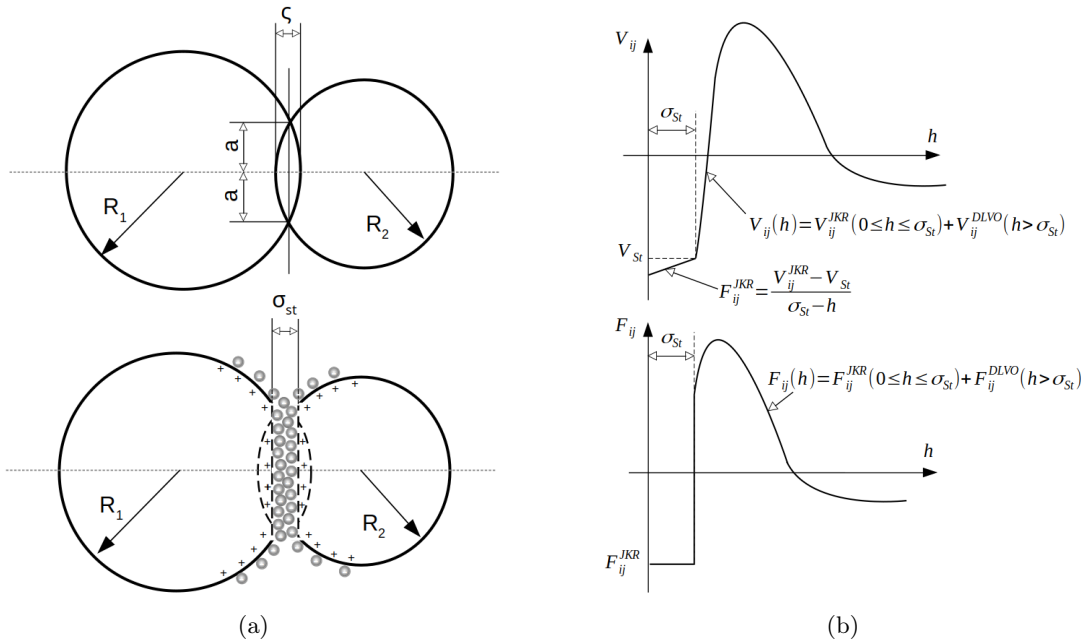

(a) (b)

Figure 3.5: (a) Sketch of the JKR adhesion seen as an overlapping of two elastic spheres. (b) Profile of the potential function and forces including JKR adhesion for distance $0 \leq h_{ij} < \sigma_{St}$.

the Stern layer ($h \leq \sigma_{St}$), the JKR adhesive force of a particle i in interaction with an object j reads (Hong, 1998),

$$\mathbf{F}_{ij}^{JKR} = -\frac{3}{2}\pi r_{ij} W_{iLj} \mathbf{n}_{ij}, \tag{3.24}$$

where $W_{iLj} = \gamma_{ij}^{L} - \gamma_{iL} - \gamma_{jL}$ is the surface energy or adhesion energy, and γ is the interfacial energy.

The JKR adhesive potential is obtained by a linear interpolation between the potential at the wall ($h_{ij} = 0$) and the potential at the slipping plane ($h_{ij} = \sigma_{St}$),

$$V_{ij}^{JKR} = V_{St}^{DLVO} + |\mathbf{F}_{ij}^{JKR}| \left(\sigma_{St} - h_{ij}\right), \tag{3.25}$$

where V_{St}^{DLVO} is the DLVO potential at $h_{ij} = \sigma_{St}$.

The adhesive JKR force acting on particle i is an attractive force that produces a slight overlap, ς, with object j, and, therefore, a finite contact radius a (see Fig. 3.5a). The adhesive overlapping distance and the equilibrium contact radius are given by (Johnson et al., 1971)

$$\varsigma = \frac{a^2}{r_{ij}}, \qquad \text{and,} \qquad a = \sqrt[3]{\frac{6\pi\ r_{ij}^2\ W_{iLj}}{k_{ij}}}, \tag{3.26}$$

where $k_{ij} = \frac{4}{3\pi E_{ij}}$ and $E_{ij} = \left(\frac{1-\nu_i^2}{E_i} + \frac{1-\nu_j^2}{E_j}\right)^{-1}$ are the equivalent elastic constant and the equivalent Young modulus respectively, and ν refer to Poisson ratio. Note that, if object j is a wall ($R_j \to \infty$), then the equivalent radius is $r_{ij} = R_i$.

When the contact appears (i.e. the contact overlap, $|\boldsymbol{\delta}_n| > 0$), two configurations exist in the DEM calculation: *(i)* If $|\boldsymbol{\delta}_n| \leq \varsigma$, the Hertzian contact force is not considered which leads to an elastic attachment of the particle and the object through the adhesive contact. *(ii)* If $|\boldsymbol{\delta}_n| > \varsigma$, then the rigid Hertzian contact force is applied with a new overlap distance as $|\boldsymbol{\delta}_n^*| = |\boldsymbol{\delta}_n| - \varsigma$.

Torques

The torque due to inter-particle and particle-wall contacts acting on a particle i is,

$$\mathbf{M}_{ij}^{c} = R_i \mathbf{n}_{ij} \times \mathbf{F}_{tij}^{c}. \tag{3.27}$$

Rolling is the dominant hydrodynamic mechanism that can cause particle removal from a wall under laminar flow. For an unresolved particle, the hydrodynamic torque is calculated when approaching an object j. For a resolved particle, the hydrodynamic torque is calculated over the cells covered by its shadow. The influence of the hydrodynamic shear on particle i is given by

$$\mathbf{M}_{i}^{hyd} = \begin{cases} 1.4\ R_i \mathbf{n}_{ij} \times \mathbf{F}_{i}^{f}, & \text{if unresolved coupling,} \\ \sum_{k}^{n^k} \mathbf{s}_k \times V_{c,k}\,(1-\epsilon_k)\,(-\rho_f \nabla p_k + \nabla.\boldsymbol{\tau}_k), & \text{if resolved coupling,} \end{cases} \tag{3.28}$$

where $\mathbf{s}_k$ is the position vector relative to the particle center and pointing to the center of the cell k. As the velocity increases with the distance from the obstacle, Torkzaban et al. (2007) pointed out that the drag force effectively acts on the particle at a distance equal to 1.4 R_i.

Adhesion of a particle to a wall or another particle occurs if the distance is within the range of the primary or secondary minimum for the interaction potential. The adhesive physicochemical forces, $\mathbf{F}_{ij}^{JKR}$ and $\mathbf{F}_{ij}^{DLVO}$, involved in the attachment process generate a torque that resists the particle detachment when hydrodynamic forces are applied. The adhesive – or resisting – torque is (Torkzaban et al., 2007),

$$\mathbf{M}_{ij}^{adh} = \begin{cases} a\mathbf{t}_{ij} \times \mathbf{F}_{ij}^{JKR}, & \text{for adhesion at the primary minimum,} \\ l_x \mathbf{t}_{ij} \times \mathbf{F}_{ij}^{DLVO}, & \text{for adhesion at the secondary minimum,} \end{cases} \tag{3.29}$$

where $\mathbf{t}_{ij} = \mathbf{v}_{tij}^{p}/|\mathbf{v}_{tij}^{p}|$ is the tangential unit vector, $\mathbf{v}_{tij}^{p}$ is the tangential slip velocity. In the secondary minimum, the DLVO force characterizes the force acting on a lever arm l_x that must be overcome to detach the particle. Since there is no overlapping area at the secondary minimum, l_x is expressed as, (Torkzaban et al., 2007)

$$l_x = \sqrt[3]{\frac{r_{ij}|\mathbf{F}_{ij}^{DLVO}|}{4k_{ij}}}. \tag{3.30}$$

3.2.3 CFD-DEM coupling strategy and numerical implementation

The unresolved-resolved four-way coupling CFD-DEM is implemented within the open-source finite-volume toolbox OpenFOAM version 9 (https://www.openfoam.org). Our implementation is built on top of the existing *dpmFoam* solver coupled with the OpenFOAM's internal DEM package to simulate dense or dilute particle packing. The algorithmic procedure is illustrated in Fig. 3.6. *dpmFoam* has strong limitations for simulating particle transport in porous media at the pore-scale. First, it uses an unresolved approach. Second, numerical instabilities occur when particles cross the Eulerian cell faces. In addition to the DEM model in which we implemented the unresolved-resolved hydrodynamic drag and torque described in Section 3.2.2: *(i)* we developed an efficient searching algorithm to identify the Eulerian cells covered by the shadow of the resolved particles (Sec. 3.2.3.a), *(ii)* we implemented a velocity-pressure solution algorithm free of numerical errors when a particle centroid crosses a cell face (Sec. 3.2.3.b), and *(iii)* we constrained the time-stepping with appropriate stability criteria (Sec. 3.2.3.c).

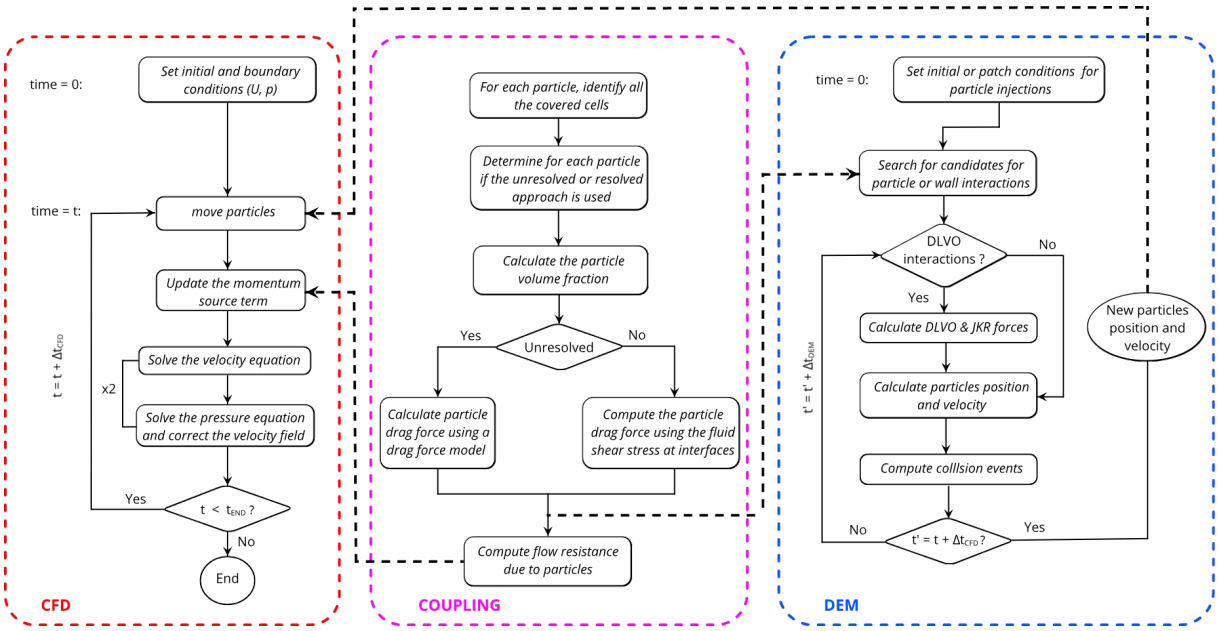

Figure 3.6: Detailled flowchart for the unresolved-resolved four-way coupling CFD–DEM numerical procedure including colloidal forces.

Mapping the resolved/unresolved local porosity: searching strategy of covered cells

A key aspect of the CFD-DEM coupling is the projection of the particle presence onto the Eulerian grid. In unresolved cases, the particle is smaller than the grid size and the local porosity is lower than 1. In a resolved case, the particle shadow covers an ensemble of cells. In both cases, the local porosity within a cell is obtained by calculating the sum of each volume of particle contained in the cell using

$$\epsilon = 1 - \frac{\sum_j \Delta V_{p,j}}{V_c}, \tag{3.31}$$

where $\Delta V_{p,j}$ is the volume of each particle j contained within the cell, and V_c is the cell volume. In CFD-DEM, the cell label in which a particle centroid is located is an attribute of the particle. This attribute changes if the particle moves to a neighboring cell. Other attributes include particle mass and diameter. Therefore, in unresolved cases, if the particle is not overlapping two or more cells, then the volume of particles within computational cells is known and the mapping operation is straightforward.

In resolved coupling ($D_p > \Delta x$) and in unresolved coupling with particle overlapping 2 or more cells, however, the cells covered by the particle shadow have to be identified by a searching algorithm knowing the particle position and diameter. The process of identifying all the cells covered by the particles can highly impact the computational cost if a search method such as traversal search (going individually through all the cells of the Eulerian grid) is used, in particular, if the numbers of particles and grid cells are extremely large. Here, we present a peer-to-peer search algorithm whose objective is to identify efficiently the cells neighboring any given cell up to a certain distance.

An example of the peer-to-peer algorithm applied to a two-dimensional 4×4 regular grid is shown in Fig. 3.7a-d. The black points represent the cell centers. The cell containing the particle centroid is identified as the starting cell (step 0) depicted with the black empty circle. The search algorithm is as follows:

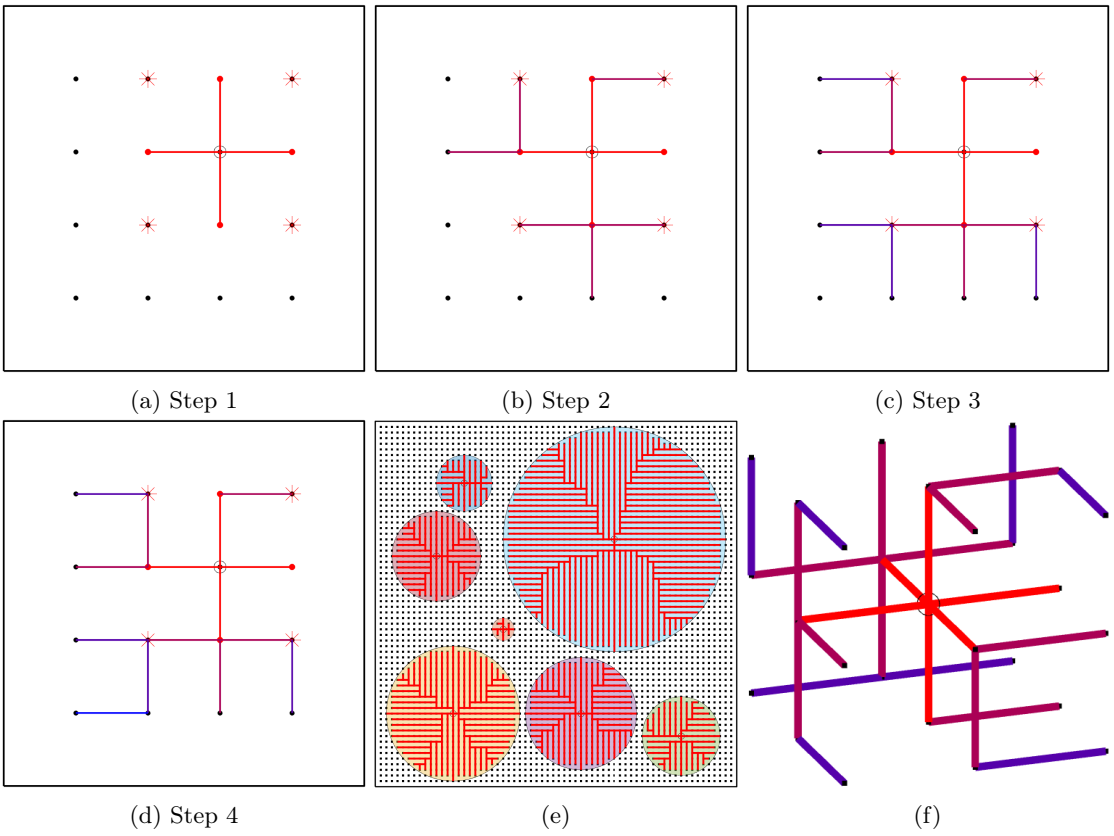

(a) Step 1 (b) Step 2 (c) Step 3

(d) Step 4 (e) (f)

Figure 3.7: Principle of the peer-to-peer search algorithm. (a)–(d) Illustrations of the steps for searching nearby grid points in a two-dimensional 4×4 grid. Points correspond to cell centers. Lines correspond to the path to a newly identified cell. Their color changes gradually at each iteration. From an initially identified cell (black empty circle), the algorithm searches for cells adjacent to the newly identified cells, and iterates. (e) The peer-to-peer search is an efficient way to identify cells covered by particles. The red lines describe the path the algorithm took to research covered cells. (f) The peer-to-peer search also works in three-dimensional structured and unstructured grids – here, a $3 \times 3 \times 3$ regular domain.

- Step 1: Identification of the cells adjacent to the starting cell (Neumann neighborhood in red points).

- Step 2: Identification of the cells adjacent to the newly identified cells. The algorithm ignores a cell previously identified to avoid duplicates. In the 4×4 grid example, we see that the 4 cells in the square lattice surrounding the starting cell (Moore neighborhood in red stars) are now identified.

- Step ≥ 3: Repeat the identification of the cells adjacent to the newly identified cells until the grid is mapped.

Notes that to find all the neighboring cells (Neumann and Moore points) of a starting cell using the peer-to-peer search, it takes only 2 steps in 2D and 3 steps in 3D (Fig. 3.7f) for both structured and unstructured grids.

To search the cells covered by particles, two rules are necessary to unmark newly identified cells: *(i)* the particle-to-cell-center distance is greater than the particle radius, *(ii)* the intersection point between the particle surface and the particle-to-cell-center line is outside the cell. Eventually, the algorithm has marked all the cells covered by particles including the particle-fluid interfaces as shown in Fig 3.7e.

Solution strategy for solving VANS equations in CFD

In this part, we describe our solution strategy for solving the Volume-Averaged-Navier-Stokes equations using the Finite-Volume Method. The system has three unknown variables solved on a collocated grid, namely the void fraction, ϵ, the fluid pressure, p, and the fluid velocity, $\mathbf{v}^f$. The void fraction results from the projection of the particle shadow onto the grid. The pressure-velocity coupling is solved using a semi-implicit time integration scheme adapted from the Pressure Implicit with Splitting of Operators (PISO) algorithm developed by Issa (1986).

A known issue in CFD-DEM coupling is the presence of numerical instability on the velocity profile when the centroid of the particle is crossing a cell boundary (Marshall and Sala, 2013; Peng et al., 2014). A way to stabilize the particle-fluid coupling is to smooth ϵ after its mapping on the computational grid (Pirker et al., 2011). We use an isotropic diffusive smoothing controlled by the smoothing length λ_s. This is achieved using the parabolic filter:

$$\frac{\partial \epsilon}{\partial t} = \nabla^2 \left(\frac{\lambda_s^2}{\Delta t_{CFD}} \epsilon \right), \tag{3.32}$$

where Δt_{CFD} is the time step used to solve Eqs. (3.2) and (3.3). A smoothing length of $\lambda_s \leq D_p/10^{-3}$ is found necessary to improve the stability of the simulations.

The pressure-velocity coupling is solved by forming a pressure equation from the continuity equation, Eq. (3.2), and a semi-discrete form of the momentum equation, Eq. (3.3). The latter is obtained using a forward Euler time integration between two successive times $n+1$ and n for each cell. We obtain,

$$\epsilon \frac{\mathbf{v}_C^{n+1} - \mathbf{v}_C^n}{\Delta t_{CFD}} = -a'_C \mathbf{v}_C^{n+1} + \sum_{NC} a'_{NC} \mathbf{v}_{NC}^{n+1} + \frac{\epsilon^2 \mu_f}{K} \mathbf{v}^p - \epsilon \nabla p^{'}, \tag{3.33}$$

where the subscript C indicates the cell owner and NC the neighboring cells. The coefficients a'_C and a'_{NC} are the diagonal and off-diagonal coefficients of the space discretization of the momentum equation that includes advection and viscous dissipation effects. The pressure variable $p^{'}$ divided by the fluid density, corresponds to the actual pressure including the hydrostatic pressure as $\nabla p^{'} = \frac{1}{\rho_f}(-\rho_f \mathbf{g} + \nabla p)$.

The semi-discrete momentum equation can be recast into,

$$a_C \mathbf{v}_C^{n+1} = H(\mathbf{v}) - \epsilon \nabla p^{'}, \tag{3.34}$$

where $a_C = \left(\frac{\epsilon}{\Delta t_{CFD}} + a'_C \right)$ is the diagonal coefficients of the matrix for the velocity, and,

$$H(\mathbf{v}) = \sum_{NC} a'_{NC} \mathbf{v}_{NC}^{n+1} + \left(\frac{\epsilon}{\Delta t_{CFD}} \right) \mathbf{v}_C^n + \frac{\epsilon^2 \mu_f}{K} \mathbf{v}^p, \tag{3.35}$$

contains the off-diagonal coefficients and the source terms. Finally, the pressure equation is formed from the combination of the fluid mass balance equation (Eq. 3.2 divided by the fluid density), the parabolic filter (Eq. 3.32), and the semi-discretized momentum (Eq. 3.34 divided by a_C),

$$\nabla . \left(\frac{\epsilon^2}{a_C} \nabla p^{'} \right) = \nabla . \left(\frac{\epsilon H(\mathbf{v})}{a_C} \right) + \nabla^2 \left(\frac{\lambda_s^2}{\Delta t_{CFD}} \epsilon \right). \tag{3.36}$$

PISO is a predictor-corrector scheme for solving pressure-velocity coupling. Within a time step, the procedure is as follows. *(i)* Solve the discretized momentum equation (Eq. 3.33) to compute a predicted velocity field, $\mathbf{v}^*$, for given boundary conditions and the pressure field, p^k calculated at the previous

time step. At this stage, the resulting guessed velocity does not satisfy the mass conservation. *(ii)* Solve the pressure equation (Eq. 3.36) and guess the pressure field, p^{**}. *(iii)* Get the corrected velocity field using Eq. 3.34 and p^{**}. *(iv)* Update the boundary conditions. *(v)* Repeat the steps 2 to 5 for at least 2 iterations (Issa, 1986). At the end of these steps, you get the velocity, $\mathbf{v}^{k+1}$, and pressure fields, p^{k+1}, for the next time-step.

Time-stepping stability criteria

Three numerical stability criteria are necessary for the fluid-particle coupling model proposed in this work: *(i)* a criterion for the pressure-velocity coupling algorithm, *(ii)* a constraint due to the calculation of colliding particles, and *(iii)* a stability criterion related to the fluid-particle interactions.

The PISO-like pressure-velocity algorithm for solving the VANS equations is not unconditionally stable and the time integration, Δt_{CFD}, is limited by a Courant-Friedrich-Lewy (CFL) condition (Ferziger et al., 2020; Courant et al., 1928),

$$CFL = \Delta t_{CFD}\ max\left(\frac{|\mathbf{v}^f|}{\Delta x}\right) < 1, \tag{3.37}$$

where Δx is the cell size.

As the constraints on the particle dynamics are stronger than the fluid flow, we use sub-cycling of Δt_{DEM} within the CFD time-step to capture particle collision events accurately (see Fig. 3.8). The DEM time-step requirements to capture the particle-particle and particle-wall collisions is the minimum of the particle relaxation time $\left(\tau_p = \frac{D_p^2 \rho_p}{18\mu_f}\right)$ and a portion of the Rayleigh time T_{Ra} (Thornton and Randall, 1988; Burns et al., 2019). The latter corresponds to the time a shear wave takes to propagate through a solid particle (Li et al., 2005). The time-step criterion for DEM reads,

$$\Delta t_{DEM} = \min(\alpha_t T_{Ra}, \tau_p) \quad \text{with} \quad T_{Ra} = \frac{\pi D_p}{2\,\Gamma}\sqrt{\frac{\rho_p}{G}}, \tag{3.38}$$

where α_t is a chosen constant lower than 1, $G = E/4(2-\nu)(1+\nu)$ is the equivalent shear modulus with E being the Young modulus, ν the Poisson ratio, and Γ is a coefficient approximated by $\Gamma = 0.1631\nu + 0.8766$ (Li et al., 2005).

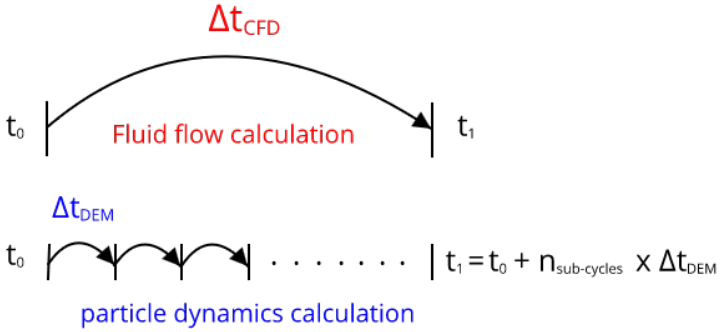

Figure 3.8: Temporal evolution for the fluid flow calculation compared to that of the particle dynamics calculation.

The stability of the unresolved coupling results from the impact of the fluid-solid interaction on the DEM equations of each particle though the drag force is linked to the particle relaxation time. By

assuming an explicit scheme on the source term integration, the coupling stability criterion is defined as :

$$\Delta t_c \leq \frac{4}{3}\frac{D_p}{C_d}\frac{\rho_p}{\rho_f}\frac{1}{|\mathbf{v}^f - \mathbf{v}_i^p|} \ . \tag{3.39}$$

In practice, Δt_{CFD} is taken as $\min(\Delta t_{CFD}, \Delta t_c)$ and is, therefore, satisfying both Eq. (3.37) and Eq. (3.39).

3.3 Model Verifications

In this section, we present test cases to verify the robustness and efficiency of the unresolved-resolved four-way coupling CFD-DEM. First, we analyze the efficiency of our search algorithm for mapping the covered cells (Section 3.3.1). Second, we verify the implementation of the resolved-unresolved momentum exchange term (Section 3.3.2). Third, we assess the accuracy of our model in the case of a steel ball sedimenting in a water tube for which experimental data exists (Section 3.3.3). Fourth, we verify the implementation of DLVO forces using test cases for which we derived semi-analytical solutions (Section 3.3.4). Then, we verify the coupling physics between the unresolved-resolved CFD-DEM model itself and the DLVO forces through the formation of particle aggregates or clusters (Section 3.3.5).

3.3.1 Searching algorithm efficiency analysis

We compare the time efficiency of our peer-to-peer search algorithm with the most frequently-used searching strategies, namely, the traverse search, the tree search (quadtree for 2D and octree for 3D) (Hernquist and Katz, 1989), and the linked-list search such as the Hilbert curve search (Monaghan, 1985; Jagadish, 1997). In traditional traverse search, the computation time is devoted to traversing all the cells of the domain, which can become very important with a large number of cells and particles. Tree search continuously divides the current domain into 8 parts until it has no overlapping with the neighborhood area or it only contains one cell. Linked-list search organizes all the cells with the advantage of positioning spatially adjacent cells close to each other in the form of a linked list and then searching for it. The peer-to-peer search belongs to the family of linked-list search. Supposing that there are N cells and N particles in the domain, the time cost of traverse search, octree search, and Hilbert curve search are $O(N^2)$, $O(N \log N)$, and $O(N)$, respectively (Wang et al., 2019).

The benchmark setup and data come from Wang et al. (2019). In this test case, the cells covered by particles are sought through traverse, octree, and Hilbert searching strategies. Particles of 1cm diameter are placed randomly in a regular grid made of 1 cm $\times$ 1 cm $\times$ 1 cm cubic cells. Because the cell and particle center coordinates do not match, a particle can overlap up to 8 cells. Two test cases are considered. First, we investigate the efficiency of the algorithms for an increasing number of particles in a 10 cm $\times$ 10 cm $\times$ 100 cm grid (i.e. 10^4 cells). Second, we compare their efficiency for a fixed number of 10^4 particles within a domain whose size varies from 10 cm $\times$ 10 cm $\times$ 50 cm (i.e. 5×10^3 cells) to 10 cm $\times$ 10 cm $\times$ 500 cm (i.e. 5×10^4 cells). In each case, the simulation is run for 100 iterations.
We see in Fig. 3.9b and Fig. 3.9a that the peer-to-peer search efficiency is comparable to the Hilbert curve search when the number of cells increases (time cost of $O(N)$) and to the octree search when the particle number increases (time cost of $O(N \log N)$). In both cases, it is more efficient than the traverse search. One of the advantages of the peer-to-peer search is the easy implementation of the algorithm regardless of the structure of the mesh.

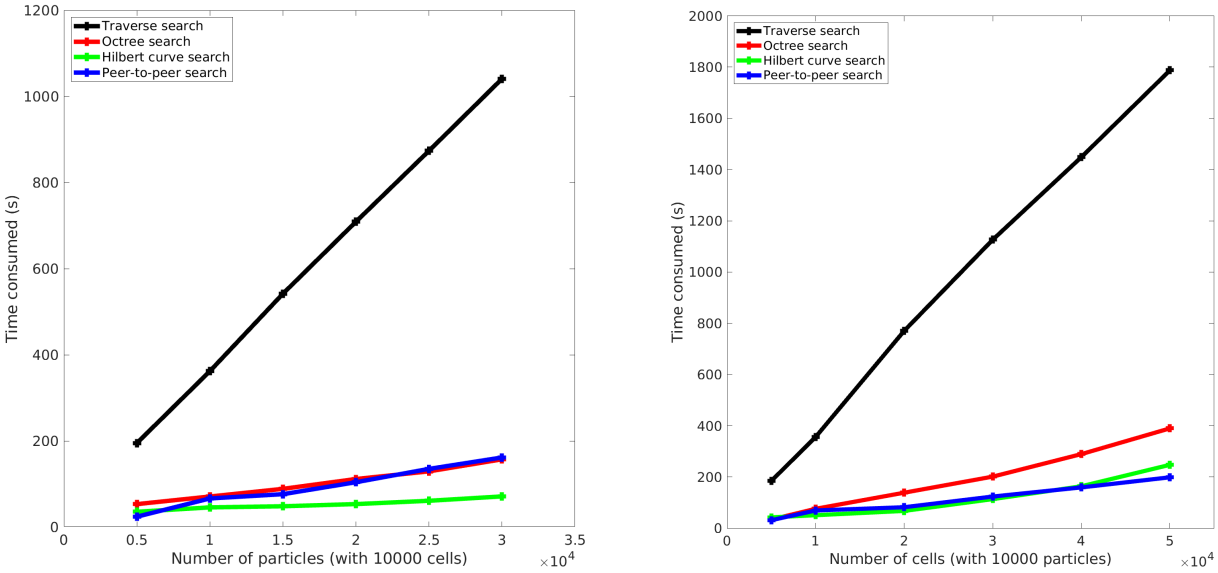

Figure 3.9: Efficiency of the peer-to-peer search compared with the traverse, octree, and Hilbert curve search results taken from Wang et al. (2019). (a) Efficiency for an increasing number of particles in a case with 10000 cells. (b) Efficiency for an increasing number of cells in a case with 10000 particles.

3.3.2 Fluid flow around a stationary spherical particle

The purpose of this section is to verify the implementation of the resolved drag force acting on both the particle (in DEM) and the fluid (in CFD). In resolved cases, the mutual drag between the fluid and the particle is not modeled by constitutive laws but it is an output of the simulation. Here, we run two sets of simulations to verify that: *(i)* in CFD, the fluid velocity profile around a resolved particle is accurate, *(ii)* in DEM, the drag applied to the particle is correct.

First, we consider a single stationary particle of diameter $D_p = 10$ μm located in the middle of a 50 μm $\times$ 50 μm square domain. The inlet is on the left-hand side and the outlet is on the right. A constant velocity $v_0 = 10^{-3}$ m/s ($Re_p = 0.01$) is applied at the inlet and the pressure is set to zero at the outlet. Lateral boundaries are set as walls with no-slip conditions. In CFD-DEM simulations, we use regular grids with different levels of refinement defined as the ratio of the particle diameter D_p to the smallest cell size Δx_{min} as illustrated in Fig. 3.10b-d. The cells mapping the particle presence are penalized according to Eq. (3.4). A reference solution, denoted "CFD" hereafter, is obtained by solving the incompressible Navier-Stokes equations (using the so-called *simpleFoam* OpenFOAM solver) on a refined conformal grid $\left(\frac{D_p}{\Delta x_{min}} = 40\right)$ in which no-slip condition is applied at the particle surface (see Fig. 3.10a). The velocity profile along the vertical axis that crosses the particle center is plotted in Fig. 3.11 for the x and y components. We observe a good agreement of the CFD-DEM with the reference CFD solution, especially for resolutions > 3.

Second, we focus on the calculated drag force acting on the particle surface. The simulation setup is similar to the first case, except that the square box is larger, corresponding to $80D_p \times 80D_p$, to avoid boundary effects, and that the particle-fluid interface is resolved through a local mesh refinement as shown in Fig. 3.12. The level of refinement at the vicinity of the particle corresponds to $\frac{D_p}{\Delta x_{min}} = 3, 5,$ and 7, respectively. The inlet velocity, v_0, is set such that the Reynolds number varies from 0.001 to 100. In Fig. 3.13, we compare the resultant drag coefficient, C_d, with the empirical model proposed by Schiller

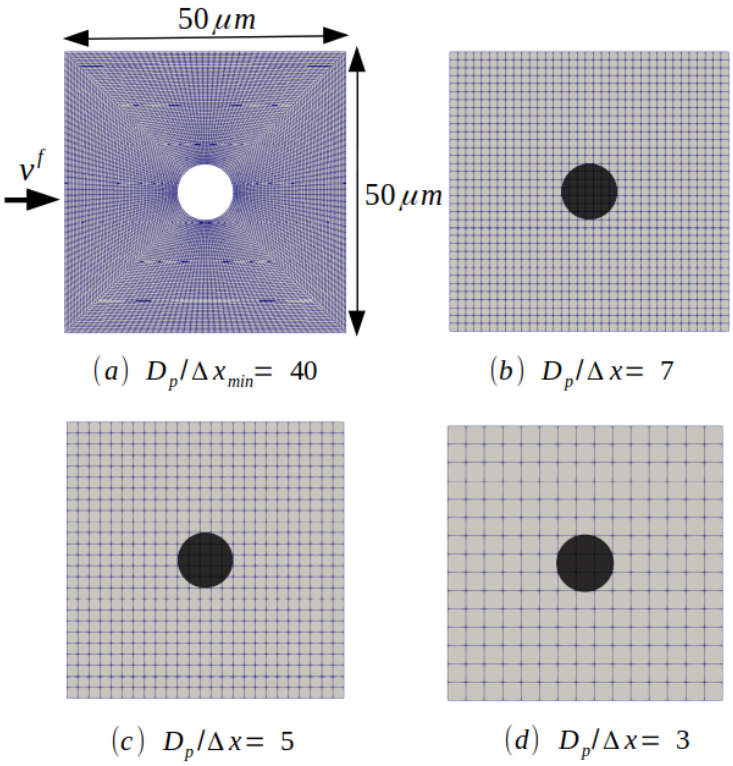

Figure 3.10: Schematic representation of the flow past a stationary single particle, (b)-(d) CFD-DEM approach with different mesh resolution, and (a) CFD approach.

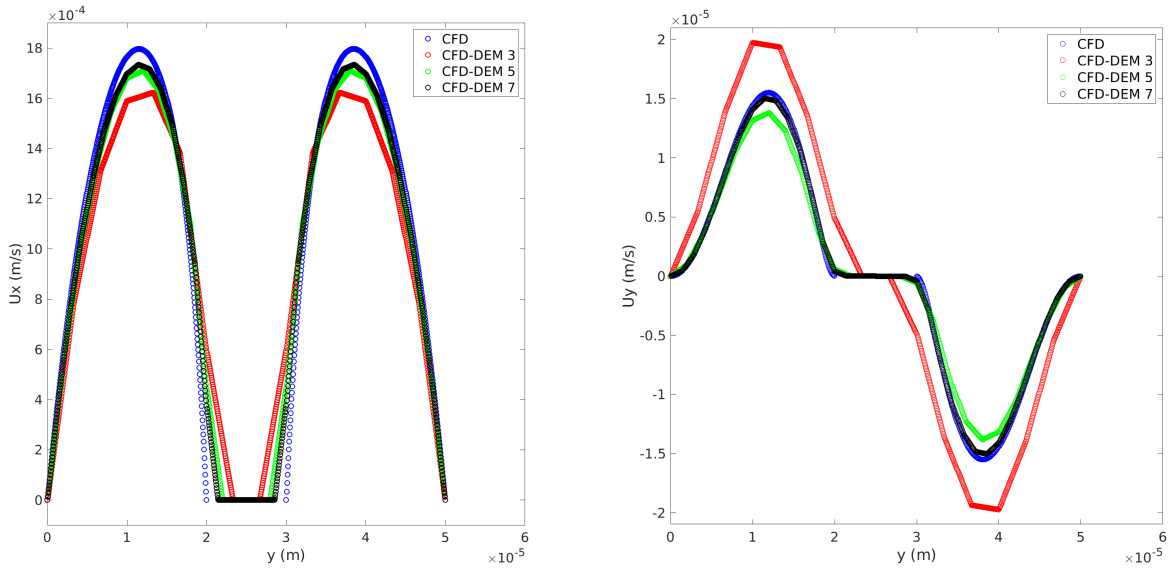

(a) (b)

Figure 3.11: (a) and (b), comparison of fluid velocity components U_x and U_y between results obtained from the model and a steady CFD solver of OpenFOAM (simpleFoam) calculated at the vertical line passing by the particle centroid.

and Naumann (1935) which is used as a reference solution (the values come from Nguyen et al. (2021)). It is calculated using $C_d = \frac{2|\mathbf{F}_d|}{\rho_f v_0^2 A_p}$ where $\mathbf{F}_d$ is the drag force acting on the particle in DEM calculated using Eq. (3.9), and A_p is the particle surface projected on the Eulerian grid. We observe a very good

agreement between the drag coefficient calculated with our resolved CFD-DEM model and the reference solution.

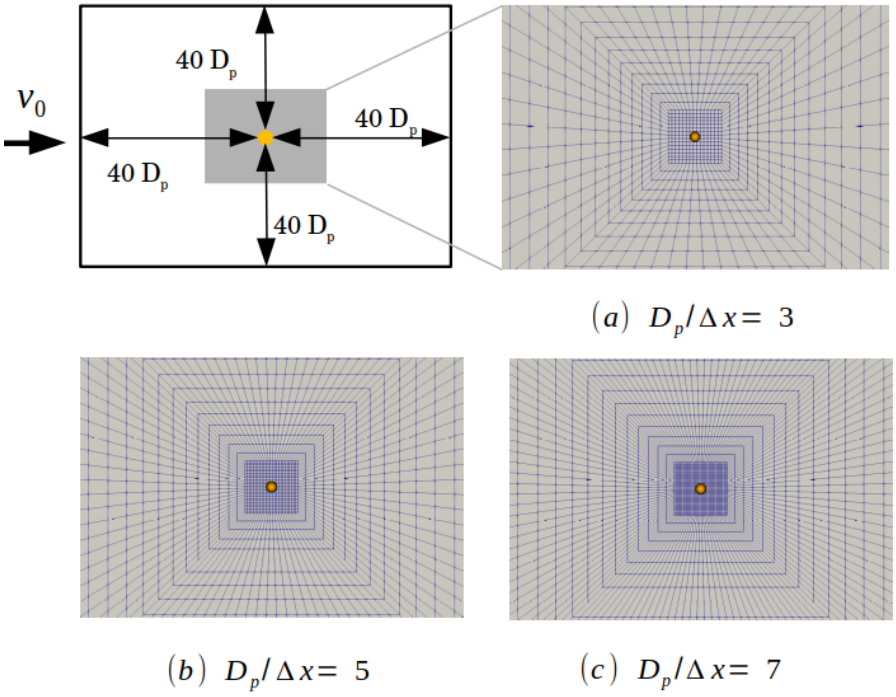

Figure 3.12: Shematic representation of the domain, with (a)-(c) the local meshes refinement.

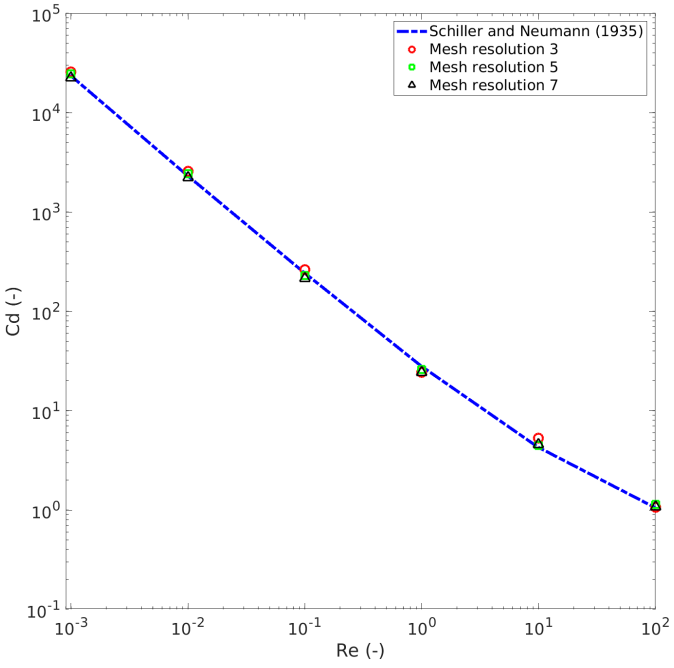

Figure 3.13: Comparison between the drag coefficient obtained with the unresolved-resolved CFD-DEM model and the empirical data of Schiller and Naumann (1935).

These simulations highlight the accuracy of the calculation of the drag force in our resolved CFD-DEM both from the CFD and the DEM sides. They also document the optimal mesh refinement in resolved

CFD-DEM.

3.3.3 Sedimentation of a steel ball in a water tube

In this test case, we simulate the sedimentation of a steel ball in a water tube and compare the results with the experimental data of Allen (1900). The experiment consists of a 3.18 mm diameter steel (density of 7820 kg/m^3) bead falling by gravity in a 11.5 cm long, 3 cm wide, and 28 cm high rectangular water tube. The fall of the particle initially placed at the top center of the domain without initial velocity is simulated using the unresolved-resolved CFD-DEM coupling on different mesh resolutions $\left(\frac{D_p}{\Delta x} = \frac{1}{3}, \frac{1}{2}, 1, 2, 3\right)$. The results are also compared with the prediction made by the unresolved CFD-DEM solver of OpenFOAM (*denseParticleFoam*) for $\frac{D_p}{\Delta x} = 1$ (which corresponds to a $33 \times 9 \times 88$ regular grid).

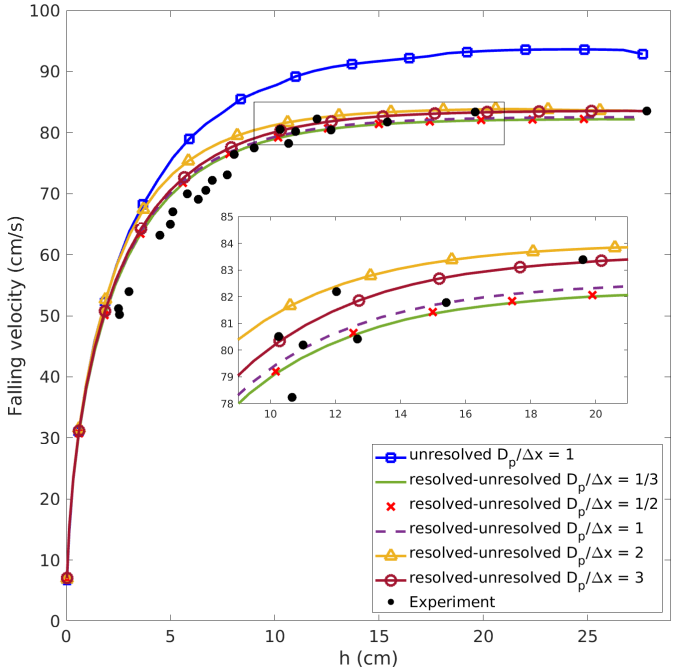

Figure 3.14: Comparison of the falling velocity obtained with unresolved CFD–DEM coupling on $D_p/\Delta x = 1$, with the resolved-unresolved CFD-DEM coupling on different mesh resolutions.

We see in Fig. 3.14 that the unresolved-resolved solver predictions are very close to the experimental value for both the resolved $\left(\frac{D_p}{\Delta x} > 1\right)$ and unresolved $\left(\frac{D_p}{\Delta x} \leq 1\right)$ cases. The terminal particle velocity calculated by the standard OpenFOAM unresolved CFD-DEM solver, however, does not match the reference data. These simulations highlight the ability of the hybrid CFD-DEM model to capture accurately the particle trajectory regardless of the mesh resolution.

3.3.4 Verification of the implementation of DLVO forces

Particle-particle DLVO interactions

We consider two identical particles of density $\rho_p = 1050$ kg/m^3 (lower than the average density of minerals around $2500 - 3000$ kg/m^3), radius $R_1 = R_2 = R = 1$ μm, and mass $m = 4.4 \times 10^{-15}$ kg initially separated from each other by h_0 as presented in Fig. 3.15. Both particles are initially immobile and immersed in a brine (water + $NaCl$) solution. Table 3.4 summarizes particle and fluid properties. There is no flow, and the drag and sedimentation forces are neglected so that only the DLVO forces are involved

in the particle displacement. The evolution of the surface-to-surface separation distance, $h(t)$, is computed using our CFD-DEM approach in pure attraction, pure repulsion, and mixed attraction-repulsion. Results are compared with semi-analytical solutions that are derived in the following.

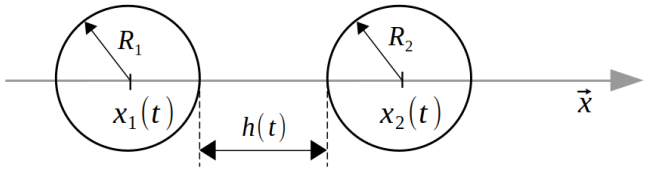

Figure 3.15: Representation of the two particles distant from h.

Parameters	Particle-Particle	Particle-Wall
Hamaker constant A	6.3×10^{-20} J	0.1×10^{-20} J
Surface electrical potential ψ	-58 mV	-52.3 mV
Inverse Debye length κ	1.05×10^{8} m^{-1}	
Relative permittivity ϵ_r	78.2	
Salinity [NaCl]	1 mM	
Temperature T	298 K	

Table 3.4: Fluid, wall, and particle properties used in the model verification simulations (Yu et al., 2017).

The CFD-DEM computational domain is a 50 μm $\times$ 50 μm square with a regular grid cell size of 1 μm $\times$ 1 μm. We use $\Delta t = 2.5 \times 10^{-6}$ s and $h_0 = 2$ μm in the attraction and mixed attraction-repulsion cases, and $\Delta t = 10^{-8}$ s and $h_0 = 0.04$ μm for the repulsive case.

Alternately, the evolution of the separation distance can also be solved using Ordinary Differential Equations (ODE). Indeed, from Eq. (3.6) and Eq. (3.20), the particle motion is governed by

$$\begin{cases} m\frac{d^2x_1}{dt^2}\vec{x} = \frac{AR}{12h^2}\vec{x} - \frac{R}{2}\kappa B e^{-\kappa h}\vec{x}, \\ m\frac{d^2x_2}{dt^2}\vec{x} = -\frac{AR}{12h^2}\vec{x} + \frac{R}{2}\kappa B e^{-\kappa h}\vec{x}, \end{cases} \tag{3.40}$$

where $x_1(t)$ and $x_2(t)$ denote the position of the two particles, and $B = 64\pi\epsilon_0\epsilon_r \left(\frac{k_B T}{Ze}\right)^2 tanh\left(\frac{Ze\psi}{4k_B T}\right)^2$. Therefore, the evolution of the surface-to-surface separation distance, $h(t) = x_2(t) - x_1(t) - 2R$, reads

$$h^2 e^{\kappa h} h'' = \frac{R}{6m}\left(6\kappa B h^2 - A e^{\kappa h}\right) \text{ for mixed attraction-repulsion,} \tag{3.41}$$

where $h''(t) = \frac{d^2h(t)}{dt^2}$. This ODE can be simplified for pure attraction and pure repulsion. On the one hand, for pure attraction, $B = 0$ and Eq. (3.41) becomes,

$$h^2 h'' = -\frac{AR}{6m}, \quad \text{for pure attraction.} \tag{3.42}$$

On the other hand, for pure repulsion, $A = 0$ and we have,

$$e^{\kappa h} h'' = \frac{\kappa B R}{m}, \quad \text{for pure repulsion.} \tag{3.43}$$

These three ODEs are solved numerically using MATLAB high-order method for solving non-stiff differential equations – *ode89* –, with absolute and relative tolerance of 10^{-10} and 10^{-8} respectively. The ODE results are used as reference solutions to compare with CFD-DEM predictions.

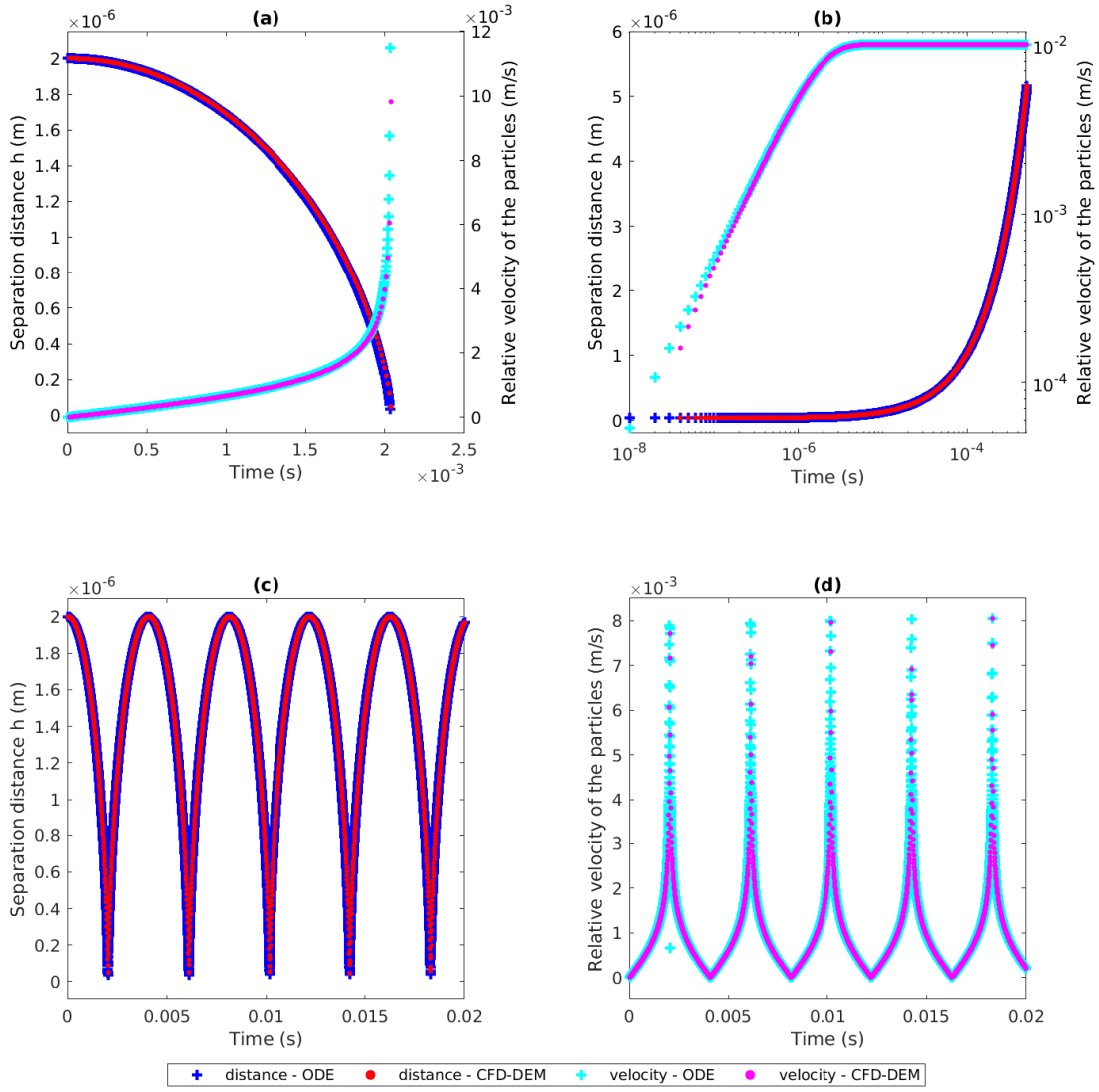

Figure 3.16: Particle-particle separation distance $h(t)$ and the relative velocity of particles $h^{'}(t)$: (a) for the attraction case with $h_0 = 2$ μm, (b) for the repulsion case with $h_0 = 0.04$ μm, and (c)-(d) for mixed attraction-repulsion with $h_0 = 2$ μm.

We see in Fig. 3.16 that the CFD-DEM including DLVO forces is in very good agreement with the reference ODE solutions. In the case of pure attraction, the surface-to-surface separation distance decreases from its initial value h_0 to a near-zero value, while the relative velocity, h', increases exponentially until the contact. For the repulsion case, the surface-to-surface separation distance increases exponentially from its initial value and the particle relative velocity increases up to a threshold value as the repulsive force decreases with the increase of separation distance. If both repulsion and attraction are considered, the separation distance describes a periodic oscillatory motion ranging from its initial value h_0 down to a minimal value $h_{min} = 0.0856$ μm. The latter corresponds to the secondary minimum at which the repulsive force takes over attraction pushing back the particles to their initial positions. The three test cases confirm the robustness of the DLVO implementation in our CFD-DEM package.

Particle-wall DLVO interactions

In this test case, we verify the implementation of the particle-wall DLVO interactions. We consider a particle of density, $\rho = 1050$ kg/m^3, radius, $R = 1$ μm, and mass, $m = 4.4 \times 10^{-15}$ kg, located at a distance, $h(t)$, from a immobile plane wall (see Fig. 3.17). Table 3.4 summarizes the particle, wall, and fluid properties. The particle is suspended in brine. The only force that applies are the attractive and repulsive DLVO interactions: there is no flow and the sedimentation and drag forces are neglected. Along the same line as the particle-particle verification cases, we consider three sets of simulations: pure attraction, pure repulsion, and mixed attraction-repulsion. The CFD-DEM predictions of the surface-to-wall separation distance $h(t)$ are compared with semi-analytical solutions.

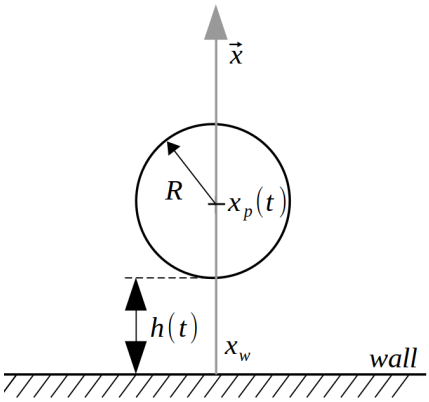

Figure 3.17: Representation of the particle and the wall distanced from h.

The computational domain is a 50 μm $\times$ 50 μm square with a regular grid cell size of 1 μm $\times$ 1 μm. We use $\Delta t = 10^{-5}$ s in the attraction case, $\Delta t = 10^{-8}$ s for the repulsion case and $\Delta t = 4 \times 10^{-5}$ s in the mixed attraction-repulsion case. $h_0 = 2\mu$m is used for the attraction and the mixed attraction-repulsion cases and $h_0 = 0.04\mu$m for the repulsion case.

Reference solutions for this configuration are obtained through an ODE that governs the evolution of the surface-to-wall distance, $h(t) = x_p(t) - x_w - R$, where $x_p(t)$ and x_w are the particle and wall positions, respectively. The particle motion is obtained by combining Eq.(3.6) and Eq. (3.23),

$$m\frac{d^2x_p}{dt^2}\vec{x} = -\frac{AR\left(1+28\frac{h}{\lambda}\right)}{6h^2\left(1+14\frac{h}{\lambda}\right)^2}\vec{x} \;+\; B\kappa R\left(\psi_p^2+\psi_w^2\right)\left[\frac{\frac{2\psi_p\psi_w}{\psi_p^2+\psi_w^2}-e^{-\kappa h}}{e^{\kappa h}-e^{-\kappa h}}\right]\vec{x}. \tag{3.44}$$

where $B = 2\pi\epsilon_0\epsilon_r$. This equation is recast into an ODE solved numerically for mixed attraction-repulsion:

$$\frac{6h^2\left(1+h\frac{14}{\lambda}\right)^2\left(e^{\kappa h}-e^{-\kappa h}\right)h''}{6\kappa BRh^2\left(1+h\frac{14}{\lambda}\right)^2\left(2\psi_p\psi_w-\left(\psi_p^2+\psi_w^2\right)e^{-\kappa h}\right)-A\left(1+28\frac{h}{\lambda}\right)\left(e^{\kappa h}-e^{-\kappa h}\right)} = \frac{R}{m}. \tag{3.45}$$

An ODE for pure attraction is obtained if $B = 0$,

$$6h^2\left(1+14\frac{h}{\lambda}\right)^2 h'' = -\frac{AR\left(1+28\frac{h}{\lambda}\right)}{m}, \quad \text{for pure attraction.} \tag{3.46}$$

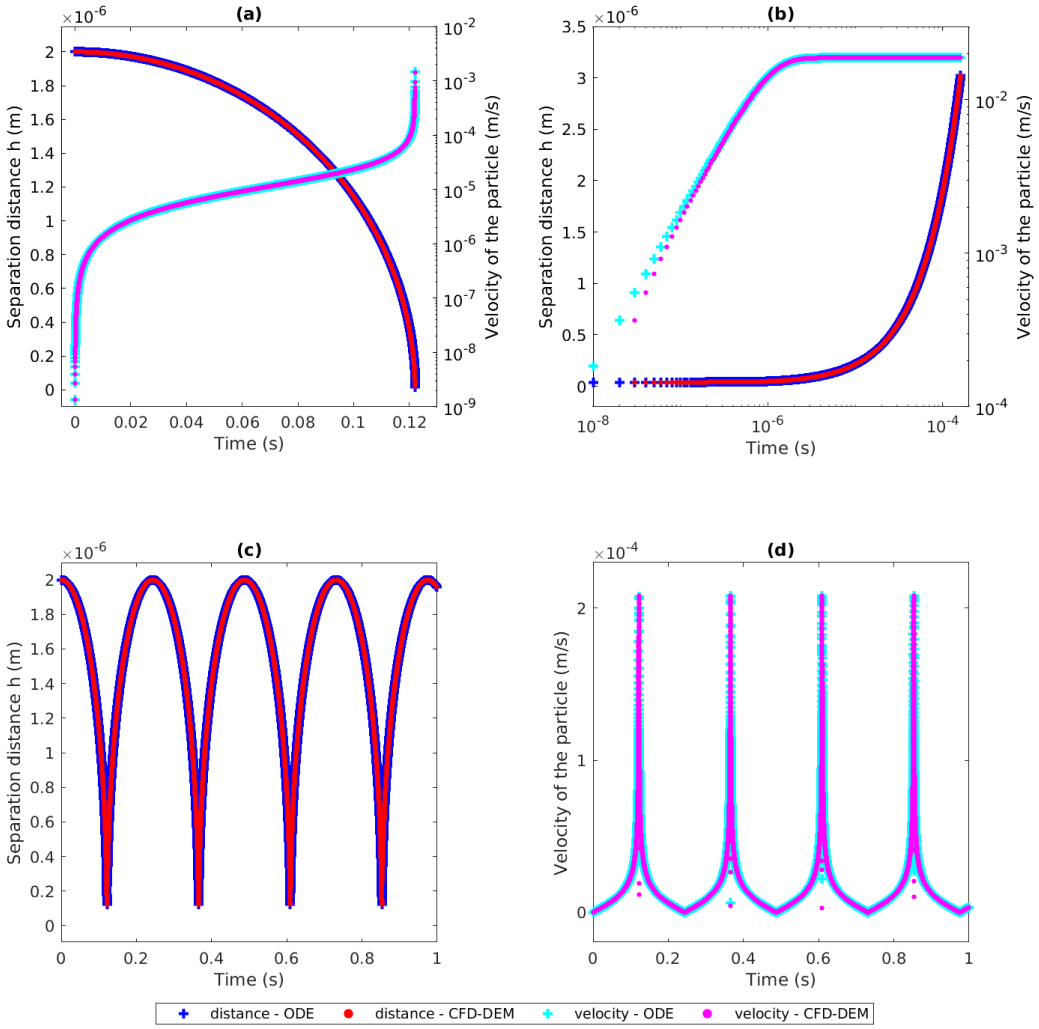

Figure 3.18: Particle-wall separation distance $h(t)$ and the velocity of the particle $h^{'}(t)$, (a) for the attraction case with $h_0 = 2$ μm, (b) for the repulsion case with $h_0 = 0.04$ μm, and (c)-(d) for mixed attraction-repulsion with $h_0 = 2$ μm.

If $A = 0$, we obtain an ODE for pure repulsive interaction,

$$\frac{\left(e^{\kappa h} - e^{-\kappa h}\right) h^{''}}{2\psi_p\psi_w - \left(\psi_p^2 + \psi_w^2\right) e^{-\kappa h}} = \frac{\kappa BR}{m}, \quad \text{for pure repulsion.} \tag{3.47}$$

Simulation results for pure attraction, pure repulsion, and mixed attraction-repulsion are shown in Fig. 3.18. The CFD-DEM results for the three cases are in very good agreement with the ODE reference solutions. We recover similar behaviors to the particle-particle interactions including the periodic oscillatory motion already observed for mixed attractive-repulsive interactions with a different secondary minimum $h_{min} = 0.12$ μm. These three test cases ensure that the DLVO forces are properly calculated when a particle arrives at the vicinity of a solid wall described by a boundary condition in CFD-DEM.

3.3.5 Colloidal aggregation of a suspension

To verify the numerical implementation of the coupling between the unresolved-resolved CFD-DEM method and the DLVO + JKR theories, we simulate the aggregation kinetics of particles initially dispersed

in a fluid at rest on a 2D plan. We compare the evolution of the total number of separated objects $N(t)$ (i.e. monomers: unattached particles and clusters: attached particles) with the experimental data obtained by Earnshaw et al. (1996). Two-dimensional colloidal systems have several attributes that make them particularly useful. They provide an experimentally convenient approach to studying the impact of DLVO forces on aggregate dynamics in which the interparticle interactions can be modified through the salinity of the aqueous solution, as shown in Fig. 3.19.

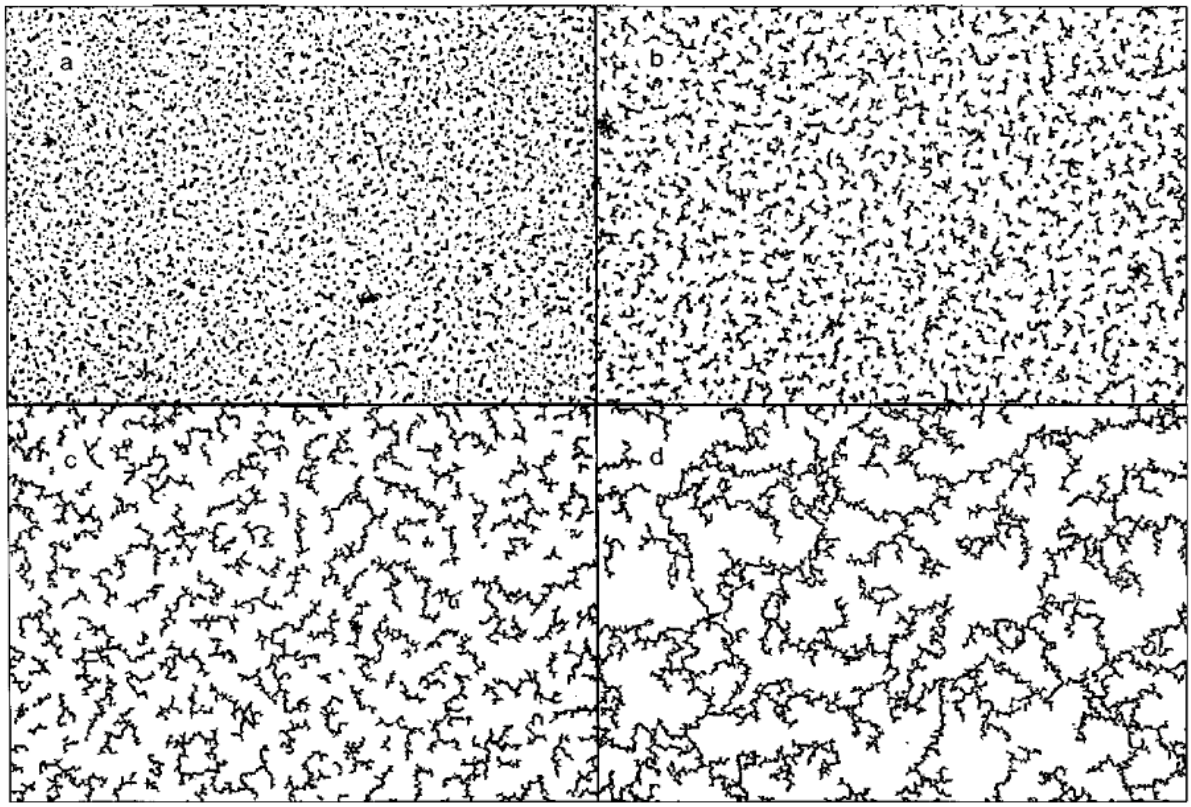

Figure 3.19: Experimental images obtained by Earnshaw et al. (1996) of an aggregating 2D layer of 1 mm polystyrene spheres on the surface of an aqueous 0.73 M $CaCl_2$ solution. The images are 768×512 pixels^2, one pixel = 0.95 mm. The images correspond to t = 60 (a), 75 (b), 105 (c), and 135 min (d).

The simulation domain consists of a two-dimensional 88.6μm $\times$ 88.6μm square box discretized with a 205×205 regular grid. The box is closed and the lateral boundaries are impermeable walls. It is filled with a brine aqueous solution ($CaCl_2$+H_2O) containing 0.73 M of salt concentration. Initially, $N_0 = 1000$ separated polystyrene latex particles (ρ = 1050 Kg/m^3, E = 3 GPa, ν = 0.34) of 1 μm diameter are randomly placed in the box (see Fig. 3.20). They occupy about 10% of the box surface area. The particle surface charge density is 0.4 μC/cm^2 which corresponds to a surface potential ψ_p = 12 mV using the Grahame equation (Butt et al., 2023). the particle-liquid-particle Hamaker constant is 3.4×10^{-21} J. The particle motions are only due to long-range double-layer (repulsive) and Van der Waals (attractive) interactions, gravity is neglected, and particle-wall interactions are not considered.

Fig. 3.20 shows the typical sequence of images of the 2D aggregating colloidal layer over time for the simulation. In Fig. 3.21, the number of objects decreases with time as the number of aggregates grows. The growth kinetics demonstrates a ramp-up from slow aggregation early to fast aggregation until it reaches a steady state. We see that the prediction of the evolution of the number of separated objects, $N(t)$, is in good agreement with the experimental measurements of Earnshaw et al. (1996), confirming

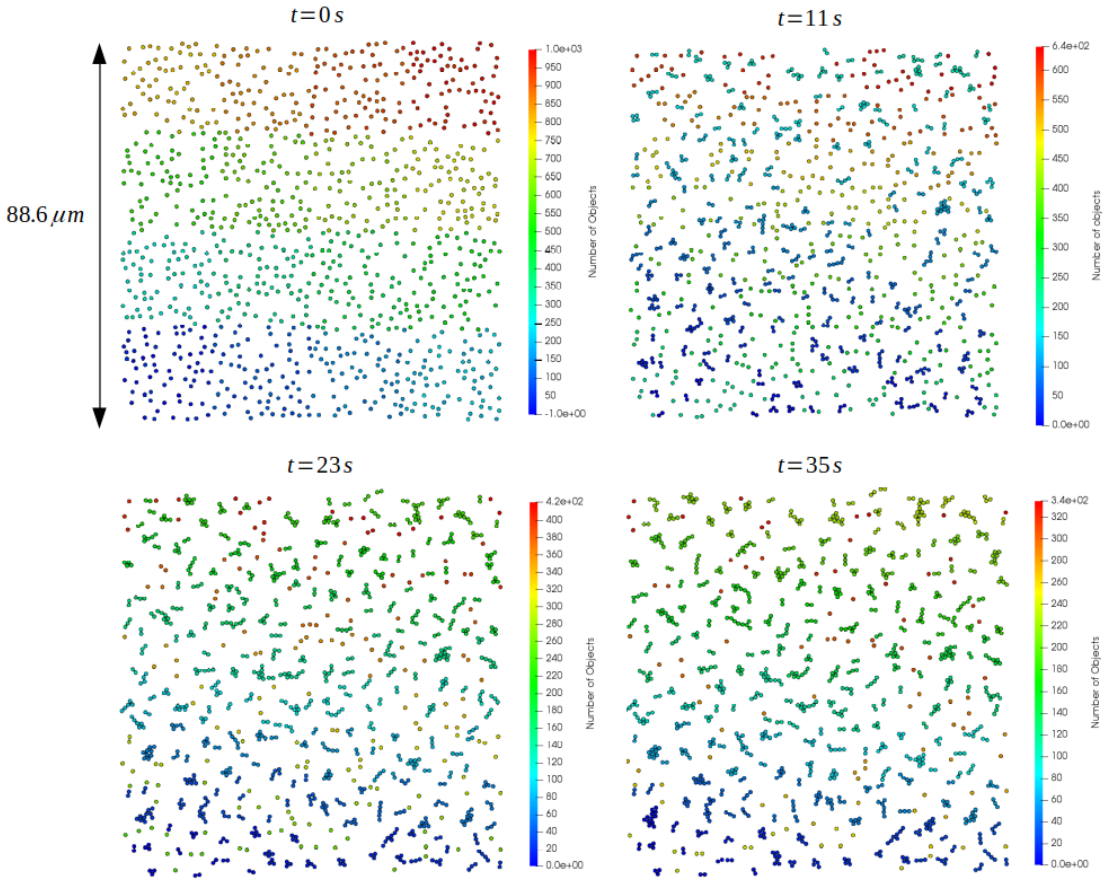

Figure 3.20: Image sequence of the simulation of 2D aggregation of the colloidal layer over time from initial setup to end time. The color represents the distinct objects (monomers+clusters) in the domain. Initially (t = 0 s), we have 1000 distinct monomers.

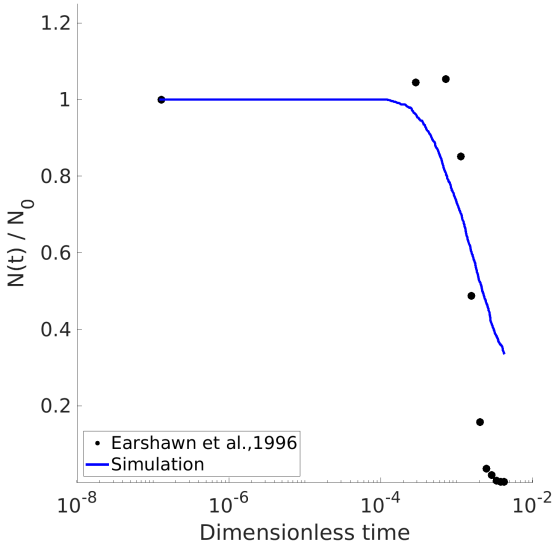

Figure 3.21: The number of separated objects (monomers and clusters) relative to their initial value at various times after the start of aggregation on a 0.73 M $CaCl_2$ brine aqueous solution, with a comparison of the experiment (obtained with $N_0 \simeq 6000$ objects) versus simulation.

that our numerical model can capture the clusterization mechanisms of the colloids.

3.4 Summary of the novelties

An unresolved-resolved four-way coupling CFD-DEM to simulate particle migration, deposition, and retention in porous media at the pore-scale is proposed. The investigation of local permeability reduction due to the injection of particles becomes, therefore, possible. Unlike other CFD-DEM, our approach is independent of the grid resolution and type (i.e. structured and unstructured) and is not limited to particles smaller than the cell size. It relies on a hybrid resolved-unresolved formulation of the drag force calculation and an efficient searching strategy – called peer-to-peer search – to identify the CFD cells covered by DEM particles. Moreover, a diffusive smoothing filter removes unphysical oscillations when particles cross the cell-to-cell interface. The method has been successfully validated using cases for which reference solutions exist. For instance, relatively good agreement is observed between model predictions and drag coefficient, sedimentation of a steel ball in a water tube, or colloidal aggregation measurements. The peer-to-peer search is as efficient as the Hilbert curve search and easier to implement. Our method has great potential to investigate the complex feedback due to the injection, retention, and remobilization of particles in porous media.

Chapter 4

Pore-scale Simulations of Particle Clogging in Porous Media

In this chapter, we use our unresolved-resolved CFD-DEM solver to simulate colloidal migration and retention in porous media at the pore scale. First, in section 4.1, we simulate bridging and sieving inside a single pore. Second, in section 4.2, we investigate the influence of particle properties, flow conditions, and pore geometry on the bridging mechanism. Then, in section 4.3 we simulate particle bridging and aggregation within a porous network.

4.1 Clogging of a single pore: sieving and bridging

Sieving and bridging are two of the main pore-clogging mechanisms. In sieving, particles larger than the pore throat block at the pore entrance (i.e. exclusion of particles by size). In bridging, particles arrive simultaneously at the pore throat forming an arch. In this part, we simulate such processes in a single pore using our CFD-DEM package. The pore geometry is made of a two-dimensional converging-diverging channel of diameter, $D_{ch} = 2$ mm, and a throat width, $W = 500$ μm. The computational domain is gridded with a 150×50 conformal mesh.

We consider two cases:

1. we inject three particles, one every three seconds, at the middle of the inlet. Particles have different diameters (100 μm$, 300$ μm$, 550$ μm) to simulate the sieving of the biggest particle ($D_p > W$).
2. A polydisperse distribution of particles with sizes ranging from 100 to 300 μm is continuously injected for 50 seconds with a rate of 2 particles per second. The objective is to simulate the arch formation of particles of different sizes.

In both cases, a constant pressure difference $\Delta p = 2$ μbar is applied between the inlet and the outlet. Simulations are stopped when the pore is clogged. The fluid is water, the particles are in polystyrene, and the pore walls are in PDMS (Polydimethylsiloxane). The properties of water, particles, and pore walls are found in Table 4.2. Snapshots of the two clogging mechanisms are presented in Fig. 4.1-4.3.

4.1.1 Pore-clogging by sieving

In the first simulation (sieving, Fig. 4.1), we see that particles smaller than the pore throat ($D_p \leq W$) can pass through the constriction as expected until a big particle ($D_p > W$) is filtered by its size. At that

point, the pore permeability decreases and the flow velocity drops to a near-zero value as shown in Fig. 4.4.

Notes that pore-clogging by size exclusion cannot be captured by the standard unresolved CFD-DEM solver of OpenFOAM. Indeed, Fig. 4.2 shows the particle trajectory and fluid velocity field of a sieving simulation of a $D_p = 550$ μm particle (the size of the particle is larger than the cell size: $D_p > \Delta x$), using *denseParticleFoam* solver of OpenFOAM which is based on the unresolved coupling. Sieving requires the particle to be larger than the grid size. Then, the simulation results in numerical errors in the fluid velocity calculations which provokes a chaotic motion of the particle because the particle shadow on the Eulerian grid is only calculated on the cell containing the particle center. Our resolved-unresolved approach, however, is not constrained by such limitations and can be used in all configurations.

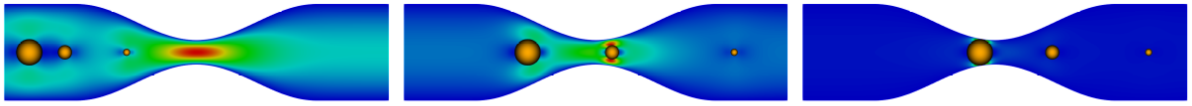

(a) *Time* = 5 *s* (b) *Time* = 10 *s* (c) *Time* = 20 *s*

Figure 4.1: Sieving of a large particle at different times. The background color corresponds to the fluid velocity magnitude (red-maximum, blue-minimum).

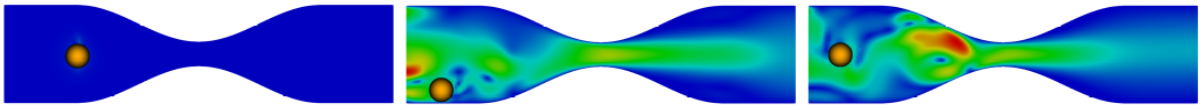

(a) *Time* = 0 *s* (b) *Time* = 0.2 *s* (c) *Time* = 0.5 *s*

Figure 4.2: Unresolved CFD-DEM simulation of the sieving of a large particle ($D_p = 550$ μm).The background color corresponds to the fluid velocity magnitude (red-maximum, blue-minimum)

4.1.2 Pore-clogging by arch formation

In the second scenario (bridging, Fig. 4.3), the suspension flows in the domain until two particles arrive simultaneously at the pore entrance, forming an arch, and blocking the flow. The time-to-plug by arch formation depends on the probability that such an event happens, the closer the ratio $\frac{D_p}{D_t}$ is to 1, the higher the probability of bridging (Dressaire and Sauret, 2017). Pore-scale modeling of particulate flow with CFD-DEM will bring new insights for assessing the time-to-plug according to flow conditions and suspension properties.

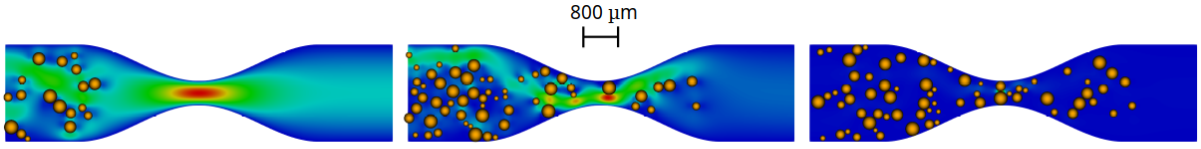

(a) *Time* = 7.5 *s* (b) *Time* = 35 *s* (c) *Time* = 85 *s*

Figure 4.3: Bridging formation of 2 particles (214 μm and 287 μm) at different times. The background color corresponds to the fluid velocity magnitude (red-maximum, blue-minimum).

Fig. 4.4, highlights the intermittent behavior of bridging. We observe that the blue curve reaches its minimal value (synonymous with clogging) two times. The first one corresponds to the formation of an

unstable arch that breaks eventually. The second one corresponds to a stable arch blocking the pore.

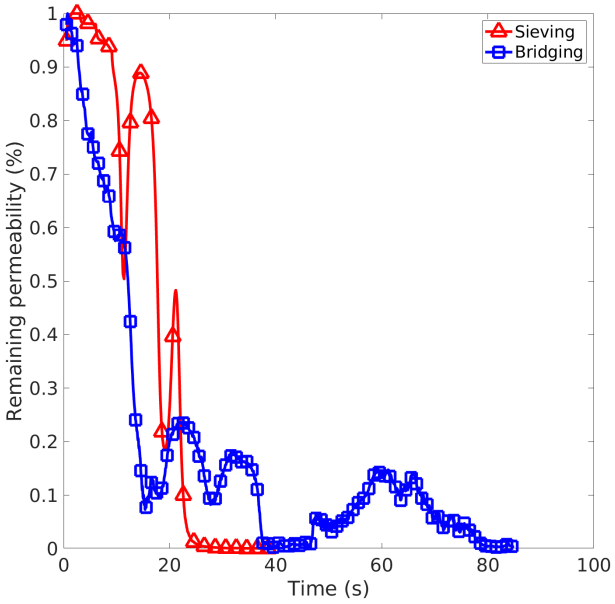

Figure 4.4: Evolution of the permeability damage calculated using Darcy's law in the case of sieving and bridging.

4.2 Sensitivity analysis of particle bridging in a single pore

In this section, we study the influence of different parameters on the bridging mechanism such as the injected particle concentration C_0, the particle-to-throat ratio D_p/W, the Reynolds number $Re = D_{ch}v^f/\nu_f$, and the pore-to-throat ratio D_{ch}/W. For each parameter, we run 4 simulations with different values presented in Table 4.1. The pore geometry is a two-dimensional converging-diverging channel of diameter $D_{ch} = 200\ \mu m$ and a throat width $W = 50\ \mu m$ (see Fig. 4.5). The computational domain is gridded with a 200×25 conformal mesh. the study concerns the parameters D_p, C_0, D_{ch}, and Re. Particles are polystyrene latex, the pore in PDMS (Polydimethylsiloxane), and their properties are listed in Table 4.2. We process two-dimensional depth-integrated simulations with VANS equations in which the depth geometry is $h = 25 \times 10^{-6}\ \mu m$. A no-slip boundary condition is applied on the walls for the fluid flow.

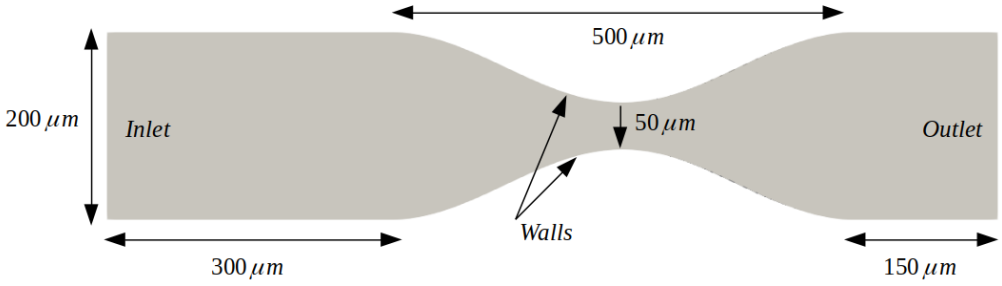

Figure 4.5: Geometry of the 2D simulation of a single pore

To study the impact of each parameter of the arch formation, we compare the different times to clog, defined as the time when particles clog the pore (see Fig. 4.6). We observe a linear decreasing behavior of

Table 4.1: Simulation configurations for bridging investigation.

Case 1: effect of the particle concentration	**Case 2: effect of the particle diameter**
$C_0 = \{0.08\%, 0.1\%, 0.115\%, 0.13\%\}$ with $Re = 0.02$, $D_p/W = 0.4$, and $D_{ch}/W = 4$	$D_p/W = \{0.4, 0.45, 0.5, 0.6\}$ with $Re = 0.02$, $C_0 = 0.13\%$, and $D_{ch}/W = 4$
Case 3: effect of the flowrate	**Case 4: effect of the geometry aspect ratio**
$Re = \{0.005, 0.01, 0.05, 0.1\}$ with $D_p/W = 0.4$, $C_0 = 0.13\%$, and $D_{ch}/W = 4$	$D_{ch}/W = \{3, 4, 6, 8\}$ with $Re = 0.02$, $C_0 = 0.13\%$, and $D_p/W = 0.4$

time for clogging with the increase of the studied parameters (C_0, Re, D_{ch}/W, D_p/W) except for those relating to the aspect ratio of the geometry D_p/W.

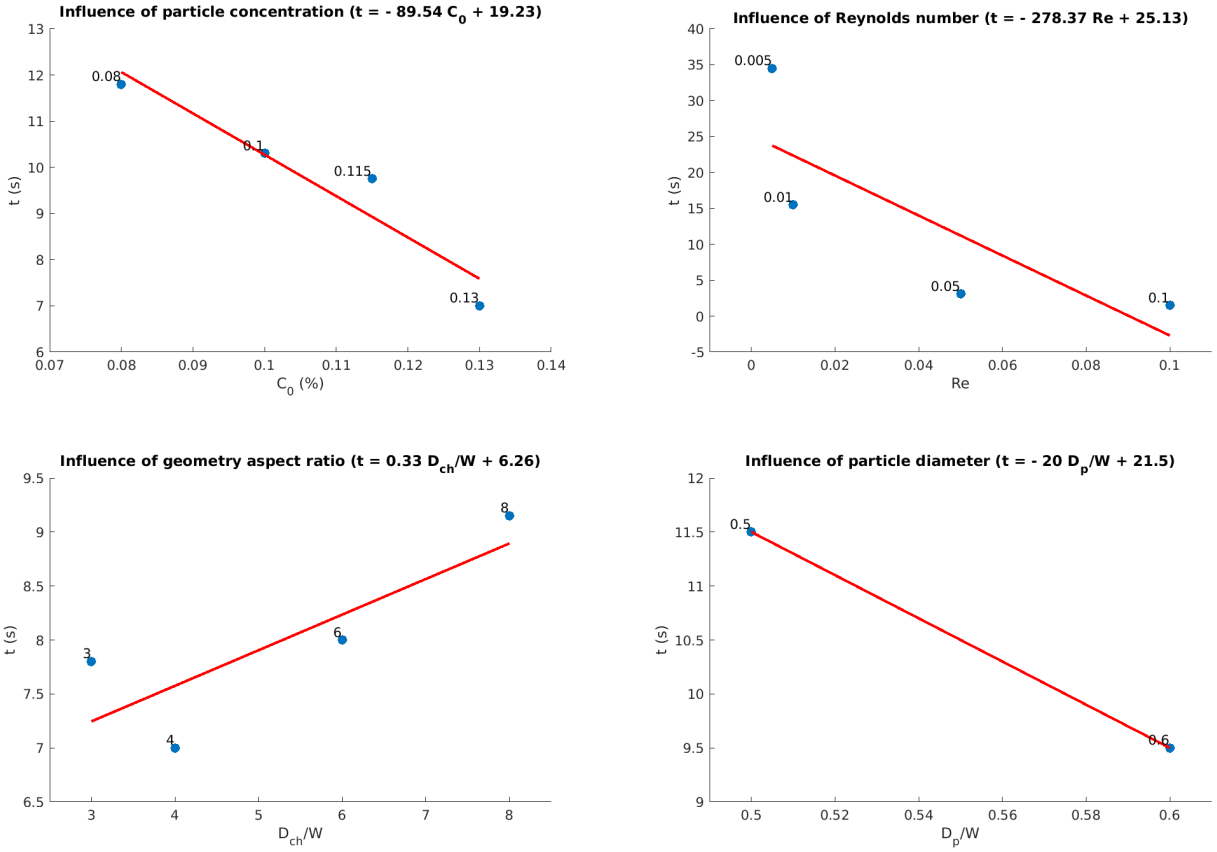

Figure 4.6: Numerical results of the time to clog a single pore by arch formation relative to the particle concentration, the Reynolds number, the geometry aspect ratio, and the particle diameter.

4.2.1 Case 1: effect of the particle concentration

Here, we vary the particle concentration by using different values of $C_0 = \{0.08\%, 0.1\%, 0.115\%, 0.13\%\}$. Snapshots corresponding to each configuration are presented in Fig. 4.7.

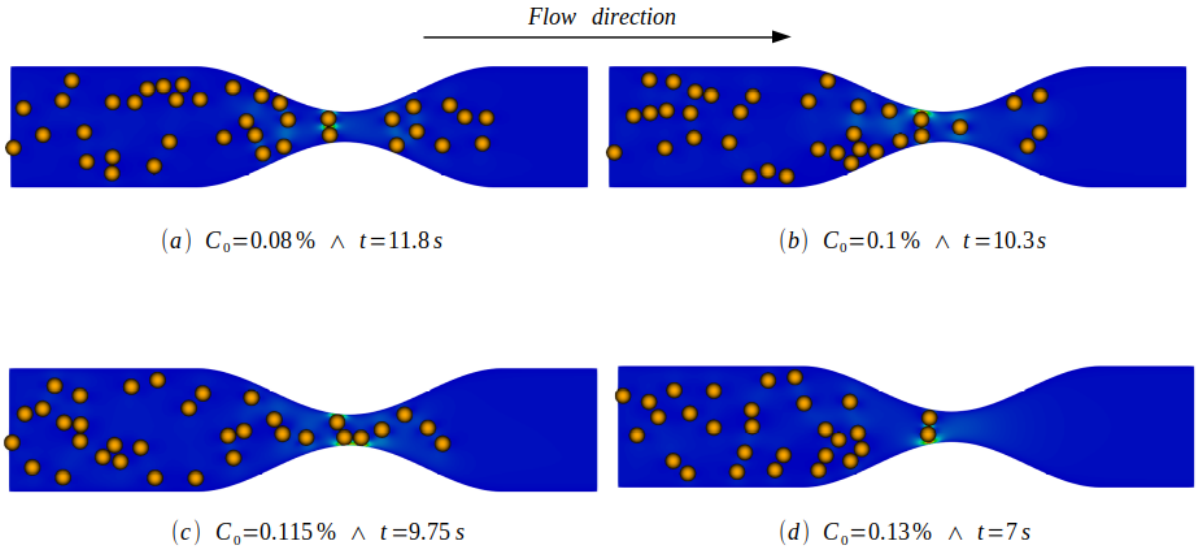

Figure 4.7: Particle arches formation and velocity magnitude field for different particle concentrations $C_0 = \{0.08\%, 0.1\%, 0.115\%, 0.13\%\}$ in a single pore. The orange spheres are particles and the color map represents the fluid velocity magnitude. t represents the time at which the clog forms.

We observe that, with the increase in particle concentration, the time to form arches of particles that will clog the pore decreases. These results are in agreement with experimental observations (Agbangla et al., 2012).

4.2.2 Case 2: effect of the particle diameter

Here, we vary the particle diameter by using different values of $D_p = \{20\ \mu m, 22.5\ \mu m, 25\ \mu m, 30\ \mu m\}$. This parameter plays a role in the amplitude of the drag force applied to the particle as well as in the particle-to-throat ratio, D_p/W, that characterizes the probability of arch formation. Snapshots corresponding to each configuration are presented in Fig. 4.8.

As expected, when the particle size approaches the size of the pore throat, the probability of clogging increases, minimizing the time needed to clog the pore. For the duration given to the simulations (20s), we do not observe clogging for $D_p/W = \{0.4, 0.45\}$.

4.2.3 Case 3: effect of the flowrate

Here, we vary the flow rate by using different values of seepage velocity $v^f = \{2.5 \times 10^{-5}\ m/s, 5 \times 10^{-5}\ m/s, 2.5 \times 10^{-4}\ m/s, 5 \times 10^{-4}\ m/s\}$. Snapshots corresponding to each configuration are presented in Fig. 4.9. Xia et al. (2023) reported that lower flow rates are prone to clogging and higher flow rates can prevent fine particles from forming bridges and clogging due to interruptions in pressure distribution and flow reversal. However, since the particles are transported more quickly at a higher flow rate, they will also tend to form clogs more quickly, as seen on the scale of a pore.

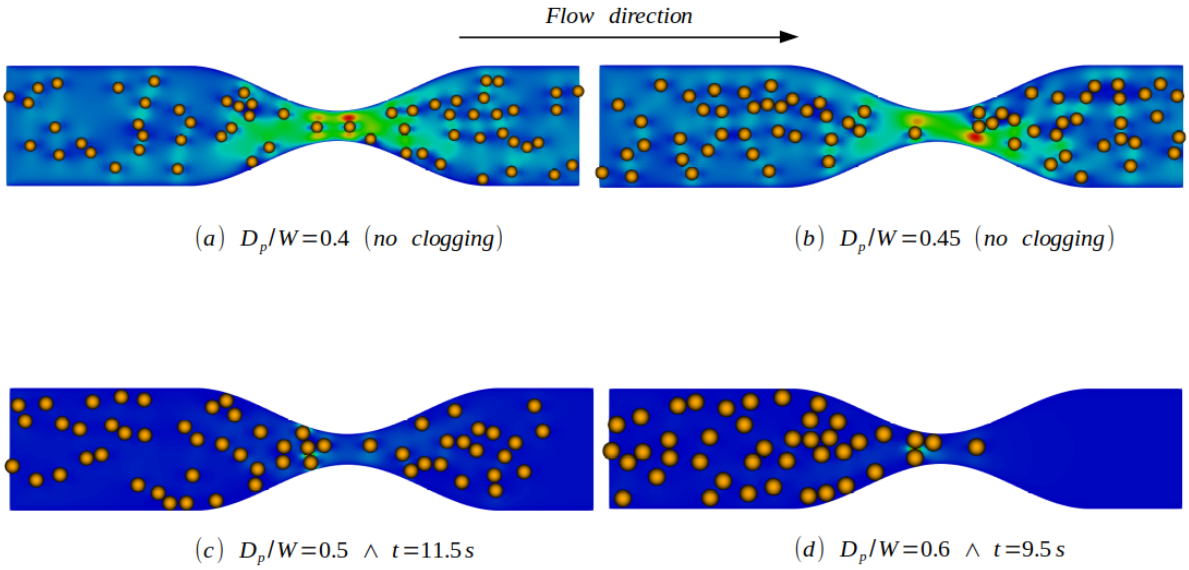

Figure 4.8: Particle arches formation and velocity magnitude field for different particle-to-throat ratios $D_p/W = \{0.4, 0.45, 0.5, 0.6\}$ in a single pore. The orange spheres are particles and the color map represents the fluid velocity magnitude. t represents the time at which the clog forms.

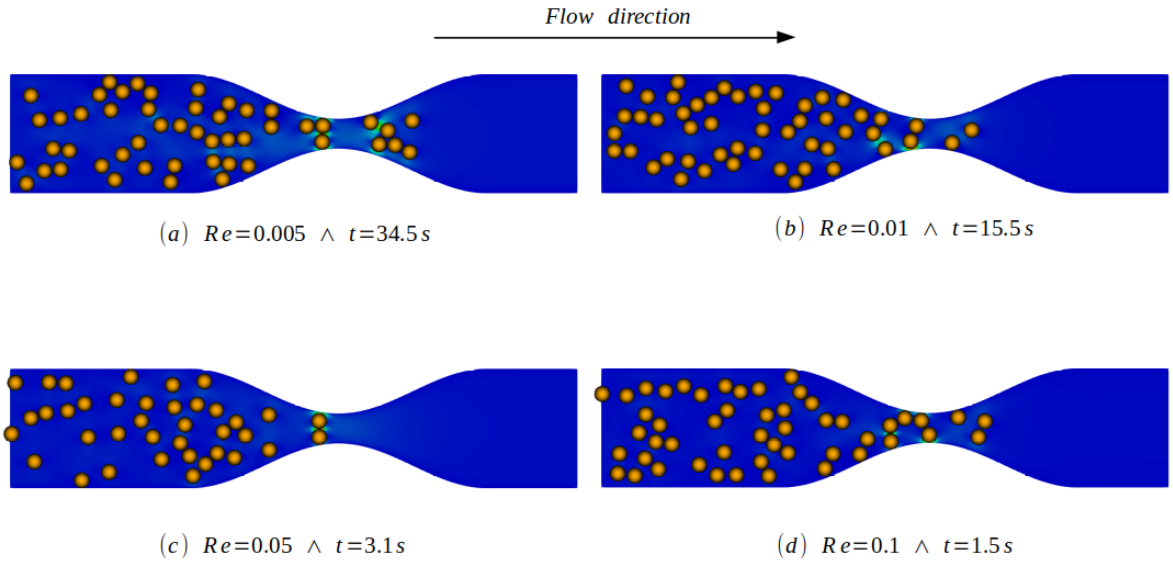

Figure 4.9: Particle arches formation and velocity magnitude field for different Reynolds numbers $Re = \{0.005, 0.01, 0.05, 0.1\}$ in a single pore. The orange spheres are particles and the color map represents the fluid velocity magnitude. t represents the time at which the clog forms.

4.2.4 Case 4: effect of the geometry aspect ratio

Here, we vary the pore-to-throat ratio which implies different streamlines near the pore throat. The lower the pore-to-throat ratio, the more convergent the streamlines at the constrictions which, in principle, increases the probability that particles arrive simultaneously at the pore entrance and form an arch. Snapshots corresponding to each configuration are presented in Fig. 4.10.

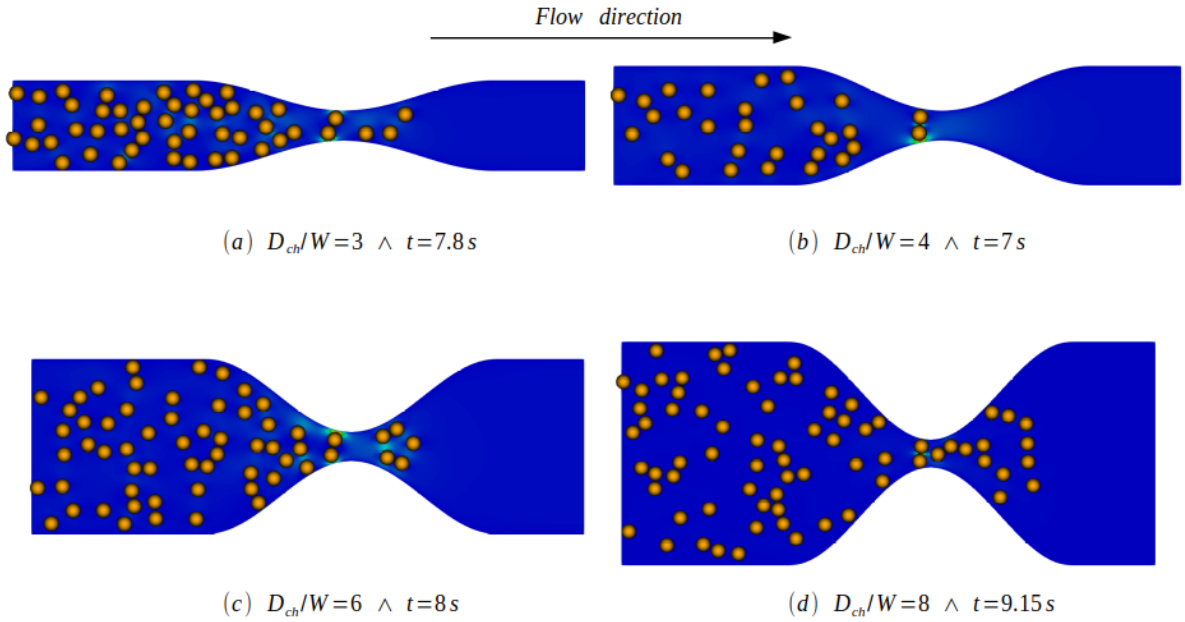

Figure 4.10: Particle arches formation and velocity magnitude field for different pore-to-throat ratios $D_{ch}/W = \{3, 4, 6, 8\}$ in a single pore. The orange spheres are particles and the color map represents the fluid velocity magnitude. t represents the time at which the clog forms. For all these geometries the throat width is $W = 50\ \mu m$.

4.3 Clogging inside heterogeneous pore network

In this part, we use our CFD-DEM package to investigate particle retention and permeability reduction in a porous medium that is a representation of a PDMS microfluidic device (Roman et al., 2016).

The pore geometry and the meshing procedure are found in Soulaine (2024). We obtain a two-dimensional 1050 μm $\times$ 310 μm pore-scale domain is shown in Fig. 4.11. The typical pore size is $d_{50} =$ 26 μm, porosity is $\epsilon_i = 0.62$, and permeability is $K_i = 1.1 \times 10^{-11}$ m^2. The domain is discretized into an unstructured mesh with 49330 cells using *snappyHexMesh*, the OpenFOAM automatic gridder. The left and right sides are inlet and outlet boundaries, respectively. The top, bottom, and grain surfaces are walls described with no-slip conditions. Fluid, particles, PDMS properties, and simulation parameters are listed in Table 4.2. We set a constant pressure difference of $\Delta p = 0.2$ mbar between the inlet and the outlet. The simulations use an additional Hele-Shaw correction term, $12\mu_f \epsilon \mathbf{v}^f / h^2$, in the volume-averaged Navier-Stokes momentum equation to account for the hydrodynamic effects in the microfluidic device thickness, h, of the microfluidic device (Soulaine et al., 2021). Temporal results are presented using the pore volume (PV) (a dimensionless measure of time defined as the ratio of the injected volume of water to the pore-space volume).

4.3.1 Pore-clogging due to hydrodynamic forces only

We consider a cloud of $D_p = 6$ μm diameter monodispersed polystyrene particles. The mean mesh resolution is $D_p/\Delta x \simeq 5$. According to the verification tests performed in the previous chapter, this allows for an accurate calculation of the drag forces. Here, simulations are run in 3 consecutive steps. First, the fluid (water) flows through the porous formation until the flow field is stable. PV is set to zero. Then, a concentration of particles, C_0 $(0.05\%, 0.1\%, 0.15\%)$, is continuously injected from the inlet until

Table 4.2: Parameters of the CFD-DEM simulations used to investigate pore-clogging by aggregation of particles.

CFD and fluid parameters		**DEM and particle parameters**	
CFD time-step Δt_{CFD}	10^{-5} s	DEM time-step Δt_{DEM}	2×10^{-9} s
Fluid density ρ_f	10^3 kg/m^3	Particle density ρ_p	1050 kg/m^3
Fluid viscosity μ_f	10^{-3} Pa s	Poisson ratio ν_p / ν_w	0.34 / 0.5
Temperature T	293 K	Young modulus E_p / E_w	3 GPa/ 2 MPa
Salinity [NaCl]	1 ; 10 ; 100 mM	Hamaker constant A_{pLp} / A_{pLw}	3.4×10^{-21} J / 10^{-21} J
Ionic valence Z	1	Surface potential ψ_p	-58 ; -26 ; -20 mV
Model depth b	20 μm	Surface potential ψ_w	-52.3 ; -45 ; -26 mV
		Surface energy W_{pLp} / W_{pLw}	41/20 mJ/m^2

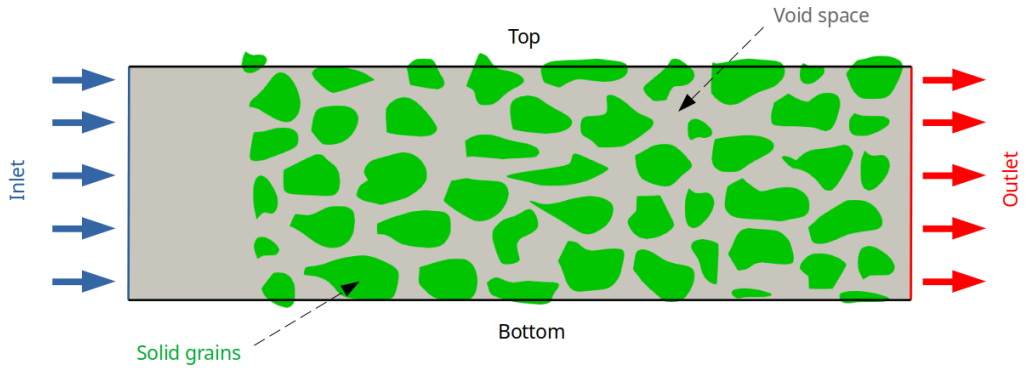

Figure 4.11: (a) Geometry of the 2D simulation model of the porous media (length = 310 μm, width = 1050 μm).

$PV = 4$. Finally, the injection of particles is stopped, and the simulation is run until a steady state is reached.

Snapshots of the particle migration and retention are shown in Fig. 4.12 ($C_0 = 0.1\%$) and Fig. 4.13 ($C_0 = 0.15\%$). We observe that some particles percolate while others remain trapped within the porous medium clogging pores. The retention of particles changes the system porosity and reroutes the local flow lines which affect the system permeability. The particle contact frequency and the probability of simultaneous arrival of particles at a pore entrance to form a clog (arch formation) increase with the particle concentration. For $C_0 = 0.05\%$ (results not shown here), there is no clog inside the porous medium – although, a few isolated particles are trapped in dead-end pores – which is not the case for higher concentrations. For $C_0 = 0.1\%$ (Fig. 4.12), we see several clogs formed by the bridging of 2 particles at the entrance of small pores and others that grow until they reach their filling limit. The clogs are very stable and remain even after we stopped the injection of particles ($PV > 4$). For $C_0 = 0.15\%$, the possibility of arch formation increases because the particles are more likely to be near each other as they reach a pore entrance due to converging trajectories. We observe (Fig. 4.13), however, several non-permanent pores clogged. These observations are also seen in the particle cumulative breakthrough curves (Fig. 4.14a) and the plot of the number of clogs over time (Fig. 4.14b). Once the injection stops, we see that almost all particles go through the porous structure for $C_0 = 0.05\%$, and up to 6% of particles remain trapped

for $C_0 = 0.1\%$, and 3% for $C_0 = 0.15\%$. For the highest concentration, more clogs are formed but they are less stable and remobilized, eventually (see Fig. 4.14b).

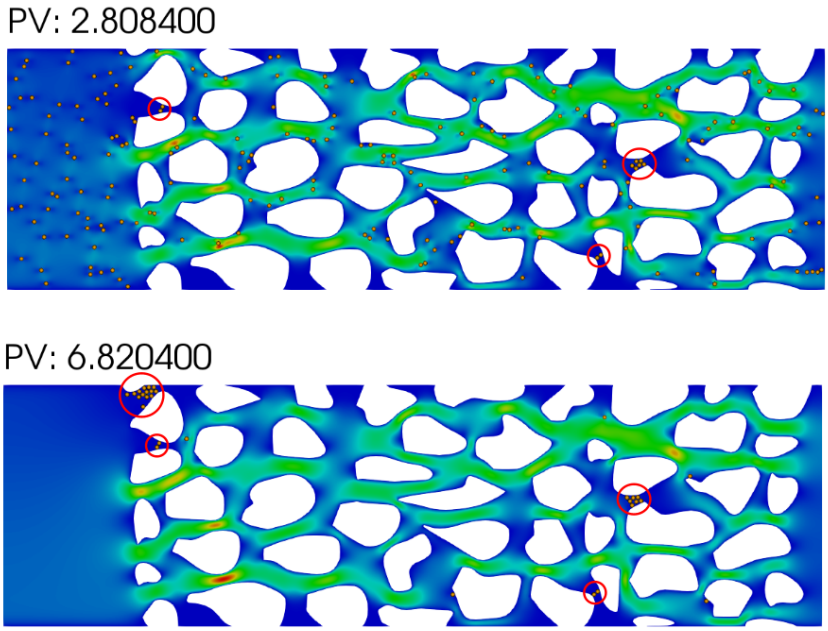

Figure 4.12: Particle deposition and velocity magnitude field for $C_0 = 0.1\%$ during the injection of particles ($PV = 2.8$) and post-injection ($PV = 6.8$). The orange spheres are particles and the color map represents the fluid velocity magnitude. The clogs formed during the particle injection and remain stable when the particle injection is stopped.

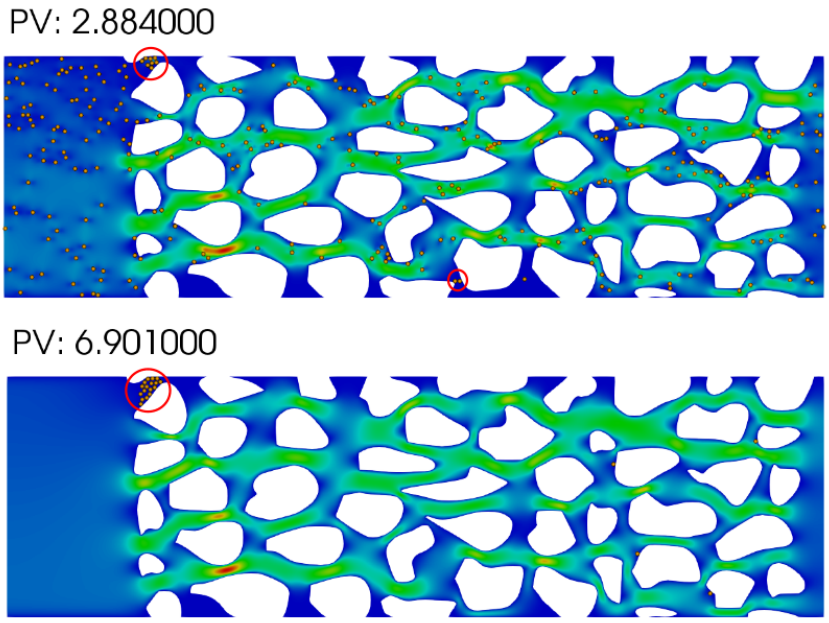

Figure 4.13: Particle deposition and velocity magnitude field for $C_0 = 0.15\%$ during the injection of particles ($PV = 2.88$) and post-injection ($PV = 6.9$). Arches of particles are formed during the injection, but they are unstable, and most of them are remobilized.

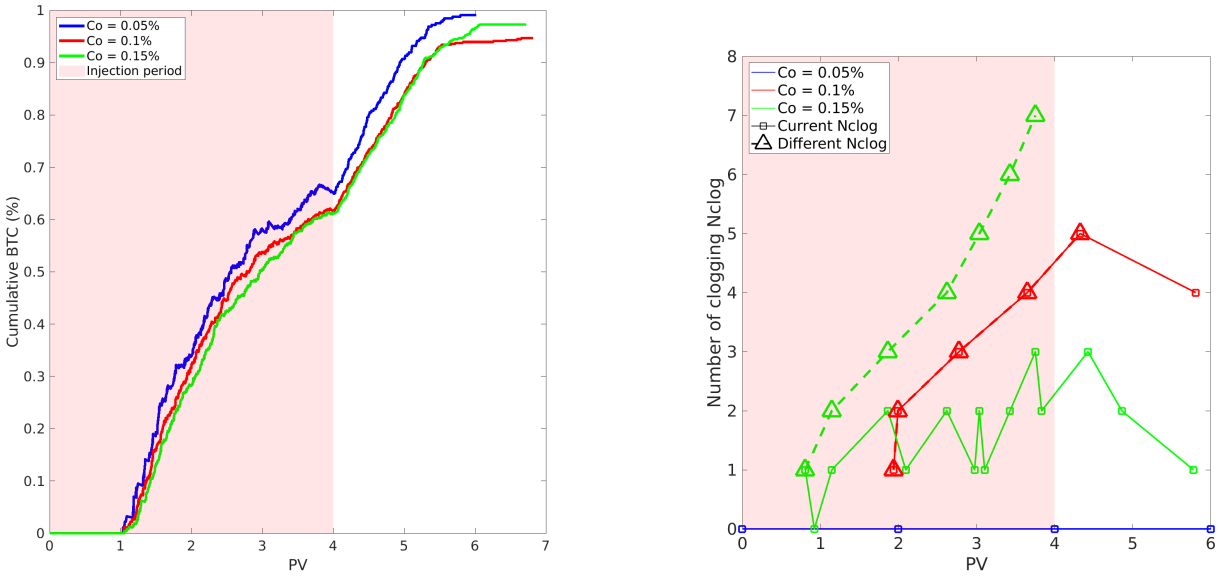

Figure 4.14: (a) Particle cumulative BTC (Breakthrough Curves) normalized by the total number of injected particles. (b) Evolution of the current number of clogs (Current Nclog) in the system, and the number of clogs formed at different positions (Different Nclog) for different C_0. For $C_0 = 0.1\%$, each clog formed at a unique position. The pink zone represents the particle injection period.

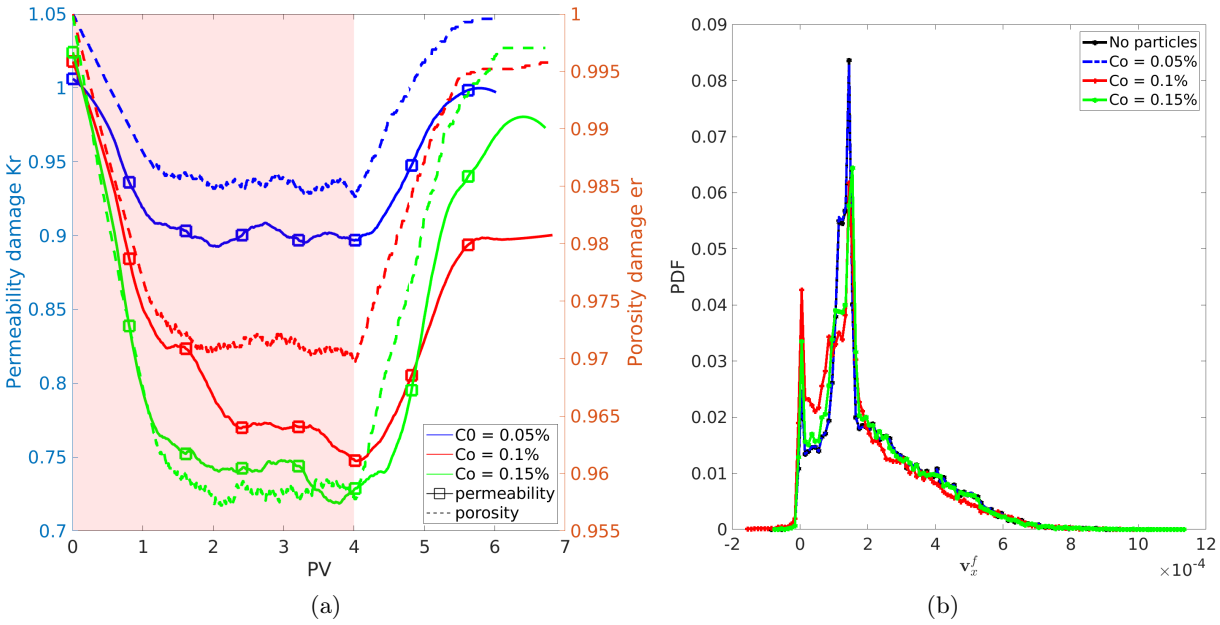

Figure 4.15: (a) Permeability damage severity, K_r, and porosity damage severity, ϵ_r, for different particle concentration, C_0. (b) The probability density function of the fluid longitudinal velocity v_x^f for different C_0 at the end of the simulation compared with the case without particles.

Pore-clogging leads to permeability reduction. The evolution of the porosity damage severity, $\epsilon_r = \langle\epsilon\rangle/\epsilon_i$, with $\langle\epsilon\rangle$ the domain-averaged porosity, and the permeability damage severity, $K_r = K_f/K_i$, is shown in Fig. 4.15a. The permeability, K_f, of the porous system is obtained using Darcy's law, $K_f = \frac{\langle v_x^f\rangle \mu_f L}{\Delta p}$, where $\langle v_x^f\rangle$ is the domain-averaged fluid velocity, L is the length of the domain, and Δp is the pressure difference. For identical hydrodynamic conditions, permeability reduction increases

with the particle concentration, which matches with experimental observations (Agbangla et al., 2012; Ramachandran and Fogler, 1999; Mustin and Stoeber, 2010). A permeability reduction of 10% is also observed for $C_0 = 0.05\%$ for which there is no pore-clogging. This reduction corresponds to the flow resistance related to the suspension itself. The permeability recovers its initial value after all the particles have been flushed out. For $C_0 = 0.1\%$ and $C_0 = 0.15\%$, we observe a hysteresis between the initial and final permeability/porosity values. It is related to the clogs formed with the retention of particles. Note that we observe at the end of the simulations a recovered permeability higher for $C_0 = 0.15\%$ compared to $C_0 = 0.1\%$. This could be explained by a certain critical concentration of particles at which the increase in concentration results in an increase in permeability damage. To know if this result was due to the randomness of a simulation or if it is a physical behavior, we simulated each of these concentrations up to 5 times and plotted the average of the permeability damage severity over the injected pore volume as presented in Fig. 4.16.

The Probability Density Function (PDF) presented in Fig. 4.15b gives information about the redistribution of local flow rates during pore-clogging. For $C_0 = 0.05\%$, it is superimposed with the PDF without particles. Indeed, as almost all the particles percolate and the remaining particles are trapped individually in dead-end pores, they do not affect the fluid flow. For $C_0 = 0.1\%$ and 0.15%, we observe an increase in the densities of low fluid velocities and a reduction of the highest value of the fluid velocities. This is characteristic of pore-clogging (Velásquez-Parra et al., 2022). The multiple permanent clogs formed with $C_0 = 0.1\%$ create additional dead-end pores and subsequent fluid recirculations that increase negative values of the velocity fluid.

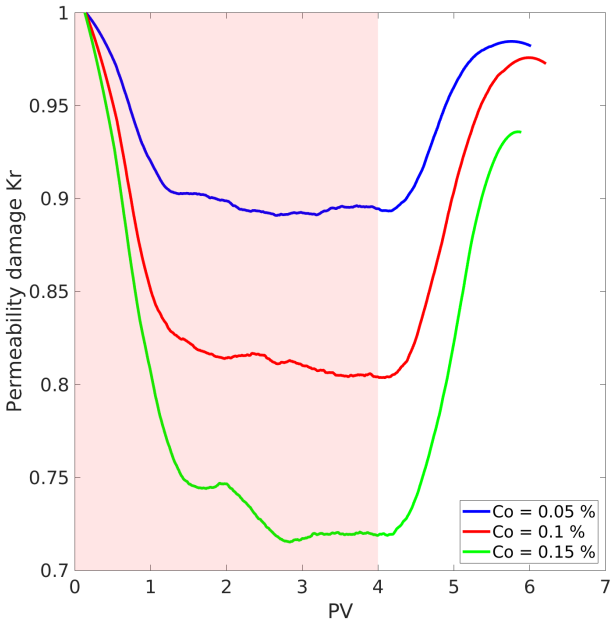

Figure 4.16: Average of the permeability damage severity, K_r, over 5 replicates for different particle concentration, C_0.

4.3.2 Pore-clogging including colloidal interactions

We consider a cloud of monodispersed polystyrene particles whose diameter is $D_p = 4$ μm. The mean mesh resolution is $D_p/\Delta x \simeq 5$, which allows for an accurate calculation of the drag forces. Three different brines with salinities [NaCl] = 1, 10, 100 mM are used. Both polystyrene and PDMS immersed in the

fluid have a negative surface charge at $T = 293$ K (Liu and Wu, 2020; Kirby and Hasselbrink, 2004). An increase in salinity increases the surface potential as well, which favors deposition (García-Salinas et al., 2000). In each case, the interactions between particles and the porous medium are different because the DLVO potential has different values. Fig. 4.17 shows that the repulsive barrier is more significant for 1 mM of salinity as the surface potential is the lowest. Overall, particle-particle and particle-wall interactions are weakly repulsive for [NaCl] = 1, 10, 100 mM with an attractive secondary minimum that will favor aggregation.

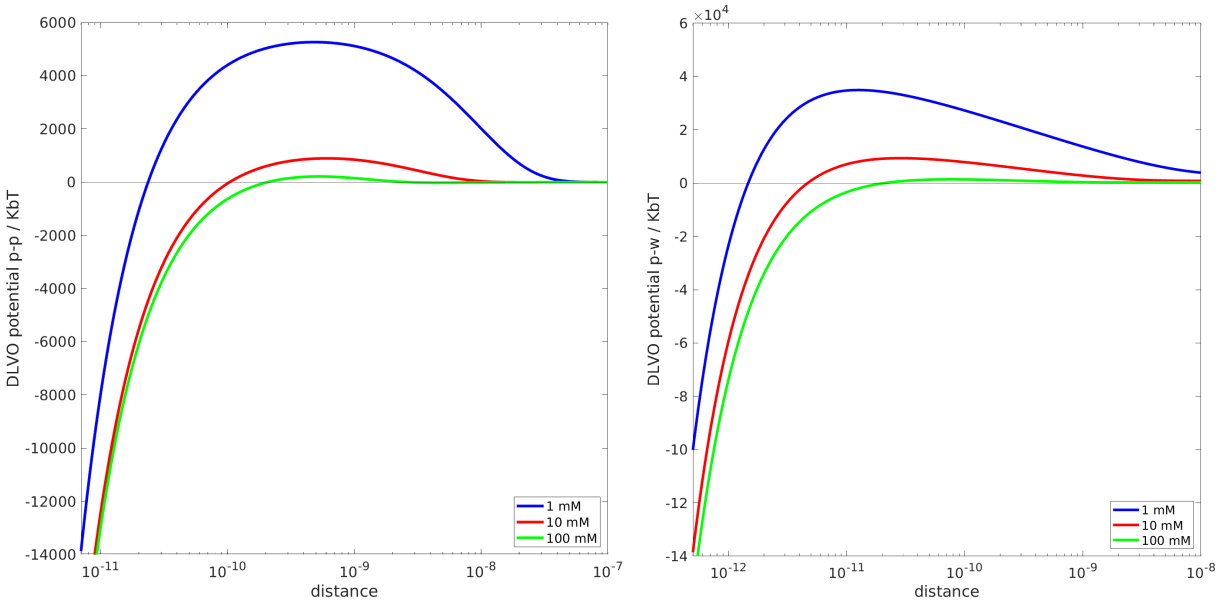

(a) (b)

Figure 4.17: DLVO potential (normalized by $k_B T$) for (a) particle-particle, and (b) particle-wall interactions for various NaCl salt concentrations.

Snapshots of the particle migration and retention are shown in Fig. 4.18. For the three simulations, we observe that some particles deposit rapidly at the entrance of the porous medium. It means that long-range interactions are dominant over the hydrodynamic forces. Layers of deposited particles grow until they clog pores. Thus, the clogs change the system porosity and reroute the local flow lines, affecting the system permeability. When all entrance pores of the porous system are clogged, the mean flow velocity drops to near zero value and no more particles percolate through the domain.

Large-scale properties such as permeability and porosity are strongly impacted by pore-clogging. The impact of salinity on the evolution of porosity damage severity and the permeability damage severity is shown in Fig. 4.19a. The first is defined as $\epsilon_{rem} = \langle\epsilon\rangle/\epsilon_i$ where $\langle\epsilon\rangle$ is the domain porosity at time t. The second is calculated using $K_r = K_f/K_i$, where K_f is the system permeability at time t obtained using Darcy's law, $K_f = \frac{\langle \mathbf{v}_x^f \rangle \mu_f L}{\Delta p}$, where $\langle \mathbf{v}_x^f \rangle$ is the domain-averaged fluid velocity, and L is the length of the domain. Both K_r and ϵ_{rem} decrease at the beginning of the injection when $PV \in [0, 0.5]$. The same evolution is observed for the three salinities. This reduction corresponds to the flow resistance related to the suspension itself. For $PV > 0.5$, pores at the medium's entrance are clogged, resulting in a sudden drop in permeability damage. We observe fluctuations in the permeability damage evolution. The remobilization of clusters of deposited particles explains them. These remobilizations happen mostly for 1 mM and 10 mM salt concentrations for which the particle-wall potential barrier is more important. For identical flow conditions, the permeability impairment by aggregation of particles increases with salinity,

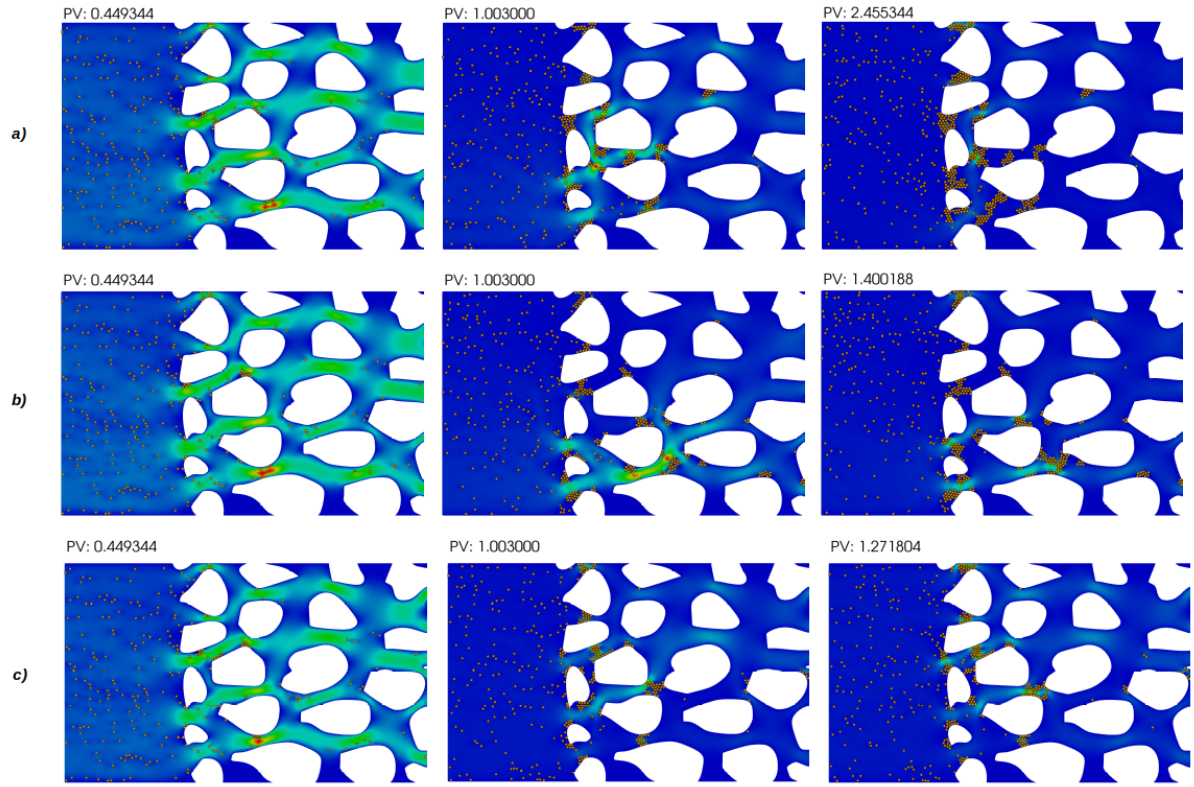

Figure 4.18: Snapshots of the particle migration and deposition for various salinity conditions: a) 1 mM, b) 10 mM, c) 100 mM NaCl. The background colors correspond to the fluid velocity field magnitude.

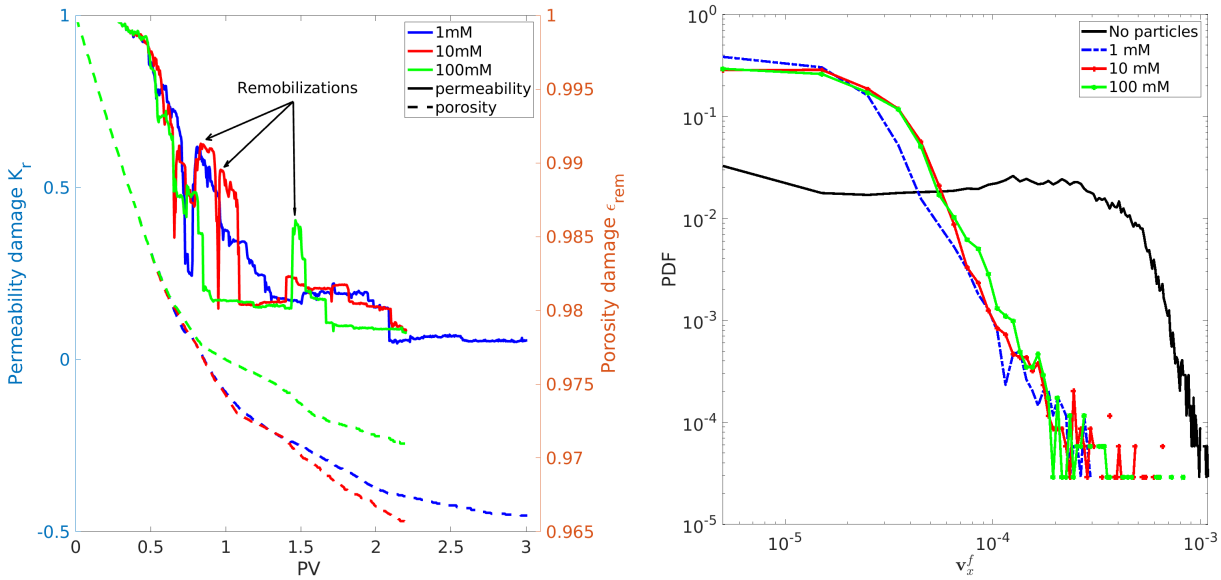

(a) (b)

Figure 4.19: (a) Evolution of permeability damage K_r and porosity damage ϵ_{rem} over the injected PV for various salt concentrations. (b) Probability density function (PDF) of the longitudinal flow velocity $|\mathbf{v}_x^f|$ over the domain-averaged flow velocity $\langle \mathbf{v}_x^f \rangle$ with no particles, and with particles for various salt concentrations at PV = 2.2

as observed experimentally (Agbangla et al., 2012; Ryan and Elimelech, 1996). It can be seen that the K_r plateau values – that indicate the clogging of the porous medium – are reached earlier for higher salinity.

4.4 Summary and partial conclusions

We use our unresolved-resolved four-way coupling CFD-DEM to simulate particle migration and retention in two typical geometries. The first one corresponds to an idealized representation of a pore, and the second one is a hand-made representation of a heterogeneous porous medium. We highlight the ability of our model to capture sieving ($D_p > W$), bridging ($D_p < W$), and aggregation of particles leading to pore-clogging. The conclusion of the investigation of local permeability reduction due to the concentration of injected particles is in line with what has been done in the literature. The more concentrated a suspension is, the more likely it is to clog pores. Note that, our study was not carried out on a range of values for concentration wide enough to rule out the existence of a critical concentration. Other parameters such as particle size, fluid salinity, flow rate, and geometry aspect ratio and their influence on the time-to-clog are discussed.

In the next chapter, we use our computational model to investigate the colloidal attachment around a single collector and develop advanced theoretical models of the mean deposition rate.

Chapter 5

Colloidal Deposition Kinetics

In this chapter, we investigate the mean kinetics rate of deposition and detachment to simulate colloidal retention in porous media at larger scales. First, in section 5.1, we describe the state-of-the-art filtration models for particle retention in porous media. Second, in section 5.2, we introduce the concept of single-collector efficiency and we review some empirical and semi-analytical correlations used in its assessment. Third, in section 5.3 we revisit the single-collector efficiency for a cylindrical collector including the mechanisms of capture by electrostatic deposition. Then, in the section 5.4 we undergo preliminary investigation on the morphology of the deposit obtained with CFD-DEM simulations and make a comparison with experimental data from the literature.

5.1 Filtration models

5.1.1 Colloid filtration theory (CFT)

CFT was developed by Yao et al. (1971) for water and waste-water filtration simulation and is widely used for the prediction of particle retention processes. Later on, CFT was used to predict the transport behavior of diverse colloidal particles such as pollutants (Yao et al., 1971), microbial particles (Harvey and Garabedian, 1991), and nanoparticles (Zhang et al., 2016; Wang et al., 2008).

Governing partial differential equations

CFT describes colloidal particle flow through saturated homogeneous porous media (e.g. a packed bed) with consideration of hydrodynamic dispersion, molecular diffusion, advection, and retention on grains' surface. The equation of transport at core-scale reads,

$$\frac{\partial C}{\partial t} + \nabla \cdot \left(\overline{\mathbf{v}}_f^f C \right) = \nabla \cdot (\mathsf{D} \cdot \nabla C) - \frac{\rho_b}{\phi} \frac{\partial S}{\partial t}, \tag{5.1}$$

where C is the mean colloidal particle concentration, ϕ is the porosity, $\overline{\mathbf{v}}_f^f$ is the intrinsic velocity obtained using Darcy's law, D is the dispersion tensor, ρ_b is the bed bulk density, and S is particle concentration attached at the matrix surface.

In CFT, the adsorption retention law is modeled as a first-order linear reaction term with a constant deposition rate k_{dep}. The deposition term reads:

$$\frac{\rho_b}{\phi} \frac{\partial S}{\partial t} = k_{dep} C. \tag{5.2}$$

A classical way for deriving the kinetic rate of deposition is to idealize a porous medium as a packed bed of identical spherical grains of diameter D_c and to calculate the mean deposition rate around an isolated grain. This is known as the single-collector concept.

Single-collector removal efficiency

The single-collector removal efficiency, η, is defined as the ratio of the overall particle deposition rate onto the collector to the advective transport of upstream particles toward the projected area of the collector (see Fig. 5.1). For an isolated spherical collector, the single-collector removal efficiency is (Yao et al., 1971):

$$\eta = \frac{I}{U_\infty C_0 \pi D_c^2}, \tag{5.3}$$

where U_∞ is the fluid velocity away from the collector, C_0 is the bulk concentration of particles, and I is the overall flux of the particles deposited at the collector surface. Practically, some particles arriving at the collector surface are attached while others flow away after the contact. Therefore, we define the single-collector contact efficiency, η_0, as the ratio of the number of particles contacting the collector over the total number of particles arriving toward the collector. We have,

$$\eta = \alpha \eta_0, \tag{5.4}$$

where α is the single-collector attachment efficiency. It is an empirical coefficient used to describe the fraction of collision with collector grains that result in attachment (Elimelech and O'melia, 1990).

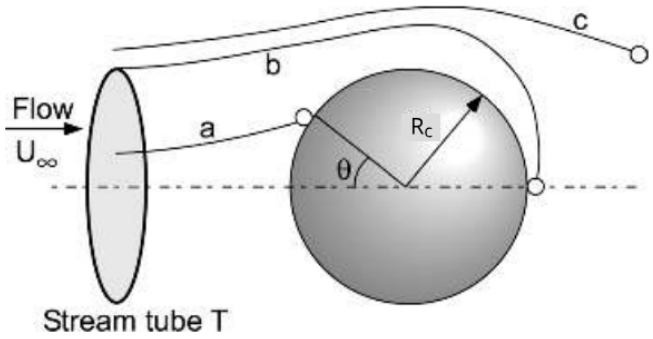

Figure 5.1: Schematic of a single-collector concept. Paths of a colloidal particle: trajectory a leads to a collision, trajectory b is the limiting trajectory, and trajectory c leads to no collision. Modified after Masliyah and Bhattacharjee (2005)

Kinetic deposition of particles

For a packed bed with n_c number of collectors per unit volume with an element of length dx, a particle number balance on the differential thickness gives,

$$[U_\infty n A_b]_x - \left[U_\infty n A_b + U_\infty A_b \frac{dn}{dx} dx\right]_{x+dx} = \left(n_c \frac{\pi}{4} D_c^2\right)(A_b dx)(U_\infty n)\,\eta, \tag{5.5}$$

where A_b is the bed cross-sectional area, and n is the number of particles at distance x per unit volume. Eq. (5.5) reduces to,

$$\frac{dn}{dx} = -\frac{\pi}{4} D_c^2 n_c n \eta. \tag{5.6}$$

The number of collector grains per unit volume is given by,

$$n_c = \frac{6(1-\phi)}{\pi D_c^3}. \tag{5.7}$$

Then, Eq. (5.6) becomes,

$$\frac{dn}{dx} = -\frac{3}{2}\frac{(1-\phi)\eta}{D_c}n. \tag{5.8}$$

For an instant infiltration of particles in the medium, we assume from Eq. (5.1) and Eq. (5.2) that:

$$\overline{v}_f^f \frac{dn}{dx} = -k_{dep}n. \tag{5.9}$$

The kinetic constant, k_{dep}, is therefore a function of porosity ϕ, grain collector diameter D_c, contact efficiency η_0, attachment efficiency α, and particle velocity magnitude v^p (here, we assume that $v^p = \overline{v}_f^f$). We have,

$$k_{dep} = \frac{3}{2}\frac{(1-\phi)}{D_c}\alpha\eta_0 v^p. \tag{5.10}$$

Eq. (5.10) shows that the deposition rate varies linearly with the particle velocity, the attachment efficiency, and the single collector efficiency. However, the relation between particle velocity and deposition is not truly linear. Indeed, Benamar et al. (2007) found that the recovery of nanoparticles increases with increasing flow rate up to a critical point and then decreases with increasing rate.

Model hypothesis and limitations

The colloid filtration theory assumes: *(i)* Homogeneous porous medium, *(ii)* incompressible fluid and medium, *(iii)* constant rate at isothermal state, *(iv)* dispersion occurs in a parallel direction, *(v)* aggregation, contact interactions between particles, and chemical reaction with matrix surface are not considered, *(vi)* undisturbed flow field in the presence of colloids. *(vii)* deposition of colloids is irreversible, *(viii)* no maximum capacity sites (deposition occurs as long as the colloids are injected).

5.1.2 Extensions of the CFT

To overcome these limitations, variations of the colloidal filtration theory have been proposed in the literature. We review below some of them.

CFT with maximum site

Classic CFT does not consider the maximum capacity of deposition sites. Therefore, Cullen et al. (2010) added maximum site capacity S_{max} parameter to accommodate site blocking. The reaction term reads:

$$\frac{\rho_b}{\phi}\frac{\partial S}{\partial t} = k_{dep}\left(1 - \frac{S}{S_{max}}\right)C, \tag{5.11}$$

Li et al. (2008) estimate S_{max} in a granular sand medium using empirical correlation as a function of particle velocity and diameter as:

$$S_{max} = 19.6\left(\left(\frac{v^p D_p}{D}\right)^{1/3}\frac{D_c}{D_{50}}\right)^{-1.2}, \tag{5.12}$$

where, D_{50} is the average diameter of the medium sand and D is the dispersion coefficient. From the previous equation, velocity has a direct effect on the maximum site capacity, which means at high velocity maximum adsorption capacity is smaller. Also, smaller particles are favorable to achieving maximum adsorption.

CFT with detachment

Classic CFT assumes the deposition of particles to be irreversible and does not consider the detachment phenomena. Therefore considering the detachment of particles already attached to the collector surface, the deposition term reads:

$$\frac{\rho_b}{\phi}\frac{\partial S}{\partial t} = k_{dep}C - \frac{\rho_b}{\phi}k_{det}S, \tag{5.13}$$

with k_{det} the detachment rate coefficient of the particle from the collector surface. The detachment phenomena results from a competition between hydrodynamic forces and deposition forces. No theoretical approaches exist to estimate k_{det}, which is only estimated using fitting. Note that, this model assumes the detachment and attachment rate coefficient to be constant and that all the attachment processes that occur are reversible (attachment leads to detachment).

Kinetic Langmuir model

The kinetic Langmuir model is derived from the classic CFT and posits adsorption is driven by chemical potential and adheres to the Langmuir isotherm rule. The kinetic Langmuir model differs from the CFT in that the attachment is reversible with a maximum capacity of attachment (Wang et al., 2008). The deposition term is expressed as,

$$\frac{\rho_b}{\phi}\frac{\partial S}{\partial t} = k_{dep}\left(1 - \frac{S}{S_{max}}\right)C - \frac{\rho_b}{\phi}k_{det}S. \tag{5.14}$$

Assuming monolayer deposition on the collector surface, the maximum attachment concentration can be estimated with additional assumptions as deposition capacity is independent of flow condition, both attachment and detachment rate coefficients are uniform, and all attached particles can't be detached. In this approach, all attached particles on the collectors can be removed by having enough post-flush (zero particle concentration). This is not correct since experimental results showed immobilized particle concentration (Caldelas et al., 2011). Therefore, several models describing immobilized particles have been proposed (Zhang et al., 2016; Seetha et al., 2017).

Two-site model

The two-site model incorporates both irreversible and reversible attachment of particles. Zhang et al. (2016) proposed a two-site model that includes maximum site capacity for both reversible and irreversible attachment. Fig. 5.2 shows a schematic of immobilized attached particles (blue) and reversibly attached particles (orange) due to an impinging flow near a rough surface. The model assumes particle attachment to behave more solute-like than colloid-like with both attachment and detachment rate coefficients independent of flow rate and the sites for attachment limited by surface area. The deposition term for a two-site model is expressed as,

$$\frac{\rho_b}{\phi}\frac{\partial S}{\partial t} = \left(\frac{\rho_b}{\phi}\frac{\partial S}{\partial t}\right)_{irr} + \left(\frac{\rho_b}{\phi}\frac{\partial S}{\partial t}\right)_{rev}, \tag{5.15}$$

$$\frac{\rho_b}{\phi}\frac{\partial S}{\partial t} = \left[k_{irr}\left(1 - \frac{S_1}{S_{1max}}\right)C\right] + \left[k_{ra}\left(1 - \frac{S_2}{S_{2max}}\right)C - \frac{\rho_b}{\phi}k_{rd}S_2\right], \tag{5.16}$$

where k_{irr} is the irreversible attachment rate coefficient, k_{ra} and k_{rd} are the reversible attachment

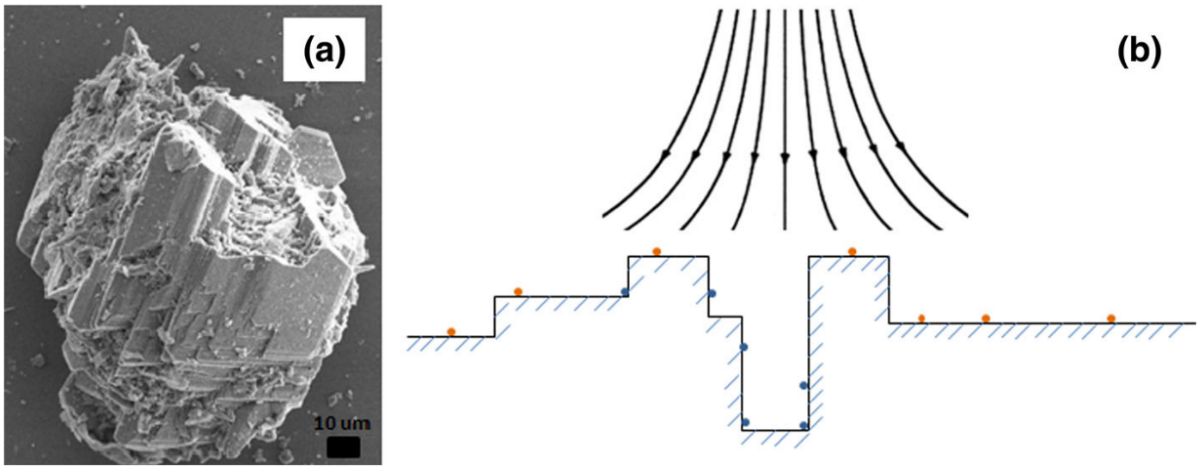

Figure 5.2: (a) SEM picture of a sand grain sieved from crushed Boise sandstone within a size range of 90–105 μm; (b) Schematic of sand grain surface roughness and an impinging fluid velocity field near the surface. The orange points are attached nanoparticles that are accessible for recovery with the detachment path parallel to the flow direction, and the blue points represent the attached particles that are hard to detach with the escape direction opposite to the flow direction. The former may be modeled as "reversible" sites for attachment/detachment, while the latter may be modeled as "irreversible" sites for attachment (Zhang et al., 2016).

and detachment rate coefficient respectively. S_1 and S_2 are the irreversible and reversible attachment concentrations, and S_{1max} and S_{2max} are the irreversible and reversible maximum attachment concentrationrespectively. The unknown parameters k_{irr}, k_{ra}, k_{rd}, S_{1max}, S_{2max} are estimated by fitting with core flood experimental data.

Modified linear adsorption model

Madhan Nur Agista (2017) proposed a modified linear adsorption model that assumes that the concentration of the particle on the collector surface, S, is linear to the concentration of particles inside the fluid, C. The deposition term of the model is expressed as,

$$S = k_c\eta_0 C, \tag{5.17}$$

$$\frac{\rho_b}{\phi}\frac{\partial S}{\partial t} = \frac{\rho_b}{\phi}\frac{\partial C}{\partial t}k_c\eta_0, \tag{5.18}$$

where k_c is the concentration distribution coefficient of particles between the medium and the fluid. k_c is obtained from history matching with experimental data and is assumed constant for similar particles, medium, and experimental conditions. The final transport equation of particles is,

$$\left(1 + \frac{\rho_b}{\phi}k_c\eta_0\right)\frac{\partial C}{\partial t} + \overline{\mathbf{v}}_f^f \cdot \nabla C = \nabla \cdot (\mathsf{D}\nabla C), \tag{5.19}$$

The additional term acts like a retardation term on the particle transport due to particle deposition. The linear expression proposes that the equilibrium between the deposited concentration on the collector and the dispersed concentration in the fluid is instantly obtained. This means that a variation in the in-

jected concentration directly affects the deposited concentration proportionally Zhang et al. (2016). Note that, since the deposited concentration has a linear relation with dispersed concentration (Eq. 5.17), the maximum retention capacity is determined by the initial concentration and the concentration distribution coefficient, instead of a function of the surface area of the pore (blocking function).

5.2 Capture efficiency of single collector

Yao et al. (1971) defined the single collector capture efficiency as the sum of capture efficiency by interception (η_I), diffusion (η_D), and gravity (η_G). We have,

$$\eta_0 = \eta_I + \eta_D + \eta_G, \tag{5.20}$$

An illustration of each capture mechanism is presented in Fig. 5.3. Note that, the simple additivity of the different mechanisms for deposition is an approximation. Although it is found to be quite accurate for some applications (Prieve and Ruckenstein, 1974), such additivity of different mechanisms that interplay each other, may not be fundamentally sound.

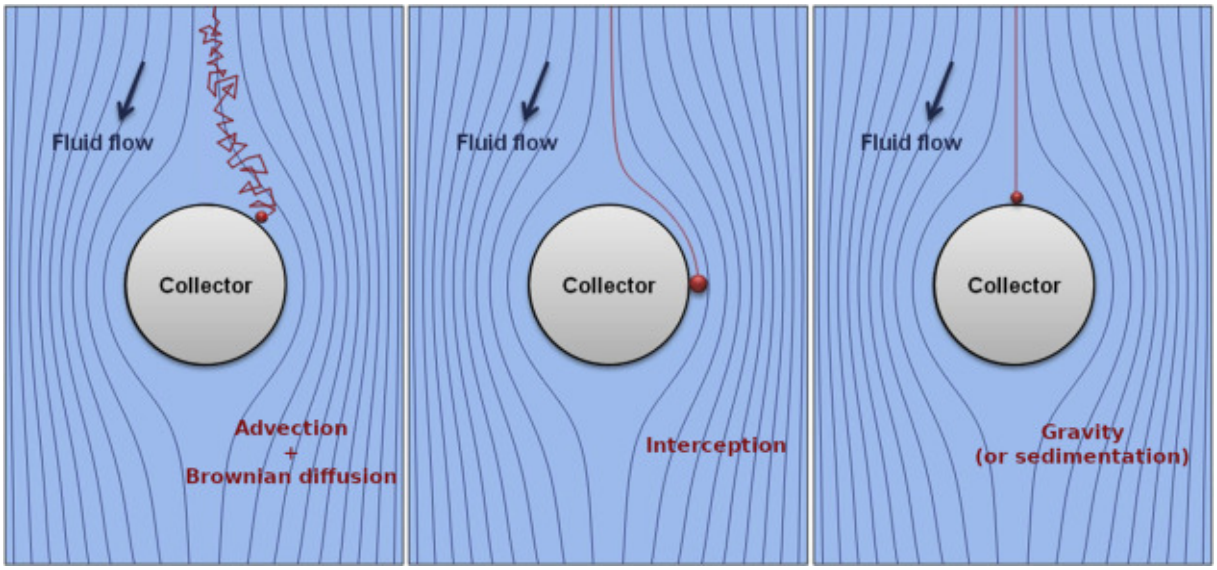

Figure 5.3: The three major mechanisms controlling particle deposition onto a collector: gravity, interception (i.e., the combination of advection and steric effect), and Brownian motion (i.e., the combination of advection and Brownian diffusion (Boccardo et al., 2020).

For the calculation of the different mechanisms, some factors are needed. We define the spherical Happel correction factor, A_{sph}, to account for the flow perturbation of surrounding collector grains as Happel (1958),

$$A_{sph} = \frac{2(1-\gamma^{5/3})}{2-\gamma^{1/3}+3\gamma^{5/3}-2\gamma^2}, \tag{5.21}$$

where $\gamma = 1-\phi$ is the volume fraction of the collector.

The aspect ratio, N_R, reads,

$$N_R = \frac{D_p}{D_c}, \tag{5.22}$$

the Peclet number, N_{Pe}, is,

$$N_{Pe} = \frac{U_\infty D_c}{\phi D}, \tag{5.23}$$

the Van der Waals number, N_{vdw}, expressed as,

$$N_{vdw} = \frac{A_H}{k_B T}, \tag{5.24}$$

the attraction number, N_A, reads,

$$N_A = \frac{A_H \phi}{12\pi\mu_f D_p^2 U_\infty}, \tag{5.25}$$

and the gravitation number, N_G, expressed as,

$$N_G = \frac{D_p^2(\rho_p - \rho_f)g\phi}{18\mu_f U_\infty}. \tag{5.26}$$

5.2.1 Interception capture

Interception deposition refers to the capture of a finite-size particle non-interacting (no long-range interactions). Here, the particle follows the undisturbed fluid streamlines driven by inertia and is captured when it touches the collector.

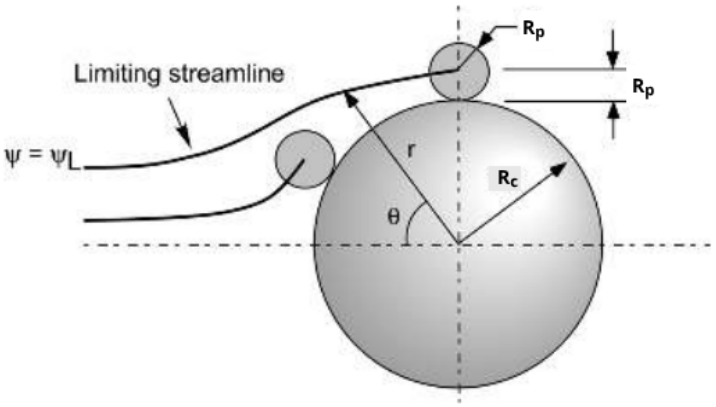

Figure 5.4: Capture due to interception by a spherical collector. Ψ_L is the limiting streamline at which the particles are intercepted by the collector. Modified after Masliyah and Bhattacharjee (2005).

Fig. 5.4 shows the sketch of the interception deposition of a spherical particle. All particles whose centers are above the limiting streamline Ψ_{Lim} will not be intercepted by the collector. In the case of large collector ($D_p/D_c \ll 1$) and Stokes flow ($Re \to 0$), the interception capture efficiency η_I for cylindrical collectors describes (Spielman and Goren, 1970),

$$\eta_I = 2A_{cyl}N_R^2, \tag{5.27}$$

where R_c and R_p are the collector and the particle radii, respectively. A_{cyl} is a dimensionless parameter that expresses the modification of the streamlines due to the presence of other collectors. Faxen (1946) provided a formula for the hydrodynamic flow parameter A_{cyl} for an isolated cylinder of length, l, as :

$$A_{cyl} = \frac{1}{2}\left[\ln\left(\frac{l}{R_c}\right) - 0.9157 + 1.724\left(\frac{R_c}{l}\right)^2 - 1.73\left(\frac{R_c}{l}\right)^4\right]^{-1} \tag{5.28}$$

Note that the interception deposition ignores the enhanced hydrodynamic resistance when the particles approach the collector.

For spherical collectors, the interception capture efficiency in a packed bed is defined by Yao et al. (1971),

$$\eta_I = \frac{3}{2} A_{sph} N_R^2. \tag{5.29}$$

5.2.2 Diffusion capture

The diffusion capture efficiency of a cylindrical collector, which is often used to describe the efficiency of particle capture by fiber in a filter or aerosol system, can be expressed by the following formula:

$$\eta_D = \frac{2N_{Pe}^{2/3}}{1 + N_{Pe}^{-1/2}}. \tag{5.30}$$

For spherical collectors, Pfeffer (1964) proposed the following equation for the diffusion capture efficiency of a packed bed:

$$\eta_D = 4A_{sph}^{1/3} N_{Pe}^{-2/3}. \tag{5.31}$$

5.2.3 Sedimentation capture

The sedimentation efficiency, η_G, gives the proportion of particles that sedimented on the collector out of the total number of particles approaching it. In the case of large collector ($D_p/D_c \ll 1$), the sedimentation capture efficiency is,

$$\eta_G = \frac{v_s}{U_\infty} \left(\frac{D_p}{D_c} \right)^2, \tag{5.32}$$

where v_s is the velocity at which a particle settles under the influence of gravity considering the balance between the gravitational force and the drag force (see Chapter 2). This formula assumes that the primary mechanism of particle capture is sedimentation where particles settle due to gravity as they approach the collector. For a spherical collector, the sedimentation capture efficiency is $\eta_s = N_G$.

5.2.4 Discussion and limits of the current collector efficiency models

Collector efficiency can be estimated using empirical correlation as shown in Table 5.1 for a spherical collector.

In Fig. 5.5, we compare the evolution of the collector efficiency with the correlation proposed by Yao et al. (1971), Rajagopalan and Tien (1976), Logan et al. (1995), Tufenkji and Elimelech (2003), and Messina et al. (2015). The correlations are plotted for a spherical collector of diameter $D_c = 400\ \mu m$, a porosity medium $\phi = 0.32$, with particle density $\rho_p = 1050\ kg/m^3$, fluid density $\rho_f = 1000\ kg/m^3$, fluid viscosity $\mu_f = 10^{-3}\ Pa.s$, fluid velocity $U_\infty = 4 \times 10^{-5}\ m/s$ and temperature $T = 288\ K$. We see that the deposition is enhanced by attraction and Brownian motion for small particles, and sedimentation for larger ones, while it is decreased by viscous interactions.

However, classic CFT fails to predict η when the repulsive double-layer predominates (Ryan and Elimelech, 1996).

5.3 A new collector efficiency including electrostatic effect

This section investigates the interactions between small particles (colloids) and a large immobile surface called a collector in creeping flow. The collector can be cylindrical as a filter mat, spherical as a granular

Table 5.1: Single collector efficiency equations for a spherical collector.

References	Equations for the collector efficiency, η_0
Yao et al. (1971)	$4A_{sph}^{1/3}N_{Pe}^{-2/3} + \frac{3}{2}N_R^2 + N_G$
Rajagopalan and Tien (1976)	$0.72A_{sph}N_A^{1/8}N_R^{15/8} + 2.4\times10^{-3}A_{sph}N_G^{1.2}N_R^{-0.4} + 4A_{sph}^{1/3}N_{Pe}^{-2/3}$
Logan et al. (1995)	$4A_{sph}^{1/3}N_{Pe}^{-2/3} + A_{sph}N_R^{15/8}N_{vdw}^{1/8} + 0.00338A_{sph}N_G^{1.2}N_R^{-0.4}$
Tufenkji and Elimelech (2003)	$2.4A_{sph}^{1/3}N_R^{-0.081}N_{Pe}^{-0.715}N_{vdw}^{0.052} + 0.55A_{sph}N_R^{1.675}N_A^{0.125} + 0.22N_R^{-0.24}N_G^{1.11}N_{vdw}^{0.053}$
Messina et al. (2015)	$\gamma^2[1.5062A_{sph}N_R^{1.9834} + N_G(1+6.0187N_R^2) + N_{Pe}^{-1}(7.5609+4.9534N_R)/(2-2\gamma) + A_{sph}^{0.1259}N_G^{0.8741}(0.0442+0.122N_R^{0.4210}) + A_{sph}^{0.3662}N_{Pe}^{-0.6338}(2.9352+2.7480N_R^{0.3737}) + N_G^{0.6550}N_{Pe}^{-0.3450}(0.9461+1.1626N_R^{0.6012}) + A_{sph}^{0.1562}N_G^{0.5873}N_{Pe}^{-0.2565}(0.6740+0.7119N_R^{0.5438})]$

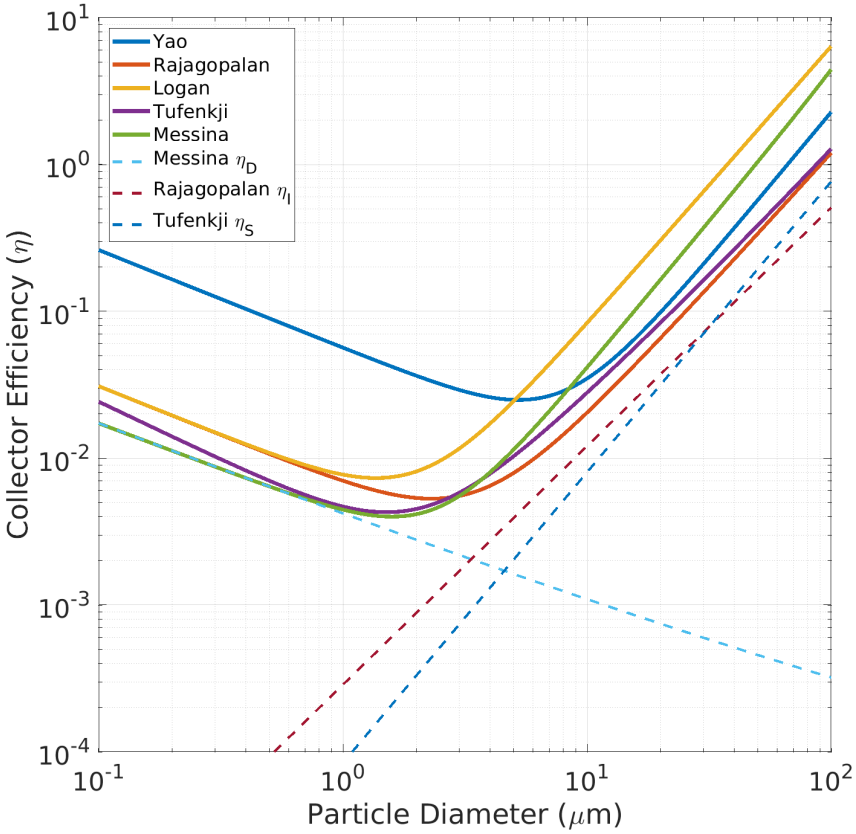

Figure 5.5: Collision efficiencies as a function of particle diameter using the relation from *i)* (Yao et al., 1971), *ii)* (Rajagopalan and Tien, 1976), *iii)* (Logan et al., 1995), *iv)* (Tufenkji and Elimelech, 2003), and *v)* (Messina et al., 2015).

particle in a packed bed, or a surface surrounding the colloidal dispersion. The focus is put on the deposition mechanism of the colloids onto a cylindrical collector as shown in Fig. 5.6. The walls are sufficiently far from the collector to not influence the streamlines near the collector. The thickness is negligible over the width of the geometry ($L \gg e$). We delimitate the study to the capture by electrochemical forces, therefore we neglect gravitational and Brownian motion forces.

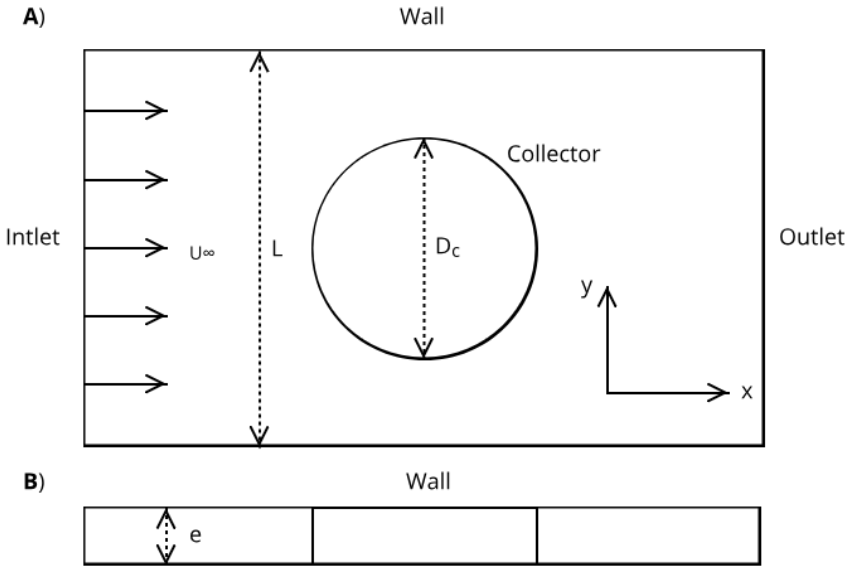

Figure 5.6: The flow geometry considered in this part. The system is two-dimensional with fluid flowing from the inlet to the outlet, with inert boundaries (wall). The central circle is a thin cylinder of diameter D_c (collector). (A) is the top view and (B) is the lateral view.

Using the Lagrangian approach, we describe the trajectories of a single particle around the collector, which led to the capture efficiency of spherical colloids on a large cylindrical collector. In the absence of gravitational forces and the Brownian motion, and hence the diffusion of particles ($Pe \to \infty$), the deposition mechanism will be guided by the particle sizes, the particle inertia, or interparticle forces (attraction + repulsion).

We consider a colloid driven near a cylindrical collector and deviating from its streamline due to Van der Waals attraction and double-layer repulsion acting between the colloid and the collector. The associated collector removal efficiency, η, for a cylindrical collector reads,

$$\eta = \frac{\pi \Psi_L}{e R_c U_\infty}, \tag{5.33}$$

where Ψ_L is the limiting streamline (see Fig. 5.4) obtained by computing the colloid trajectory around the collector.

5.3.1 Colloidal trajectory

To obtain the trajectory of the particle, we use the stream function of the fluid to calculate the particle velocity near the collector. Then with a balance of forces applied to the particle, we obtained a relationship between the radial and the angular and displacement components of the particle.

Fluid stream function

Neglecting the fluid inertia, the flow field is described by a Stokes solution. The undisturbed flow stream function Ψ around an isolated cylindrical collector for $Re \leq 0.5$ is given by (Schrijver et al., 1981),

$$\Psi = \frac{2U_\infty A_{cyl}}{R_c} (r - R_c)^2 \sin\theta, \tag{5.34}$$

where θ is the angular component of the particle position and r is its radial component. The center of the coordinates system is the collector centroid (see Fig. 5.7).

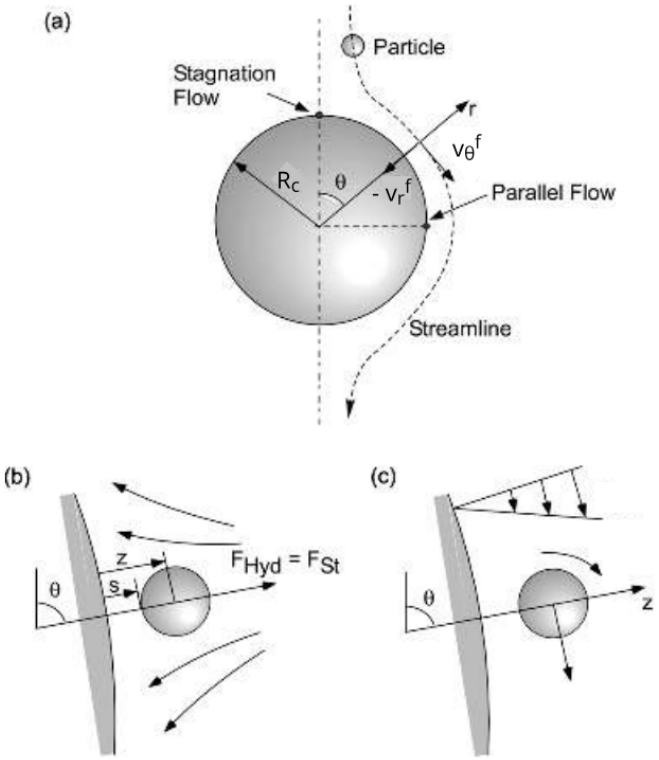

Figure 5.7: Flow geometry of a particle at the vicinity of a larger spherical collector. (a) Overall geometry. The radial and angular velocity components of the fluid, v_r^f, and v_θ^f respectively, are shown for the polar coordinate system with the collector center as the origin. This velocity field can be represented as a linear superposition of two types of flow, namely, stagnation flow (b) and shear flow (c). Modified after Masliyah and Bhattacharjee (2005).

Finally, the radial and angular components of the fluid velocity are obtained using $v_r^f = \frac{1}{r}\frac{\partial\Psi}{\partial\theta}$ and $v_\theta^f = -\frac{\partial\Psi}{\partial r}$, respectively. We have,

$$v_r^f = 2U_\infty A_{cyl} \frac{r}{R_c} \left(1 - \frac{R_c}{r}\right)^2 \cos\theta, \tag{5.35}$$

$$v_\theta^f = -4U_\infty A_{cyl} \frac{r}{R_c} \left(1 - \frac{R_c}{r}\right) \sin\theta. \tag{5.36}$$

Particle trajectory at the vicinity of the collector

Following the approach of Spielman and Fitzpatrick (1973), the velocity of the particle entrained near the collector is a combination of a normal velocity, v_{st}^p, and tangential velocity, v_{sh}^p. We have,

$$v^p = v_{st}^p + v_{sh}^p. \tag{5.37}$$

These velocities are related to the flow velocities around the collector, Eqs. (5.35)-(5.36), using correction functions that account for the wall effects. The particle normal and tangential velocities are related to the stagnant and shear flows using,

$$v_{st}^p = f_2 v_r^f, \tag{5.38}$$

and

$$v_{sh}^p = f_3 v_\theta^f, \tag{5.39}$$

where f_2 and f_3 are dimensionless correction functions accounting for the wall effects. These functions depend on the surface-to-surface separation distance between the collector and the colloid, $s = r - R_c - R_p$. In practice, we use the dimensionless separation gap, $h = s/R_p$. The asymptotic values of the correction functions are given in Table 5.2.

Table 5.2: Asymptotic behavior of the functions characterizing the hydrodynamic interactions (Spielman and Fitzpatrick, 1973).

Functions	$h \to 0$	$h \to \infty$
$f_1(h)$	h	$1 - \frac{9}{8}(h+1)^{-1}$
$f_2(h)$	3.230	$\left(1 - \frac{9}{8}(h+1)^{-1}\right)^{-1}$
$f_3(h)$	$\frac{0.7431}{(0.6376 - 0.2\ln h)}$	$1 - \frac{5}{16}(h+1)^{-3}$

Deposition forces

Then the balance of forces acting on the colloids consisting of the attraction, the repulsion, and the drag forces writes,

$$v_{st}^p = \frac{ds}{dt} = \frac{F_n f_1}{6\pi\mu_f R_p}, \tag{5.40}$$

where

$$F_n = F_{vdw} + F_{edl} + F_{hyd}, \tag{5.41}$$

is the total force entraining the colloid normal to the collector surface and f_1 is the hydrodynamic universal retardation correction function introduced by Brenner (1961) and given in Table 5.2.

The hydrodynamic force is due to flow stagnation by,

$$F_{hyd} = -6\pi\mu_f R_p f_2 v_{st}^p = -\left(6\pi\mu_f R_p f_2\right) 2U_\infty A_{cyl} \frac{r}{R_c}\left(1 - \frac{R_c}{r}\right)^2 \cos\theta. \tag{5.42}$$

Using the dimensionless separation gap, h, the hydrodynamic force acting on the colloid reads,

$$F_{hyd} = -12U_{\infty}A_{cyl}\pi\mu_f R_p f_2 \frac{N_R^2\,(h+1)^2}{N_R\,(h+1)+1}\cos\theta. \tag{5.43}$$

For simplification of the analysis, the non-retarded expression of the London-Van der Waals potential is used, likewise, the zeta potential ζ of the particle and collector are equal. With that, the Van der Waals and the double-layer repulsion forces are expressed as (Suzuki et al., 1969; Usui, 1973),

$$F_{vdw} = -\frac{2A_H}{3R_p(h+2)^2h^2}, \tag{5.44}$$

$$F_{edl} = 4\pi\epsilon_0\epsilon_r\kappa R_p\zeta_p\zeta_c\frac{\exp(-\kappa R_p h)}{1+\exp\left(-\kappa R_p h\right)}, \tag{5.45}$$

where A_H is the Hamaker constant of the particle-liquid-collector system, κ is the inverse Debye length, $\epsilon_0\epsilon_r$ is the absolute permittitivity.

Trajectory equation

From Eq. (5.40) and replacing with Eq. (5.43)-(5.45), the variation of h with time reads,

$$\begin{aligned}\frac{dh}{dt}\left(\frac{6\pi\mu_f R_p^2}{f1}\right) = &-\frac{2A_H}{3R_p(h+2)^2h^2} + 4\pi\epsilon_0\epsilon_r\kappa R_p\zeta_p\zeta_c\frac{\exp(-\kappa R_p h)}{1+\exp(-\kappa R_p h)}\\ &- 12U_{\infty}A_{cyl}\pi\mu_f R_p f_2\frac{N_R^2\,(h+1)^2}{N_R\,(h+1)+1}\cos\theta.\end{aligned} \tag{5.46}$$

The angular motion of the particles around the collector due to the shear velocity is obtained with,

$$R_c\frac{d\theta}{dt} = 4U_{\infty}A_{cyl}N_R\,(1+h)\,f_3\sin\theta. \tag{5.47}$$

The particle trajectory equation, $h(\theta)$, is obtained by the elimination of time combining Eqs. (5.46) and (5.47) and using the chain rule $\frac{dh}{dt} = \frac{dh}{d\theta}\frac{d\theta}{dt}$. We have,

$$4\,(1+h)\,f_3\frac{\sin\theta}{f_1}\frac{dh}{d\theta} = -\frac{Att}{(h+2)^2h^2} + \delta * Att * Dl\frac{\exp(-\delta h)}{1+\exp(-\delta h)} - \frac{2\,(h+1)^2}{N_R\,(h+1)+1}f_2\cos\theta, \tag{5.48}$$

where $\delta = \kappa R_p$ is the dimensionless Debye length, Att is the attraction parameter defined as,

$$Att = \frac{A_H R_c^2}{9\pi\mu_f R_p^4 U_{\infty}A_{cyl}}, \tag{5.49}$$

and Dl, the double-layer parameter defined as,

$$Dl = \frac{6\pi\epsilon_0\epsilon_r R_p\zeta_p\zeta_c}{A_H}. \tag{5.50}$$

The integration of Eq. (5.48) gives the trajectory of the particle. Because we are only interested in the trajectory at the vicinity of the collector to characterize the deposition, this equation can be simplified using an asymptotic analysis in the limits $h \to 0$.

5.3.2 Asymptotic analysis of the particle trajectory near the collector

To perform an asymptotic analysis of Eq. (5.48), we analyze the behavior of the equation in the limits $h \to 0$. This limit provides insights into the dominant terms and how the particles behave near the collector surface.

Let's substitute the asymptotic forms of $f_1(h)$, $f_2(h)$, and $f_3(h)$ as $h \to 0$ into Eq. (5.48) :

$$4\,(1+h)\,\frac{0.7431}{(0.6376-0.2\ln h)}\,\frac{\sin\theta}{h}\,\frac{dh}{d\theta} = -\frac{Att}{(h+2)^2h^2} + \delta Att * Dl\,\frac{\exp(-\delta h)}{1+\exp(-\delta h)} - \frac{2\,(h+1)^2}{N_R\,(h+1)+1} * 3.230\cos\theta.$$

- Then, $\frac{Att}{(h+2)^2h^2}$ can be approximated as $\frac{Att}{4h^2}$ because $h+2 \approx 2$.
- Also, $\exp(-\delta h) \approx 1-\delta h$, and $1+\exp(-\delta h) \approx 2-\delta h$.
- Hence, $\frac{\exp(-\delta h)}{1+\exp(-\delta h)} \approx \frac{1}{2} - \frac{\delta h}{4}$.
- The last term simplifies to $\frac{2}{N_R+1} \cdot 3.230 \cdot \cos\theta$.

The equation simplifies to:

$$4\,(1+h)\,\frac{0.7431\sin\theta}{h\,(0.6376-0.2\ln h)}\,\frac{dh}{d\theta} = -\frac{Att}{4h^2} + \frac{\delta Att * Dl}{2}\left(1-\frac{\delta h}{2}\right) - \frac{6.46\cos\theta}{N_R+1} \tag{5.51}$$

As $h \to 0$, the dominant term on the left is $\frac{1}{h}$, and on the right, the dominant term is $-\frac{Att}{4h^2}$. The equation, therefore, primarily balances these two terms:

$$4 \cdot \frac{0.7431\sin\theta}{0.6376h}\,\frac{dh}{d\theta} \sim -\frac{Att}{4h^2}. \tag{5.52}$$

Rearranging:

$$h\frac{dh}{d\theta} \sim -\frac{0.053626699\,Att}{\sin\theta}. \tag{5.53}$$

This shows that at $h \to 0$, the dominant term is the attraction one. An analytical solution of this equation is:

$$h(\theta) = \sqrt{2k_1 + 2k_2 \ln|\csc\theta - \cot\theta|}. \tag{5.54}$$

where k_1 is obtained using the boundary conditions and $k_2 = 0.053626699 * Att$. However, this particle trajectory equation does not consider the influence of the electrical double layer. A solution for this limitation is presented below.

5.3.3 New collector efficiency

The limiting streamline reads,

$$\Psi_L = \lim_{\theta\to 0}\Psi. \tag{5.55}$$

Therefore, the collector efficiency η reads,

$$\eta = \frac{2\pi A_{cyl}}{eR_c^2}\lim_{\theta\to 0}\left((r(\theta)-R_c)^2\sin\theta\right) \tag{5.56}$$

This equation is only valid near the collector, where particles of small θ coincide with a fluid streamline with a sufficiently small particle ratio ($N_R \ll 1$). Then assuming small angles approximation ($\sin\theta \sim \theta$

and $\cos\theta \sim 1$), Eq. (5.51) becomes,

$$9.3237h \cdot \sin\theta \frac{dh}{d\theta} \sim -2Att + \delta \cdot Att \cdot Dl \cdot h^2, \tag{5.57}$$

which gives the following trajectory equation:

$$h(\theta) = \sqrt{\frac{1}{\delta \cdot Att \cdot Dl}\left(k_1'' \theta^{2\delta \cdot Att \cdot Dl/9.3237} + 2Att\right)}. \tag{5.58}$$

Then by replacing r by h, in Eq. (5.56) we obtain:

$$\eta = \frac{4\pi A_{cyl} N_R^2}{e\delta Dl}. \tag{5.59}$$

This new collector efficiency involves a dimensionless parameter Dl that quantifies the ratio between intermolecular Van der Waals attraction and electric double-layer repulsion forces, and another parameter δ that quantifies the size ratio between the electric double layer and the particles.

5.4 Analysis of deposits morphology

The theoretical approach proposed in this chapter does not account for the morphology of the deposits around the collector. Indeed, because of the strong interplay between advection, diffusion, and deposition, the deposit can be formed by a non-uniform succession of particle layers. This modifies the shape of the collector and implies feedback on the flow profile. The CFD-DEM simulator developed in this Ph.D thesis can bring new insights into the morphology of the deposits. It is also another way to compute the kinetic of deposition. In this section, we first introduce reference microfluidic experiments from the literature that highlight the deposit morphology. Then, we present preliminary simulations of the particle deposition around a single collector.

5.4.1 Experimental results from the literature

Kusaka et al. (2010) study the morphology and breaking of latex particle deposits at a cylindrical collector placed in a microfluidic channel. They use PDMS for the microfluidic channel, and the dimensions of the geometry are presented in Fig. 5.8. The cylindrical collector has a diameter, $D_c = 0.2\ mm$, and is located at the center of the rectilinear flow channel. The width of the channel is $w = 0.9\ mm$ and the micromodel thickness is $e = 0.1\ mm$. Particles consist of polystyrene sulfate latex (PSL) particles of two different diameters 1.04 and 3.6 μm (hereafter denoted as 1040PSL and 3600PSL, respectively).

The deposition patterns obtained in their experiments are plotted in Fig. 5.9 for different injection velocities characterized by the Péclet number. For low Péclet numbers in the limit of their experiment configurations (i.e. $0.3 < Pe < 5$), particle deposits are nearly uniform all over the collector surface except at the rear where particles do not attach. This asymmetry increases along with the Péclet number with more deposits upstream than downstream. For larger flow rates (i.e. $Pe > 120$), a formation of conical dendrites is observed at the upstream stagnation point of the collector. By continuously increasing the Péclet number to values larger than 2000, particles in the dendrite originally formed upstream migrate to the downstream stagnation point to form a new deposit by rolling all around the collector surface.

This set of experiments highlights the variety of deposition patterns around a single collector. However, they do not cover the entire spectrum of parameters. In particular, they were working at high salinity

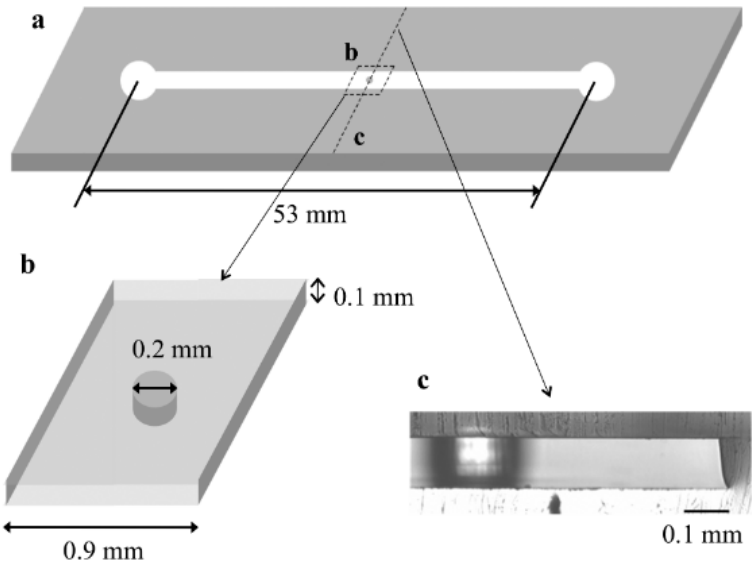

Figure 5.8: (a) Schematic drawing of the PDMS microfluidic channel, (b) Geometrical details for the cylindrical collector surface (zoom of the dashed rectangular part of the microchannel as drawn in panel a), and (c) Cross-section image (along the dashed line indicated in panel a) for the microchannel and cylindrical collector (obtained by optical microscopy). After Kusaka et al. (2010)

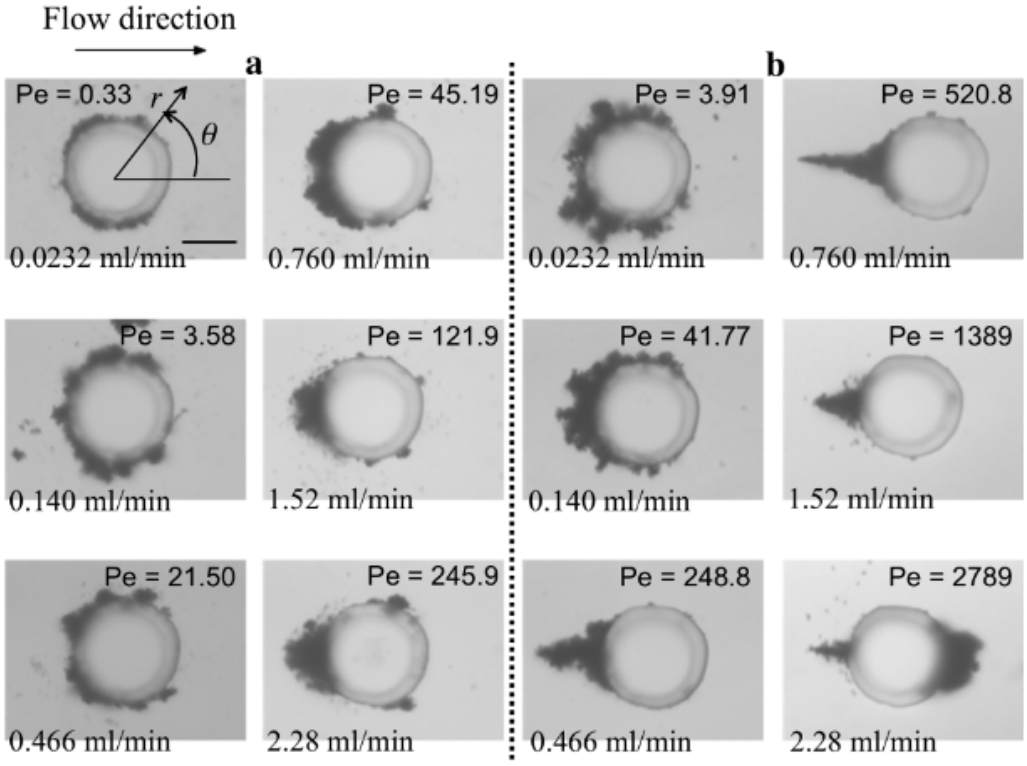

Figure 5.9: Snapshots of deposit morphologies at various flow rates (indicated together with the corresponding Peclet numbers) for 1040PSL (panels a) and 3600PSL (panels b). Deposits were generated in 1.5 M KCl solution at $pH \simeq 6.9$. PSL denominates polystyrene sulfate latex. The scale bar indicates 0.1 mm (Kusaka et al., 2010).

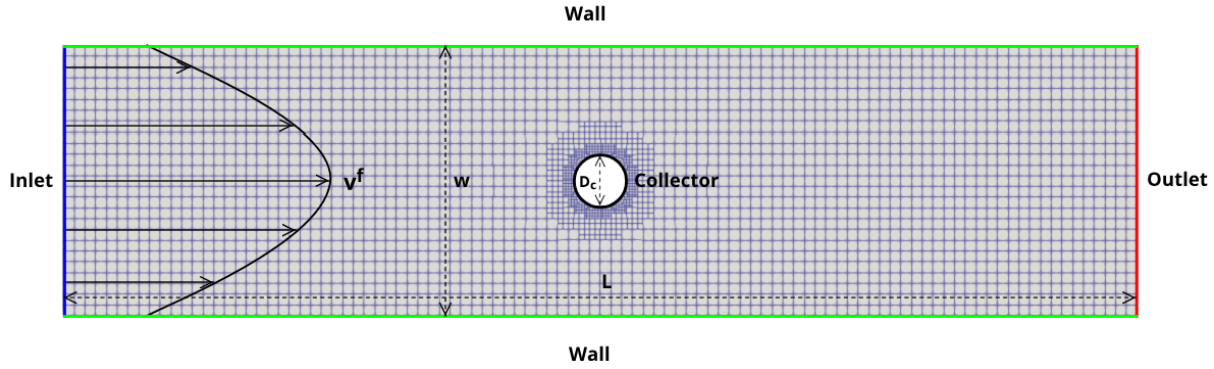

Figure 5.10: Illustrations of the geometry and the mesh of the numerical domain.

(i.e. 1.5 M KCl) and did not probe the impact of repulsive interactions on the particle deposition.

5.4.2 Numerical results with CFD-DEM for colloids

In this part, we use our unresolved-resolved CFD-DEM to investigate colloid deposition on a cylindrical collector. In particular, we want to look at the interplay between fluid salinity and velocity. The geometry is a $L = 366\ \mu m$ long, $w = 100\ \mu m$ wide, and $20\ \mu m$ high rectangular microchannel. A cylindrical collector with a diameter $D_c = 20\ \mu m$ is positioned at the center of the domain. The computational domain is gridded with 41760 cells. A grid refinement is applied at the collector vicinity (see Fig. 5.10). The smallest cell size is $0.62\ \mu m$ and the largest is $3.178\ \mu m$. The cells containing the collector are removed. We apply a constant flow rate at the inlet and a constant pressure at the outlet. No-slip boundary conditions are used for the wall and collector surfaces. Carboxylate polystyrene latex particles of $4.5\ \mu m$ of diameter are injected with a concentration of $C_0 = 0.125\%$ through the inlet. With such particle and grid sizes, the maximum and minimum particle-to-cell ratios are 1.416 and 7.258, respectively, which guarantees resolved simulations at the vicinity of the collector. The properties of the particles and walls are found in Chapter 4. Simulations are three-dimensional.

To highlight the influence of the fluid salinity and velocity, we simulate different couples of flow rate-salinity as (i) $Q = 1\ \mu l/min$ and [NaCl] $= 1\ mM$, (ii) $Q = 1\ \mu l/min$ and [NaCl] $= 10\ mM$, (iii) $Q = 1\ \mu l/min$ and [NaCl] $= 100\ mM$, (iv) $Q = 5\ \mu l/min$ and [NaCl] $= 100\ mM$ and (v) $Q = 10\ \mu l/min$ and [NaCl] $= 100\ mM$. Snapshots of the deposit morphologies are presented in Fig. 5.11. We observe different trends in the deposition patterns.

For slow flow rates (i.e. $Q = 1\ \mu l/min$), the deposition of particles is quasi-uniform around the cylinder. This is consistent with the experiments of Kusaka et al. (2010). However, unlike what we were expecting, we did not observe significant changes with variation of the solution salinity for that flow rate. For higher flow rate (i.e. $Q > 5\ \mu l/min$) and high salinity (i.e. [NaCl] $= 100\ mM$), fewer particles attach to the collector surface and we do not observe the dendrites experimentally obtained by Kusaka et al. (2010).

Several reasons can explain the differences with the experimental data. First, the particle size to the collector diameter is larger in our case which reduces the deposition capacity. Second, we used carboxylate-coated particles while Kusaka et al. (2010) used polystyrene sulfate latex particles. This difference in particle surface properties changes the attractive and repulsive interactions. Moreover, Kusaka et al. (2010) used a solution with a salinity 15 times higher than our simulations which changes the value of the ionic strength in the repulsive potential. Finally, we stop the simulations before they

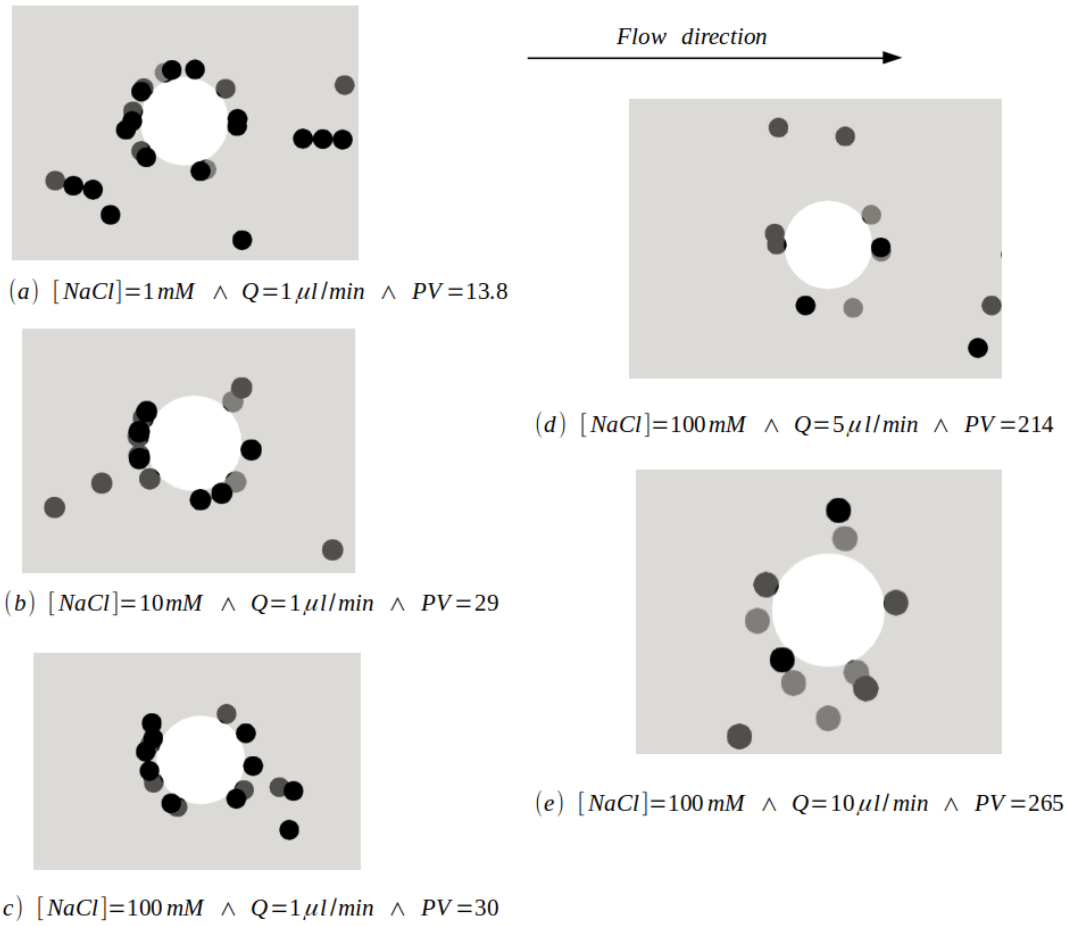

Figure 5.11: Snapshots of deposit morphologies at various flow rates and fluid salinities [NaCl], for 4.5 μm of polystyrene carboxylated latex around a 20 μm cylindrical collector in PDMS obtained with CFD-DEM 3D simulations.

reach a steady morphology.

These simulations highlight the ability of the CFD-DEM model to investigate colloidal deposition kinetics. The results are still preliminary and future work will use parameters closer than the work of Kusaka et al. (2010) for a better comparison.

5.5 Summary of the novelties

This chapter discusses the modeling of particle retention using the colloidal filtration theory. We reviewed the assertions and limitations of the CFT models that describe particle deposition by diffusion, interception, and sedimentation. While some extended CFT models can simulate particle deposition due to attraction, it remains a challenge for cases where the electrical double-layer repulsion is dominant.

We developed a theoretical model in which the secondary minimum capture (repulsion dominant) and the primary minimum capture (attraction dominant) are held together. We derived a new collector efficiency involving the ratio of intermolecular Van der Waals force and the electrical double-layer force through parameters such as δ and Dl. Future work will focus on the confrontation of our model prediction with experimental data. In that regard, well-controlled microfluidic experiments could be developed to assess the deposition over a wide range of flow conditions, particle properties, and fluid salinity.

Another way to validate the approach is to run CFD-DEM simulations. However, it is still necessary to be sure that they can capture the deposit morphology properly. We have performed preliminary simulations in this direction.

Chapter 6

General Conclusion and Perspectives

6.1 General conclusion

Renewable energies such as conventional geothermal power plants exploit natural hydrothermal resources, which include reservoirs of hot water or steam located relatively close to the Earth's surface. One of the critical challenges in the effective exploitation of these systems in interaction with the subsurface through underground wells is maintaining high injectivity into the reservoir. A significant factor influencing injectivity is pore clogging, a phenomenon where the permeability of the reservoir rock decreases due to the accumulation of particles and other substances in the pore spaces. The impact of pore-clogging on injectivity is profound. As the reservoir permeability decreases, the resistance to fluid flow increases, leading to a drop in injectivity. This reduction in injectivity can result in higher operational costs, reduced heat extraction efficiency, and, ultimately, premature decline of the geothermal reservoir. Understanding and mitigating pore clogging is thus crucial for the sustainable management of geothermal resources.

Various physicochemical mechanisms of pore-clogging contribute to the disruption and reduction of injectivity in reservoirs. The subsurface, consisting of a porous matrix (e.g., rocks) and pore spaces (e.g., cavities, fractures), describes a porous medium. Injected fluids contain colloids (including nanoparticles, bacteria, and fine particles) that are ubiquitous and can be suspended or attached to the pore walls. For instance, in-situ precipitation and subsequent transport of reactive solid particles under non-equilibrium conditions or detachment and mobilization of fines—small particles of sand or clay loosely attached to pore walls—by hydrodynamic forces threaten the productivity of geothermal and oil reservoirs by reducing permeability near wells.

We focused on permeability reduction due to particle retention. Three mechanisms are responsible for pore clogging by particles: (i) sieving, (ii) bridging, and (iii) particle aggregation. Sieving refers to the blocking of particles based on size exclusion. Bridging involves the formation of bridge-like structures composed of a few particles arriving simultaneously at the pore entrance where the flow converges. Particle aggregation results from successive deposits of colloidal particles driven by long-range electrochemical forces between the fluid, particles, and the solid surface. Thus, a good understanding of these clogging mechanisms involves a precise method for modeling particle transport. However, the transport of colloids leading to pore clogging is influenced by physical, chemical, and topological parameters. Local fluctuations in fluid parameters such as flow rate, temperature, pH, ionic strength, and ion composition have a significant impact on clogging regimes. Additionally, particle concentration, size, and shape have

been reported as guiding clogging behavior as well as the porous structure.

In this Ph.D. thesis, we present an innovative approach to simulate colloidal transport at the pore scale. We developed a new simulator based on the Computational Fluid Dynamics-Discrete Element Method (CFD-DEM) approach. This approach belongs to the Eulerian-Lagrangian method in which fluid flow is solved on a fixed Eulerian grid using finite volume methods on a computational fluid dynamics platform, and particles are tracked individually in a Lagrangian manner using a discrete element method. CFD-DEM is a four-way coupling. This means that particles are transported by the flow field, there is feedback from particles on the flow, and particles interact with each other and with the walls. Unlike other CFD-DEM approaches, our method is independent of grid resolution and type (i.e., structured and unstructured) and is not limited to particles smaller than cell size. It relies on a hybrid resolved-unresolved formulation for drag force calculation and an efficient search strategy—called peer-to-peer search—to identify CFD cells covered by DEM particles. We also implemented a diffusive smoothing filter to eliminate non-physical oscillations when particles pass through cell-to-cell interfaces.

The continuous flow of the carrying fluid is calculated by solving volume-averaged Navier-Stokes equations (VANS) on the Eulerian grid, which accounts for the presence of particles in grid cells. These equations include a source term corresponding to flow resistance due to the presence of particles. The porosity field of the cells, ϵ, describes the presence of particles in a grid block. It is obtained from the projection of the particle shadow on the grid. The drag force on fluid particles is modeled either using sub-grid models (e.g., Stokes drag force) if the particles are smaller than the grid size (unresolved approach) or by calculating the shear stress at the fluid-particle interface if the particles are larger than the grid size (resolved approach). In contrast, the movement of the particle cloud is calculated by solving Newton's second law for each particle.

Long-range interactions are modeled using the well-established DLVO theory, which consists of combining the attractive van der Waals potential with the repulsive electrical double-layer potential (Stern layer + diffuse layer) as indicated below. Their effect depends on the distance between two particles and between a particle and a solid surface. The DLVO potential has an infinite primary minimum well if the distance between particle surfaces reaches zero. To avoid significant non-physical interpenetration of particles during adhesion, we modified the Hertzian contact by adding an elastic solid-body behavior based on Johnson-Kendall-Robert (JKR) theory. The JKR theory involves applying a constant adhesive force when the distance between two objects is less than the Stern layer thickness (a few nanometers).

Our unresolved-resolved four-way coupling CFD-DEM for colloidal transport is implemented in the open-source finite-volume platform *OpenFOAM version 9*. Our implementation builds upon the existing *denseparticleFoam* solver, coupled with OpenFOAM's internal DEM package to simulate dense or dilute particle flow. We performed a comprehensive set of test cases to verify the robustness and efficiency of our implementation: *(i)* We analyze the efficiency of peer-to-peer search for mapping covered cells: it turns out that our search algorithm is as efficient as the state-of-the-art Hilbert curve search and easier to implement. *(ii)* We verify the implementation of the resolved-unresolved momentum exchange term. For resolved particles, we observe good agreement with reference solutions for different mesh resolutions. *(iii)* We assess the accuracy of our model for different mesh resolutions (resolved and unresolved) in the case of a steel ball sedimenting in a cubic fluid-filled cell. We find excellent agreement with reference datasets, showing a stable and accurate simulation of colloidal transport.

We then used our simulator to study the impact of particle size and concentration on the reduction of permeability. We examined the pore-clogging effect of different particle types (e.g., silica, polystyrene) under various flow and chemical conditions (e.g., pH, ionic strength). Our simulations demonstrated that particle size and concentration significantly impact clogging dynamics. For instance, larger particles tend to bridge and block pore throats more effectively, while smaller particles may penetrate deeper into the pore network and cause clogging further from the well. High particle concentrations lead to a more pronounced reduction in permeability, often resulting in rapid clogging near the injection point. We also observed that the interaction of particles with the porous medium, including the effect of surface charge and roughness, plays a crucial role in clogging behavior. The results obtained from the CFD-DEM simulations provide valuable insights into the mechanisms of pore-clogging and highlight the importance of considering particle properties and environmental conditions in the design and management of geothermal systems. This approach offers a more detailed and accurate understanding of particle transport and retention, which is essential for optimizing fluid injection strategies and maintaining reservoir productivity.

After that, we have revisited the modeling of particle retention using the Colloidal Filtration Theory (CFT). CFT and its variations predict particle deposition due to diffusion, interception, sedimentation, and Van der Waals attraction. Cases for which electric double-layer repulsion is dominant remains misevaluated. Thus, we have developed a theoretical model that considers both the capture at the secondary minimum (in cases of dominant repulsion) and capture at the primary minimum (in cases of dominant attraction). To this end, we derived a new collector efficiency involving a dimensionless parameter Dl that quantifies the ratio between intermolecular Van der Waals attraction and electric double-layer repulsion forces, and another parameter δ that quantifies the size ratio between the electric double layer and the particles.

Finally, we have investigated the deposit morphology using preliminary CFD-DEM simulations around a cylindrical collector in which we vary the salinity and the flow rate. For low flow rates, we observe a quasi uniform particle deposition around the collector in agreement with experimental dataset of the literature. These simulations have highlighted the ability of the CFD-DEM model to investigate colloidal deposition kinetics. The results are still preliminary, and future work will confront the simulation results with microfluidic experiments using identical parameters.

In summary, this PhD thesis presents a novel CFD-DEM-based simulator for colloidal transport and pore-clogging in porous media. The developed approach allows for detailed and accurate simulations of particle movement and interactions, providing valuable insights into the factors affecting permeability reduction in geothermal reservoirs. This research contributes to the sustainable management of geothermal resources by enhancing our understanding of pore-clogging mechanisms and offering tools for optimizing fluid injection practices.

6.2 Perspectives

We highlight several critical perspectives that impact the study of particle behavior in porous media. One significant challenge is the computational intensity of CFD-DEM simulations. While these simulations provide highly detailed insights into colloidal flow and particle interactions at the pore-scale, they require substantial computational resources, making them impractical for large-scale or long-term studies. This

limitation highlights the need for more efficient algorithms or alternative modeling approaches that can reduce the computational burden without sacrificing accuracy. A solution could be to implement the diffusion algorithm for dynamic load balancing (Hu and Blake, 1999). This method is used in parallel computing to distribute computational workload evenly across multiple processors or computing nodes. The goal is to minimize the overall computation time by ensuring that no single processor is overloaded while others are underutilized.

Another important perspective is the necessity of determining the colloidal dispersion coefficient and understanding the relationship between permeability and porosity during particle clogging. This upscaling strategy is essential for translating pore-scale findings to reservoir-scale predictions, yet it remains a complex task. Accurate estimation of the colloidal dispersion coefficient is crucial for predicting how particles will distribute and interact under long-range forces within a larger reservoir, affecting overall injectivity and long-term reservoir performance.

Finally, an innovative averaged Lagrangian approach as a potential solution for upscaling particle transport is required. This approach aims to balance the need for detailed particle tracking with the computational feasibility required for larger-scale simulations. By averaging particle behavior over time and space, this method could provide a more efficient yet accurate means of predicting clogging behavior across different scales. This will represent a significant step forward in making particle transport simulations more accessible for practical geothermal reservoir management in the requirement of validations.

Bibliography

R. Bertani, Geothermal power generation in the world 2010–2014 update report, Geothermics 60 (2016) 31–43.

C. M. Cerda, Mobilization of kaolinite fines in porous media, Colloids and Surfaces 27 (1987) 219–241. doi:10.1016/0166-6622(87)80339-6.

W. Song, X. Liu, T. Zheng, J. Yang, A review of recharge and clogging in sandstone aquifer, Geothermics 87 (2020) 101857. doi:10.1016/j.geothermics.2020.101857.

E. Dressaire, A. Sauret, Clogging of microfluidic systems, Soft Matter 13 (2017) 37–48. doi:10.1039/c6sm01879c.

S. A. Bradford, S. Torkzaban, S. L. Walker, Coupling of physical and chemical mechanisms of colloid straining in saturated porous media, Water Research 41 (2007) 3012–3024. doi:10.1016/j.watres.2007.03.030.

Y. Li, Y. Wang, K. D. Pennell, L. M. Abriola, Investigation of the transport and deposition of fullerene (c60) nanoparticles in quartz sands under varying flow conditions, Environmental Science amp; Technology 42 (2008) 7174–7180. doi:10.1021/es801305y.

S. Torkzaban, S. A. Bradford, J. L. Vanderzalm, B. M. Patterson, B. Harris, H. Prommer, Colloid release and clogging in porous media: Effects of solution ionic strength and flow velocity, Journal of Contaminant Hydrology 181 (2015) 161–171. doi:10.1016/j.jconhyd.2015.06.005.

J. Xia, H. Tian, B. Dou, P. Xiao, J. Zheng, X. Lai, Experimental review: Particle clogging in porous sandstone geothermal reservoirs during tail water reinjection, Journal of Hydrology 625 (2023) 130066. doi:10.1016/j.jhydrol.2023.130066.

E. Rosenbrand, C. Kjøller, J. F. Riis, F. Kets, I. L. Fabricius, Different effects of temperature and salinity on permeability reduction by fines migration in berea sandstone, Geothermics 53 (2015) 225–235. doi:10.1016/j.geothermics.2014.06.004.

Z. Yan, X. Huang, L. Shui, C. Yang, Kinetics of colloidal particle deposition in microfluidic systems under temperature gradients: experiment and modelling, Soft Matter 16 (2020) 3649–3656. doi:10.1039/c9sm02102g.

R. Muneer, M. R. Hashmet, P. Pourafshary, Fine migration control in sandstones: Surface force analysis and application of dlvo theory, ACS Omega 5 (2020) 31624–31639. doi:10.1021/acsomega.0c03943.

R. Yuan, W. Zhang, X. Tao, S. Wang, L. Zhang, Coupled effects of high ph and chemical heterogeneity on colloid retention and release in saturated porous media, Colloids and Surfaces A: Physicochemical and Engineering Aspects 586 (2020) 124285. doi:10.1016/j.colsurfa.2019.124285.

A. J. Pelley, N. Tufenkji, Effect of particle size and natural organic matter on the migration of nano- and microscale latex particles in saturated porous media, Journal of Colloid and Interface Science 321 (2008) 74–83. doi:10.1016/j.jcis.2008.01.046.

W. Sang, V. L. Morales, W. Zhang, C. R. Stoof, B. Gao, A. L. Schatz, Y. Zhang, T. S. Steenhuis, Quantification of colloid retention and release by straining and energy minima in variably saturated porous media, Environmental Science amp; Technology (2013) 130724151622003. doi:10.1021/es400288c.

G. Gerber, M. Bensouda, D. Weitz, P. Coussot, Self-limited accumulation of colloids in porous media, Physical Review Letters 123 (2019) 158005. doi:10.1103/physrevlett.123.158005.

M. Elimelech, C. R. O'Melia, Kinetics of deposition of colloidal particles in porous media, Environmental Science amp; Technology 24 (1990) 1528–1536. doi:10.1021/es00080a012.

G. C. Agbangla, Climent, P. Bacchin, Experimental investigation of pore clogging by microparticles: Evidence for a critical flux density of particle yielding arches and deposits, Separation and Purification Technology 101 (2012) 42–48. doi:10.1016/j.seppur.2012.09.011.

Particles migrating and plugging mechanism in loosen sandstone heavy oil reservoir and the strategy of production with moderate sanding, International Conference on Porous Media and Their Applications inScience, Engineering and Industr, 2014.

G. M. Litton, T. M. Olson, Particle size effects on colloid deposition kinetics: evidence of secondary minimum deposition, Colloids and Surfaces A: Physicochemical and Engineering Aspects 107 (1996) 273–283. doi:10.1016/0927-7757(95)03343-2.

L. Bennacer, N.-D. Ahfir, A. Alem, H. Wang, Coupled effects of ionic strength, particle size, and flow velocity on transport and deposition of suspended particles in saturated porous media, Transport in Porous Media 118 (2017) 251–269. doi:10.1007/s11242-017-0856-6.

A. Hafez, Q. Liu, T. Finkbeiner, R. A. Alouhali, T. E. Moellendick, J. C. Santamarina, The effect of particle shape on discharge and clogging, Scientific Reports 11 (2021). doi:10.1038/s41598-021-82744-w.

M. Auset, A. A. Keller, Pore-scale visualization of colloid straining and filtration in saturated porous media using micromodels, Water Resources Research 42 (2006). doi:10.1029/2005wr004639.

C. Soulaine, L. Girolami, L. Arbaret, S. Roman, Digital rock physics: computation of hydrodynamic dispersion, Oil amp; Gas Science and Technology – Revue d'IFP Energies nouvelles 76 (2021) 51. doi:10.2516/ogst/2021032.

J. Dennis, Properties of stationary (bubbling) fluidised beds relevant to combustion and gasification systems (2013) 77–148e. doi:10.1533/9780857098801.1.77.

Y. Tsuji, T. Kawaguchi, T. Tanaka, Discrete particle simulation of two-dimensional fluidized bed, Powder Technology 77 (1993) 79–87. doi:10.1016/0032-5910(93)85010-7.

S. Whitaker, The Forchheimer equation: A theoretical development, Transport in Porous Media 25 (1996) 27–61. doi:10.1007/bf00141261.

P. A. Cundall, O. D. L. Strack, A discrete numerical model for granular assemblies, Géotechnique 29 (1979) 47–65. doi:10.1680/geot.1979.29.1.47.

B. Derjaguin, Untersuchungen ueber die reibung und adhaesion, iv: Theorie des anhaftens kleiner teilchen, Kolloid-Zeitschrift 69 (1934) 155–164.

E. J. W. E. J. W. Verwey, Theory of the stability of lyophobic colloids; the interaction of sol particles having an electric double layer, by E. J. W. Verwey and J. Th. G. Overbeek, with the collaboration of K. van Nes., Elsevier Pub. Co., New York, 1948.

K. Johnson, K. Kendall, A. Roberts, Surface energy and the contact of elastic solids, Proceedings of the Royal Society of London. A. Mathematical and Physical Sciences 324 (1971) 301–313. doi:10.1098/rspa.1971.0141.

S. Roman, C. Soulaine, M. A. AlSaud, A. Kovscek, H. Tchelepi, Particle velocimetry analysis of immiscible two-phase flow in micromodels, Advances in Water Resources 95 (2016) 199–211. doi:10.1016/j.advwatres.2015.08.015.

C. Soulaine, Micro-continuum modeling: An hybrid-scale approach for solving coupled processes in porous media, Water Resources Research 60 (2024). doi:10.1029/2023wr035908.

Y. Kusaka, J. F. L. Duval, Y. Adachi, Morphology and breaking of latex particle deposits at a cylindrical collector in a microfluidic chamber, Environmental Science amp; Technology 44 (2010) 9413–9418. doi:10.1021/es1026689.

Y. Hu, R. Blake, An improved diffusion algorithm for dynamic load balancing, Parallel Computing 25 (1999) 417–444. doi:10.1016/s0167-8191(99)00002-2.

I. Kaminskaite, S. Piazolo, A. R. Emery, N. Shaw, Q. J. Fisher, The importance of physiochemical processes in decarbonisation technology applications utilizing the subsurface: A review, Earth Science, Systems and Society 2 (2022). doi:10.3389/esss.2022.10043.

H. M. Wyss, T. Franke, E. Mele, D. A. Weitz, Capillary micromechanics: Measuring the elasticity of microscopic soft objects, Soft Matter 6 (2010) 4550. doi:10.1039/c003344h.

V. Ramachandran, H. S. Fogler, Plugging by hydrodynamic bridging during flow of stable colloidal particles within cylindrical pores, Journal of Fluid Mechanics 385 (1999) 129–156. doi:10.1017/s0022112098004121.

B. Dersoir, M. R. de Saint Vincent, M. Abkarian, H. Tabuteau, Clogging of a single pore by colloidal particles, Microfluidics and Nanofluidics 19 (2015) 953–961. doi:10.1007/s10404-015-1624-y.

F. Tale, A. Kalantariasl, M. R. Malayeri, Estimating transition time from deep filtration of particles to external cake during produced water re-injection and disposal, Particulate Science and Technology 39 (2020) 312–321. doi:10.1080/02726351.2020.1713941.

C. L. Gaol, L. Ganzer, S. Mukherjee, H. Alkan, Investigation of clogging in porous media induced by microorganisms using a microfluidic application, Environmental Science: Water Research amp; Technology 7 (2021) 441–454. doi:10.1039/d0ew00766h.

M. O. S. F. V. Anna Kottsova, David Bruhn, M. Brehme, Clogging mechanisms in geothermal operations: theoretical examples and an applied study, Conference: European Geothermal Congress 2022 (2022).

M. Lv, Z. Liu, L. Jia, C. Ji, Visualizing pore-scale foam flow in micromodels with different permeabilities, Colloids and Surfaces A: Physicochemical and Engineering Aspects 600 (2020) 124923. doi:10.1016/j.colsurfa.2020.124923.

F. Civan, Reservoir Formation Damage. FUndamentals Modeling, Assessment and Mitigation, Gulf Professional Publishing, 2007.

Y. Guo, J. Lou, J. K. Cho, N. Tilton, J. Chun, W. Um, X. Yin, K. B. Neeves, N. Wu, Transport of colloidal particles in microscopic porous medium analogues with surface charge heterogeneity: Experiments and the fundamental role of single-bead deposition, Environmental Science amp; Technology 54 (2020) 13651–13660. doi:10.1021/acs.est.0c03225.

A. H. De Zwart, Investigation of clogging processes in unconsolidated aquifers near water supply wells, Ponaen and Looyen BV, Delft (2007).

H. Lindqvist, O. Jokinen, K. Kandler, D. Scheuvens, T. Nousiainen, Single scattering by realistic, inhomogeneous mineral dust particles with stereogrammetric shapes, Atmospheric Chemistry and Physics 14 (2014) 143–157. doi:10.5194/acp-14-143-2014.

C. Fernandes, D. Semyonov, L. L. Ferrás, J. M. Nóbrega, Validation of the cfd-dpm solver dpmfoam in openfoam through analytical, numerical and experimental comparisons, Granular Matter 20 (2018). doi:10.1007/s10035-018-0834-x.

C. Daish, R. Blanchard, K. Gulati, D. Losic, D. Findlay, D. Harvie, P. Pivonka, Estimation of anisotropic permeability in trabecular bone based on microct imaging and pore-scale fluid dynamics simulations, Bone Reports 6 (2017) 129–139. doi:10.1016/j.bonr.2016.12.002.

M. Chaaban, Y. Heider, B. Markert, Upscaling lbm-tpm simulation approach of darcy and non-darcy fluid flow in deformable, heterogeneous porous media, International Journal of Heat and Fluid Flow 83 (2020) 108566. doi:10.1016/j.ijheatfluidflow.2020.108566.

M. Hefny, C. Qin, M. O. Saar, A. Ebigbo, Synchrotron-based pore-network modeling of two-phase flow in nubian sandstone and implications for capillary trapping of carbon dioxide, International Journal of Greenhouse Gas Control 103 (2020) 103164. doi:10.1016/j.ijggc.2020.103164.

Z. Yang, X. Lian, C. Savari, M. Barigou, Evaluating the effectiveness of cfd-dem and sph-dem for complex pipe flow simulations with and without particles, Chemical Engineering Science 288 (2024) 119788. doi:10.1016/j.ces.2024.119788.

Z. Shen, G. Wang, D. Huang, F. Jin, A resolved cfd-dem coupling model for modeling two-phase fluids interaction with irregularly shaped particles, Journal of Computational Physics 448 (2022) 110695. doi:10.1016/j.jcp.2021.110695.

L. Zhan, C. Peng, B. Zhang, W. Wu, A surface mesh represented discrete element method (smr-dem) for particles of arbitrary shape, Powder Technology 377 (2021) 760–779. doi:10.1016/j.powtec.2020.09.046.

V. Puderbach, K. Schmidt, S. Antonyuk, A coupled cfd-dem model for resolved simulation of filter cake formation during solid-liquid separation, Processes 9 (2021) 826. doi:10.3390/pr9050826.

M. Kanitz, J. Grabe, Influence of suction dredging on the failure mechanism of sandy submarine slopes: Revisited with a coupled numerical approach, in: Volume 1: Offshore Technology; Offshore Geotechnics, OMAE2019, American Society of Mechanical Engineers, 2019. doi:10.1115/omae2019-95151.

L. Kinsale, D. S. Nobes, The study of flow through porous media within the near-slot region of sagd operations using psv, in: Proceedings of the 5th International Conference on Experimental Fluid Mechanics-ICEFM, Munich, Germany, 2018, pp. 2–4.

F. Razavi, A. Komrakova, C. F. Lange, Cfd–dem simulation of sand-retention mechanisms in slurry flow, Energies 14 (2021) 3797. doi:10.3390/en14133797.

W. Liu, C.-Y. Wu, Modelling complex particle–fluid flow with a discrete element method coupled with lattice boltzmann methods (dem-lbm), ChemEngineering 4 (2020) 55. doi:10.3390/chemengineering4040055.

L. Huang, J. Liu, F. Zhang, E. Dontsov, B. Damjanac, Exploring the influence of rock inherent heterogeneity and grain size on hydraulic fracturing using discrete element modeling, International Journal of Solids and Structures 176–177 (2019) 207–220. doi:10.1016/j.ijsolstr.2019.06.018.

Y. Wu, Q. Hou, Z. Qi, A. Yu, Particle–pore scale modelling of particle–fluid flows, Chemical Engineering Science 235 (2021) 116500. doi:10.1016/j.ces.2021.116500.

C. Peng, L. Zhan, W. Wu, B. Zhang, A fully resolved sph-dem method for heterogeneous suspensions with arbitrary particle shape, Powder Technology 387 (2021) 509–526. doi:10.1016/j.powtec.2021.04.044.

T. Dymala, S. Wang, K. Jarolin, T. Song, L. Shen, M. Dosta, S. Heinrich, Mp-pic simulation of biomass steam gasification using ilmenite as an oxygen carrier, Atmosphere 13 (2022) 1009. doi:10.3390/atmos13071009.

G. Boccardo, D. L. Marchisio, R. Sethi, Microscale simulation of particle deposition in porous media, Journal of Colloid and Interface Science 417 (2014) 227–237. doi:10.1016/j.jcis.2013.11.007.

C. Soulaine, Computational Microfluidics for Geosciences, Technical Report, Université d'Orléans,, 2022. URL: https://insu.hal.science/tel-03840078.

H. Xu, L. Gong, C. Zhao, Y. Yang, Z. Xu, Analytical considerations of local thermal non-equilibrium conditions for thermal transport in metal foams, International Journal of Thermal Sciences 95 (2015) 73–87. doi:10.1016/j.ijthermalsci.2015.04.007.

N. Nishiyama, T. Yokoyama, Permeability of porous media: Role of the critical pore size, Journal of Geophysical Research: Solid Earth 122 (2017) 6955–6971. doi:10.1002/2016jb013793.

J. Bear, Dynamics of Fluids in Porous Media, Courier Corporation, 1988.

Z. Wang, Y. Teng, M. Liu, A semi-resolved CFD–DEM approach for particulate flows with kernel based approximation and hilbert curve based searching strategy, Journal of Computational Physics 384 (2019) 151–169. doi:10.1016/j.jcp.2019.01.017.

L. Schiller, A. Naumann, A drag coefficient correlation, Zeitschrift des Vereins Deutscher Ingenieure (1935).

J. C. Earnshaw, M. B. J. Harrison, D. J. Robinson, Local order in two-dimensional colloidal aggregation, Physical Review E 53 (1996) 6155–6163. doi:10.1103/physreve.53.6155.

J. H. Masliyah, S. Bhattacharjee, Electrokinetic and Colloid Transport Phenomena, Wiley, 2005. doi:10.1002/0471799742.

T. Zhang, M. Murphy, H. Yu, C. Huh, S. L. Bryant, Mechanistic model for nanoparticle retention in porous media, Transport in Porous Media 115 (2016) 387–406. doi:10.1007/s11242-016-0711-1.

G. Boccardo, T. Tosco, A. Fujisaki, F. Messina, A. Raoof, D. R. Aguilera, E. Crevacore, D. L. Marchisio, R. Sethi, A review of transport of nanoparticles in porous media, Elsevier, 2020, pp. 351–381. doi:10.1016/b978-0-12-818489-9.00013-x.

K.-M. Yao, M. T. Habibian, C. R. O'Melia, Water and waste water filtration. concepts and applications, Environmental Science amp; Technology 5 (1971) 1105–1112. doi:10.1021/es60058a005.

R. Rajagopalan, C. Tien, Trajectory analysis of deep-bed filtration with the sphere-in-cell porous media model, AIChE Journal 22 (1976) 523–533. doi:10.1002/aic.690220316.

B. E. Logan, D. G. Jewett, R. G. Arnold, E. J. Bouwer, C. R. O'Melia, Clarification of clean-bed filtration models, Journal of Environmental Engineering 121 (1995) 869–873. doi:10.1061/(asce)0733-9372(1995)121:12(869).

N. Tufenkji, M. Elimelech, Correlation equation for predicting single-collector efficiency in physicochemical filtration in saturated porous media, Environmental Science amp; Technology 38 (2003) 529–536. doi:10.1021/es034049r.

F. Messina, D. L. Marchisio, R. Sethi, An extended and total flux normalized correlation equation for predicting single-collector efficiency, Journal of Colloid and Interface Science 446 (2015) 185–193. doi:10.1016/j.jcis.2015.01.024.

C. Kleinstreuer, Y. Feng, Computational analysis of non-spherical particle transport and deposition in shear flow with application to lung aerosol dynamics–a review., Journal of biomechanical engineering 135 (2013) 021008–021008.

H. Zhu, Z. Zhou, R. Yang, A. Yu, Discrete particle simulation of particulate systems: Theoretical developments, Chemical Engineering Science 62 (2007) 3378–3396. doi:10.1016/j.ces.2006.12.089.

C. Neuzil, Permeability of clays and shales, Annual Review of Earth and Planetary Sciences 47 (2019) 247–273. doi:10.1146/annurev-earth-053018-060437.

Y.-S. Yu, M.-C. Wang, X. Huang, Evaporative deposition of polystyrene microparticles on PDMS surface, Scientific Reports 7 (2017). doi:10.1038/s41598-017-14593-5.

L. A. Spielman, J. A. Fitzpatrick, Theory for particle collection under london and gravity forces, Journal of Colloid and Interface Science 42 (1973) 607–623. doi:10.1016/0021-9797(73)90047-7.

I. Stober, K. Bucher, Uses of Geothermal Energy, Springer International Publishing, 2021, pp. 43–79. doi:10.1007/978-3-030-71685-1_4.

M. H. Dickson, M. Fanelli, Geothermal energy: utilization and technology, Unesco publishing, 2003.

J. W. Lund, Chena Hot Springs, volume 27, KlamathFalls, 2006.

J. W. Lund, D. H. Freeston, T. L. Boyd, Direct utilization of geothermal energy 2010 worldwide review, Geothermics 40 (2011) 159–180.

A. Manzella, A. Allansdottir, A. Pellizzone, Geothermal energy and society, Springer, 2019.

P. Fleuchaus, B. Godschalk, I. Stober, P. Blum, Worldwide application of aquifer thermal energy storage – a review, Renewable and Sustainable Energy Reviews 94 (2018) 861–876. doi:10.1016/j.rser.2018.06.057.

V.- Stefansson, Geothermal reinjection experience, Geothermics 26 (1997) 99–139. doi:10.1016/s0375-6505(96)00035-1.

R. Itoi, M. Fukuda, K. Jinno, K. Hirowatari, N. Shinohara, T. Tomita, Long-term experiments of waste water injection in the otake geothermal field, japan, Geothermics 18 (1989) 153–159. doi:10.1016/0375-6505(89)90022-9.

S. M. Benson, D. R. Cole, Co2 sequestration in deep sedimentary formations, Elements 4 (2008) 325–331.

S. Fuss, W. F. Lamb, M. W. Callaghan, J. Hilaire, F. Creutzig, T. Amann, T. Beringer, W. de Oliveira Garcia, J. Hartmann, T. Khanna, et al., Negative emissions—part 2: Costs, potentials and side effects, Environmental research letters 13 (2018) 063002.

F. Crotogino, S. Donadei, U. Bünger, H. Landinger, Large-scale hydrogen underground storage for securing future energy supplies, in: 18th World hydrogen energy conference, volume 78, 2010, pp. 37–45.

A. S. Lord, P. H. Kobos, D. J. Borns, Geologic storage of hydrogen: Scaling up to meet city transportation demands, International journal of hydrogen energy 39 (2014) 15570–15582.

C. Smith, J. Mouli-Castillo, D. Van Der Horst, S. Haszeldine, M. Lane, Towards a 100% hydrogen domestic gas network: Regulatory and commercial barriers to the first demonstrator project in the united kingdom, International Journal of Hydrogen Energy 47 (2022) 23071–23083.

H. Bouwer, Artificial recharge of groundwater: hydrogeology and engineering, Hydrogeology Journal 10 (2002) 121–142. doi:10.1007/s10040-001-0182-4.

S. Rinck-Pfeiffer, S. Ragusa, P. Sztanjnbok, T. Vandevelde, Interrelationships between biological, chemical, and physical processes as an analog to clogging in aquifer storage and recovery (asr) wells, Water Research 34 (2000) 2110–2118. doi:10.1016/s0043-1354(99)00356-5.

W. Song, X. Liu, C. Zheng, H. Wang, Migration-deposition characteristics of exogenous particles near the injection well in a groundwater heat pump system, Geothermics 94 (2021) 102097. doi:10.1016/j.geothermics.2021.102097.

M. Russell, Clogging issues associated with managed aquifer recharge methods, IAH Commission on Managing Aquifer Recharge (2013).

S. Feia, J. C. Dupla, S. Ghabezloo, J. Sulem, J. Canou, A. Onaisi, H. Lescanne, E. Aubry, Experimental investigation of particle suspension injection and permeability impairment in porous media, Geomechanics for Energy and the Environment 3 (2015) 24–39. doi:10.1016/j.gete.2015.07.001.

D. Grolimund, M. Borkovec, Long-term release kinetics of colloidal particles from natural porous media, Environmental Science and Technology 33 (1999) 4054–4060. doi:10.1021/es990194m.

F. Eppner, P. Pasquier, P. Baudron, A coupled thermo-hydro-geochemical model for standing column well subject to co_2 degassing and installed in fractured calcareous aquifers, Geomechanics for Energy and the Environment 11 (2017) 14–27. doi:10.1016/j.gete.2017.05.003.

S. L. Sanderson, A. Y. Cheer, J. S. Goodrich, J. D. Graziano, W. T. Callan, Crossflow filtration in suspension-feeding fishes, Nature 412 (2001) 439–441. doi:10.1038/35086574.

H. Wei, B.-h. Chueh, H. Wu, E. W. Hall, C.-w. Li, R. Schirhagl, J.-M. Lin, R. N. Zare, Particle sorting using a porous membrane in a microfluidic device, Lab Chip 11 (2011) 238–245. doi:10.1039/c0lc00121j.

J. Kim, J. Erath, A. Rodriguez, C. Yang, A high-efficiency microfluidic device for size-selective trapping and sorting, Lab Chip 14 (2014) 2480–2490. doi:10.1039/c4lc00219a.

B. Mustin, B. Stoeber, Deposition of particles from polydisperse suspensions in microfluidic systems, Microfluidics and Nanofluidics 9 (2010) 905–913. doi:10.1007/s10404-010-0613-4.

P. Duru, Y. Hallez, A three-step scenario involved in particle capture on a pore edge, Langmuir 31 (2015) 8310–8317. doi:10.1021/acs.langmuir.5b01298.

K. V. Sharp, R. J. Adrian, On flow-blocking particle structures in microtubes, Microfluidics and Nanofluidics 1 (2005) 376–380. doi:10.1007/s10404-005-0043-x.

I. Zuriguel, Invited review: Clogging of granular materials in bottlenecks, Papers in Physics 6 (2014) 060014. doi:10.4279/pip.060014.

D. Genovese, J. Sprakel, Crystallization and intermittent dynamics in constricted microfluidic flows of dense suspensions, Soft Matter 7 (2011) 3889. doi:10.1039/c0sm01338b.

G. H. Goldsztein, J. C. Santamarina, Suspension extraction through an opening before clogging, Applied Physics Letters 85 (2004) 4535–4537. doi:10.1063/1.1818342.

S. S. Massenburg, E. Amstad, D. A. Weitz, Clogging in parallelized tapered microfluidic channels, Microfluidics and Nanofluidics 20 (2016). doi:10.1007/s10404-016-1758-6.

B. Dersoir, La physique du colmatage: de la particule colloïdale au bouchon, Ph.D. thesis, Rennes 1, 2015.

C. Fetter Jr, R. Holzmacher, Groundwater recharge with treated wastewater, Journal (Water Pollution Control Federation) (1974) 260–270.

L. Zhao, W. Zhu, W. Tong, Clogging processes caused by biofilm growth and organic particle accumulation in lab-scale vertical flow constructed wetlands, Journal of Environmental Sciences 21 (2009) 750–757. doi:10.1016/s1001-0742(08)62336-0.

P. Dillon, J. Vanderzalm, D. Page, K. Barry, D. Gonzalez, M. Muthukaruppan, M. Hudson, Analysis of asr clogging investigations at three australian asr sites in a bayesian context, Water 8 (2016) 442. doi:10.3390/w8100442.

P. Ungemach, Reinjection of cooled geothermal brines into sandstone reservoirs, Geothermics 32 (2003) 743–761. doi:10.1016/s0375-6505(03)00074-9.

K. Yuhara, H. Maruyama, Model experiment of effects of air bubbles on the decrease of the ability of the reinjection well, 1996.

Seki, Miyazaki, Nakano, Effects of microorganisms on hydraulic conductivity decrease in infiltration, European Journal of Soil Science 49 (1998) 231–236. doi:10.1046/j.1365-2389.1998.00152.x.

J. Holocher, F. Peeters, W. Aeschbach-Hertig, W. Kinzelbach, R. Kipfer, Kinetic model of gas bubble dissolution in groundwater and its implications for the dissolved gas composition, Environmental Science amp; Technology 37 (2003) 1337–1343. doi:10.1021/es025712z.

C. W. Beckwith, A. J. Baird, Effect of biogenic gas bubbles on water flow through poorly decomposed blanket peat, Water Resources Research 37 (2001) 551–558. doi:10.1029/2000wr900303.

Z. Zhou, Construction and application of clay-swelling diagrams by use of xrd methods, Journal of Petroleum Technology 47 (1995) 306–306. doi:10.2118/29224-pa.

K. Khilar, H. Fogler, The existence of a critical salt concentration for particle release, Journal of Colloid and Interface Science 101 (1984) 214–224. doi:10.1016/0021-9797(84)90021-3.

A. Gens, L. do N. Guimarães, S. Olivella, M. Sánchez, Analysis of the Thmc Behaviour of Compacted Swelling Clay for Radioactive Waste Isolation, Elsevier, 2004, pp. 317–322. doi:10.1016/s1571-9960(04)80060-0.

B. Bennion, Formation damage-the impairment of the invisible, by the inevitable and uncontrollable, resulting in an indeterminate reduction of the unquantifiable!, Journal of Canadian Petroleum Technology 38 (1999). doi:10.2118/99-02-da.

S. R. Bishop, The experimental investigation of formation damage due to the induced flocculation of clays within a sandstone pore structure by a high salinity brine, in: All Days, 97EFDC, SPE, 1997. doi:10.2118/38156-ms.

Q. Zhang, A. Raoof, S. M. Hassanizadeh, Pore-scale study of flow rate on colloid attachment and remobilization in a saturated micromodel, Journal of Environmental Quality 44 (2015) 1376–1383. doi:10.2134/jeq2015.01.0058.

G. Gabriel, G. Inamdar, An experimental investigation of fines migration in porous media, in: SPE Annual Technical Conference and Exhibition?, SPE, 1983, pp. SPE–12168.

J. Ochi, J.-F. Vernoux, Permeability decrease in sandstone reservoirs by fluid injection, Journal of Hydrology 208 (1998) 237–248. doi:10.1016/s0022-1694(98)00169-3.

E. Rosenbrand, C. Haugwitz, P. S. M. Jacobsen, C. Kjøller, I. L. Fabricius, The effect of hot water injection on sandstone permeability, Geothermics 50 (2014) 155–166. doi:10.1016/j.geothermics.2013.09.006.

R. Vaidya, H. Fogler, Formation damage due to colloidally induced fines migration, Colloids and Surfaces 50 (1990) 215–229. doi:10.1016/0166-6622(90)80265-6.

V. L. Morales, B. Gao, T. S. Steenhuis, Grain surface-roughness effects on colloidal retention in the vadose zone, Vadose Zone Journal 8 (2009) 11–20. doi:10.2136/vzj2007.0171.

S. A. Bradford, S. Torkzaban, Colloid interaction energies for physically and chemically heterogeneous porous media, Langmuir 29 (2013) 3668–3676. doi:10.1021/la400229f.

F. A. H. Al-Abduwani, Internal filtration and external filter cake build-up in sandstones (2005).

R. D. Fopa, C. Bianco, N. L. Archilha, A. C. Moreira, T. Pak, A pore-scale investigation of the effect of nanoparticle injection on properties of sandy porous media, Journal of Contaminant Hydrology 253 (2023) 104126. doi:10.1016/j.jconhyd.2022.104126.

J. N. Ryan, M. Elimelech, Colloid mobilization and transport in groundwater, Colloids and surfaces A: Physicochemical and engineering aspects 107 (1996) 1–56.

C. O'Sullivan, Particulate Discrete Element Modelling: A Geomechanics Perspective, volume 4 of *Applied Geotechnics*, Spon Press, 2011.

A. J. Goldman, R. G. Cox, H. Brenner, Slow viscous motion of a sphere parallel to a plane wall—i motion through a quiescent fluid, Chemical engineering science 22 (1967) 637–651.

C. Wen, Y. Yu, Mechanics of fluidization, The Chemical Engineering Progress Symposium Series (1966).

S. Ergun, Fluid flow through packed columns, Chemical Engineering Progress 48 (1952) 89–94.

P. G. Saffman, The lift on a small sphere in a slow shear flow, Journal of fluid mechanics 22 (1965) 385–400.

Y. Xiong, M. Zhang, Z. Yuan, Three-dimensional numerical simulation method for gas–solid injector, Powder Technology 160 (2005) 180–189. doi:10.1016/j.powtec.2005.08.029.

J. N. Israelachvili, Intermolecular and surface forces, Academic press, 2011.

H. Hamaker, The london—van der waals attraction between spherical particles, Physica 4 (1937) 1058–1072. doi:10.1016/s0031-8914(37)80203-7.

D. C. Grahame, The electrical double layer and the theory of electrocapillarity., Chemical Reviews 41 (1947) 441–501. doi:10.1021/cr60130a002.

P. Leroy, N. Devau, A. Revil, M. Bizi, Influence of surface conductivity on the apparent zeta potential of amorphous silica nanoparticles, Journal of Colloid and Interface Science 410 (2013) 81–93. doi:10.1016/j.jcis.2013.08.012.

R. Hogg, T. W. Healy, D. W. Fuerstenau, Mutual coagulation of colloidal dispersions, Transactions of the Faraday Society 62 (1966) 1638. doi:10.1039/tf9666201638.

D. L. Feke, N. D. Prabhu, J. A. Mann, J. A. Mann, A formulation of the short-range repulsion between spherical colloidal particles, The Journal of Physical Chemistry 88 (1984) 5735–5739. doi:10.1021/j150667a055.

E. C. Donaldson, W. Alam, Surface Forces, Elsevier, 2008, pp. 57–119. doi:10.1016/b978-1-933762-29-6.50008-9.

B. Derjaguin, L. Landau, Theory of the stability of strongly charged lyophobic sols and of the adhesion of strongly charged particles in solutions of electrolytes, Progress in Surface Science 43 (1941) 30–59. doi:10.1016/0079-6816(93)90013-l.

R. Feynman, The brownian movement, The Feynman Lectures of Physics 1 (1964) 41. URL: https://feynmanlectures.caltech.edu/I_41.html.

A. Einstein, Un the movement of small particles suspended in statiunary liquids required by the molecular-kinetic theory 0f heat (1905).

Y. Zhou, B. Wright, R. Yang, B. Xu, A. Yu, Rolling friction in the dynamic simulation of sandpile formation, Physica A: Statistical Mechanics and its Applications 269 (1999) 536–553. doi:10.1016/s0378-4371(99)00183-1.

H. P. Zhu, A. B. Yu, Averaging method of granular materials, Physical Review E 66 (2002) 021302. doi:10.1103/physreve.66.021302.

O. R. Walton, R. L. Braun, Viscosity, granular-temperature, and stress calculations for shearing assemblies of inelastic, frictional disks, Journal of Rheology 30 (1986) 949–980. doi:10.1122/1.549893.

O. R. Walton, Numerical simulation of inclined chute flows of monodisperse, inelastic, frictional spheres, Mechanics of Materials 16 (1993) 239–247. doi:10.1016/0167-6636(93)90048-v.

J. H. Ferziger, M. Perić, R. L. Street, Computational Methods for Fluid Dynamics, Springer International Publishing, 2020. doi:10.1007/978-3-319-99693-6.

R. Issa, Solution of the implicitly discretized fluid flow equations by operator-splitting, Journal of Computational Physics 62 (1986) 40–65. doi:10.1016/0021-9991(86)90099-9.

X. He, L.-S. Luo, Lattice boltzmann model for the incompressible navier–stokes equation, Journal of Statistical Physics 88 (1997) 927–944. doi:10.1023/b:joss.0000015179.12689.e4.

H. Chen, S. Kandasamy, S. Orszag, R. Shock, S. Succi, V. Yakhot, Extended boltzmann kinetic equation for turbulent flows, Science 301 (2003) 633–636. doi:10.1126/science.1085048.

Z. Guo, C. Zheng, B. Shi, Discrete lattice effects on the forcing term in the lattice boltzmann method, Physical Review E 65 (2002) 046308. doi:10.1103/physreve.65.046308.

L. Zhu, G. He, S. Wang, L. Miller, X. Zhang, Q. You, S. Fang, An immersed boundary method based on the lattice boltzmann approach in three dimensions, with application, Computers and Mathematics with Applications 61 (2011) 3506–3518. doi:10.1016/j.camwa.2010.03.022.

I. Fatt, The network model of porous media, Transactions of the AIME 207 (1956) 144–181.

Y. Wu, Q. Hou, A. Yu, Pore-scale study of fluid flow and drag force in randomly packed beds of different porosities, Industrial and Engineering Chemistry Research 58 (2019) 5041–5053. doi:10.1021/acs.iecr.8b06418.

R. A. Gingold, J. J. Monaghan, Smoothed particle hydrodynamics: theory and application to non-spherical stars, Monthly Notices of the Royal Astronomical Society 181 (1977) 375–389. doi:10.1093/mnras/181.3.375.

W. K. Liu, S. Jun, Y. F. Zhang, Reproducing kernel particle methods, International Journal for Numerical Methods in Fluids 20 (1995) 1081–1106. doi:10.1002/fld.1650200824.

J. Monaghan, Simulating free surface flows with sph, Journal of Computational Physics 110 (1994) 399–406. doi:10.1006/jcph.1994.1034.

Z.-B. Wang, R. Chen, H. Wang, Q. Liao, X. Zhu, S.-Z. Li, An overview of smoothed particle hydrodynamics for simulating multiphase flow, Applied Mathematical Modelling 40 (2016) 9625–9655. doi:10.1016/j.apm.2016.06.030.

K. Matyash, R. Schneider, F. Taccogna, A. Hatayama, S. Longo, M. Capitelli, D. Tskhakaya, F. X. Bronold, Particle in cell simulation of low temperature laboratory plasmas, Contributions to Plasma Physics 47 (2007) 595–634. doi:10.1002/ctpp.200710073.

C. Hirt, B. Nichols, Volume of fluid (vof) method for the dynamics of free boundaries, Journal of Computational Physics 39 (1981) 201–225. doi:10.1016/0021-9991(81)90145-5.

D. Peng, B. Merriman, S. Osher, H. Zhao, M. Kang, A pde-based fast local level set method, Journal of Computational Physics 155 (1999) 410–438. doi:10.1006/jcph.1999.6345.

D. J. Price, Smoothed particle hydrodynamics: Things i wish my mother taught me, 2011. doi:10.48550/ARXIV.1111.1259.

C. Coetzee, Review: Calibration of the discrete element method, Powder Technology 310 (2017) 104–142. doi:10.1016/j.powtec.2017.01.015.

F. Guo, J. Ye, A study on the applicability and accuracy of the discrete element method for plates based on parameter sensitivity analysis, Buildings 13 (2023) 1567. doi:10.3390/buildings13061567.

H. Kruggel-Emden, S. Rickelt, S. Wirtz, V. Scherer, A study on the validity of the multi-sphere discrete element method, Powder Technology 188 (2008) 153–165. doi:10.1016/j.powtec.2008.04.037.

D. L. van der Haven, I. S. Fragkopoulos, J. A. Elliott, A physically consistent discrete element method for arbitrary shapes using volume-interacting level sets, Computer Methods in Applied Mechanics and Engineering 414 (2023) 116165. doi:10.1016/j.cma.2023.116165.

J. Hanley, Kevin, C. O'Sullivan, Analytical study of the accuracy of discrete element simulations, International Journal for Numerical Methods in Engineering 109 (2016) 29–51. doi:10.1002/nme.5275.

M. van der Hoef, M. van Sint Annaland, N. Deen, J. Kuipers, Numerical simulation of dense gas-solid fluidized beds: A multiscale modeling strategy, Annual Review of Fluid Mechanics 40 (2008) 47–70. doi:10.1146/annurev.fluid.40.111406.102130.

W. Zhong, A. Yu, X. Liu, Z. Tong, H. Zhang, Dem/cfd-dem modelling of non-spherical particulate systems: Theoretical developments and applications, Powder Technology 302 (2016) 108–152. doi:10.1016/j.powtec.2016.07.010.

C. Kloss, C. Goniva, A. Hager, S. Amberger, S. Pirker, Models, algorithms and validation for opensource dem and cfd-dem, Progress in Computational Fluid Dynamics, An International Journal 12 (2012) 140. doi:10.1504/pcfd.2012.047457.

X. Chen, W. Zhong, X. Zhou, B. Jin, B. Sun, Cfd–dem simulation of particle transport and deposition in pulmonary airway, Powder Technology 228 (2012) 309–318. doi:10.1016/j.powtec.2012.05.041.

J. Zhao, T. Shan, Coupled cfd–dem simulation of fluid–particle interaction in geomechanics, Powder Technology 239 (2013) 248–258. doi:10.1016/j.powtec.2013.02.003.

C. Rettinger, U. Rüde, A comparative study of fluid-particle coupling methods for fully resolved lattice boltzmann simulations, Computers and Fluids 154 (2017) 74–89. doi:10.1016/j.compfluid.2017.05.033.

Q. Li, V. Prigiobbe, Numerical simulations of the migration of fine particles through porous media, Transport in Porous Media 122 (2018) 745–759. doi:10.1007/s11242-018-1024-3.

K. Zhou, J. Hou, Q. Sun, L. Guo, S. Bing, Q. Du, C. Yao, A study on particle suspension flow and permeability impairment in porous media using lbm–dem–imb simulation method, Transport in Porous Media 124 (2018) 681–698. doi:10.1007/s11242-018-1089-z.

M. Samari Kermani, S. Jafari, M. Rahnama, A. Raoof, Direct pore scale numerical simulation of colloid transport and retention. part i: Fluid flow velocity, colloid size, and pore structure effects, Advances in Water Resources 144 (2020) 103694. doi:10.1016/j.advwatres.2020.103694.

T. Lu, G. Zang, Y. Yang, S. Wang, Y. Gong, L. Chen, Pore-scale simulation of the influence of grain material of artificial porous media on the motion and deposition of suspended particle, Advances in Water Resources 189 (2024) 104733. doi:10.1016/j.advwatres.2024.104733.

T. Wang, F. Zhang, J. Furtney, B. Damjanac, A review of methods, applications and limitations for incorporating fluid flow in the discrete element method, Journal of Rock Mechanics and Geotechnical Engineering 14 (2022) 1005–1024. doi:10.1016/j.jrmge.2021.10.015.

B. Chareyre, A. Cortis, E. Catalano, E. Barthélemy, Pore-scale modeling of viscous flow and induced forces in dense sphere packings, Transport in Porous Media 92 (2011) 473–493. doi:10.1007/s11242-011-9915-6.

Y. Zhu, C. Liu, H. Liu, Y.-d. Kou, B. Shi, A multi-field and fluid–solid coupling method for porous media based on dem-pnm, Computers and Geotechnics 154 (2023) 105118. doi:10.1016/j.compgeo.2022.105118.

E. Catalano, B. Chareyre, E. Barthélémy, Pore-scale modeling of fluid-particles interaction and emerging poromechanical effects, International Journal for Numerical and Analytical Methods in Geomechanics 38 (2013) 51–71. doi:10.1002/nag.2198.

Y. Tang, Q. Jiang, C. Zhou, A lagrangian-based sph-dem model for fluid–solid interaction with free surface flow in two dimensions, Applied Mathematical Modelling 62 (2018) 436–460. doi:10.1016/j.apm.2018.06.013.

M. Robinson, M. Ramaioli, S. Luding, Fluid–particle flow simulations using two-way-coupled mesoscale sph–dem and validation, International Journal of Multiphase Flow 59 (2014) 121–134. doi:10.1016/j.ijmultiphaseflow.2013.11.003.

M. Shadloo, G. Oger, D. Le Touzé, Smoothed particle hydrodynamics method for fluid flows, towards industrial applications: Motivations, current state, and challenges, Computers and Fluids 136 (2016) 11–34. doi:10.1016/j.compfluid.2016.05.029.

M. Andrews, P. O'Rourke, The multiphase particle-in-cell (mp-pic) method for dense particulate flows, International Journal of Multiphase Flow 22 (1996) 379–402. doi:10.1016/0301-9322(95)00072-0.

D. Snider, An incompressible three-dimensional multiphase particle-in-cell model for dense particle flows, Journal of Computational Physics 170 (2001) 523–549. doi:10.1006/jcph.2001.6747.

B. Tian, J. Zeng, B. Meng, Q. Chen, X. Guo, K. Xue, Compressible multiphase particle-in-cell method (cmp-pic) for full pattern flows of gas-particle system, Journal of Computational Physics 418 (2020) 109602. doi:10.1016/j.jcp.2020.109602.

W. Kinzelbach, The Random Walk Method in Pollutant Transport Simulation, Springer Netherlands, 1988, pp. 227–245. doi:10.1007/978-94-009-2889-3_15.

E. M. LaBolle, G. E. Fogg, A. F. B. Tompson, Random-walk simulation of transport in heterogeneous porous media: Local mass-conservation problem and implementation methods, Water Resources Research 32 (1996) 583–593. doi:10.1029/95wr03528.

R. Herman, I. Prigogine, A two-fluid approach to town traffic, Science 204 (1979) 148–151. doi:10.1126/science.204.4389.148.

S. Schneiderbauer, A. Aigner, S. Pirker, A comprehensive frictional-kinetic model for gas–particle flows: Analysis of fluidized and moving bed regimes, Chemical Engineering Science 80 (2012) 279–292. doi:10.1016/j.ces.2012.06.041.

S. Wang, L. Zhao, C. Wang, Y. Liu, J. Gao, Y. Liu, Q. Cheng, Numerical simulation of gas–solid flow with two fluid model in a spouted-fluid bed, Particuology 14 (2014) 109–116. doi:10.1016/j.partic.2013.04.011.

J. Zhao, G. Liu, X. Yin, X. Li, Z. Gao, H. Lu, Two-fluid simulation of a three-dimensional spout-fluid bed: Flow structures, regimes, and insight into the mechanism of particle–particle momentum transfer, Industrial and Engineering Chemistry Research 60 (2021) 7950–7965. doi:10.1021/acs.iecr.1c00928.

B. Esgandari, S. Rauchenzauner, C. Goniva, P. Kieckhefen, S. Schneiderbauer, A comprehensive comparison of two-fluid model, discrete element method and experiments for the simulation of single- and multiple-spout fluidized beds, Chemical Engineering Science 267 (2023) 118357. doi:10.1016/j.ces.2022.118357.

P. Biesheuvel, Two-fluid model for the simultaneous flow of colloids and fluids in porous media, Journal of Colloid and Interface Science 355 (2011) 389–395. doi:10.1016/j.jcis.2010.12.006.

F. J. Carrillo, I. C. Bourg, A darcy-brinkman-biot approach to modeling the hydrology and mechanics of porous media containing macropores and deformable microporous regions, Water Resources Research 55 (2019) 8096–8121. doi:10.1029/2019wr024712.

M. Quintard, S. Whitaker, Aerosol filtration: An analysis using the method of volume averaging, Journal of Aerosol Science 26 (1995) 1227–1255. doi:10.1016/0021-8502(95)00051-8.

D. Gidaspow, Multiphase flow and fluidization: continuum and kinetic theory descriptions, Academic press, 1994.

A. Ogata, R. B. Banks, A solution of the differential equation of longitudinal dispersion in porous media: fluid movement in earth materials, US Government Printing Office, 1961.

J. Rubin, Transport of reacting solutes in porous media: Relation between mathematical nature of problem formulation and chemical nature of reactions, Water Resources Research 19 (1983) 1231–1252. doi:10.1029/wr019i005p01231.

R. J. LeVeque, Finite Volume Methods for Hyperbolic Problems, Cambridge University Press, 2002. doi:10.1017/cbo9780511791253.

P. Sachdev, Nonlinear Ordinary Differential Equations and Their Applications, Chapman & Hall Pure and Applied Mathematics, Taylor & Francis, 1990. URL: https://books.google.fr/books?id=ngt_QgAACAAJ.

B. Olivier, B. L. Mulongo, Hydrogéologie : multiscience environnementale des eaux souterraines, Universités francophones, Presses de l'Université du Québec AUPELF-UREF, Sainte-Foy (Québec) [Lieu de publication inconnu, 1997.

L. Kristensen, M. L. Hjuler, P. Frykman, M. Olivarius, R. Weibel, L. H. Nielsen, A. Mathiesen, Predrilling assessments of average porosity and permeability in the geothermal reservoirs of the danish area, Geothermal Energy 4 (2016). doi:10.1186/s40517-016-0048-6.

S. H. Wadas, H. von Hartmann, Porosity estimation of a geothermal carbonate reservoir in the german molasse basin based on seismic amplitude inversion, Geothermal Energy 10 (2022). doi:10.1186/s40517-022-00223-5.

J. Kozeny, Uber kapillare lei tung des wassers im boden, sitzungberichte, Royal Academy of Science, Vienna (1927).

P. Carman, Fluid flow through a granular bed: Transactions of the institution of chemical engineers, 1937.

F. Lucia, Petrophysical parameters estimated from visual descriptions of carbonate rocks: a field classification of carbonate pore space, Journal of petroleum technology 35 (1983) 629–637.

E. D. Pittman, Relationship of porosity and permeability to various parameters derived from mercury injection-capillary pressure curves for sandstone (1), AAPG bulletin 76 (1992) 191–198.

G. E. Archie, The electrical resistivity log as an aid in determining some reservoir characteristics, Transactions of the AIME 146 (1942) 54–62.

R. Hilfer, Local porosity theory for electrical and hydrodynamical transport through porous media, Physica A: Statistical Mechanics and its Applications 194 (1993) 406–414. doi:10.1016/0378-4371(93)90372-b.

P. H. Nelson, Permeability-porosity relationships in sedimentary rocks, The log analyst 35 (1994).

S. Whitaker, Flow in porous media i: A theoretical derivation of darcy's law, Transport in Porous Media 1 (1986) 3–25. doi:10.1007/bf01036523.

H. Darcy, Les fontaines publiques de la ville de Dijon: exposition et application des principes à suivre et des formules à employer dans les questions de distribution d'eau, volume 1, Victor dalmont, 1856.

Madhan Nur Agista, A Literature Review and Transport Modelling of Nanoparticles for Enhanced Oil Recovery, Master's thesis, Univesity of Stavanger, 2017. doi:10.13140/RG.2.2.15515.57124.

X. Liu, D. M. O'Carroll, E. J. Petersen, Q. Huang, C. L. Anderson, Mobility of multiwalled carbon nanotubes in porous media, Environmental Science amp; Technology 43 (2009) 8153–8158. doi:10.1021/es901340d.

E. Cullen, D. M. O'Carroll, E. K. Yanful, B. Sleep, Simulation of the subsurface mobility of carbon nanoparticles at the field scale, Advances in Water Resources 33 (2010) 361–371. doi:10.1016/j.advwatres.2009.12.001.

S. A. Bradford, S. R. Yates, M. Bettahar, J. Simunek, Physical factors affecting the transport and fate of colloids in saturated porous media, Water Resources Research 38 (2002). doi:10.1029/2002wr001340.

Y. Wang, Y. Li, J. D. Fortner, J. B. Hughes, L. M. Abriola, K. D. Pennell, Transport and retention of nanoscale c60aggregates in water-saturated porous media, Environmental Science amp; Technology 42 (2008) 3588–3594. doi:10.1021/es800128m.

S. Pirker, D. Kahrimanovic, C. Goniva, Improving the applicability of discrete phase simulations by smoothening their exchange fields, Applied Mathematical Modelling 35 (2011) 2479–2488. doi:10.1016/j.apm.2010.11.066.

J. Marshall, K. Sala, Comparison of methods for computing the concentration field of a particulate flow, International Journal of Multiphase Flow 56 (2013) 4–14. doi:10.1016/j.ijmultiphaseflow.2013.05.009.

Z. Peng, E. Doroodchi, C. Luo, B. Moghtaderi, Influence of void fraction calculation on fidelity of CFD-DEM simulation of gas-solid bubbling fluidized beds, AIChE Journal 60 (2014) 2000–2018. doi:10.1002/aic.14421.

A. Hager, CFD-DEM on Multiple Scales : An Extensive Investigation of Particle-Fluid Interactions, Ph.D. thesis, Johannes Kepler Universitat Linz, 2014.

M. Uhlmann, An immersed boundary method with direct forcing for the simulation of particulate flows, Journal of Computational Physics 209 (2005) 448–476. doi:10.1016/j.jcp.2005.03.017.

S. T. W. Kuruneru, E. Marechal, M. Deligant, S. Khelladi, F. Ravelet, S. C. Saha, E. Sauret, Y. Gu, A comparative study of mixed resolved–unresolved CFD-DEM and unresolved CFD-DEM methods for the solution of particle-laden liquid flows, Archives of Computational Methods in Engineering 26 (2018) 1239–1254. doi:10.1007/s11831-018-9282-3.

W. Poon, M. Haw, Mesoscopic structure formation in colloidal aggregation and gelation, Advances in Colloid and Interface Science 73 (1997) 71–126. doi:10.1016/s0001-8686(97)90003-8.

Y. Liang, N. Hilal, P. Langston, V. Starov, Interaction forces between colloidal particles in liquid: Theory and experiment, Advances in Colloid and Interface Science 134-135 (2007) 151–166. doi:10.1016/j.cis.2007.04.003.

I. Sameut Bouhaik, P. Leroy, P. Ollivier, M. Azaroual, L. Mercury, Influence of surface conductivity on the apparent zeta potential of tio2 nanoparticles: Application to the modeling of their aggregation kinetics, Journal of Colloid and Interface Science 406 (2013) 75–85. doi:10.1016/j.jcis.2013.05.034.

P. Leroy, A. Maineult, S. Li, J. Vinogradov, The zeta potential of quartz. surface complexation modelling to elucidate high salinity measurements, Colloids and Surfaces A: Physicochemical and Engineering Aspects 650 (2022) 129507. doi:10.1016/j.colsurfa.2022.129507.

G. C. Agbangla, É. Climent, P. Bacchin, Numerical investigation of channel blockage by flowing microparticles, Computers and Fluids 94 (2014) 69–83. doi:10.1016/j.compfluid.2014.01.018.

M. Samari-Kermani, S. Jafari, M. Rahnama, A. Raoof, Ionic strength and zeta potential effects on colloid transport and retention processes, Colloid and Interface Science Communications 42 (2021) 100389. doi:10.1016/j.colcom.2021.100389.

H. Abbasfard, G. Evans, R. Moreno-Atanasio, Effect of van der waals force cut-off distance on adhesive collision parameters in DEM simulation, Powder Technology 299 (2016) 9–18. doi:10.1016/j.powtec.2016.05.020.

M. Mihajlovic, I. Roghair, M. V. S. Annaland, On the numerical implementation of the van der waals force in soft-sphere discrete element models for gas-solid fluidization, Chemical Engineering Science 226 (2020) 115794. doi:10.1016/j.ces.2020.115794.

E. Ruckenstein, D. C. Prieve, Adsorption and desorption of particles and their chromatographic separation, AIChE Journal 22 (1976) 276–283. doi:10.1002/aic.690220209.

G. A. Schumacher, T. G. M. van de Ven, Brownian motion of charged colloidal particles surrounded by electric double layers, Faraday Discussions of the Chemical Society 83 (1987) 75. doi:10.1039/dc9878300075.

S. Liu, I. Shikhov, Y. Cui, C. H. Arns, Pore-scale morphology effects on colloid deposition by trajectory tracking simulations, Geoenergy Science and Engineering 227 (2023) 211772. doi:10.1016/j.geoen.2023.211772.

T. Mahmood, A. Amirtharajah, T. W. Sturm, K. E. Dennett, A micromechanics approach for attachment and detachment of asymmetric colloidal particles, Colloids and Surfaces A: Physicochemical and Engineering Aspects 177 (2001) 99–110. URL: https://api.semanticscholar.org/CorpusID:95152653.

C. J. van Oss, Interfacial forces in aqueous media, 2006. doi:10.1201/9781420015768.

C. J. van Oss, The Extended DLVO Theory, Elsevier, 2008, pp. 31–48. doi:10.1016/s1573-4285(08)00203-2.

M. Trofa, G. D'Avino, L. Sicignano, G. Tomaiuolo, F. Greco, P. L. Maffettone, S. Guido, CFD-DEM simulations of particulate fouling in microchannels, Chemical Engineering Journal 358 (2019) 91–100. doi:10.1016/j.cej.2018.09.207.

Y. Zhou, L. Chen, Y. Gong, S. Wang, Pore-scale simulations of particles migration and deposition in porous media using LBM-DEM coupling method, Processes 9 (2021) 465. doi:10.3390/pr9030465.

K. Cheng, J. Zhu, F. Qian, B. Cao, J. Lu, Y. Han, Cfd–dem simulation of particle deposition characteristics of pleated air filter media based on porous media model, Particuology 72 (2023) 37–48. doi:10.1016/j.partic.2022.02.003.

C. Soulaine, S. Roman, A. Kovscek, H. A. Tchelepi, Mineral dissolution and wormholing from a pore-scale perspective, Journal of Fluid Mechanics 827 (2017) 457–483. doi:10.1017/jfm.2017.499.

Z. Y. Zhou, S. B. Kuang, K. W. Chu, A. B. Yu, Discrete particle simulation of particle–fluid flow: model formulations and their applicability, Journal of Fluid Mechanics 661 (2010) 482–510. doi:10.1017/s002211201000306x.

J.-L. Auriault, On the domain of validity of Brinkman's equation, Transport in Porous Media 79 (2009) 215–223. doi:10.1007/s11242-008-9308-7.

C. Soulaine, H. A. Tchelepi, Micro-continuum approach for pore-scale simulation of subsurface processes, Transport in Porous Media 113 (2016) 431–456. doi:10.1007/s11242-016-0701-3.

P. Angot, C.-H. Bruneau, P. Fabrie, A penalization method to take into account obstacles in incompressible viscous flows, Numerische Mathematik 81 (1999) 497–520. doi:10.1007/s002110050401.

J. M. Minto, R. J. Lunn, G. E. Mountassir, Development of a reactive transport model for field-scale simulation of microbially induced carbonate precipitation, Water Resources Research 55 (2019) 7229–7245. doi:10.1029/2019wr025153.

H. Hertz, Uber die beruhrung fester elastischer korper (on the contact of elastic solids), J Reine Angew Math (1882).

N. Deen, M. V. S. Annaland, M. V. der Hoef, J. Kuipers, Review of discrete particle modeling of fluidized beds, Chemical Engineering Science 62 (2007) 28–44. doi:10.1016/j.ces.2006.08.014.

C. V. Oss, R. Good, M. Chaudhury, The role of van der waals forces and hydrogen bonds in "hydrophobic interactions" between biopolymers and low energy surfaces, Journal of Colloid and Interface Science 111 (1986) 378–390. doi:10.1016/0021-9797(86)90041-x.

F. London, The general theory of molecular forces, Transactions of the Faraday Society 33 (1937) 8b. doi:10.1039/tf937330008b.

J. H. Schenkel, J. A. Kitchener, A test of the derjaguin-verwey-overbeek theory with a colloidal suspension, Trans. Faraday Soc. 56 (1960) 161–173. URL: http://dx.doi.org/10.1039/TF9605600161. doi:10.1039/TF9605600161.

J. Gregory, Approximate expressions for retarded van der waals interaction, 1981.

C.-W. Hong, From long-range interaction to solid-bodycontact between colloidal surfaces duringforming, Journal of the European Ceramic Society (1998).

S. Torkzaban, S. A. Bradford, S. L. Walker, Resolving the coupled effects of hydrodynamics and DLVO forces on colloid attachment in porous media, Langmuir 23 (2007) 9652–9660. doi:10.1021/la700995e.

R. Courant, K. Friedrichs, H. Lewy, ber die partiellen differenzengleichungen der mathematischen physik, Mathematische Annalen 100 (1928) 32–74. doi:10.1007/bf01448839.

C. Thornton, C. Randall, Applications of theoretical contact mechanics to solid particle system simulation, Studies in Applied Mechanics 20 (1988) 133–142.

S. J. Burns, P. T. Piiroinen, K. J. Hanley, Critical time step for dem simulations of dynamic systems using a hertzian contact model, International Journal for Numerical Methods in Engineering 119 (2019) 432–451. URL: https://onlinelibrary.wiley.com/doi/abs/10.1002/nme.6056. doi:https://doi.org/10.1002/nme.6056.

Y. Li, Y. Xu, C. Thornton, A comparison of discrete element simulations and experiments for 'sandpiles' composed of spherical particles, Powder Technology 160 (2005) 219–228. doi:10.1016/j.powtec.2005.09.002.

L. Hernquist, N. Katz, TREESPH - a unification of SPH with the hierarchical tree method, The Astrophysical Journal Supplement Series 70 (1989) 419. doi:10.1086/191344.

J. Monaghan, Particle methods for hydrodynamics, Computer Physics Reports 3 (1985) 71–124. doi:10.1016/0167-7977(85)90010-3.

H. Jagadish, Analysis of the hilbert curve for representing two-dimensional space, Information Processing Letters 62 (1997) 17–22. doi:10.1016/s0020-0190(97)00014-8.

G. T. Nguyen, E. L. Chan, T. Tsuji, T. Tanaka, K. Washino, Resolved CFD–DEM coupling simulation using volume penalisation method, Advanced Powder Technology 32 (2021) 225–236. doi:10.1016/j.apt.2020.12.004.

H. Allen, The motion of a sphere in a viscous fluid, The London, Edinburgh, and Dublin Philosophical Magazine and Journal of Science 50 (1900) 519–534. doi:10.1080/14786440009463941.

H.-J. Butt, K. Graf, M. Kappl, Physics and chemistry of interfaces, John Wiley & Sons, 2023.

A. Velásquez-Parra, T. Aquino, M. Willmann, Y. Méheust, T. Le Borgne, J. Jiménez-Martínez, Sharp transition to strongly anomalous transport in unsaturated porous media, Geophysical Research Letters 49 (2022). doi:10.1029/2021gl096280.

B. J. Kirby, E. F. Hasselbrink, Zeta potential of microfluidic substrates: 2. data for polymers, ELECTROPHORESIS 25 (2004) 203–213. doi:10.1002/elps.200305755.

M. J. García-Salinas, M. S. Romero-Cano, F. J. Nieves, Zeta potential study of a polystyrene latex with variable surface charge: influence on the electroviscous coefficient (2000) 112–116. doi:10.1007/3-540-46545-6_23.

J. N. Ryan, M. Elimelech, Colloid mobilization and transport in groundwater, Colloids and Surfaces A: Physicochemical and Engineering Aspects 107 (1996) 1–56. doi:10.1016/0927-7757(95)03384-x.

R. W. Harvey, S. P. Garabedian, Use of colloid filtration theory in modeling movement of bacteria through a contaminated sandy aquifer, Environmental Science and Technology 25 (1991) 178–185. doi:10.1021/es00013a021.

M. Elimelech, C. R. O'melia, Effect of particle size on collision efficiency in the deposition of brownian particles with electrostatic energy barriers, Langmuir 6 (1990) 1153–1163. URL: https://api.semanticscholar.org/CorpusID:96925195.

A. Benamar, N.-D. Ahfir, H. Wang, A. Alem, Particle transport in a saturated porous medium: Pore structure effects, Comptes Rendus. Géoscience 339 (2007) 674–681. doi:10.1016/j.crte.2007.07.012.

F. Caldelas, M. J. Murphy, C. Huh, S. L. Bryant, Factors governing distance of nanoparticle propagation in porous media, in: All Days, 11POS, SPE, 2011. doi:10.2118/142305-ms.

N. Seetha, A. Raoof, M. Mohan Kumar, S. Majid Hassanizadeh, Upscaling of nanoparticle transport in porous media under unfavorable conditions: Pore scale to darcy scale, Journal of Contaminant Hydrology 200 (2017) 1–14. doi:10.1016/j.jconhyd.2017.03.002.

D. C. Prieve, E. Ruckenstein, Effect of london forces upon the rate of deposition of brownian particles, AIChE Journal 20 (1974) 1178–1187. doi:10.1002/aic.690200618.

J. Happel, Viscous flow in multiparticle systems: Slow motion of fluids relative to beds of spherical particles, AIChE Journal 4 (1958) 197–201. doi:10.1002/aic.690040214.

L. Spielman, S. Goren, Particle capture by london forces from low speed flows, Env. Sci. Tech 4 (1970) 135.

H. Faxen, Proc. Roy. Swedish Inst. Eng. Res. (Stockolm) (1946) 1.

R. Pfeffer, Heat and mass transport in multiparticle systems, Industrial amp; Engineering Chemistry Fundamentals 3 (1964) 380–383. doi:10.1021/i160012a018.

J. Schrijver, C. Vreeken, J. Wesselingh, Deposition of particles on a cylindrical collector, Journal of Colloid and Interface Science 81 (1981) 249–256. doi:10.1016/0021-9797(81)90320-9.

H. Brenner, The slow motion of a sphere through a viscous fluid towards a plane surface, Chemical Engineering Science 16 (1961) 242–251. doi:10.1016/0009-2509(61)80035-3.

A. Suzuki, N. Ho, W. Higuchi, Predictions of the particle size distribution changes in emulsions and suspensions by digital computation, Journal of Colloid and Interface Science 29 (1969) 552–564. doi:10.1016/0021-9797(69)90140-4.

S. Usui, Interaction of electrical double layers at constant surface charge, Journal of Colloid and Interface Science 44 (1973) 107–113. doi:10.1016/0021-9797(73)90197-5.

Laurez MAYA FOGOUANG

Transport de Particules Fines. Application à l'Injectivité dans les Réservoirs Géothermaux

Résumé :

Lors de l'exploitation de ressources renouvelables, comme pour l'énergie géothermique, l'injection de fluides dans les réservoirs souterrains peut impacter drastiquement la perméabilité du milieu poreux au voisinage des puits d'injection. Les particules fines en suspension chargées (colloïdes), qu'elles soient initialement présentes dans les fluides injectés ou qu'elles soient détachées de la matrice poreuse par le gradient de pression, vont être transportées, s'agréger, se déposer irréversiblement ou non, et/ou conduire au colmatage des pores. La conséquence de ce colmatage des pores (filtration, pontage ou agrégation de particules) sur la perméabilité conduit à une diminution drastique de l'injectivité dans les puits pouvant entraîner leur abandon. L'étude des phénomènes de colmatage est primordiale pour mieux contrôler l'injectivité et proposer des solutions de décolmatage efficaces afin de maintenir l'exploitation des puits. Ainsi l'enjeu de ce travail porte sur la connaissance de l'évolution de la perméabilité d'un milieu poreux, lors de l'injection d'une suspension en son sein, afin de prédire la chute d'injectivité et d'optimiser des processus d'injections à travers des modèles numériques. A l'échelle des sites d'exploitation (macroscopique), les approches classiques pour modéliser le transport particulaire et le colmatage reposent sur des paramètres heuristiques et des hypothèses restrictives qui limitent leurs capacités prédictives. Notamment, la prise en compte des effets électrochimiques sur le dépôt, l'agrégation et le détachement de particule ainsi que leur rétroaction sur l'écoulement est perfectible. Dans cette thèse, il est donc question d'apporter une solution quant à la modélisation du transport colloïdal dans des milieux poreux. La stratégie adoptée est basée sur une approche de modélisation en cascade d'échelles spatio-temporelles du milieu poreux. Dans un premier temps, nous nous intéressons aux échelles microscopiques (échelle moléculaire, du pore, et du réseaux de pores) où les interfaces particule-fluide et fluide-matrice, sièges des phénomènes hydromécaniques et électrochimiques contrôlant les mécanismes de colmatage, sont bien décrites. Nous avons développé et validé une nouvelle approche numérique pour simuler le transport colloïdal à l'échelle du pore. Elle s'appuie sur une méthode Euler-Lagrange du type CFD-DEM où le fluide est décrit par une phase continue et le transport des particules est représenté par une phase discrète (suivi individuel). En particulier, notre approche s'affranchit des limitations classiques sur la taille des cellules de calcul par rapport à la taille des particules. Le modèle développé nous sert de socle pour étudier la prépondérance des grandeurs physico-chimiques sur le colmatage (vitesse d'infiltration, concentration des particules, pH et salinité de la solution, taille des pores et des particules, etc...). Dans un second temps et dans une logique de remontée en échelle, nous ne considérons les particules non plus comme des éléments discrets mais comme un champ de concentration. Pour ce faire, nous revisitons la théorie de le dépôt des colloïdes autour d'un cylindre afin de déterminer analytiquement des lois macroscopiques de cinétique de dépôt. Enfin, le modèle numérique est utilisé pour simuler la rétention de particules dans le milieux poreux. Il capture les trois principaux mécanismes de colmatage (exclusion de taille, formation d'arche, et agrégation). Il permet de déterminer des relations porosité-perméabilité et la cinétique de rétention en fonction des régimes d'écoulement, de la chimie de la solution et des propriétés de la suspension représentés par des nombres adimensionnés adéquats. Les avancées apportées par ces travaux améliorent la compréhension des mécanismes de colmatage et guident le développement de modèles à plus larges échelles.

Mots clés : Milieux poreux, Transport colloïdal, Agrégation de colloïdes, Colmatage de pores, CFD-DEM, Échelle du pore.

Transport of Fine Particles: Application to Injectivity in Geothermal Reservoirs

Abstract:

When exploiting renewable resources, such as geothermal energy, the injection of fluids into underground reservoirs can drastically impact the permeability of the porous medium near the injection wells. Fine suspended particles (colloids), whether initially present in the injected fluids or detached from the porous matrix by the pressure gradient, are transported, aggregated, irreversibly or reversibly deposited, and/or lead to pore clogging. The consequence of this pore-clogging (filtration, bridging, or particle aggregation) on permeability results in a drastic decrease in injectivity in the wells, potentially leading to their abandonment. Studying clogging phenomena is crucial to control injectivity better and propose effective unclogging solutions to maintain well exploitation. Thus, this work aims to understand the evolution of the permeability of a porous medium during the injection of a suspension, to predict the injectivity drop, and to optimize injection processes through numerical models. At the scale of exploitation sites (macroscopic), classical approaches for modeling particle transport and clogging rely on heuristic parameters and restrictive assumptions that limit their predictive capabilities. Notably, considering electrochemical effects on particle deposition, aggregation, and detachment and their feedback on flow can be improved. This thesis aims to provide a solution for modeling colloidal transport in porous media. The strategy adopted is based on a cascade modeling approach across spatio-temporal scales of the porous medium. First, we focus on microscopic scales (molecular, pore, and pore network scale) where particle-fluid and fluid-matrix interfaces, the sites of hydromechanical and electrochemical phenomena controlling clogging mechanisms, are well described. We have developed and validated a new numerical approach to simulate colloidal transport at the pore scale. It is based on an Euler-Lagrange method of the CFD-DEM type, where a continuous phase describes the fluid, and particle transport is represented by a discrete phase (individual tracking). In particular, our approach overcomes the classical limitations on the size of computational cells relative to the size of particles. The developed model is a foundation for studying the predominance of physicochemical variables on clogging (infiltration velocity, particle concentration, solution pH and salinity, pore and particle size, etc.). Subsequently, and in a logic of upscaling, we no longer consider particles as discrete elements but as a concentration field. To do this, we revisit the theory of colloidal deposition around a cylinder to analytically determine macroscopic deposition kinetic laws. Finally, the numerical model simulates particle retention in porous media. It captures the three main clogging mechanisms (size exclusion, arch formation, and aggregation). It allows for determining porosity-permeability relationships and retention kinetics depending on flow regimes, solution chemistry, and suspension properties represented by appropriate dimensionless numbers. The advances brought by this work improve the understanding of clogging mechanisms and guide the development of models on larger scales.

Keywords: Porous media, Colloidal transport, Colloid aggregation, Pore-clogging, CFD-DEM, Pore-scale.

Geoscience for a sustainable Earth brgm

Institut des Sciences de la Terre d'Orléans (ISTO)
1A rue de la Férollerie, 45071, Orléans, France

RÉGION CENTRE VAL DE LOIRE